TECHNISCHE UNIVERSITÄT
BERGAKADEMIE FREIBERG
The University of Resources. Since 1765.

3-D Inversion of Helicopter-borne Electromagnetic Data

Von der Fakultät für Geowissenschaften, Geotechnik und Bergbau
der Technischen Universität Bergakademie Freiberg

genehmigte

Dissertation

zur Erlangung des akademischen Grades

doctor rerum naturalium
(Dr. rer. nat.)

vorgelegt von **Mathias Scheunert**

geboren am 31.07.1983 in Stollberg i.E.

Gutachter: Prof. Dr. rer. nat. habil. Klaus Spitzer

Tag der Verleihung: Freiberg, den 27.11.2015

To my parents

Abstract

In an effort to improve the accuracy of common 1-D analysis for frequency domain helicopter-borne electromagnetic data at reasonable computing costs, a 3-D inversion approach is developed. The strategy is based on the prior localization of an entire helicopter-borne electromagnetic survey to parts which are actually affected by expected local 3-D anomalies and a separate inversion of those sections of the surveys (*cut-&-paste* strategy).

The discrete forward problem, adapted from the complete Helmholtz equation, is formulated in terms of the secondary electric field employing the finite difference method. The analytical primary field calculation incorporates an interpolation strategy that allows to effectively handle the enormous number of transmitters. For solving the inverse problem, a straightforward Gauss-Newton method and a Tikhonov-type regularization scheme are applied. In addition, different strategies for the restriction of the domain where the inverse problem is solved are used as an implicit regularization. The derived linear least squares problem is solved with Krylov-subspace methods, such as the LSQR algorithm, that are able to deal with the inherent ill-conditioning.

As the helicopter-borne electromagnetic problem is characterized by a unique transmitter-receiver relation, an explicit representation of the Jacobian matrix is used. It is shown that this ansatz is the crucial component of the 3-D HEM inversion. Furthermore, a tensor-based formulation is introduced that provides a fast update of the linear system of the forward problem and an effective handling of the sensitivity related algebraic quantities.

Based on a synthetic data set of a predefined model problem, different application examples are used to demonstrate the principal functionality of the presented algorithm. Finally, the algorithm is applied to a data set obtained from a real field survey in the Northern German Lowlands.

Kurzfassung

Die vorliegende Arbeit beschäftigt sich mit der 3-D Inversion von Hubschrauberelektromagnetikdaten im Frequenzbereich. Das vorgestellte Verfahren basiert auf einer vorhergehenden Eingrenzung des Messgebiets auf diejenigen Bereiche, in denen tatsächliche 3-D Strukturen im Untergrund vermutet werden. Die Resultate der 3-D Inversion dieser Teilbereiche können im Anschluss wieder in die Ergebnisse der Auswertung des komplementären Gesamtdatensatzes integriert werden, welche auf herkömmlichen 1-D Verfahren beruht (sog. *Cut-&-Paste-Strategie*).

Die Diskretisierung des Vorwärtsproblems, abgeleitet von einer Sekundärfeldformulierung der vollständigen Helmholtzgleichung, erfolgt mithilfe der Methode der Finiten Differenzen. Zur analytischen Berechnung der zugehörigen Primärfelder wird ein Interpolationsansatz verwendet, welcher den Umgang mit der enorm hohen Anzahl an Quellen ermöglicht. Die Lösung des inversen Problems basiert auf dem Gauß-Newton-Verfahren und dem Tichonow-Regularisierungsansatz. Als Mittel der zusätzlichen impliziten Regularisierung dient eine räumliche Eingrenzung des Gebiets, auf welchem das inverse Problem gelöst wird. Zur iterativen Lösung des zugrundeliegenden Kleinste-Quadrate-Problems werden Krylov-Unterraum-Verfahren, wie der LSQR Algorithmus, verwendet.

Aufgrund der charakteristischen Sender-Empfänger-Beziehung wird eine explizit berechnete Jakobimatrix genutzt. Ferner wird eine tensorbasierte Problemformulierung vorgestellt, welche die schnelle Assemblierung leitfähigkeitsabhängiger Systemmatrizen und die effektive Handhabung der zur Berechnung der Jakobimatrix notwendigen algebraischen Größen ermöglicht.

Die Funktionalität des beschriebenen Ansatzes wird anhand eines synthetischen Datensatzes zu einem definierten Testproblem überprüft. Abschließend werden Inversionsergebnisse zu Felddaten gezeigt, welche im Norddeutschen Tiefland erhoben worden.

Contents

Abbreviations

1-D	one-dimensional
2-D	two-dimensional
3-D	three-dimensional
BGR	Federal Institute for Geosciences and Natural Resources, Hanover
CG	conjugate gradients
DOF	degrees of freedom
EM	electromagnetic
FD	finite difference
HEM	helicopter-borne electromagnetic
LSQR	an algorithm for sparse linear equations and sparse least squares
RHS	right-hand side
TX/RX	transmitter-receiver
VMD	vertical magnetic dipole

1 Introduction

This study presents a full 3-D inversion approach for frequency domain helicopter-borne electromagnetic (HEM) data. The aim of the inversion is the identification of a 3-D distribution of the electric conductivity in the ground based on a near-surface measurement of artificially induced electromagnetic (EM) fields. It is therefore possible to infer the spatial distribution of geological structures in the soil by the help of the reconstructed information.

Since the early 70s helicopter-borne measurements were established in geophysical electromagnetic surveying (Fraser 1972; Fraser 1978a). A comprehensive review of the historical development of airborne frequency domain EM methods is given by Holladay and Lo (1997). The helicopter-borne electromagnetic method facilitates to manage huge surveys in a very short time and additionally has nearly no application limitations due to the surface appearance of the survey sites. A variety of applications, for example mineral exploration (Fraser 1974; Fraser 1978b), the determination of sea-ice thickness (Becker et al. 1983; Liu and Becker 1990; Haas et al. 2007), ground water exploration (Siemon, Christiansen, et al. 2009), or the imaging of permafrost (Minsley et al. 2012) have been investigated by this method. Today's high demand for metallic raw materials (Gutzmer and Klossek 2014) will assure the future of HEM.

1.1 Principles of helicopter-borne electromagnetic surveying

The physics behind HEM measurement systems, as illustrated in fig. 1.1, can be approximated by an inductive coupling of a three-loop system (Knödel et al. 2005, cf.). An EM transmitter coil exciting a harmonic oscillating magnetic field with constant frequency induces eddy currents particularly in the conductive parts of the subsurface which can be simplified by a fictitious induction coil in the earth. Therefore, the receiver coil records the EM interaction of the free-space source field $\boldsymbol{h}^{\mathrm{air}} \in \mathbb{C}^3$ and a secondary magnetic field $\boldsymbol{h}^{\mathrm{earth}} \in \mathbb{C}^3$, $\boldsymbol{h} = \boldsymbol{h}^{\mathrm{air}} + \boldsymbol{h}^{\mathrm{earth}}$, resulting from the emitted fields of the transmitter coil in the air and the secondary induction processes caused by the eddy currents in the earth, respectively. While the source field is already physically compensated during the measurement (Siemon, Christiansen, et al. 2009), the remaining measured secondary magnetic field is additionally normalized to $\boldsymbol{h}^{\mathrm{air}}$ and given as parts per million (ppm). The transmitter-receiver (TX/RX) geometry considered in this thesis is a horizontal coplanar configuration so that the transmitter loop can be represented by a vertical magnetic dipole (VMD). Due to the receiver coil orientation, a single observed datum $d^{\mathrm{obs}} \in \mathbb{C}^1$ comprises only the vertical component of the magnetic field. Due to the induction processes, the observed field is a complex-valued quantity which is typically split up in a real part and an imaginary part

$$d^{\mathrm{obs}} := R + \mathrm{i}Q. \tag{1.1}$$

Here, R and Q are given by

$$R = 10^6 \cdot \Re\left([h_z - h_z^{\text{air}}]/h_z^{\text{air}}\right) = 10^6 \cdot \Re\left(h_z^{\text{earth}}/h_z^{\text{air}}\right) \in \mathbb{R}^1,$$
$$Q = 10^6 \cdot \Im\left([h_z - h_z^{\text{air}}]/h_z^{\text{air}}\right) = 10^6 \cdot \Im\left(h_z^{\text{earth}}/h_z^{\text{air}}\right) \in \mathbb{R}^1. \tag{1.2}$$

Because of this definition, d^{obs} is occasionally denoted as the *relative secondary field*. The induced currents are mainly horizontal which makes the system particularly sensitive for conductive lateral anomalies. Usually, HEM surveys consist of a grid of parallel flight profiles in two perpendicular flight directions which cover an area up to several hundreds of square kilometers. These surveys are characterized by very short sampling distances (ca. 4 m) along the single flight profiles and comparatively large inter-profile spacings of 50 m to 200 m. In general, magnetic fields for 4 to 6 frequencies from 0.3 kHz to 200 kHz are measured simultaneously at a height of ca. 30 m above the earth's surface with a TX/RX coil separation of 3 m to 8 m (Knödel et al. 2005).

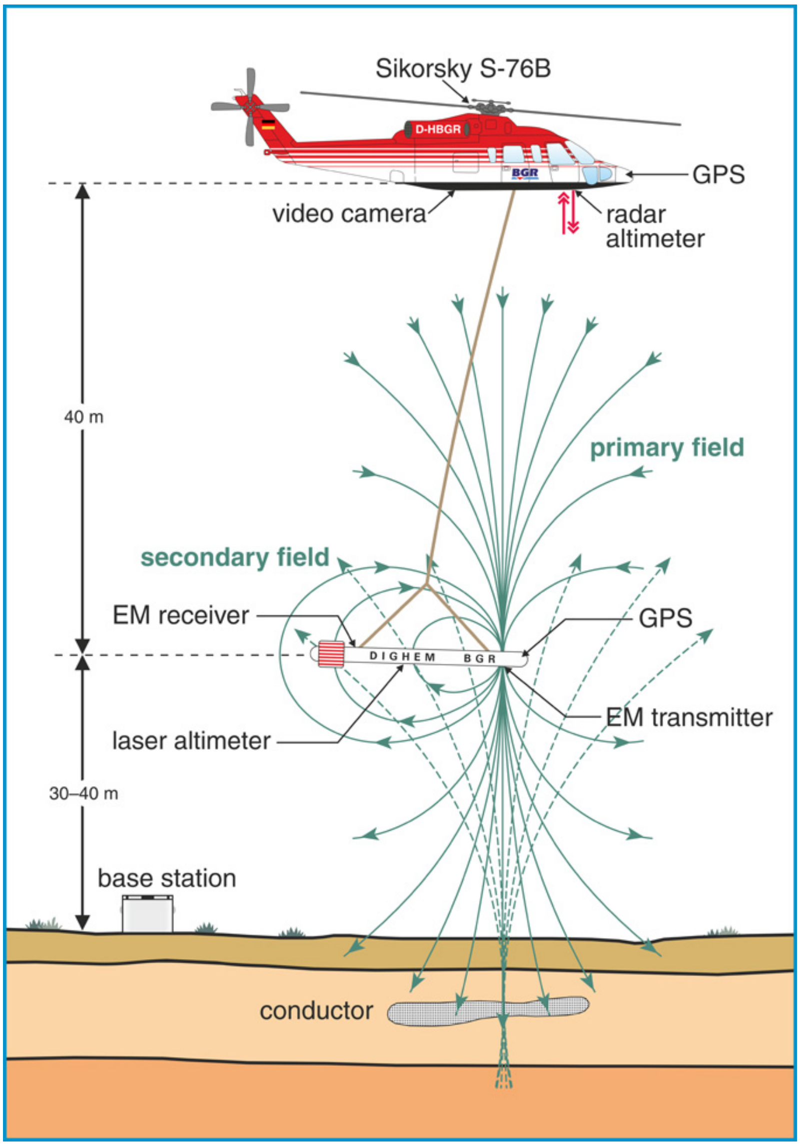

Figure 1.1: Sketch of the HEM two-coil system with the conductor acting as additional coupling coil. Source: Federal Institute for Geosciences and Natural Resources, Hannover

1.2 Necessity of 3-D inversion

Due to the enormous data and model sizes, data interpretation by 1-D inversion schemes (Sattel 2005; Tølbøll and Christensen 2006; Yin and Hodges 2007; Arab-Amiri et al. 2010; Siemon 2012, e. g.) for each single TX/RX position of the entire HEM surveys are still state of the art, even for those parts of the surveys where 3-D conductivity anomalies are expected. Therefore, poorly resolved and distorted structure mappings in those regions are inevitable, especially with regard to their depth extension (Cox et al. 2012; Götze et al. 2013). To overcome that issue, 3-D inversion algorithms are the mandatory next step. A short review of current 3-D approaches was given by Wilson et al. (2012). The most promising idea was introduced by Cox and Zhdanov (2007a) and Cox et al. (2010) with the concept of a moving footprint. Based on the 3-D integral equation method (Cox and Zhdanov 2007b) and the localized quasi-linear inversion (Zhdanov and Tartaras 2002), the approach exploits the spatial narrowness of the sensitivity footprints for each TX/RX pair. Hence, the computational effort of evaluating the forward problem and the elements of the Jacobian matrix is governed only by small sub problems, which tremendously reduces the total calculation time. The resulting sparse minimization problem is finally solved by Krylov-subspace methods.

1.3 Merging the benefits of 1-D and 3-D inversion

The inversion approach presented in this thesis is based on a cut-&-paste strategy. In a first preliminary step, the entire HEM survey is localized to only those parts which are actually affected by an expected local 3-D anomaly (Ullmann, Siemon, et al. 2013). For that, image processing algorithms are applied to the horizontal gradient of the apparent conductivity which is directly derived from the HEM field data. After locating the distorted areas, an averaged half-space parameter set can be excluded. While the remaining parts are effectively inverted with standard 1-D routines, the small sub-areas (only a few km^2) are proceeded with the introduced 3-D inversion algorithm, ensuring accurate inversion models. Subsequently, these results are reintegrated in the 1-D solution which itself acts as reference model providing a smooth transition at the internal boundaries.

The presented algorithm exploits a discrete forward operator that is formulated in terms of the secondary electric field (Schwarzbach et al. 2011) and employs the finite difference method (Newman and Alumbaugh 1995; Börner 2010). The required primary fields are analytically calculated by a recursion algorithm (Ward and Hohmann 1988; Scheunert et al. 2013), incorporating an interpolation approach that facilitates to deal with several thousands of TX/RX positions. The resulting systems of linear equations subsequently yield expressions for the gradient and the Jacobian matrix (Rodi 1976; McGillivray and Oldenburg 1990) of the minimization problem that is, however, formulated in terms of the total field. An elegant handling of the related algebraic expressions is provided by a tensor-based problem formulation. The inverse problem is based on a straightforward Gauss-Newton method which incorporates a Tikhonov-type regularization scheme (Nocedal and Wright 2006). Therein, different types of weighting strategies are introduced, including implicit regularization approaches which focus on reducing the number of model parameters by decoupling the discretization grids of the forward and inverse problem (Commer and Newman 2008). Resulting from the unique TX/RX relation of the HEM problem, an explicit representation of the Jacobian matrix is used. The derived linear least squares problem is solved with Krylov-subspace methods, such as the LSQR algorithm (Hestenes and Stiefel 1952; Paige and Saunders 1982), that are able to deal with the inherent ill-conditioning. Finally, an inexact line search strategy is applied (Nocedal and Wright 2006) which ensures the convergence of the minimization problem. Numerical examples mainly refer to the airborne geophysical system of the Federal Institute for Geosciences and Natural Resources (BGR) that utilizes a horizontal coplanar coil pair, operating at 5 frequencies of 387 Hz, 1820 Hz, 8225 Hz, 41 550 Hz and 133 200 Hz with appropriate coil separations of about 7 m.

1.4 Outline of this thesis

The thesis consists of four main chapters: In the first part, the continuous forward problem in terms of the boundary value problem is introduced. An analytic solution for the 1-D problem (i. e. the variation of the parameter $\sigma(z)$ with respect to the depth z) is derived which also considers displacement currents and that is later on used as a component of the numerical solution approach of the 3-D problem. The second part deals with the numerical solution of the discretized forward problem for complex conductivity distributions (i. e. the arbitrary variation of the parameter $\sigma(x, y, z)$ in all coordinate directions). Beside the description of the applied finite difference scheme, the secondary field approach is explained. Furthermore, a novel tensor formulation and a problem specific notation of the measurement operator, considering the block structure of the multiple source terms, is introduced. A detailed examination of the concrete assembling of the respective quantities used for the implementation in MATLAB® can be found in the appendix. The third chapter is attended to the topic of the HEM inverse problem. It particularity focuses on the derivation and the explicit calculation of the sensitivity related quantities. A HEM-specific regularization setup incorporating implicit approaches is presented and finally, a convenient line search strategy is explained. Straightforward approaches of calculating an initial regularization parameter and defining a convenient termination condition are given. In the last chapter, inversion results are shown that are obtained by the presented inversion approach. Whereas up to this point examples are solely based on a predefined synthetic model, also a concluding inversion result of a field data set is presented.

2 Continuous forward problem

Notation

f	$\in \mathbb{R}_+$	frequency
i		imaginary unit
q	$\in \mathbb{R}_+$	electric charge density
ϵ	$\in \mathbb{R}_+$	electric permittivity
μ	$\in \mathbb{R}_+$	magnetic permeability
σ	$\in \mathbb{R}_+$	electric conductivity
ω	$\in \mathbb{R}_+$	angular frequency
$\boldsymbol{e}$	$\in \mathbb{C}^3$	electric field
$\boldsymbol{f}$	$\in \mathbb{C}^3$	electric vector potential
$\boldsymbol{h}$	$\in \mathbb{C}^3$	magnetic field
$\boldsymbol{j}$	$\in \mathbb{C}^3$	current density
$\boldsymbol{m}_d$	$\in \mathbb{R}^3$	magnetic dipole moment
G	$\in \mathbb{C}$	Green's function
J_i	$\in \mathbb{C}$	Bessel function of the first kind and order i
S_3		cubic spline interpolation
V, Q	$\in \mathbb{C}$	amplitude ratios

2.1 Governing equations

The relations of the time harmonic electric ($\boldsymbol{e}$) and magnetic ($\boldsymbol{h}$) fields with $\boldsymbol{e}, \boldsymbol{h} \sim \mathrm{e}^{i\omega t}$ are stated by the well-known Maxwell's equations

$$\nabla\times \boldsymbol{e} = -\mathrm{i}\omega\mu\, \boldsymbol{h} - \boldsymbol{j}_m, \tag{2.1}$$

$$\nabla\times \boldsymbol{h} = \boldsymbol{j} + \mathrm{i}\omega\epsilon\, \boldsymbol{e} + \boldsymbol{j}_e, \tag{2.2}$$

$$\nabla\cdot \boldsymbol{e} = 0, \tag{2.3}$$

$$\nabla\cdot \boldsymbol{h} = 0. \tag{2.4}$$

Therein, the vector $\boldsymbol{j}$ denotes the electric current density and the terms $\boldsymbol{j}_m$ and $\boldsymbol{j}_e$ are specific source current densities (Ward and Hohmann 1988). Furthermore, $\omega = 2\pi\mathrm{f}$ is the angular frequency, μ the magnetic permeability, and $\epsilon = \epsilon_0\epsilon_r$ the absolute electric permittivity with the vacuum (ϵ_0) and relative (ϵ_r) permittivity, respectively. It is assumed that the medium is isotropic, non-dispersive and free of electric charges. Since only a fixed set of frequencies is utilized in the common HEM measurement systems, it is convenient to consider the problem in the frequency domain.

Initially, concerning the electric field as being excited by an electrical source representation, thus, $\boldsymbol{j}_m = 0$. By substituting Ampère's circuital law (2.2) into the curl of Faraday's law of induction (2.1) and additionally introducing Ohm's law

$$\boldsymbol{j} = \sigma \boldsymbol{e}, \tag{2.5}$$

with the electrical conductivity distribution $\sigma(x, y, z)$, the complete Helmholtz equation for electromagnetic problems in $\mathbb{R}^3$ can be written as

$$\nabla\times \nabla\times \boldsymbol{e} + \mathrm{i}\omega\mu_0 \, \sigma\boldsymbol{e} - \omega^2\mu_0\epsilon \, \boldsymbol{e} = -\mathrm{i}\omega\mu_0 \, \boldsymbol{j}_e. \tag{2.6}$$

Here, without loss of generality, $\mu = \mu_0$ is set to have its vacuum value for the entire space because variations in the magnetic permeability are expected to be negligible compared to the variation in σ or ϵ. Because $\boldsymbol{e}$ is the problem-inherent field (the induction of eddy currents takes place in the conductive medium) it is set to be the modeled quantity, although $\boldsymbol{h}$ is the actually measured field by the HEM method.

To find a solution of (2.6) in a finite modeling domain $\Omega \subset \mathbb{R}^3$, boundary conditions are mandatory. Due to the typical HEM receiver-transmitter geometry, the air is included in that modeling domain. Hence, in general, inhomogeneous Dirichlet boundary conditions are set on the whole model boundary

$$\boldsymbol{e} = \boldsymbol{e}_g \quad \text{on } \mathit{\Gamma} = \delta\Omega. \tag{2.7}$$

Igneous earth

Typically, HEM problems are reduced to the quasi-static approximation

$$\nabla\times \nabla\times \boldsymbol{e} + \mathrm{i}\omega\mu_0 \, \sigma\boldsymbol{e} = -\mathrm{i}\omega\mu_0 \, \boldsymbol{j}_e, \tag{2.8}$$

which can be validated by a simple appraisal, based on the ratio of the occurring displacement ($\boldsymbol{j}_d$) and conduction ($\boldsymbol{j}_c$) currents (Knödel et al. 2005) with

$$\begin{aligned} \boldsymbol{j} &:= \boldsymbol{j}_d + \boldsymbol{j}_c, \\ \boldsymbol{j}_d &= \omega\epsilon \, \boldsymbol{e}, \\ \boldsymbol{j}_c &= \sigma\boldsymbol{e}. \end{aligned} \tag{2.9}$$

Expecting the highest frequency $\mathrm{f} = 133\,200\,\mathrm{Hz}$, a substratum conductivity for igneous rocks of $\sigma = 10^{-4}\,\frac{\mathrm{S}}{\mathrm{m}}$, as well as $\epsilon = \epsilon_0$, the ratio

$$\frac{|\boldsymbol{j}_d|}{|\boldsymbol{j}_c|} \approx 7.4 \times 10^{-2}, \tag{2.10}$$

indicates sufficiently small displacement currents and therefore motivates the neglect of the wave term $\omega^2\mu_0\epsilon \, \boldsymbol{e}$ in (2.6).

Sedimentary and metamorphic earth

If, in contrast, higher resistivities for dry sedimentary or metamorphic rocks of $\sigma = 10^{-6}\,\frac{\mathrm{S}}{\mathrm{m}}$ to $10^{-8}\,\frac{\mathrm{S}}{\mathrm{m}}$ in combination with a relative permittivity of up to $\epsilon_r = 5\,\frac{\mathrm{A\,s}}{\mathrm{V\,m}}$ are assumed (Telford et al. 1990)

$$\frac{|\boldsymbol{j}_d|}{|\boldsymbol{j}_c|} \approx 3.7 \times 10^{3}, \tag{2.11}$$

and thus, a validation of the above mentioned simplification fails. As stated by Yin and Hodges (2005), significant deviations between the solutions of the complete (2.6) and approximated (2.8) equation can be observed.

To consider the general case, the electric permittivity is incorporated in most of the investigations within this thesis. Although displacement currents are included, $\epsilon = \epsilon_0$ is set for numeric examples without any loss of generality.

2.2 1-D solution

If a piece-wise constant conductivity distribution $\sigma = \sigma(z)$ for a horizontally layered earth is given, an analytic solution of (2.6) to (2.7) at arbitrary points within the domain can be evaluated. The basic ideas of its derivation, presented in the following paragraphs, emanate from Ward and Hohmann (1988) and Zhdanov (2009). Deviating from traditional approaches, the electric permittivity and air conductivity are allowed to vary from their vacuum value.

2.2.1 General expressions

The aim is to find expressions for the EM fields with a time dependence of $\mathrm{e}^{i\omega t}$, emitted by a VMD with dipole moment $\boldsymbol{m}_d$, and located at $x = y = 0$ and $z = -h, h > 0$ above a stratified half-space. Without loss of generality, the interface between air and the conductive half-space is set at $z = 0$. It is convenient to describe the behavior of the fields with a vector potential which is consistent to the Maxwell's equations (2.1) to (2.4). Now, concerning a source representation by a pure magnetic source type ($\boldsymbol{j}_e = 0$), it is convenient to use the electric vector potential $\boldsymbol{f}(\boldsymbol{x}, \omega)$, such that there holds

$$\begin{aligned} \boldsymbol{e} &:= -\nabla\times \boldsymbol{f}, \\ \boldsymbol{h} &= -(\sigma + \mathrm{i}\omega\epsilon)\boldsymbol{f} - \nabla\phi, \end{aligned} \tag{2.12}$$

with $\boldsymbol{e} = \boldsymbol{e}(\boldsymbol{x}, \omega)$ and $\boldsymbol{h} = \boldsymbol{h}(\boldsymbol{x}, \omega)$ and the arbitrary scalar potential ϕ. After the application of a gauge condition (Ward and Hohmann 1988)

$$\nabla\phi := -\frac{1}{\mathrm{i}\omega\mu_0}\nabla(\nabla\cdot \boldsymbol{f}), \tag{2.13}$$

and exploiting the vector identity

$$\nabla^2(.) := \nabla\,\nabla\cdot(.) - \nabla\times\nabla\times(.), \tag{2.14}$$

the vector potential $\boldsymbol{f}(\boldsymbol{x}, \omega)$ forms the solution of the inhomogeneous Helmholtz equation

$$\begin{aligned} \nabla^2\boldsymbol{f} + k^2\boldsymbol{f} &= -\boldsymbol{j}_m = -\mathrm{i}\omega\mu_0\,\boldsymbol{m}_d\delta(x, y, z + h)\,, \\ k^2 &= -\mathrm{i}\omega\mu_0\,\sigma + \omega^2\mu_0\epsilon\,, \end{aligned} \tag{2.15}$$

by inserting (2.12) in (2.1). The problem incorporates the specific source term or right-hand side (RHS) vector $\boldsymbol{j}_m$ which expresses a source magnetization current density, associated with a vertical magnetic dipole of moment $\boldsymbol{m}_d$, located in the air at $x = y = 0, z = -h$.

When the source dipole moment is aligned with the downwards oriented z-axis, i. e. $\boldsymbol{m}_d = [0, 0, m]^\top$, also the observed vector potential comprises only a single component

$$\boldsymbol{f}(x, y, z) = [0, 0, f_z(x, y, z)]^\top, \tag{2.16}$$

and (2.12) reads component-wise as

$$\begin{aligned} e_x &= -\frac{\partial f_z}{\partial y} & h_x &= \frac{1}{\mathrm{i}\omega\mu_0}\frac{\partial^2 f_z}{\partial x \partial z}, \\ e_y &= -\frac{\partial f_z}{\partial x} & h_y &= \frac{1}{\mathrm{i}\omega\mu_0}\frac{\partial^2 f_z}{\partial y \partial z}, \\ e_z &= 0 & h_z &= \frac{1}{\mathrm{i}\omega\mu_0}\left(\frac{\partial^2 f_z}{\partial z^2} + k^2 f_z\right). \end{aligned} \tag{2.17}$$

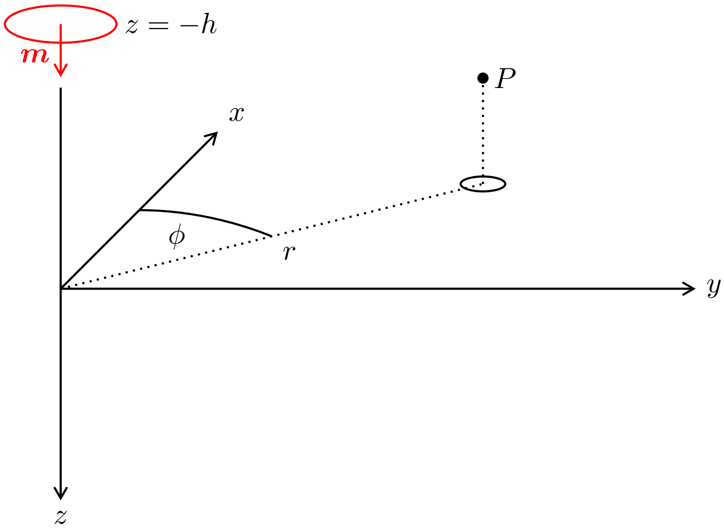

Figure 2.1: Sketch of the cylindrical coordinate system with position of the VMD at height $z = -h$, $h > 0$ and dipole moment m, indicated by a red circle. At the point P, the components of the EM fields shall be calculated.

Due to the symmetry of the problem (cf. fig. 2.1), the choice of cylindrical coordinates with

$$\begin{aligned} x &= r\cos\phi, \\ y &= r\sin\phi, \end{aligned} \tag{2.18}$$

is appropriate, yielding

$$\begin{aligned} e_\phi &= \frac{\partial f_z}{\partial r} & h_r &= \frac{1}{\mathrm{i}\omega\mu_0}\frac{\partial^2 f_z}{\partial r \partial z}, \\ & & h_z &= -\frac{1}{\mathrm{i}\omega\mu_0}\frac{1}{r}\frac{\partial}{\partial r}\left(r\frac{\partial f_z}{\partial r}\right), \end{aligned} \tag{2.19}$$

or inversely

$$\begin{aligned} e_x &= -e_\phi\frac{y}{r} & h_x &= h_r\frac{x}{r}, \\ e_y &= e_\phi\frac{x}{r} & h_y &= h_r\frac{y}{r}. \end{aligned} \tag{2.20}$$

2.2.2 Continuity conditions

To completely describe the behavior of the EM fields in the 1-D domain, two conditions regarding the potential f_z are imposed. First, due to damping effects occurring in a real medium, it is convenient to set the potential to zero at an infinite distance

$$\lim_{R\to\infty} f_z \to 0 \quad \text{for} \quad R = \sqrt{r^2 + (z+h)^2}. \tag{2.21}$$

By virtue of the continuity of the tangential electric field $\boldsymbol{e}^{\tan} = [e_\phi, 0, 0]$ and magnetic field $\boldsymbol{h}^{\tan} = [0, h_r, 0]$ at the interface between two media 0 and 1, the continuity conditions are

$$\begin{aligned} f_z^0 &= f_z^1, \\ \frac{\partial f_z^0}{\partial z} &= \frac{\partial f_z^1}{\partial z}. \end{aligned} \tag{2.22}$$

The continuity of the potential and its vertical derivative is a direct consequence of the continuity of the tangential components of e_ϕ and h_r, which can be obtained by integrating the associated expressions in (2.19) with respect to r.

2.2.3 Solution approach

By exploiting the principle of superposition, the observed or total field $f_{z,\text{tot}}$ in the air, at $z < 0$, can be composed of a (primary) source-related singular potential of the full-space f_z^* and a (secondary) potential f_z^0 that originates from induced currents in the conducting half-space (Zhdanov 2009). If this half-space is considered to consist of N conducting layers with N layer boundaries at $z \in \{z_0, \dots, z_{N-1}\}$ (including the air-earth boundary), furthermore, the total potential in $z > 0$ can be formed of N separate solutions $f_z^1, \dots, f_z^N$, which are mutually coupled by the continuity conditions (2.22) and are assumed to be driven by the incident primary potential at the air-earth interface at $z = 0$. The approach is based on the idea, that the entire problem is considered as a superposition of plane wave solutions in the spatial wavenumber domain (Zhdanov 2009), where the transformed potentials in the layers $j = 0, \dots, N$ are associated with incident, reflected, and transmitted waves (see fig. 2.2). This is feasible, since the specific 1-D parameter distribution of the layered half-space allows the application of the spatial 2-D Fourier transform in the x- and y-direction (Ward and Hohmann 1988).

Altogether, for

$$z_{j-1} \le z \le z_j, \quad j = 0, \dots, N, \tag{2.23}$$

with

$$z_{-1} = -h, \quad z_N = \infty, \tag{2.24}$$

and by setting $f = f_z$, it holds that

$$f_{\text{tot}} = \begin{cases} f_{\text{tot}}^0 = f^* + f^0 & \text{for } z \le 0 \\ f_{\text{tot}}^j = f^j & \text{for } z \ge 0,\ j \ne 0 \end{cases}. \tag{2.25}$$

Since for scalar expressions, $\nabla^2(.) \to \Delta(.)$, this yields the inhomogeneous Helmholtz equation for the primary potential

$$\begin{aligned} &\Delta f^* + k_0^2 f^* = -\mathrm{i}\omega\mu_0\, m\delta(x,y,z+h)\,, \\ &k_0^2 = -\mathrm{i}\omega\mu_0\,\sigma_0 + \omega^2\mu_0\epsilon_{\,0}, \end{aligned} \tag{2.26}$$

and $N+1$ homogeneous Helmholtz equations, associated with the induction processes of the layered half-space

$$\begin{aligned} &\Delta f^j + k_j^2 f^j = 0, \\ &k_j^2 = -\mathrm{i}\omega\mu_0\,\sigma_j + \omega^2\mu_0\epsilon_{\,j}. \end{aligned} \tag{2.27}$$

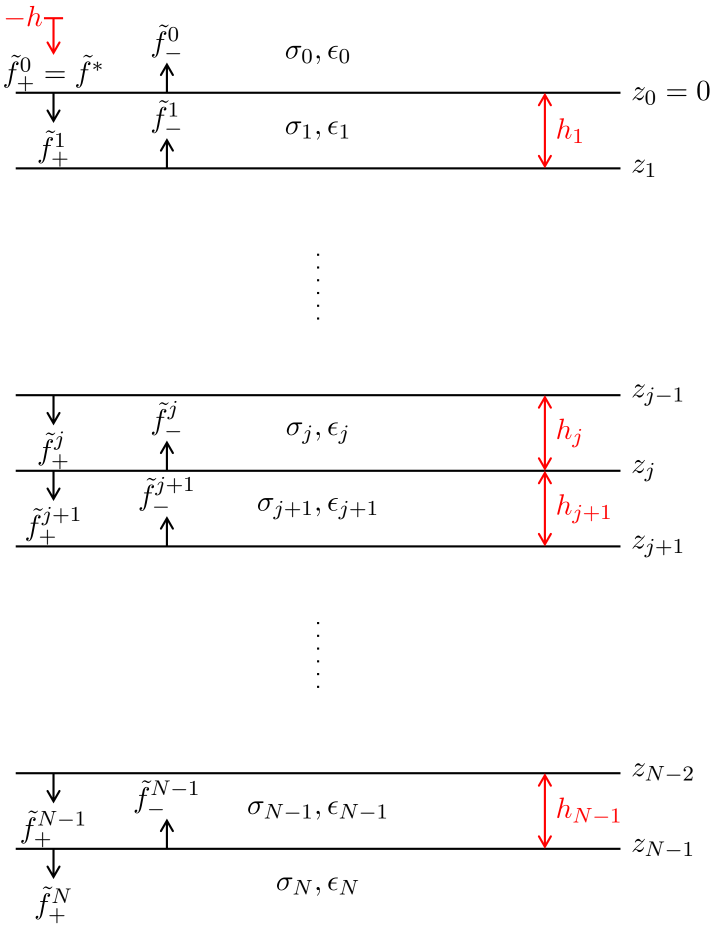

Figure 2.2: Sketch of the layered half-space model with downward ($\tilde{f}_+$) and upward ($\tilde{f}_-$) traveling waves.

Applying the 2-D spatial Fourier transform with its representation

$$\tilde{f}(k_x,k_y,z) = \int_{-\infty}^{\infty}\int_{-\infty}^{\infty} f(x,y,z)\,\mathrm{e}^{-i(k_x x + k_y y)}\,\mathrm{d}x\,\mathrm{d}y, \tag{2.28}$$

and

$$f(x,y,z) = \frac{1}{4\pi^2}\int_{-\infty}^{\infty}\int_{-\infty}^{\infty} \tilde{f}(k_x,k_y,z)\,\mathrm{e}^{i(k_x x + k_y y)}\,\mathrm{d}k_x\,\mathrm{d}k_y, \tag{2.29}$$

to (2.27), leads to homogeneous 1-D Helmholtz equations

$$\frac{\partial^2 \tilde{f}^j(k_x,k_y,z)}{\partial z^2} + u_j^2 \tilde{f}^j(k_x,k_y,z) = 0, \tag{2.30}$$

with the wavenumbers

$$u_j = \sqrt{k_x^2 + k_y^2 - k_j^2}. \tag{2.31}$$

The solutions for these potentials have the general form

$$\tilde{f}^j(k_x,k_y,z) = \tilde{f}^j_+(k_x,k_y,z)\,\mathrm{e}^{-u_j(z-z_{j-1})} + \tilde{f}^j_-(k_x,k_y,z)\,\mathrm{e}^{u_j(z-z_j)}, \tag{2.32}$$

which represents the sum of plane waves, traveling in positive ($\tilde{f}^j_+$) and negative ($\tilde{f}^j_-$) z-direction (Ward and Hohmann 1988). To ensure physical reasonable damping properties as well as the above mentioned propagation directions, the square root of the complex wavenumber u has to be chosen such that $\Re(u) > 0$ and $\Im(u) > 0$ (Zhdanov 2009). By conceiving the upward traveling wave as reflected from the bottom layer boundary (referred to z_j), the downward traveling wave originates as transmitted wave from the top layer boundary (referred to z_{j-1}), respectively. In the layers $j = 0$ and $j = N$ only emanating waves, can be observed

$$\tilde{f}^0_+ = \tilde{f}^N_- \overset{!}{=} 0, \tag{2.33}$$

since no reflections from $z = \pm\infty$ are expected. Hence, the solutions are

$$\tilde{f}^0 = \tilde{f}^0_-\,\mathrm{e}^{u_0 z}, \tag{2.34}$$

$$\tilde{f}^N = \tilde{f}^N_+\,\mathrm{e}^{-u_N(z-z_{N-1})}, \tag{2.35}$$

which ensures that the continuity condition (2.21) is valid. For the total potential $\tilde{f}^0_{\text{tot}}$ in the air layer $j = 0$, the primary potential $\tilde{f}^* = \tilde{f}^0_+\,\mathrm{e}^{-u_0|z+h|}$ has to be added (cf. (2.25)) which acts like the potential of an incident wave. The respective amplitude reads

$$\tilde{f}^0_+ := \frac{\mathrm{i}\omega\mu_0\, m}{2}\frac{1}{u_0}. \tag{2.36}$$

The derivation of this expression is given in the subsequent section 2.2.4 (particularly cf. (2.47)). It results from the scaling of the Green's function G with the source $\boldsymbol{j}_m$ in the domain of the horizontal wavenumbers. The application of the continuity conditions (2.22) at the interfaces $z \in \{z_0, \dots, z_j, \dots, z_{N-1}\}$ leads to a system of $2N$ boundary conditions for $2(N-1)+2$ unknown coefficients as illustrated in fig. 2.2.

It holds at $z = z_0 = 0$ and for the source located at $z = -h$:

$$\tilde{f}^0_+\,\mathrm{e}^{-u_0 h} + \tilde{f}^0_- = \tilde{f}^1_+ + \tilde{f}^1_-\,\mathrm{e}^{-u_1 h_1}, \tag{2.37}$$

$$-u_0\tilde{f}^0_+\,\mathrm{e}^{-u_0 h} + u_0\tilde{f}^0_- = -u_1\tilde{f}^1_+ + u_1\tilde{f}^1_-\,\mathrm{e}^{-u_1 h_1}, \tag{2.38}$$

at $z = z_j$:

$$\tilde{f}^j_+\,\mathrm{e}^{-u_j h_j} + \tilde{f}^j_- = \tilde{f}^{j+1}_+ + \tilde{f}^{j+1}_-\,\mathrm{e}^{-u_{j+1} h_{j+1}}, \tag{2.39}$$

$$-u_j\tilde{f}^j_+\,\mathrm{e}^{-u_j h_j} + u_j\tilde{f}^j_- = -u_{j+1}\tilde{f}^{j+1}_+ + u_{j+1}\tilde{f}^{j+1}_-\,\mathrm{e}^{-u_{j+1} h_{j+1}}, \tag{2.40}$$

and at $z = z_{N-1}$:

$$\tilde{f}^{N-1}_+\,\mathrm{e}^{-u_{N-1} h_{N-1}} + \tilde{f}^{N-1}_- = \tilde{f}^N_+, \tag{2.41}$$

$$-u_{N-1}\tilde{f}^{N-1}_+\,\mathrm{e}^{-u_{N-1} h_{N-1}} + u_{N-1}\tilde{f}^{N-1}_- = -u_N\tilde{f}^N_+, \tag{2.42}$$

with

$$h_j = z_j - z_{j-1}. \tag{2.43}$$

The resulting system of equations for the determination of the $2N$ coefficients $\tilde{f}_+^1, \ldots, \tilde{f}_+^N$, and $\tilde{f}_-^0, \ldots, \tilde{f}_-^{N-1}$ can be solved explicitly. In fact, the recursion formulae given in the literature and derived in this thesis are equivalent to the application of a straightforward Gauss elimination scheme.

2.2.4 Solution of the primary potential f^* and EM fields in full-space

The full-space expression of $f^* = f_z^*$ can be obtained by applying the 3-D spatial Fourier transform to (2.15) (Ward and Hohmann 1988). The respective Fourier representation is given by

$$\tilde{f}^*(k_x, k_y, k_z) = \int\limits_{-\infty}^{\infty}\int\limits_{-\infty}^{\infty}\int\limits_{-\infty}^{\infty} f^*(x, y, z)\, \mathrm{e}^{-i(k_x x + k_y y + k_z z)}\, \mathrm{d}x\, \mathrm{d}y\, \mathrm{d}z, \tag{2.44}$$

and

$$f^*(x, y, z) = \frac{1}{8\pi^3}\int\limits_{-\infty}^{\infty}\int\limits_{-\infty}^{\infty}\int\limits_{-\infty}^{\infty} \tilde{f}^*(k_x, k_y, k_z)\, \mathrm{e}^{i(k_x x + k_y y + k_z z)}\, \mathrm{d}k_x\, \mathrm{d}k_y\, \mathrm{d}k_z. \tag{2.45}$$

After the transformation of (2.15), an algebraic expression is obtained, which has a representation as a convolution integral in space domain given by

$$f^*(x, y, z) = \int\limits_{-\infty}^{\infty}\int\limits_{-\infty}^{\infty}\int\limits_{-\infty}^{\infty} G(x - x', y - y', z - z') j_s(x', y', z')\, \mathrm{d}x'\, \mathrm{d}y'\, \mathrm{d}z'. \tag{2.46}$$

Here, the Green's function $G\colon \mathbb{R}^3 \to \mathbb{C}$ is the impulse response $\Delta G + k^2 G = -\delta(x, y, z)$ of the conductive full-space and j_s denotes the specific source term. The Fourier transform of G with respect to the horizontal coordinates of the wavenumber domain and a source located at $x = y = 0$, and $z = -h$, reads

$$\tilde{G}(k_x, k_y, z) = \frac{\mathrm{e}^{-u|z+h|}}{2u}, \tag{2.47}$$

where

$$\begin{aligned} u &= \sqrt{\lambda^2 - k^2}, \\ \lambda^2 &= k_x^2 + k_y^2. \end{aligned} \tag{2.48}$$

The 2-D Fourier synthesis of (2.47) can be expressed by the Hankel transformation

$$\frac{1}{4\pi^2}\int\limits_{-\infty}^{\infty}\int\limits_{-\infty}^{\infty} \tilde{f}(k_x, k_y, z)\, \mathrm{e}^{i(k_x x + k_y y)}\, \mathrm{d}k_x\, \mathrm{d}k_y = \frac{1}{2\pi}\int\limits_{0}^{\infty} f(\lambda)\lambda J_0(\lambda r)\, \mathrm{d}\lambda, \tag{2.49}$$

as the integrand is an axi-symmetric function (Ward and Hohmann 1988). Here $J_0\colon \mathbb{R} \to \mathbb{R}$ denotes a Bessel function of the first kind and order 0. By virtue of the Sommerfeld identity (Ward and Hohmann 1988), G has the representation

$$\frac{1}{4\pi} \int\limits_0^\infty \frac{\lambda}{u} \, \mathrm{e}^{-u|z+h|} \, J_0(\lambda r) \, \mathrm{d}\lambda = G(x, y, z) = G(R(r, z)) = \frac{\mathrm{e}^{-\mathrm{i}kR}}{4\pi R}. \tag{2.50}$$

For that, and by introducing $j_s = \mathrm{i}\omega\mu_0 \, m\delta(x, y, z + h)$ to (2.46), $f^*(r, z)$ can finally be written as a weighted Green's function in the space domain and cylindrical coordinates

$$f^*(R(r, z)) = \frac{\mathrm{i}\omega\mu_0 \, m}{4\pi R} \, \mathrm{e}^{-\mathrm{i}kR}. \tag{2.51}$$

The respective field components can be obtained by applying (2.19) to (2.51)

$$\begin{aligned} e^*_\phi &= -\frac{\mathrm{i}\omega\mu_0 \, m}{4\pi} \frac{r}{R^3} \, (\mathrm{i}kR + 1) \, \mathrm{e}^{-\mathrm{i}kR}, \\ h^*_r &= -\frac{m}{4\pi} \frac{r(z+h)}{R^5} \left(k^2R^2 - 3\mathrm{i}kR - 3\right) \mathrm{e}^{-\mathrm{i}kR}, \\ h^*_z &= \frac{m}{4\pi} \frac{1}{R^5} \left[2\mathrm{i}kR^3 + \left(k^2r^2 + 2\right) R^2 - 3\mathrm{i}kr^2R - 3r^2\right] \mathrm{e}^{-\mathrm{i}kR}. \end{aligned} \tag{2.52}$$

2.2.5 Solution of the secondary potential f^0 in $z \leq 0$

To obtain the potentials in $z \leq 0$, the amplitudes have to be transferred across the layer boundaries, starting from the substratum up to the surface. This can be accomplished by introducing the amplitude ratio

$$V := \begin{cases} \frac{\tilde{f}_-}{\tilde{f}_+} & \text{for } z < z_N \\ 0 & \text{for } z \geq z_N \end{cases}. \tag{2.53}$$

The first equation also holds for $z \leq 0$ due to the presence of the wave f^*. The continuity conditions (2.39) and (2.40) at an arbitrary layer boundary $z \in \{z_0, \ldots, z_j, \ldots, z_{N-1}\}$ therefore are

$$\tilde{f}^j_+ \left(\mathrm{e}^{-u_jh_j} + V_j\right) = \tilde{f}^{j+1}_+ \left(1 + V_{j+1} \, \mathrm{e}^{-u_{j+1}h_{j+1}}\right), \tag{2.54}$$

$$u_j\tilde{f}^j_+ \left(-\mathrm{e}^{-u_jh_j} + V_j\right) = u_{j+1}\tilde{f}^{j+1}_+ \left(-1 + V_{j+1} \, \mathrm{e}^{-u_{j+1}h_{j+1}}\right). \tag{2.55}$$

Now, dividing (2.55) by (2.54) and separating V_j, gives an upward-directed recursion for the amplitude ratio $V_j(V_{j+1})$

$$V_j = \frac{u_ja_{j+1} - u_{j+1}b_{j+1}}{u_ja_{j+1} + u_{j+1}b_{j+1}} \, \mathrm{e}^{-u_jh_j}, \tag{2.56}$$

with

$$a_{j+1} = 1 + V_{j+1} \, \mathrm{e}^{-u_{j+1}h_{j+1}} \quad \text{and} \quad b_{j+1} = 1 - V_{j+1} \, \mathrm{e}^{-u_{j+1}h_{j+1}}. \tag{2.57}$$

The resulting wavenumber-domain potentials for $z \leq 0$ can be obtained by including (2.56) and (2.36) into (2.32)

$$\begin{aligned} \tilde{f}^0 &= \tilde{f}^0_+ \left[\mathrm{e}^{-u_0|z+h|} + V_0 \, \mathrm{e}^{u_0 z} \right], \\ &= \frac{\mathrm{i}\omega\mu_0 \, m}{2} \frac{1}{u_0} \left[\mathrm{e}^{-u_0|z+h|} + \frac{u_0 a_1 - u_1 b_1}{u_0 a_1 + u_1 b_1} \, \mathrm{e}^{u_0(z-h)} \right]. \end{aligned} \tag{2.58}$$

The total potential, obtained by applying the Hankel transform, therefore reads

$$f^0_{\mathrm{tot}}(r,z) = \frac{\mathrm{i}\omega\mu_0 \, m}{4\pi} \int\limits_0^\infty \frac{\lambda}{u_0} \left[\mathrm{e}^{-u_0|z+h|} + \left(\frac{u_0 a_1 - u_1 b_1}{u_0 a_1 + u_1 b_1} \right) \mathrm{e}^{u_0(z-h)} \right] J_0(\lambda r) \, \mathrm{d}\lambda, \tag{2.59}$$

where the coefficients $a_1 = a_1(V_{N-1}, \ldots, V_1)$ and $b_1 = b_1(V_{N-1}, \ldots, V_1)$ have to be evaluated by the recursion (2.56) and (2.57), exploiting (2.53).

2.2.6 Stabilization of f^0 and the solution of the EM fields in $z \leq 0$

When the field components $e^0_{\phi,\mathrm{tot}}$ and $h^0_{z,\mathrm{tot}}$ have to be evaluated in $z \leq 0$, the appearance of the coefficient $\frac{\lambda}{u_0}$ (cf. (2.59)) leads to inaccuracies in the numerical evaluation of the associated Hankel integrals, particularly at frequencies above 100 kHz (Xiong and Tripp 1997). These problems arise from complex zeros in $u_0 = \sqrt{\lambda^2 - k_0^2}$. For certain combinations of λ^2 and $k_0^2 = \omega^2 \mu_0 \epsilon_0 - i\omega\mu_0\sigma_0$, the real part of u_0 vanishes. To significantly reduce the effect of those poles, an integration by parts can be applied (Siemon 2012). Because the primary potential f^* can be expressed analytically by (2.51), only the secondary part

$$f^0 = \frac{\mathrm{i}\omega\mu_0 \, m}{4\pi} \int\limits_0^\infty \frac{\lambda}{u_0} \left(\frac{u_0 a_1 - u_1 b_1}{u_0 a_1 + u_1 b_1} \right) \mathrm{e}^{u_0(z-h)} \, J_0(\lambda r) \, \mathrm{d}\lambda, \tag{2.60}$$

has to be considered. At first, the term

$$\frac{\lambda}{u_0} \left(\frac{u_0 a_1 - u_1 b_1}{u_0 a_1 + u_1 b_1} \right) = \frac{-\lambda}{u_0} \left(\frac{u_0 a_1 + u_1 b_1 - 2 u_0 a_1}{u_0 a_1 + u_1 b_1} \right) = \underbrace{\frac{2\lambda a_1}{u_0 a_1 + u_1 b_1}}_{\mathbf{A}} - \underbrace{\frac{\lambda}{u_0}}_{\mathbf{B}}, \tag{2.61}$$

is split into a sum. Because the media 0 and $j \geq 1$ are expected to differ in their physical properties, the singularity problem is attached to part **B** only (Siemon 2012).

In the following, the Bessel function identities (Abramowitz and Stegun 1972):

$$\begin{aligned} \partial_r J_0(\lambda r) &= -\lambda J_1(\lambda r), \\ \partial_\lambda J_0(\lambda r) &= -r J_1(\lambda r), \\ \partial_r J_1(\lambda r) &= \lambda \left[J_0(\lambda r) - \frac{1}{\lambda r} J_1(\lambda r) \right], \\ \partial_r \left(r J_1(\lambda r) \right) &= \lambda r J_0(\lambda r), \end{aligned} \tag{2.62}$$

are exploited. By making use of

$$-\int\limits_0^\infty x(\lambda) \partial_\lambda y(\lambda) \, \mathrm{d}\lambda = -x(\lambda) y(\lambda) \Big|_0^\infty + \int\limits_0^\infty \partial_\lambda x(\lambda) y(\lambda) \, \mathrm{d}\lambda, \tag{2.63}$$

and the substitutions

$$\begin{aligned} y &:= \mathrm{e}^{u_0(z-h)} & \qquad \partial_\lambda y &= \frac{\lambda(z-h)}{u_0}\,\mathrm{e}^{u_0(z-h)}, \\ x &= \frac{1}{(z-h)} J_0(\lambda r) & \qquad \partial_\lambda x &= -\frac{r}{(z-h)} J_1(\lambda r), \end{aligned} \tag{2.64}$$

(2.60) can be expressed by

$$\begin{aligned} f^0 = \frac{\mathrm{i}\omega\mu_0\, m}{4\pi} \Bigg[& \int_0^\infty \frac{2\lambda a_1}{u_0 a_1 + u_1 b_1}\,\mathrm{e}^{u_0(z-h)}\, J_0(\lambda r)\,\mathrm{d}\lambda \\ & - \int_0^\infty \frac{r}{(z-h)}\,\mathrm{e}^{u_0(z-h)}\, J_1(\lambda r)\,\mathrm{d}\lambda \\ & + \frac{1}{(z-h)} J_0(\lambda r)\,\mathrm{e}^{u_0(z-h)}\Big|_0^\infty \Bigg]. \end{aligned} \tag{2.65}$$

Here

$$\frac{1}{(z-h)} J_0(\lambda r)\,\mathrm{e}^{u_0(z-h)}\Big|_0^\infty = \frac{1}{(z-h)}\,\mathrm{e}^{\mathrm{i}k_0(z-h)}, \tag{2.66}$$

since $z \le 0$ and

$$J_0(\lambda) = \begin{cases} 0 & \text{for } \lambda \to \infty \\ 1 & \text{for } \lambda \to 0 \end{cases}. \tag{2.67}$$

Since (2.66) is independent of r, the term doesn't contribute to the respective field components e^0_ϕ and h^0_z (cf. (2.19)). The total field components in $z \le 0$, including the primary fields (2.52), therefore read

$$\begin{aligned} e^0_{\phi,\mathrm{tot}}(r,z) = \frac{-\mathrm{i}\omega\mu_0\, m}{4\pi} \Bigg[& \frac{r}{R^3}\,(\mathrm{i}kR + 1)\,\mathrm{e}^{-\mathrm{i}kR} \\ & + \int_0^\infty \frac{2\lambda^2 a_1}{u_0 a_1 + u_1 b_1}\,\mathrm{e}^{u_0(z-h)}\, J_1(\lambda r)\,\mathrm{d}\lambda \\ & + \int_0^\infty \frac{\lambda r}{(z-h)}\,\mathrm{e}^{u_0(z-h)}\, J_0(\lambda r)\,\mathrm{d}\lambda \Bigg], \end{aligned} \tag{2.68}$$

$$\begin{aligned} h^0_{r,\mathrm{tot}}(r,z) = -\frac{m}{4\pi} \Bigg[& \frac{r(z+h)}{R^5}\,\big(k^2R^2 - 3\mathrm{i}kR - 3\big)\,\mathrm{e}^{-\mathrm{i}kR} \\ & + \int_0^\infty \lambda^2 \left(\frac{u_0 a_1 - u_1 b_1}{u_0 a_1 + u_1 b_1}\right) \mathrm{e}^{u_0|z-h|}\, J_1(\lambda r)\,\mathrm{d}\lambda \Bigg], \end{aligned} \tag{2.69}$$

$$\begin{aligned} h^0_{z,\mathrm{tot}}(r,z) = \frac{m}{4\pi} \Bigg[& \frac{1}{R^5}\,\big(2\mathrm{i}kR^3 + \big(k^2r^2 + 2\big)\,R^2 - 3\mathrm{i}kr^2R - 3r^2\big)\,\mathrm{e}^{-\mathrm{i}kR} \\ & + \int_0^\infty \left(\frac{2\lambda^3 a_1}{u_0 a_1 + u_1 b_1} + \frac{2\lambda}{z-h}\right) \mathrm{e}^{u_0(z-h)}\, J_0(\lambda r)\,\mathrm{d}\lambda \\ & - \int_0^\infty \frac{\lambda^2 r}{(z-h)}\,\mathrm{e}^{u_0(z-h)}\, J_1(\lambda r)\,\mathrm{d}\lambda \Bigg]. \end{aligned} \tag{2.70}$$

The influence of the integration by part approach is illustrated in fig. 2.3. For that, a synthetic half-space model with conductivities of $10^{-9}\,\frac{\mathrm{S}}{\mathrm{m}}$ in the upper and $10^{-3}\,\frac{\mathrm{S}}{\mathrm{m}}$ in the lower domain is considered. The interface is set at $z = 0\,\mathrm{m}$ and a VMD source is included at $x = y = 0\,\mathrm{m}$, and $z = -30\,\mathrm{m}$. An adequate high frequency of 133 200 Hz is used, as the influence of the singularity effect vanishes in the quasi-static approximation (Xiong and Tripp 1997). The curves show the absolute value of the horizontal electric field e_ϕ which is observed at $O = 500$ points that are equidistantly distributed along a horizontal profile, located at $z = -15\,\mathrm{m}$ and with the radial distances from the source $r_j \in [0\,\mathrm{m}, 200\,\mathrm{m}]$, $j = 1, \ldots, O$. While the upper figure illustrates the real part, the lower figure shows the imaginary part. Strong peaks, resulting from the singularities, occur if no integration by parts is used (red curve). In contrast the integration approach leads to reasonable smooth solutions (yellow curve). As reference, the blue curve shows the solution for the quasi-static approximation where $\epsilon_r = 0$.

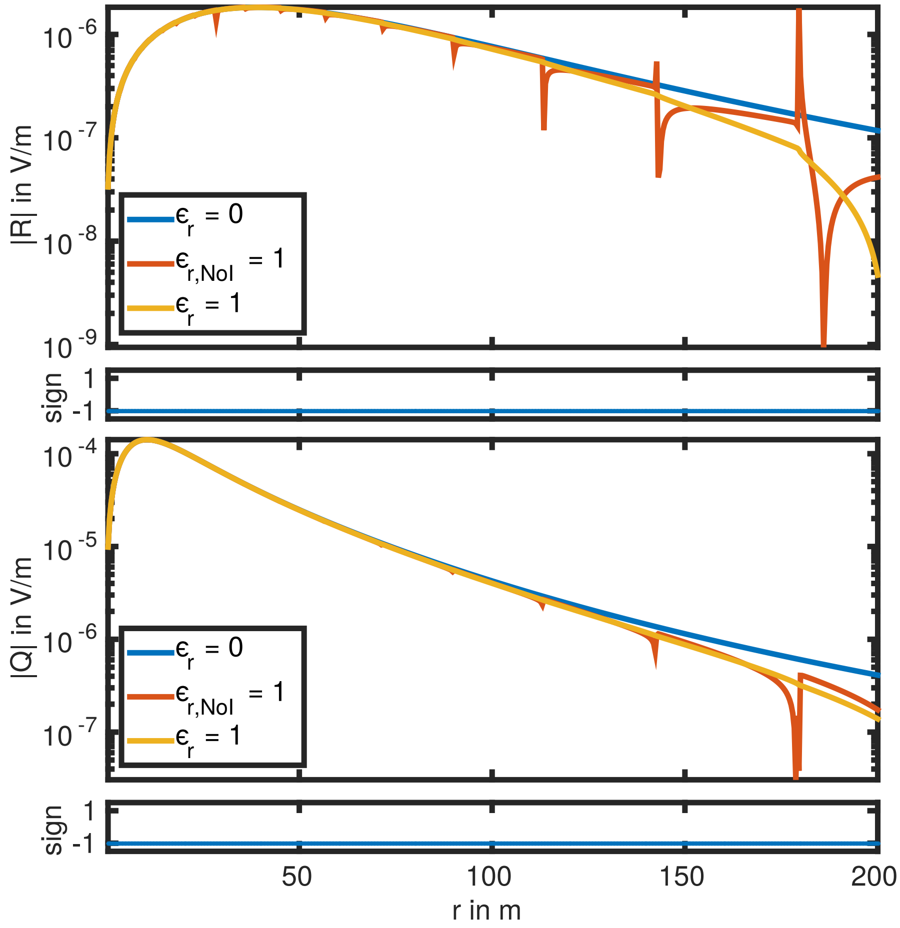

Figure 2.3: Effect of the singularity problem in the numerical evaluation of e_ϕ, shown for a horizontal profile located at $z = -15\,\mathrm{m}$ and for arbitrary radial distances r from the source. The curve denoted by '$\epsilon_\mathrm{r} = 0$' represents the solution of the quasi-static approximation, '$\epsilon_\mathrm{r,NoI} = 1$' the solution of the complete Helmholtz equation but without integration by part, and '$\epsilon_\mathrm{r} = 1$' the solution including the stabilization.

2.2.7 Solution of the total potential f^j_{tot} and EM fields in $z > 0$

Once the recursion (2.56), for the calculation of the amplitude ratio $V_j(V_{j+1})$, has been carried out, the surface amplitude can be propagated back into the ground, i. e. for $z \geq 0$. Hence, a downward-directed recursion algorithm for the unknown amplitudes $\tilde{f}^{j+1}_+(\tilde{f}^j_+)$ can be derived by solving (2.54) for $\tilde{f}^{j+1}_+$

$$\tilde{f}^{j+1}_+ = \frac{\tilde{f}^j_+ \left(\mathrm{e}^{-u_j h_j} + V_j\right)}{\left(1 + V_{j+1}\,\mathrm{e}^{-u_{j+1} h_{j+1}}\right)}, \tag{2.71}$$

which gives, after exploiting (2.56) and (2.57),

$$\tilde{f}^{j+1}_+ = \tilde{f}^j_+ \frac{2u_j}{u_j a_{j+1} + u_{j+1} b_{j+1}}\,\mathrm{e}^{-u_j h_j}. \tag{2.72}$$

The coefficient $\tilde{f}^{j+1}_-$ can be obtained using the relation (2.53)

$$\tilde{f}^{j+1}_- = V_{j+1} \tilde{f}^{j+1}_+. \tag{2.73}$$

To arrive at a compact formulation for the potentials within an arbitrary layer j, i. e., for $z_{j-1} < z < z_j$, the recursion (2.72) for the amplitudes $\tilde{f}^j_+$ is expressed as a function of $\tilde{f}^1_+$ and the amplitude decay over each layer, which yields

$$\begin{aligned}\tilde{f}^j_+ &= \frac{\mathrm{i}\omega\mu_0\, m}{2u_0}\left(\frac{2u_0\,\mathrm{e}^{-u_0 h}}{u_0 a_1 + u_1 b_1}\right)\cdot\left(\frac{2u_1\,\mathrm{e}^{-u_1 h_1}}{u_1 a_2 + u_2 b_2}\right)\cdot\ldots\cdot\left(\frac{2u_{j-1}\,\mathrm{e}^{-u_{j-1} h_{j-1}}}{u_{j-1} a_j + u_j b_j}\right),\\ &= \tilde{f}^0_+ \cdot \underbrace{\frac{\tilde{f}^1_+}{\tilde{f}^0_+}\cdot\frac{\tilde{f}^2_+}{\tilde{f}^1_+}\cdot\ldots\cdot\frac{\tilde{f}^j_+}{\tilde{f}^{j-1}_+}}_{Q_j}.\end{aligned} \tag{2.74}$$

Here, the amplitude decay function Q_j

$$Q_j = \prod_{k=2}^{j} \frac{\tilde{f}^k_+}{\tilde{f}^{k-1}_+}, \quad j \geq 2, \tag{2.75}$$

is incorporated. Finally, the wavenumber potential at an arbitrary depth, expressed by (2.32) and including (2.53), is given by

$$\begin{aligned}\tilde{f}^j &= \tilde{f}^1_+ Q_j\left[\mathrm{e}^{-u_j(z-z_{j-1})} + V_j\,\mathrm{e}^{u_j(z-z_j)}\right],\\ &= \frac{\mathrm{i}\omega\mu_0\, m}{2}\left(\frac{2Q_j}{u_0 a_1 + u_1 b_1}\right)\mathrm{e}^{-u_0 h}\left[\mathrm{e}^{-u_j(z-z_{j-1})} + V_j\,\mathrm{e}^{u_j(z-z_j)}\right].\end{aligned} \tag{2.76}$$

The total potential in the spatial domain at $z \geq 0$ and $z_{j-1} < z < z_j$ reads

$$\begin{aligned}f^j_{\mathrm{tot}}(r,z) = \frac{\mathrm{i}\omega\mu_0\, m}{4\pi}\int\limits_0^\infty \frac{2\lambda Q_j}{u_0 a_1 + u_1 b_1}\,\mathrm{e}^{-u_0 h}\\ \cdot\left[\mathrm{e}^{-u_j(z-z_{j-1})} + V_j\,\mathrm{e}^{u_j(z-z_j)}\right] J_0(\lambda r)\,\mathrm{d}\lambda,\end{aligned} \tag{2.77}$$

and the respective total field components are

$$
\begin{aligned}
e^j_{\phi,\text{tot}}(z,r) &= \frac{-\mathrm{i}\omega\mu_0\, m}{4\pi} \int\limits_0^\infty \left(\frac{2\lambda^2 Q_j}{u_0 a_1 + u_1 b_1}\right) \mathrm{e}^{-u_0 h} \\
&\quad \cdot \left[\mathrm{e}^{-u_j(z-z_{j-1})} + V_j\, \mathrm{e}^{u_j(z-z_j)}\right] J_1(\lambda r)\, \mathrm{d}\lambda, \qquad (2.78) \\
h^j_{r,\text{tot}}(z,r) &= \frac{m}{4\pi} \int\limits_0^\infty \left(\frac{2\lambda^2 Q_j u_j}{u_0 a_1 + u_1 b_1}\right) \mathrm{e}^{-u_0 h} \\
&\quad \cdot \left[\mathrm{e}^{-u_j(z-z_{j-1})} - V_j\, \mathrm{e}^{u_j(z-z_j)}\right] J_1(\lambda r)\, \mathrm{d}\lambda, \qquad (2.79) \\
h^j_{z,\text{tot}}(z,r) &= \frac{m}{4\pi} \int\limits_0^\infty \left(\frac{2\lambda^3 Q_j}{u_0 a_1 + u_1 b_1}\right) \mathrm{e}^{-u_0 h} \\
&\quad \cdot \left[\mathrm{e}^{-u_j(z-z_{j-1})} + V_j\, \mathrm{e}^{u_j(z-z_j)}\right] J_0(\lambda r)\, \mathrm{d}\lambda. \qquad (2.80)
\end{aligned}
$$

2.2.8 Calculation of Hankel integrals

The occurring Hankel integrals are evaluated by exploiting the theory of linear filtering (Ward and Hohmann 1988). Concerning a fixed depth z, the respective expressions for the Bessel functions $J_p(\lambda r)$ of order $p \in \{0, 1\}$ can be substituted into a convolution integral (Ghosh 1971)

$$f(r) = \int\limits_0^\infty k(\lambda)\lambda J_p(\lambda r)\, \mathrm{d}\lambda \quad \Rightarrow \quad F(x) = \int\limits_{-\infty}^\infty K(y) H_p(x-y)\, \mathrm{d}y, \qquad (2.81)$$

with

$$
\begin{aligned}
x &= \ln(r), \\
y &= \ln(\frac{1}{\lambda}), \\
F(x) &= \mathrm{e}^x\, f(\mathrm{e}^x), \\
K(y) &= \mathrm{e}^{-y}\, k(\mathrm{e}^{-y}), \\
H_p(x-y) &= \mathrm{e}^{x-y}\, J_p(\mathrm{e}^{x-y}). \qquad (2.82)
\end{aligned}
$$

For that, (2.81) can be approximated by a convolution sum

$$f(r) \approx \frac{1}{r} \sum_i K(y_i) \tilde{H}_p(x - y_i) = \frac{1}{r} \sum_i K(x - y_i) \tilde{H}_p(y_i), \qquad (2.83)$$

utilizing a known set of $i = 100$ appropriate discrete filter coefficients $\tilde{H}_p(y_i)$ (Christensen 1990). For an arbitrary number $j = 1 \ldots O$ of observation points $r_{min} \leq r_j \leq r_{max}$, $r_j > 0$, the output function $f(r_j)$ is determined only for a few logarithmic equidistantly distributed nodes r_l, $l = 1 \ldots L$, $L < O$. These radii are chosen such that 10 nodes are allotted to a single decade for the range between r_{min} and r_{max}. As the nodes y_i of the filter coefficient are designed for the same logarithmic equidistant sample rate ($\sim \ln 10 \cdot 0.1$), once calculated input functions $K(x_{l=1} - y_i)$ can be stored and reused. For $l = 2 \ldots L$, just a single update is required which leads to a sustainable speedup of the algorithm (Anderson 1975). Arbitrary outputs $f(r_j)$ of sufficient accuracy are finally obtained e. g. by a cubic spline interpolation S_3 (Johansen and Sørensen 1979; Anderson 1982)

$$f(r_j) \approx S_3(f(r_1), \ldots, f(r_L)). \tag{2.84}$$

An example of this interpolation approach is presented in figs. 2.5 to 2.6. Again, the half-space model from section 2.2.6 is used where the horizontal electric field is calculated for a VMD source, located at $x = y = 0\,\mathrm{m}$ and $z = -30\,\mathrm{m}$ over a conductive half-space at a frequency of 133 200 Hz. Furthermore, the fields are given in Cartesian coordinates where, due the axis symmetry, only a single component is presented. Figure 2.4 shows a section from the horizontal profile at $z = -15\,\mathrm{m}$. Peaks in the point-wise evaluation (blue curve) denote leftovers from the singularities which are already considerably damped by the application of the integration by parts. As a positive side effect, the interpolation approach (red curve) totally smooths out those non-differentiable segments. Note, that the strong anomaly between $r = 150\,\mathrm{m}$ to $200\,\mathrm{m}$ results from a change in sign, in consequence of the representation by the logarithm of the absolute value.

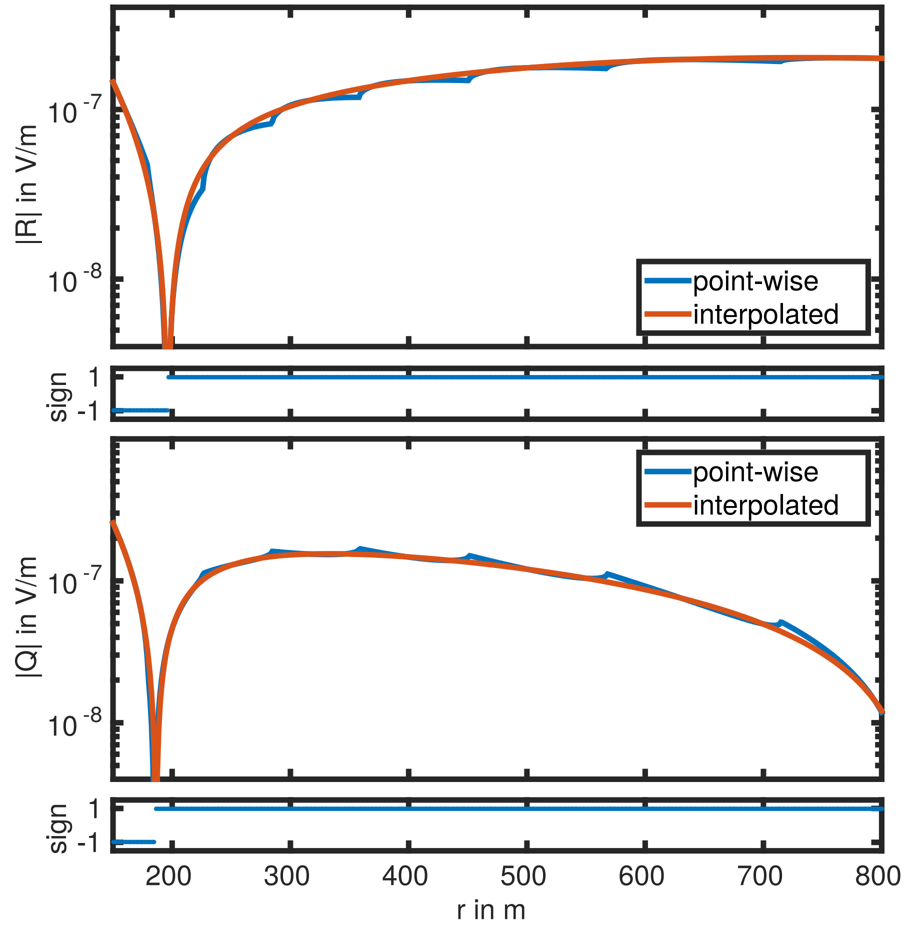

Figure 2.4: Inaccuracies from numerical Hankel transformation smoothed by interpolation, shown for e_x at $z = -15\,\mathrm{m}$ and for arbitrary horizontal distances r from the source.

To get a non-disturbed error estimation for the interpolation approach, the electric permittivity is set to 0 for each subarea of the model. Hence, the relative interpolation error for the real part (fig. 2.5) and the imaginary part (fig. 2.6) are shown for $O = 1000$ equidistant distributed observation points along the known profile. The point-wise and the interpolated solutions are represented by the blue and dashed red curves, respectively. An overall good agreement with relative errors below 1 % is reached, exploiting a set of only $L = 31$ nodes. In addition to the sign of the solution, the relative error with respect to point-wise evaluation is shown in the lower parts of the pictures. The peak in the real part near $r = 1475\,\mathrm{m}$ results from a change in the sign and field amplitudes that are close to zero.

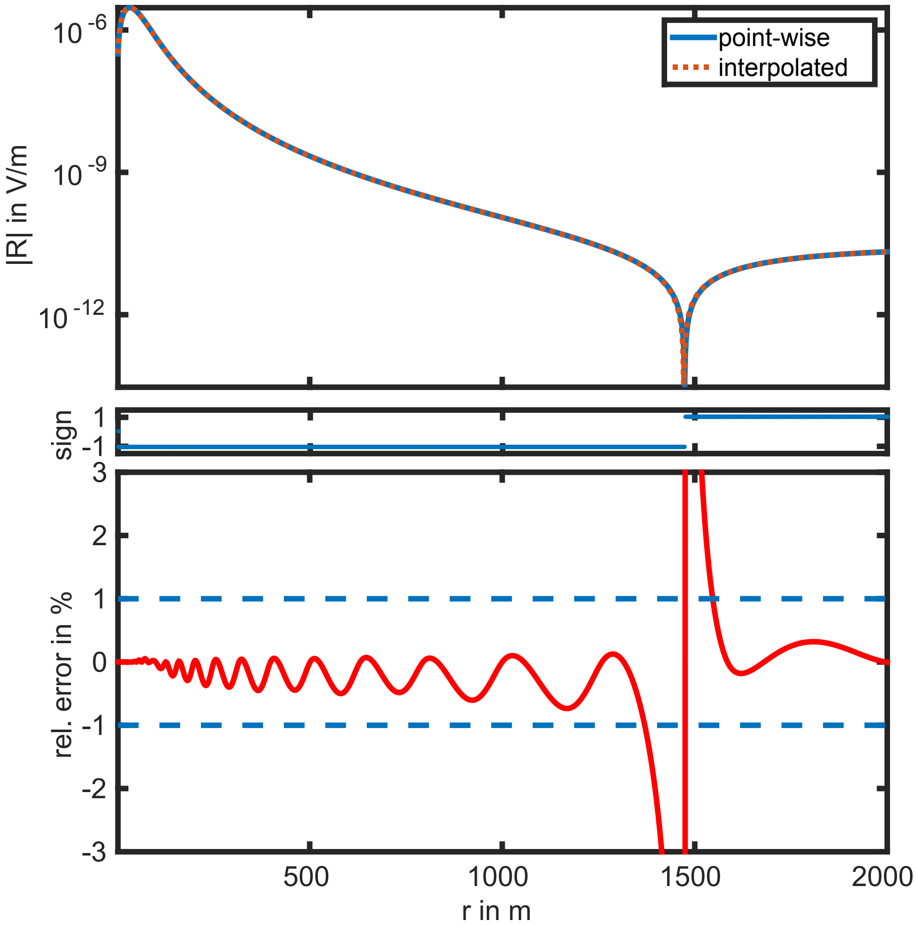

Figure 2.5: Interpolation of the real part of e_x at $z = -15\,\mathrm{m}$ along a profile in radial direction.

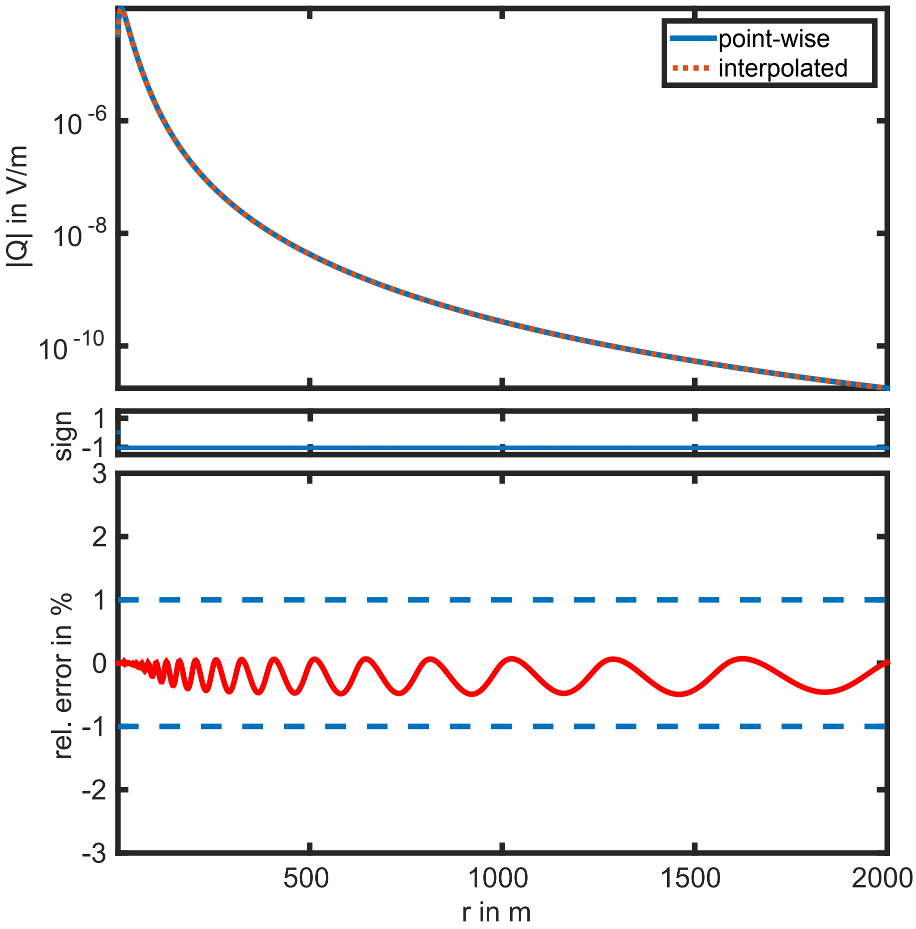

Figure 2.6: Interpolation of the imaginary part of e_x at $z = -15\,\mathrm{m}$ along a profile in radial direction.

3 Discretized forward problem

Notation

$(\cdot)_{\text{pri}}$, $(\cdot)_{\text{sec}}$		primary and secondary component of the expression $(\cdot)$
K	$\in \mathbb{R}_+$	number of degrees of freedom
K^h	$\in \mathbb{R}_+$	number of discrete magnetic field components
N	$\in \mathbb{R}_+$	number of data points
N_f	$\in \mathbb{R}_+$	number of frequencies
N_p	$\in \mathbb{R}_+$	number of TX/RX positions
S	$\in \mathbb{R}_+$	number of discrete elements (cells)
$\boldsymbol{b}$	$\in \mathbb{C}^K$	right-hand side vector of the discretized problem
$\boldsymbol{c}_{\text{tot}}$	$\in \mathbb{R}^S$	cumulative divergence of $\boldsymbol{h}^{\text{d}}$
$\boldsymbol{d}$	$\in \mathbb{C}^N$	data vector
$\boldsymbol{d}^{\boldsymbol{h}}$	$\in \mathbb{C}^S$	divergence of $\boldsymbol{h}^{\text{d}}$
$\boldsymbol{g}^{\boldsymbol{\sigma}}$	$\in \mathbb{R}^{K^h}$	gradient of $\boldsymbol{\sigma}$
$\boldsymbol{h}^{\text{d}}$	$\in \mathbb{C}^{K^h}$	vector of the discrete magnetic field
$\boldsymbol{i}$	$\in \mathbb{R}^{K^h}$	interpolation operator
$\boldsymbol{s}^{\boldsymbol{\sigma}}$	$\in \mathbb{R}^S$	second derivative of $\boldsymbol{\sigma}$
$\boldsymbol{u}$	$\in \mathbb{C}^K$	solution vector of the discrete problem
$\boldsymbol{q}$	$\in \mathbb{C}^K$	measurement operator, vector definition
$\boldsymbol{\sigma}$	$\in \mathbb{R}^S$	parameter vector, i. e. discrete electric conductivity
$\boldsymbol{A}$	$\in \mathbb{C}^{K\times K}$	system matrix
$\boldsymbol{C}^e$	$\in \mathbb{R}^{K^h\times K}$	curl-$\boldsymbol{e}$ operator
$\boldsymbol{C}^h$	$\in \mathbb{R}^{K\times K^h}$	curl-$\boldsymbol{h}$ operator
$\boldsymbol{D}$	$\in \mathbb{R}^{S\times K^h}$	divergence operator
$\boldsymbol{G}$	$\in \mathbb{R}^{K^h\times S}$	gradient operator
$\boldsymbol{K}$	$\in \mathbb{C}^{K\times K}$	stiffness matrix
$\boldsymbol{M}$	$\in \mathbb{C}^{K\times K}$	conductivity-depending part of mass matrix
$\boldsymbol{Q}$	$\in \mathbb{C}^{N\times NK}$	measurement operator, matrix definition
$\boldsymbol{S}$	$\in \mathbb{C}^{K\times K}$	wave term part of mass matrix
$\boldsymbol{T}$	$\in \mathbb{C}^{K\times K}$	symmetrization matrix
$\boldsymbol{V}$	$\in \mathbb{C}^{S\times S}$	cell volume matrix
$\widetilde{\boldsymbol{T}}$	$\in \mathbb{C}^{K\times K\times S}$	tensor of derivatives $\partial_{\boldsymbol{\sigma}}\boldsymbol{M}$

3.1 Governing equations

In the general case of arbitrary complex conductivity distributions $\sigma = \sigma(x, y, z)$, analytic solutions are no longer available. Therefore, the solution of (2.6) and (2.7) has to be approximated with the help of numerical approaches. In this thesis the finite difference (FD) method[1], based on a Yee-cell (Yee 1966) tensor-product grid, is utilized. The chapter provides insight into the formulation and implementation of the discrete forward problem as well as the derivation of the required operator which allows to obtain synthetic data at any receiver position.

Considering a single frequency ω and a single physical source, by changing from the continuous conductivity distribution $\sigma(x,y,z)$ with $[x,y,z]^\top \in \Omega \subset \mathbb{R}^3$ to a discrete conductivity or *parameter* distribution $\boldsymbol{\sigma} \in \mathbb{R}^S$ on subsets $\Omega_p \subset \Omega$ (Günther 2004)

$$\sigma(x,y,z) = \sum_{p=1}^{S} \sigma_p \phi_p(x,y,z), \tag{3.1}$$

with

$$\boldsymbol{\sigma} = [\sigma_1, \sigma_2, \ldots, \sigma_S]^\top, \tag{3.2}$$

and

$$\phi_p(x,y,z) = \begin{cases} 1 & \text{for } [x,y,z]^\top \in \Omega_p \\ 0 & \text{elsewhere} \end{cases}, \tag{3.3}$$

associated with the S subsets which are formed by a regular tensor-product grid, the approach ends up with a linear system of equations

$$\boldsymbol{A}(\boldsymbol{\sigma})\boldsymbol{u} = \boldsymbol{b}. \tag{3.4}$$

This system yields the appropriate solution vector $\boldsymbol{u} \in \mathbb{C}^K$ for the electric field components assigned to the K unknowns or *degrees of freedom* (DOF). The system matrix $\boldsymbol{A}(\boldsymbol{\sigma}) \in \mathbb{C}^{K\times K}$ is typically sparse, complex-valued, and quite large. $\boldsymbol{A}$ can be linearly composed of the discretized counterparts of the three terms related to the left-hand side of Helmholtz equation (2.6)

$$\boldsymbol{A}(\boldsymbol{\sigma}) = \boldsymbol{K} + \mathrm{i}\omega\mu_0\,\boldsymbol{M}(\boldsymbol{\sigma}) - \omega^2\mu_0\,\boldsymbol{S}(\boldsymbol{\epsilon}). \tag{3.5}$$

It has to mentioned, that $\boldsymbol{\sigma}$ and $\boldsymbol{\epsilon}$ are typically associated with the same spatial discretization. While only the conductivity will be considered as varying parameter in the inversion process, the electric permittivity is incorporated in the forward problem but is set to $\boldsymbol{\epsilon} = \epsilon_0 \mathbf{1}_S$, w. l. o. g. Here

$$\mathbf{1}_S := [1, 1, \ldots, 1]^\top \in \mathbb{R}^S, \tag{3.6}$$

is the vector of ones of length S. The decomposition of $\boldsymbol{A}$ yields the parameter independent stiffness matrix $\boldsymbol{K} \in \mathbb{R}^{K\times K}$, belonging to the purely geometric curl-curl part of the Helmholtz equation, a mass matrix part $\boldsymbol{M}(\boldsymbol{\sigma}) \in \mathbb{R}^{K\times K}$ which linearly depends on the conductivity, and a second mass matrix part $\boldsymbol{S} \in \mathbb{R}^{K\times K}$ that represents the conductivity-independent wave term. The RHS vector $\boldsymbol{b} \in \mathbb{C}^K$ results from the projection of the source term $-\mathrm{i}\omega\mu_0\,\boldsymbol{j}_e$ and the boundary conditions (2.7) onto the DOF.

Because of the singularity of the curl-curl operator, the solvability of the problem is ensured by the mass matrix $(\mathrm{i}\omega\mu_0\,\boldsymbol{M}(\boldsymbol{\sigma}) - \omega^2\mu_0\,\boldsymbol{S})$. The property might get lost, if the frequencies are very low (Schwarzbach 2009). This case can be dismissed, since $\omega_{\min}$ is expected to constitute at least a few hundred Hz. Furthermore, even for very low conductivities, the system remains invertible due to the influence of the wave term $\omega^2\mu_0\,\boldsymbol{S}$.

---

[1] In principle, the inverse problem, described in chapter 4, can be considered as independent of the underlying forward operator. Hence, the choice of finite differences instead of e. g. finite elements rather follows reasons of practicability. While the latter facilitates the consideration of surface topography, finite differences are comfortable to implement and they easily provide first and second order derivatives with respect to the coordinate directions. Additionally, the finite difference approach naturally allows to follow the HEM survey geometry while it exploits regular tensor-product grids.

3.2 Secondary field approach

As a consequence of the systems' RHS, problems arise in the numerical simulation of the point source singularity. Tremendously small subsets are required to achieve a reasonable accurate projection of the infinite source term on the surrounding DOF which leads to gratuitous fine grids in $z < 0$ where the HEM sources are located. To overcome that negative issue, the *secondary field approach* or scattered field approach (Lowry et al. 1989; Newman and Alumbaugh 2002; Börner 2010) is used where the singular point source is removed from the numerical solution by splitting up the problem in two superposed parts. At first, concerning the continuous problem or *total field problem*

$$\nabla\times\nabla\times \boldsymbol{e} + \left(\mathrm{i}\omega\mu_0\,\sigma - \omega^2\mu_0\epsilon\right)\boldsymbol{e} = -\mathrm{i}\omega\mu_0\,\boldsymbol{j}_e, \tag{3.7}$$

the conductivity σ and the total electric field $\boldsymbol{e}$ can be decomposed in a *primary* and a *secondary* component

$$\begin{aligned}\boldsymbol{e} &= \boldsymbol{e}_{\mathrm{pri}} + \boldsymbol{e}_{\mathrm{sec}},\\ \sigma &= \sigma_{\mathrm{pri}} + \sigma_{\mathrm{sec}}.\end{aligned} \tag{3.8}$$

Here, only the primary field $\boldsymbol{e}_{\mathrm{pri}}$, associated with the primary or background conductivity distribution σ_{pri}, is supposed to be excited by the total field source

$$\nabla\times\nabla\times \boldsymbol{e}_{\mathrm{pri}} + \left(\mathrm{i}\omega\mu_0\,\sigma_{\mathrm{pri}} - \omega^2\mu_0\epsilon\right)\boldsymbol{e}_{\mathrm{pri}} = -\mathrm{i}\omega\mu_0\,\boldsymbol{j}_e. \tag{3.9}$$

Subtracting the primary from the total field problem

$$\nabla\times\nabla\times \boldsymbol{e} - \nabla\times\nabla\times \boldsymbol{e}_{\mathrm{pri}} + \left(\mathrm{i}\omega\mu_0\,\sigma - \omega^2\mu_0\epsilon\right)\boldsymbol{e} - \left(\mathrm{i}\omega\mu_0\,\sigma_{\mathrm{pri}} - \omega^2\mu_0\epsilon\right)\boldsymbol{e}_{\mathrm{pri}} = 0, \tag{3.10}$$

gives the Helmholtz equation of the secondary field

$$\nabla\times\nabla\times \boldsymbol{e}_{\mathrm{sec}} + \left(\mathrm{i}\omega\mu_0\,\sigma - \omega^2\mu_0\epsilon\right)\boldsymbol{e}_{\mathrm{sec}} = -\mathrm{i}\omega\mu_0\,\sigma_{\mathrm{sec}}\boldsymbol{e}_{\mathrm{pri}}, \tag{3.11}$$

that is, in contrast to the total field equation, caused by the action of the separated primary field on the secondary conductivity distribution. The RHS $-\mathrm{i}\omega\mu_0\,\sigma_{\mathrm{sec}}\boldsymbol{e}_{\mathrm{pri}}$ of the secondary field problem is free of singularities which are solely related to the solution of the primary field problem. Besides, the secondary source vanishes if the total and the primary conductivity coincides, i. e. $\sigma_{\mathrm{sec}} = \sigma - \sigma_{\mathrm{pri}} = 0$, which implies to choose $\sigma_{\mathrm{pri}} = \sigma$ in the vicinity of the source singularity. Accompanying with the electric conductivity and the electric field, the boundary conditions are also subject to this mathematical partitioning. If the value $\boldsymbol{e}_g$ of inhomogeneous Dirichlet boundary condition (2.7) for the total field problem is set to the primary field, i. e. $\boldsymbol{e}_g = \boldsymbol{e}_{\mathrm{pri}}$, this implies that

$$\boldsymbol{e}_{\mathrm{sec}} = \mathbf{0}_3 \quad \text{on } \mathit{\Gamma} = \delta\Omega, \tag{3.12}$$

homogeneous boundary conditions apply to the secondary field problem. The expression $\mathbf{0}_3$ denotes the zero vector of length 3, appropriate to the definition given in (A.11).

The validation of the boundary conditions is given, if secondary sources, associated with changes in conductivity σ_{sec} with respect to the background σ_{pri}, are assumed to be located inside the modeling domain. To ensure this assumption, the model area, provided by the cut-&-paste strategy, has to be defined with adequate extent. However, the resulting model areas are still comparatively small so that the problem can usually be restricted to a flat-earth model. For a horizontal air-earth interface, the secondary field approach can be implemented straightforward. The primary conductivity distribution $\sigma_{\text{pri}}(z)$, given by a layered half-space, can be obtained as a priori information by the cut-&-paste approach (Ullmann, Scheunert, et al. 2015). Thus, remarkable numerical problems arising from aliasing effects at higher frequencies, associated with displacement currents, as well as discretization errors resulting from the sharp jump of the electric conductivity at the air-earth interface can be avoided. The latter inevitably occur if topographic features are considered. Thereby, the gradient between the total conductivity σ and the background conductivity gives rise to strong secondary sources. A dense grid representation of the topography is required to avoid inaccuracies interrelate to those sources. Despite of current modeling strategies that allow to totally remove the air from the modeling domain in order to circumvent the related numerical errors (cf. Zhengyong (2012)), the discretization of the HEM problem explicitly requires to incorporate those areas. This drawback results from the receiver positions which are typically located coplanar to the transmitter coil. The associated primary field $\boldsymbol{e}_{\text{pri}}$ can be evaluated, exploiting the analytic solutions of the Helmholtz equation for a VMD at height $h > 0$ over a layered half-space as described in section 2.2. Anticipating chapter 4, σ_{pri} is always kept fixed while updates in σ are assumed to be related to changes in σ_{sec}. Hence, the primary fields need to be calculated only once during the whole inversion process.

Switching over to the discretized forward problem, (3.11) can be expressed in terms of the discrete approximation (3.4), where

$$\begin{aligned} \boldsymbol{u} &= \boldsymbol{u}_{\text{pri}} + \boldsymbol{u}_{\text{sec}}, \\ \boldsymbol{\sigma} &= \boldsymbol{\sigma}_{\text{pri}} + \boldsymbol{\sigma}_{\text{sec}}. \end{aligned} \tag{3.13}$$

According the assumption (3.9),

$$\boldsymbol{A}(\boldsymbol{\sigma}_{\text{pri}})\boldsymbol{u}_{\text{pri}} = \boldsymbol{b}, \tag{3.14}$$

the discrete primary field solution $\boldsymbol{u}_{\text{pri}}$ is associated with the representation of the total fields' source term $\boldsymbol{b}$. Hence, it follows that

$$\boldsymbol{A}(\boldsymbol{\sigma})\boldsymbol{u} = \boldsymbol{A}(\boldsymbol{\sigma}_{\text{pri}})\boldsymbol{u}_{\text{pri}}, \tag{3.15}$$

so that the discretized secondary field problem is described by

$$\boldsymbol{A}(\boldsymbol{\sigma})\boldsymbol{u}_{\text{sec}} = -\left[\boldsymbol{A}(\boldsymbol{\sigma}) - \boldsymbol{A}(\boldsymbol{\sigma}_{\text{pri}})\right]\boldsymbol{u}_{\text{pri}} =: \boldsymbol{b}_{\text{sec}}, \tag{3.16}$$

where it should be mentioned that

$$\left[\boldsymbol{A}(\boldsymbol{\sigma}) - \boldsymbol{A}(\boldsymbol{\sigma}_{\text{pri}})\right] \neq \boldsymbol{A}(\boldsymbol{\sigma}_{\text{sec}}). \tag{3.17}$$

Using the expression (3.5) and the linear dependency of $\boldsymbol{M}$ on $\boldsymbol{\sigma}$, the secondary field forward problem can finally be reformulated as a component-wise description

$$\left[\boldsymbol{K} + \mathrm{i}\omega\mu_0\, \boldsymbol{M}(\boldsymbol{\sigma}) - \omega^2\mu_0\, \boldsymbol{S}\right] \boldsymbol{u}_{\text{sec}} = -\mathrm{i}\omega\mu_0\, \boldsymbol{M}(\boldsymbol{\sigma}_{\text{sec}})\boldsymbol{u}_{\text{pri}}, \tag{3.18}$$

comprising all required quantities that needs to be assembled.

Calculation of primary fields $\boldsymbol{u}_{\text{pri}}$

To evaluate the primary electric fields $\boldsymbol{u}_{\text{pri}}$ in terms of a secondary field approach, analytic solutions are required at every degree of freedom within the entire modeling domain. Depending on the grid roughness, calculations for up to several hundred of nodes in z-direction need to be considered. For observation points being distributed over a set of depths $z_{min} \leq z \leq z_{max}$, the 1-D interpolation approach with respect to r (see section 2.2.8) can be extended to the 2-D case where $\boldsymbol{e}_{\text{pri}}$ is additionally evaluated at only a few depths $z_d, d = 1 \dots D$

$$f(r, z) \approx S_3(f(r_1, z_1), \dots, f(r_L, z_1), f(r_1, z_2), \dots, f(r_L, z_D)). \tag{3.19}$$

A node distribution of 10 equidistantly distributed nodes per layer is employed, leading to adequate accuracy. An additional refinement is included, if observation points are required at the source vicinity.

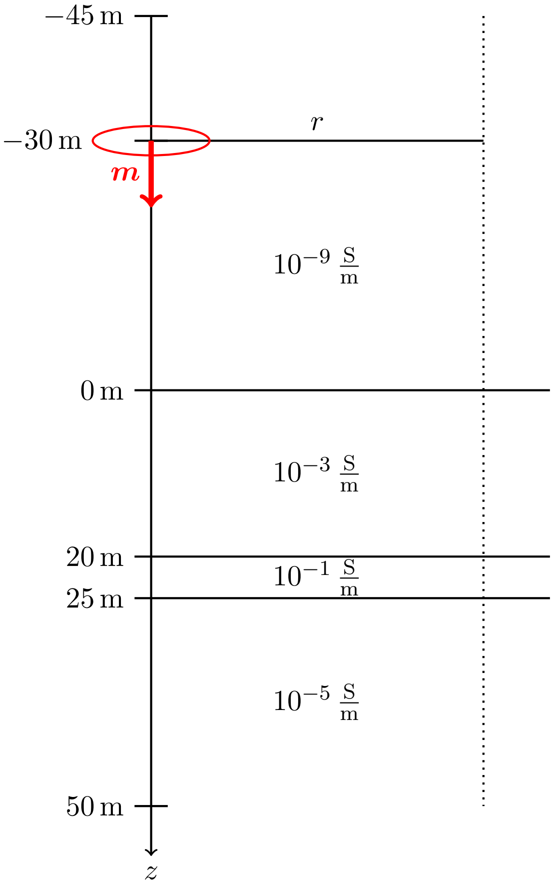

Figure 3.1: Sketch of the layered half-space model. The dotted line shows the profile on which e_x is observed.

To illustrate the resulting interpolation error, the half-space model, as introduced in section 2.2, is extended by two additional layers (fig. 3.1). The associated conductivities are $10^{-9}\,\frac{\mathrm{S}}{\mathrm{m}}$ for the air, $10^{-3}\,\frac{\mathrm{S}}{\mathrm{m}}$ and $10^{-1}\,\frac{\mathrm{S}}{\mathrm{m}}$ for the interior layers starting from the top, and $10^{-4}\,\frac{\mathrm{S}}{\mathrm{m}}$ for the substratum. The corresponding thicknesses of the interior layers are 20 m and 5 m. All calculations are based on the quasi-static approximation to exclude the singularity effects. The electric field e_x is observed along a vertical profile that is located at a tiny horizontal distance $r = 2\,\mathrm{m}$ from the source. $O = 1000$ observation points are equidistantly distributed at $z_j \in [-45\,\mathrm{m}, 50\,\mathrm{m}]$, $j = 1, \dots, O$. A total of $D = 68$ nodes are used for the interpolation scheme. Figures 3.2 to 3.3 show the real and imaginary parts of the observed fields and the corresponding relative errors with respect to the point-wise evaluation. The vertical dashed lines denote the positions of layer boundaries at $z = 0\,\mathrm{m}$, 20 m and 25 m. Again a overall good agreement, with errors basically below 1 %, can be achieved. Negligible errors only occur near the source position ($z = -30\,\mathrm{m}$) and the layer boundaries.

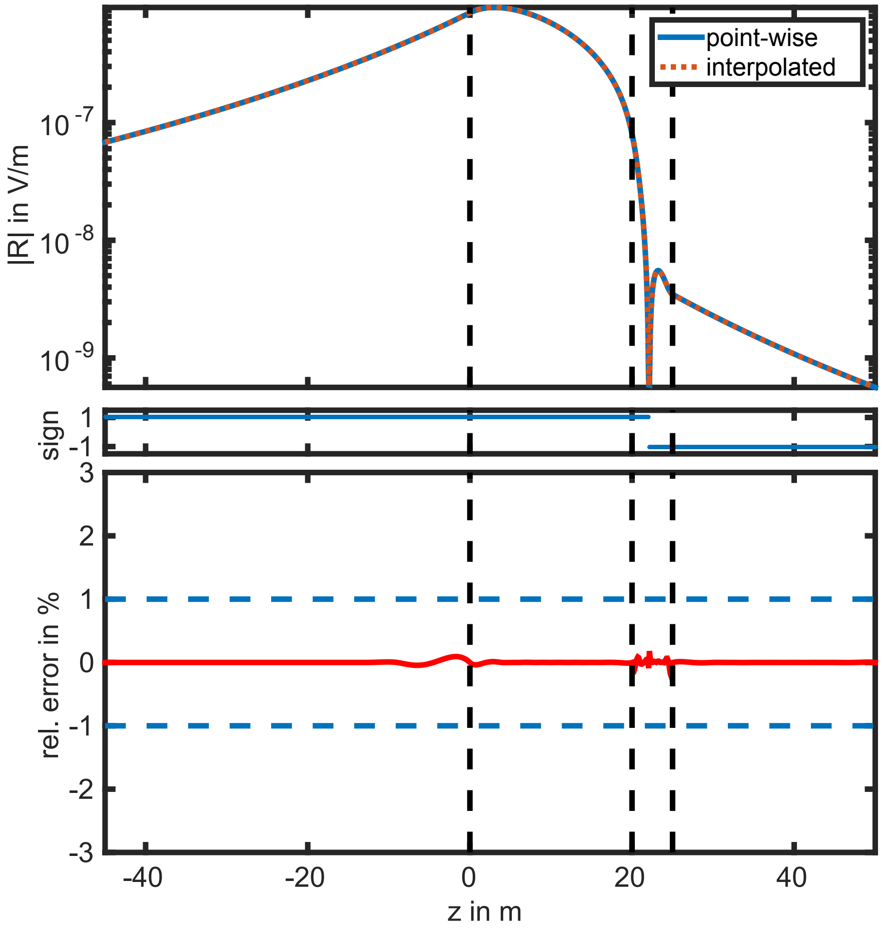

Figure 3.2: Interpolation of the real part of e_x at $r = 2\,\mathrm{m}$ along a vertical profile.

It has to mentioned that an interpolation of $\boldsymbol{u}_{\mathrm{pri}}$ becomes crucial if discretization schemes are employed that are not based on tensor-product grids. For example in case of the finite elements approach, nearly each DOF is expected to be located at a different height which requires a primary field evaluation at up to some millions of nodes in z-direction. As an alternative to the interpolation scheme, a parallel calculation can be exploited, since calculations for arbitrary depths z are completely independent from each other. However, non-smooth solutions, due to the singularity effects, may be observed (cf. section 2.2.8).

A comparison of the runtime with respect to the number of observation points is given in table 3.1[2]. The first column shows the number of randomly distributed points within the three-layer model. In the second and third column, the runtime for a point-wise evaluation and for the 2-D interpolation approach are given, respectively. While the point-wise evaluation is determined by the expected strict linear dependency ($\sim c_a O$, $c_a \approx 10^{-3}$), the interpolation shows a rather beneficial behavior. Since the application of a simple interpolation scheme is a quite economic task, compared to the evaluation of the analytical primary field, the computational effort of the 2-D interpolation approach per observation point even diminishes for moderate problem sizes (cf. fig. 3.4). Only for large scales of over 10^6 observation points, the interpolation likewise converges into linear dependency ($\sim c_i O$, $c_i \approx 10^{-6}$).

---

[2] Calculations carried out on an individual core of an AMD Opteron$^{\mathrm{TM}}$Processor 6136 (2.4 GHz)

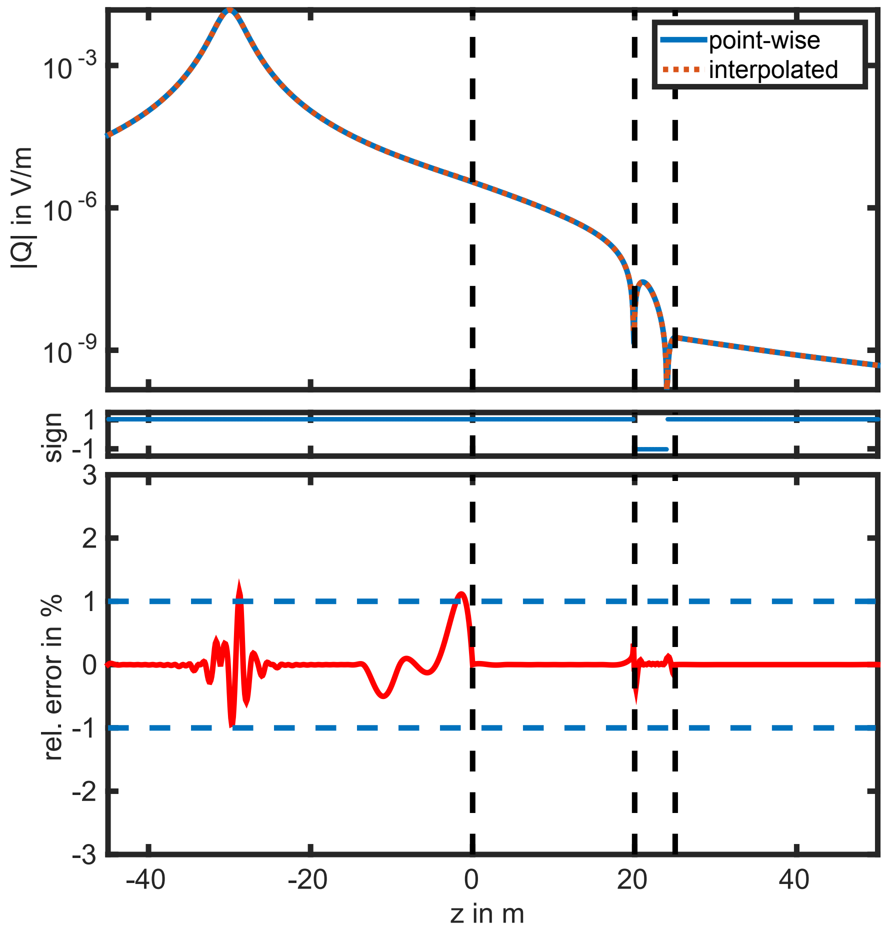

Figure 3.3: Interpolation of the imaginary part of e_x at $r = 2\,\mathrm{m}$ along a vertical profile.

3.3 Direct solver strategy

Up to this point, only a single RHS at a fixed frequency is considered. However, when dealing with the simulation of HEM problems, the main issue is the simultaneous handling of several hundreds or even some thousands of source positions. Each requires the solution of a forward problem with a unique right-hand side $\boldsymbol{b}_{\mathrm{sec}}^{r}$, for $r = 1, \dots, N_p$. Thus, for N_p transmitter positions, the RHS in (3.16) forms a block $\boldsymbol{B}_{\mathrm{sec}}$ with N_p columns, such that

$$\boldsymbol{B}_{\mathrm{sec}} = \left[\boldsymbol{b}_{\mathrm{sec}}^{1}, \boldsymbol{b}_{\mathrm{sec}}^{2}, \dots, \boldsymbol{b}_{\mathrm{sec}}^{N_p}\right] \in \mathbb{C}^{K \times N_p}. \tag{3.20}$$

Associated with N_p right-hand sides is the block of solution vectors

$$\boldsymbol{U}_{\mathrm{sec}} = \left[\boldsymbol{u}_{\mathrm{sec}}^{1}, \boldsymbol{u}_{\mathrm{sec}}^{2}, \dots, \boldsymbol{u}_{\mathrm{sec}}^{N_p}\right] \in \mathbb{C}^{K \times N_p}, \tag{3.21}$$

leading to the subsequent sparse block linear system

$$\boldsymbol{A}\boldsymbol{U}_{\mathrm{sec}} = \boldsymbol{B}_{\mathrm{sec}}. \tag{3.22}$$

The parallel sparse direct solver library PARDISO (Karypis and Kumar 1998; Schenk and Gärtner 2004; Schenk and Gärtner 2006) is used to obtain a factorization of the system matrix

points	point-wise	interpolated
5e1	0.0577 s	0.0593 s
1e2	0.1116 s	0.0589 s
5e2	0.5595 s	0.0622 s
1e3	1.1055 s	0.0654 s
5e3	5.5146 s	0.0687 s
1e4	11.0460 s	0.0713 s
5e4	54.9064 s	0.1345 s
1e5	109.7030 s	0.1734 s
5e5	547.4308 s	0.4945 s
1e6	1096.1542 s	0.8991 s

Table 3.1: Runtime of the primary field calculation for randomly distributed points in a three-layer model.

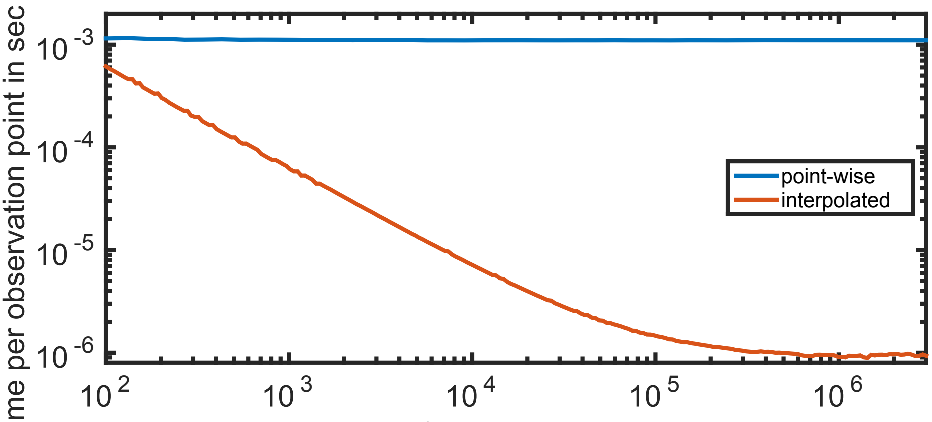

Figure 3.4: Computational effort per observation point.

$\boldsymbol{A}$. Furthermore, it provides the task of linear system solves, optimized for a block RHS, at substantial low numerical costs by inexpensive triangular solves. Because high memory requirement is becoming less and less problematic with the ongoing development of modern computer architecture, the choice of a direct solver provides both, accuracy and high computing speed. The latter particularly applies for a huge number of multiple RHS, as already shown by Everett (2011) and Grayver (2013).

Nevertheless, continuously advanced iterative strategies like (block) Krylov-subspace methods (Newman and Alumbaugh 2002; Saad 2003; Commer and Newman 2008; Grayver and Bürg 2014) as well as multigrid approaches (Aruliah and U. M. Ascher 2003; Haber and Heldmann 2007; Börner 2010) might depict comparable alternatives which are, however, not considered in this thesis. Furthermore, exploiting the independence of the single right-hand sides as proposed in Commer and Newman (2008) or Yang et al. (2013), a segmentation into N forward problems which are carried out on comparatively small unique grids seems to be a promising idea. This approach benefits from a much faster evaluation of $\boldsymbol{u}_{\mathrm{pri}}$ since the number of related DOF is likewise reduced. However, this approach necessitates to deal with a demanding projection of the individual forward grids on a single parameter grid which is required to handle the inverse problem.

The handling of different frequencies ω_f, for $f = 1, \ldots, N_f$, inevitably requires a separate factorization of the N_f system matrices $\boldsymbol{A}^f(\omega_f, \boldsymbol{\sigma})$. Thus, the solution of the entire forward problem is implemented sequentially for each frequency. However, it might be carried out in parallel, as the problems are thoroughly independent from each other.

3.4 Finite difference scheme

The employed finite difference discretization scheme, already introduced by Yee (1966), is still an effective and common approach (Newman and Alumbaugh 2002; Avdeev 2005; Börner 2010; Börner et al. 2012) to model the interaction of the electromagnetic fields in terms of the Maxwell's equations (2.1) to (2.4). The model domain Ω is divided into $S = n_x \times n_y \times n_z$ rectangular subsets or *cells*, $\Omega_p, p = 1 \dots S$, with a total number of $P = (n_x + 1) \times (n_y + 1) \times (n_z + 1)$ nodes. An overview of the appropriate grid spacings is given in appendix A and is illustrated in fig. A.1. The discrete electric conductivity σ_p and permittivity ϵ_p are set piece-wise constant for a single cell and are related to the cells' midpoints. The edge midpoints are related to discrete electrical field components e_x, e_y, and e_z which are oriented parallel to the edge-tangential directions (fig. 3.5). Furthermore, the face midpoints of the cells are associated with the magnetic field components h_x, h_y, and h_z, oriented parallel to the face normal directions. The definitions similarly apply to the total, primary, and secondary components of $\boldsymbol{e}$ and $\boldsymbol{h}$. The homogeneous Dirichlet boundary conditions, represented by

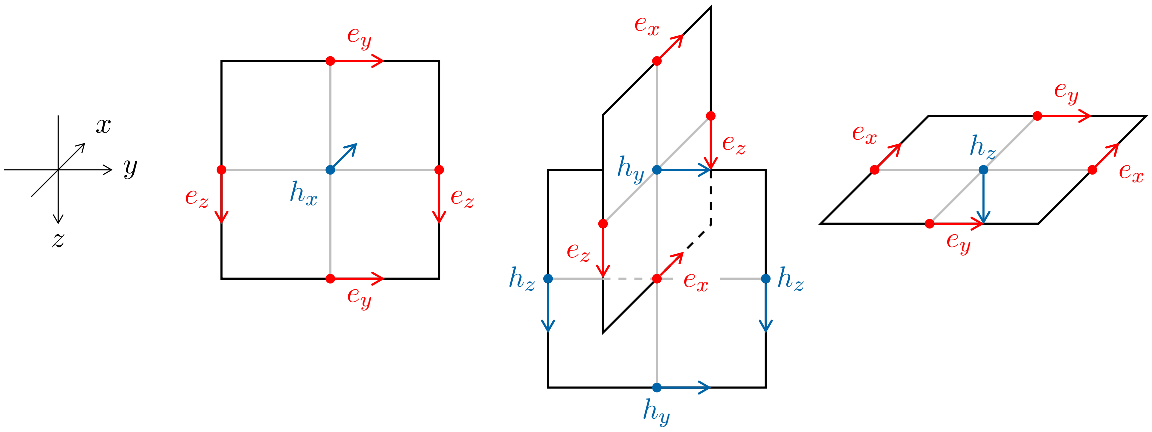

Figure 3.5: Definition of electrical (red) and magnetic field (blue) components on the tensor-product grid. Source: M. Afanasjew, TU Bergakademie Freiberg

$$\begin{aligned} \boldsymbol{n} \times \boldsymbol{e} &= \boldsymbol{0}_3 \quad \text{on } \mathit{\Gamma}, \\ \boldsymbol{n} \cdot \boldsymbol{h} &= \boldsymbol{0}_3 \quad \text{on } \mathit{\Gamma}, \end{aligned} \tag{3.23}$$

are consistently incorporated for the tangential components of $\boldsymbol{e}$ and the normal components of $\boldsymbol{h}$ (Newman and Alumbaugh 1995). A summary of the total number of resulting unknown field components (cf. appendix A.1) for

$$\boldsymbol{e}(x, y, z) \in \mathbb{C}^3 \rightarrow \boldsymbol{u} = \left[e_x^1, \dots, e_x^{K_x}, e_y^1, \dots, e_y^{K_y}, e_z^1, \dots, e_z^{K_z}\right]^\top \in \mathbb{C}^K, \tag{3.24}$$

and

$$\boldsymbol{h}(x, y, z) \in \mathbb{C}^3 \rightarrow \boldsymbol{h}^\mathrm{d} = \left[h_x^1, \dots, e_x^{K_x^h}, h_y^1, \dots, h_y^{K_y^h}, h_z^1, \dots, h_z^{K_z^h}\right]^\top \in \mathbb{C}^{K^h}, \tag{3.25}$$

is given in table 3.2. Associated with the electrical field components at the interior of the model domain is the number K of the degrees of freedom

component	without boundary	with boundary
e_x	$n_x \times (n_y - 1) \times (n_z - 1)$	$n_x \times (n_y + 1) \times (n_z + 1)$
e_y	$(n_x - 1) \times n_y \times (n_z - 1)$	$(n_x + 1) \times n_y \times (n_z + 1)$
e_z	$(n_x - 1) \times (n_y - 1) \times n_z$	$(n_x + 1) \times (n_y + 1) \times n_z$
h_x	$(n_x - 1) \times n_y \times n_z$	$(n_x + 1) \times n_y \times n_z$
h_y	$n_x \times (n_y - 1) \times n_z$	$n_x \times (n_y + 1) \times n_z$
h_z	$n_x \times n_y \times (n_z - 1)$	$n_x \times n_y \times (n_z + 1)$

Table 3.2: Numbers of field components defined on the tensor-product grid which consists of $S = n_x \times n_y \times n_z$ cells.

$$K := \underbrace{n_x(n_y-1)(n_z-1)}_{K_x} + \underbrace{(n_x-1)n_y(n_z-1)}_{K_y} + \underbrace{(n_x-1)(n_y-1)n_z}_{K_z}. \tag{3.26}$$

With

$$K^h := \underbrace{(n_x-1)n_y n_z}_{K_x^h} + \underbrace{n_x(n_y-1)n_z}_{K_y^h} + \underbrace{n_x n_y(n_z-1)}_{K_z^h}, \tag{3.27}$$

the total number of discrete magnetic field components without the boundary values is given.

The system matrix and the RHS vector are assembled component-wise, according to the decomposition (3.18). Without exception, the central differences scheme and a lexicographic order of the grid-related quantities are applied (cf. appendix A.1). The spatial discretization $\boldsymbol{K} \in \mathbb{R}^{K \times K}$ of the curl-curl operator, $\nabla \times \nabla \times \boldsymbol{e}$, is set up in two steps. At first,

$$\nabla \times \boldsymbol{e} = \begin{bmatrix} 0 & -\partial_z & \partial_y \\ \partial_z & 0 & -\partial_x \\ -\partial_y & \partial_x & 0 \end{bmatrix} \begin{bmatrix} e_x \\ e_y \\ e_z \end{bmatrix}, \tag{3.28}$$

is expressed by using the matrix $\boldsymbol{C}^e \in \mathbb{R}^{K^h \times K}$ which can be applied on the solution vector $\boldsymbol{u}$, providing the vector of the discrete magnetic field components

$$\boldsymbol{h}^{\mathrm{d}} = \frac{-1}{\mathrm{i}\omega\mu_0} \boldsymbol{C}^e \boldsymbol{u}. \tag{3.29}$$

In the second step,

$$\nabla \times \boldsymbol{h} = \begin{bmatrix} 0 & -\partial_z & \partial_y \\ \partial_z & 0 & -\partial_x \\ -\partial_y & \partial_x & 0 \end{bmatrix} \begin{bmatrix} h_x \\ h_y \\ h_z \end{bmatrix}, \tag{3.30}$$

is discretized by $\boldsymbol{C}^h \in \mathbb{R}^{K \times K^h}$ which in turn provides

$$\boldsymbol{u} = \frac{1}{\mathrm{i}\omega\epsilon} \boldsymbol{C}^h \boldsymbol{h}^{\mathrm{d}}. \tag{3.31}$$

The specific assembling of $\boldsymbol{C}^h$ and $\boldsymbol{C}^e$, implicitly including the homogeneous boundary conditions (3.23), is shown in appendix A.2. Finally, the discretized curl-curl operator can be composed by the matrix-matrix product

$$\boldsymbol{K} = \boldsymbol{C}^h \boldsymbol{C}^e. \tag{3.32}$$

Since the assignment of the conductivity as well as the permittivity is related to the midpoints of the cells and the electrical field components are defined on the cells' edges, the assembling of the mass matrices $\boldsymbol{M} \in \mathbb{R}^{K\times K}$ and $\boldsymbol{S} \in \mathbb{R}^{K\times K}$ has to be based on an interpolation scheme. Typically, a single entry of $\boldsymbol{M}$ incorporates a volume weighted summation of the conductivities of the four adjacent cells. Thus, a diagonal structure of $\boldsymbol{M}$ can be obtained. A detailed description of the complete mass matrix assembling is given in section 3.5. Contrary to the common approach of an explicit assembling in shape of a matrix, rather a tensor-based assembling of the two mass matrix parts is used. It exploits tensor-vector products with a tensor $\widetilde{\boldsymbol{T}}$, only containing geometrical information, and either the vector $\boldsymbol{\sigma}$ of cell conductivities or the vector $\boldsymbol{\epsilon}$ of the electric permittivity, respectively.

Two additional linear operators $\boldsymbol{G} \in \mathbb{R}^{K^h\times S}$ and $\boldsymbol{D} \in \mathbb{R}^{S\times K^h}$ are introduced (see appendix A.3) which provide the gradient of the conductivities $\nabla\sigma \rightarrow \boldsymbol{g}^{\boldsymbol{\sigma}}$ with

$$\boldsymbol{g}^{\boldsymbol{\sigma}} = \boldsymbol{G}\boldsymbol{\sigma} \quad \in \mathbb{R}^{K^h}, \tag{3.33}$$

located at the midpoints of the cell faces, and the divergence of the magnetic field $\nabla\cdot\boldsymbol{h} \rightarrow \boldsymbol{d}^{\boldsymbol{h}}$ with

$$\boldsymbol{d}^{\boldsymbol{h}} = \boldsymbol{D}\boldsymbol{h}^{\mathrm{d}} \quad \in \mathbb{R}^{S}. \tag{3.34}$$

Because the latter is defined at the same spatial position as the cell conductivities, i. e. at the midpoints of the grid cells, the second order spatial derivatives of the conductivity $\nabla^2\sigma \rightarrow \boldsymbol{s}^{\boldsymbol{\sigma}}$ with

$$\boldsymbol{s}^{\boldsymbol{\sigma}} = \boldsymbol{D}\boldsymbol{G}\boldsymbol{\sigma} \quad \in \mathbb{R}^{S}, \tag{3.35}$$

can easily be accessed. The homogeneous boundary condition within $\boldsymbol{D}$ ensures the conductivity to be consistently sustained outside the model domain.

To achieve the symmetry of the system matrix $\boldsymbol{A}$, a geometrical weighting

$$\boldsymbol{T}\boldsymbol{A}^{\mathrm{unweight}}\boldsymbol{u}_{\mathrm{sec}} = \boldsymbol{T}\boldsymbol{b}_{\mathrm{sec}}^{\mathrm{unweight}}, \tag{3.36}$$

with a diagonal matrix $\boldsymbol{T} \in \mathbb{R}^{K\times K}$ is required (Newman and Alumbaugh 1995). Therein, the contributions of the inhomogeneous grid spacings at the denominator of the central difference expressions, assigned to each row of the curl-curl operator $\boldsymbol{K}$, are removed by a straightforward volume weighting (appendix A.4). In the following parts of the thesis each representation of $\boldsymbol{A}$ and $\boldsymbol{b}_{\mathrm{sec}}$ are always considered as being left multiplied in terms of (3.36).

3.5 Tensor-based notation

For a convenient reassembling of the the system matrix $\boldsymbol{A}(\boldsymbol{\sigma})$ and the RHS vector $\boldsymbol{b}_{\mathrm{sec}}(\boldsymbol{\sigma}_{\mathrm{sec}})$ for a continuously changing parameter vector at an iterative inversion process, as well as an effective evaluation of the derivatives $\partial_{\boldsymbol{\sigma}}\boldsymbol{u}(\boldsymbol{\sigma})$ (cf. section 4.3), the properties of the *three-way tensor* or third-order tensor $\widetilde{\boldsymbol{T}}$ are exploited.

Considering the mass matrix part $\boldsymbol{M}$ which depends linearly on a projection of the cell conductivities on the location of degrees of freedom. The partial derivative with respect to an arbitrary cell conductivity σ_p, for $p = 1, \ldots, S$, is given by

$$\boldsymbol{M}(\mathbf{e}_p^S) = \left[\frac{\partial m_{i,j}(\boldsymbol{\sigma})}{\partial \sigma_p}\right]_{1\leq i,j\leq K} \quad \in \mathbb{R}^{K\times K}, \tag{3.37}$$

where $\mathbf{e}_p^S$ is the p-th unit vector in $\in \mathbb{R}^S$. The matrices $\boldsymbol{M}(\mathbf{e}_p^S)$ are always independent of $\boldsymbol{\sigma}$. The compact concatenation of the p derivatives is given in form of the tensor representation

$$\widetilde{\boldsymbol{T}} := \left[\frac{\partial m_{i,j}(\boldsymbol{\sigma})}{\partial \sigma_p}\right]_{1\leq i,j\leq K, 1\leq p\leq S} \in \mathbb{R}^{K\times K\times S}, \tag{3.38}$$

where the matrix $\boldsymbol{M}(\mathbf{e}_p^S)$ now refers to the p-th *slice* of the tensor $\widetilde{\boldsymbol{T}}$. The tensor contains the conductivity-independent geometric information of the mass matrix with respect to the grid cells. Since $\widetilde{\boldsymbol{T}}$ has a very sparse structure, it can smoothly be stored in memory, despite of its remarkable size. The explicit assembling of the tensor with respect to the finite difference discretization is shown in appendix A.7. Once, $\widetilde{\boldsymbol{T}}$ is available, it can be utilized in different useful ways. At first, the derivative of the system matrix $\boldsymbol{A}$ with respect to the parameter vector $\boldsymbol{\sigma}$ is given by

$$\frac{\partial \boldsymbol{A}}{\partial \boldsymbol{\sigma}} = \mathrm{i}\omega\mu_0 \frac{\partial \boldsymbol{M}}{\partial \boldsymbol{\sigma}} = \mathrm{i}\omega\mu_0 \widetilde{\boldsymbol{T}}, \tag{3.39}$$

since the conductivity is only related to the mass matrix part $\boldsymbol{M}$ (cf. (3.5)). Furthermore, it allows to easily assemble

$$\boldsymbol{M}(\boldsymbol{\sigma}) = \widetilde{\boldsymbol{T}} \times_3 \boldsymbol{\sigma} \quad \in \mathbb{R}^{K\times K}, \tag{3.40}$$

for arbitrary conductivity distributions $\boldsymbol{\sigma}$. Here the *tensor-vector* product $\times_3$ along the third dimension of $\widetilde{\boldsymbol{T}}$ is exploited which is described in detail in the following section. Since the geometric dependency of the permittivity $\boldsymbol{\epsilon}$ on the mass matrix part of the wave term $\boldsymbol{S}(\boldsymbol{\epsilon})$ has to equal the above described relations of $\boldsymbol{\sigma}$ and $\boldsymbol{M}(\boldsymbol{\sigma})$, it holds that

$$\boldsymbol{M}(\mathbf{e}_p^S) = \left[\frac{\partial m_{i,j}(\boldsymbol{\sigma})}{\partial \sigma_p}\right]_{1\leq i,j\leq K} \overset{!}{=} \left[\frac{\partial s_{i,j}(\boldsymbol{\epsilon})}{\partial \epsilon_p}\right]_{1\leq i,j\leq K} = \boldsymbol{S}(\mathbf{e}_p^S). \tag{3.41}$$

Therefore, $\widetilde{\boldsymbol{T}}$ can also be exploited to assemble

$$\boldsymbol{S}(\boldsymbol{\epsilon}) = \widetilde{\boldsymbol{T}} \times_3 \boldsymbol{\epsilon} \quad \in \mathbb{R}^{K\times K}, \tag{3.42}$$

for arbitrary permittivity distributions $\boldsymbol{\epsilon}$.

Tensor-vector product

For an arbitrary vector $\boldsymbol{x} \in \mathbb{R}^C$ and a tensor $\widetilde{\boldsymbol{T}} \in \mathbb{R}^{A\times B\times C}$, the tensor-vector product $\times_3$ is defined by

$$\begin{aligned} \widetilde{\boldsymbol{T}} \times_3 \boldsymbol{x} &:= \left[\sum_{c=1}^{C} t_{a,b,c} x_c\right]_{1\leq a\leq A, 1\leq b\leq B} \qquad \in \mathbb{R}^{A\times B}, \\ &= x_1 \left[t_{a,b,1}\right]_{1\leq a\leq A, 1\leq b\leq B} + \dots + x_C \left[t_{a,b,C}\right]_{1\leq a\leq A, 1\leq b\leq B} . \end{aligned} \tag{3.43}$$

The operation can be recognized as a summation of the $c = 1, \dots, C$ tensor slices $\boldsymbol{T}_c = [t_{a,b,c}]_{1\leq a\leq A, 1\leq b\leq B}$ along the third dimension where each slice is weighted by an element of $\boldsymbol{x}$. By analogy,

$$\begin{aligned} \widetilde{\boldsymbol{T}} \times_2 \boldsymbol{y} &:= \left[\sum_{b=1}^{B} t_{a,b,c} y_b\right]_{1\leq a\leq A, 1\leq c\leq C} \qquad \in \mathbb{R}^{A\times C}, \\ &= y_1 \left[t_{a,1,c}\right]_{1\leq a\leq A, 1\leq c\leq C} + \dots + y_B \left[t_{a,B,c}\right]_{1\leq a\leq A, 1\leq c\leq C} , \end{aligned} \tag{3.44}$$

for $\boldsymbol{y} \in \mathbb{R}^B$, denotes tensor-vector product along the second dimension of $\widetilde{\boldsymbol{T}}$, and

$$\begin{aligned} \widetilde{\boldsymbol{T}} \times_1 \boldsymbol{z} &:= \left[\sum_{a=1}^{A} t_{a,b,c} z_a\right]_{1\le b\le B, 1\le c\le C} \in \mathbb{R}^{B\times C}, \\ &= z_1 \left[t_{1,b,c}\right]_{1\le b\le B,1\le c\le C} + \ldots + z_A \left[t_{A,b,c}\right]_{1\le b\le B,1\le c\le C}, \end{aligned} \tag{3.45}$$

for $\boldsymbol{z} \in \mathbb{R}^A$, denotes tensor-vector product along the first dimension of $\widetilde{\boldsymbol{T}}$.

Tensor-matrix product

Additionally, the $\times_2$ tensor-matrix product with an arbitrary matrix $\boldsymbol{Y} \in \mathbb{R}^{B\times D}$ is defined as

$$\widetilde{\boldsymbol{T}} \times_2 \boldsymbol{Y} := \left[\sum_{b=1}^{B} t_{a,b,c} y_{b,d}\right]_{1\le a\le A, 1\le d\le D, 1\le c\le C} \in \mathbb{R}^{A\times D\times C}, \tag{3.46}$$

which acts as a replacement of the tensor slices $\boldsymbol{T}_c$ with the matrix-matrix products $\boldsymbol{T}_c\boldsymbol{Y}$. For $\widetilde{\boldsymbol{T}} \times_3 \boldsymbol{X} \in \mathbb{R}^{A\times B\times E}$ with $\boldsymbol{X} \in \mathbb{R}^{C\times E}$, the slices $\boldsymbol{T}_b = \left[t_{a,b,c}\right]_{1\le a\le A,1\le c\le C}$ and $\boldsymbol{T}_b\boldsymbol{X}$, for $b = 1, \ldots, B$ are affected instead.

Considering the conjunction of the tensor products

$$\left(\widetilde{\boldsymbol{T}} \times_2 \boldsymbol{Y}\right) \times_3 \boldsymbol{x} := \left[\sum_{c=1}^{C} \left(\sum_{b=1}^{B} t_{a,b,c} y_{b,d}\right) x_c\right]_{1\le a\le A, 1\le d\le D} \in \mathbb{R}^{A\times D}, \tag{3.47}$$

the commutative property allows the interchange of the order of summation as well as the order of multiplication such that

$$\begin{aligned} &= \left[\sum_{b=1}^{B}\sum_{c=1}^{C} t_{a,b,c} x_c y_{b,d}\right]_{1\le a\le A, 1\le d\le D} \\ &= \left(\widetilde{\boldsymbol{T}} \times_3 \boldsymbol{x}\right) \times_2 \boldsymbol{Y}, \end{aligned} \tag{3.48}$$

which is equivalent to

$$= \left(\widetilde{\boldsymbol{T}} \times_3 \boldsymbol{x}\right) \boldsymbol{Y}. \tag{3.49}$$

3.6 Measurement operator Q

In general, the spatial locations of sampled vertical magnetic field components $\boldsymbol{d}^{\mathrm{obs}}$ differ from the location of the discrete field components $\boldsymbol{u}$ within the computational domain. Additionally, the modeled electric field $\boldsymbol{u}_{\mathrm{sec}}$ needs to be transformed into a vertical magnetic field $h_{\mathrm{sec},z}$, to be normalized by the free-space source field h_z^{air}, and to be rescaled to ppm.

At first, considering a single frequency ω. The elements of the vector of forward modeled or *synthetic data*

$$\boldsymbol{d} = \left[R_1 + \mathrm{i}Q_1, \ldots, R_{N_p} + \mathrm{i}Q_{N_p}\right]^\top \in \mathbb{C}^{N_p}, \tag{3.50}$$

below for $i = 1, \ldots, N_p$, with the number of TX/RX positions N_p, and

$$d_i(\boldsymbol{u}_{\text{sec}}) = 10^6 \left(\frac{h_{\text{pri},z,i}(\boldsymbol{u}_{\text{pri}}) + h_{\text{sec},z,i}(\boldsymbol{u}_{\text{sec}}) - h_{z,i}^{\text{air}}}{h_{z,i}^{\text{air}}} \right), \tag{3.51}$$

are expected to be consistent with the definition (1.1) and (1.2) of the observed data (or the relative secondary magnetic fields)

$$d_i^{\text{obs}} = 10^6 \left(\frac{h_{z,i}^{\text{earth}}}{h_{z,i}^{\text{air}}} \right), \tag{3.52}$$

when the equality

$$\boldsymbol{h}_z = \boldsymbol{h}_z^{\text{air}} + \boldsymbol{h}_z^{\text{earth}} = \boldsymbol{h}_{\text{pri},z} + \boldsymbol{h}_{\text{sec},z}, \tag{3.53}$$

for the underlying total vertical magnetic fields $\boldsymbol{h}_z = \left[h_{z,1}, \ldots, h_{z,N_p}\right]^\top \in \mathbb{C}^{N_p}$ at the receivers is assumed.

Concerning the unique HEM situation where only a single datum is obtained from one TX/RX position, i. e. only a scalar $d \in \mathbb{C}$ is observed from the vector solution $\boldsymbol{u}_{\text{sec}}$. A *mapping* or *measurement operator* $\boldsymbol{q} \in \mathbb{C}^K$ (for its definition see (3.58) below) yields

$$d = \boldsymbol{q}^\top (\boldsymbol{u}_{\text{sec}} + \boldsymbol{u}_{\text{pri}}) - h_z^{\text{air}} = \boldsymbol{q}^\top \boldsymbol{A}^{-1} \boldsymbol{b}_{\text{sec}} + d_{\text{pri}}, \tag{3.54}$$

at a distinct receiver site, where the primary part of the data vector $d_{\text{pri}} \in \mathbb{C}$ is incorporated by

$$d_{\text{pri}} = 10^6 \left(\frac{h_{\text{pri},z} - h_z^{\text{air}}}{h_z^{\text{air}}} \right). \tag{3.55}$$

For $z = -h$, a vanishing conductivity in air ($\sigma_{\text{air}} = 0$), and the TX/RX distance r, the free-space source field $h_z^{\text{air}} \in \mathbb{C}$, cf. (2.52), is given by

$$h_z^{\text{air}}(r) = \frac{m}{4\pi} \frac{1}{r^3} \left(k^2 r^2 - \mathrm{i}kr - 1\right) \mathrm{e}^{-\mathrm{i}kr}, \tag{3.56}$$

with

$$k = \omega^2 \mu_0 \epsilon_0. \tag{3.57}$$

In order to avoid inaccuracies by the numerical transformation of the primary electric fields, i. e. by calculating $\boldsymbol{q}^\top \boldsymbol{u}_{\text{pri}}$, it is advisable to analytically evaluated the primary magnetic fields $\boldsymbol{h}_{\text{pri}} = \left[h_{\text{pri}}^1, \ldots, h_{\text{pri}}^{N_p}\right]^\top \in \mathbb{C}^{N_p}$, for providing d_{pri} by (3.55).

The measurement operator is defined as a complex vector

$$\boldsymbol{q} := \left[\frac{-1}{\mathrm{i}\omega\mu_0} \frac{10^6}{h_z^{\text{air}}} \boldsymbol{i}^\top \boldsymbol{C}^e \right]^\top \in \mathbb{C}^K, \tag{3.58}$$

including the transformation to magnetic fields $\frac{-1}{\mathrm{i}\omega\mu_0} \boldsymbol{C}^e$, a trilinear interpolation operator $\boldsymbol{i} \in \mathbb{R}^{K^h}$, and the data scaling $\frac{10^6}{h_z^{\text{air}}}$. For a RX coil, located at an arbitrary point $\boldsymbol{x}_{\text{RX}} = [x, y, z]^\top$ within the model domain Ω, the interpolated vertical magnetic field is given by

$$h_{\text{sec}}(\boldsymbol{x}_{\text{RX}}) = \boldsymbol{i}(\boldsymbol{x}_{\text{RX}}) \cdot \boldsymbol{h}^{\text{d}}. \tag{3.59}$$

The interpolation operator $\boldsymbol{i}(\boldsymbol{x}_{\mathrm{RX}})$ (see appendix A.6) incorporates a maximum number of 1 ($\boldsymbol{x}_{\mathrm{RX}}$ coincides with the spatial position of an element of $\boldsymbol{h}_z^{\mathrm{d}}$) up to 8 (no agreement in the spatial position of $\boldsymbol{x}_{\mathrm{RX}}$ and any element of $\boldsymbol{h}^{\mathrm{d}}$ in any coordinate direction) non-zero entries that are associated with the surrounding components of the discrete magnetic field $\boldsymbol{h}^{\mathrm{d}}$. Hence, $\boldsymbol{q}$ comprises 4 up to 24 non-zero entries, associated with the structure of $\boldsymbol{C}^e$ (see appendix A.2), which leads to a very sparse structure of the measurement operator especially for a large number of DOF.

In order to deal with the block structure of the solution $\boldsymbol{U}_{\mathrm{sec}} = \left[\boldsymbol{u}_{\mathrm{sec}}^1, \boldsymbol{u}_{\mathrm{sec}}^2, \dots, \boldsymbol{u}_{\mathrm{sec}}^{N_p}\right]$ that needs to be projected on a vector-shaped parametrization of the data $\boldsymbol{d}$, a common approach is to vectorize the entire problem. Thus, a general description

$$\boldsymbol{d} = \boldsymbol{Q}\boldsymbol{u}_{\mathrm{sec}} + \boldsymbol{d}_{\mathrm{pri}} \quad \in \mathbb{C}^N, \tag{3.60}$$

with

$$\boldsymbol{u}_{\mathrm{sec}} = \boldsymbol{A}^{-1}\boldsymbol{b}_{\mathrm{sec}}, \tag{3.61}$$

and

$$N = N_f N_p, \tag{3.62}$$

can be obtained which is typically used in the context of geophysical inversion. For that, $\boldsymbol{U}_{\mathrm{sec}}$ and the independent treatment of the different frequencies are equivalently handled by an overall concatenation, leading to very huge and sparse matrices

$$\boldsymbol{Q} = \begin{bmatrix} \boldsymbol{q}_1^{1\top} & \boldsymbol{0}_K^\top & \cdots & & & & \\ \boldsymbol{0}_K^\top & \boldsymbol{q}_2^{1\top} & \ddots & & & & \\ \vdots & \ddots & \ddots & & & & \\ & & & \boldsymbol{q}_{N_p}^{1\top} & & & \\ & & & & \boldsymbol{q}_1^{2\top} & & \\ & & & & & \ddots & \\ & & & & & & \boldsymbol{q}_{N_p}^{N_f\top} \end{bmatrix} \in \mathbb{C}^{N\times NK}, \tag{3.63}$$

$$\boldsymbol{A} = \begin{bmatrix} \mathrm{diag}\left(\boldsymbol{1}_{N_p}\right)\otimes\boldsymbol{A}^1 & \boldsymbol{0}_{N_pK,N_pK} & \cdots & \\ \boldsymbol{0}_{N_pK,N_pK} & \mathrm{diag}\left(\boldsymbol{1}_{N_p}\right)\otimes\boldsymbol{A}^2 & \ddots & \\ \vdots\ddots & & \ddots & \\ & & & \mathrm{diag}\left(\boldsymbol{1}_{N_p}\right)\otimes\boldsymbol{A}^{N_f} \end{bmatrix} \in \mathbb{C}^{NK\times NK}, \tag{3.64}$$

and large dense vectors

$$\boldsymbol{b}_{\mathrm{sec}} = \begin{bmatrix} \boldsymbol{b}_{\mathrm{sec},1}^1 \\ \boldsymbol{b}_{\mathrm{sec},2}^1 \\ \vdots \\ \boldsymbol{b}_{\mathrm{sec},N_p}^1 \\ \boldsymbol{b}_{\mathrm{sec},1}^2 \\ \vdots \\ \boldsymbol{b}_{\mathrm{sec},N_p}^{N_f} \end{bmatrix} \in \mathbb{C}^{NK}, \quad \boldsymbol{d}_{\mathrm{pri}} = \begin{bmatrix} \boldsymbol{d}_{\mathrm{pri},1}^1 \\ \boldsymbol{d}_{\mathrm{pri},2}^1 \\ \vdots \\ \boldsymbol{d}_{\mathrm{pri},N_p}^1 \\ \boldsymbol{d}_{\mathrm{pri},1}^2 \\ \vdots \\ \boldsymbol{d}_{\mathrm{pri},N_p}^{N_f} \end{bmatrix} \in \mathbb{C}^{NK}, \tag{3.65}$$

without loss of generality. In the above expressions, $\mathrm{diag}\left(\boldsymbol{x}\right)$ denotes a diagonal matrix with the main diagonal elements formed by the vector $\boldsymbol{x}$ and the symbol $\otimes$ denotes the Kronecker product, as introduced in (A.19).

Deviating from that standard notation, a more compact description can be achieved when the measurement operator is defined as a sparse complex matrix

$$\boldsymbol{Q} := \begin{bmatrix} \boldsymbol{q}_1^\top \\ \vdots \\ \boldsymbol{q}_{N_p}^\top \end{bmatrix} \quad \in \mathbb{C}^{N_p \times K}, \tag{3.66}$$

which, consistent to (3.63), row-wise contains the N_p individual operators $\boldsymbol{q}_i$ for a single frequency. To obtain the vector of synthetic data $\boldsymbol{d} = \boldsymbol{d}_{\mathrm{pri}} + \boldsymbol{d}_{\mathrm{sec}}$, containing the information of all TX/RX positions, the *Hadamard* or *element-wise product* is exploited

$$\boldsymbol{d}_{\mathrm{sec}} = \left[\mathbf{1}_K^\top \left(\boldsymbol{Q}^\top \circ \boldsymbol{U}_{\mathrm{sec}}\right)\right]^\top \quad \in \mathbb{C}^{N_p}, \tag{3.67}$$

which primarily provides the total secondary data components for all N_p data points. The binary operation symbol $\circ$ denotes element-wise multiplication that is given for arbitrary matrices $\boldsymbol{A}, \boldsymbol{B} \in \mathbb{C}^{N \times M}$ by

$$\begin{aligned} \boldsymbol{C} &= \boldsymbol{A} \circ \boldsymbol{B} \in \mathbb{C}^{N \times M} \\ &:= \begin{bmatrix} a_{1,1}b_{1,1} & \cdots & a_{1,M}b_{1,M} \\ \vdots & \ddots & \vdots \\ a_{N,1}b_{N,1} & \cdots & a_{N,M}b_{N,M} \end{bmatrix}. \end{aligned} \tag{3.68}$$

Finally, the sequentially evaluated data vector components for $f = 1, \dots, N_f$ different frequencies ω_f are concatenated

$$\boldsymbol{d} := \begin{bmatrix} \boldsymbol{d}_{\mathrm{sec}}^1 \\ \vdots \\ \boldsymbol{d}_{\mathrm{sec}}^{N_f} \end{bmatrix} + \begin{bmatrix} \boldsymbol{d}_{\mathrm{pri}}^1 \\ \vdots \\ \boldsymbol{d}_{\mathrm{pri}}^{N_f} \end{bmatrix} \quad \in \mathbb{C}^{N_f N_p}, \tag{3.69}$$

yielding the total vector of data which comprises $N = N_f N_p \ll K$ complex-valued data points.

3.7 Case study on a synthetic model

For numerical simulation studies a synthetic model is exploited that is based on a description published by Siemon, Christiansen, et al. (2009) and that is shown in fig. 3.6. The modeling domain covers a volume of 1200 m×1600 m×350 m where a rectangular block (500 m×100 m×20 m) of 0.02 $\frac{\mathrm{S}}{\mathrm{m}}$ is embedded in a horizontally layered half-space with conductivities of 0.005 $\frac{\mathrm{S}}{\mathrm{m}}$, 0.01 $\frac{\mathrm{S}}{\mathrm{m}}$, 0.2 $\frac{\mathrm{S}}{\mathrm{m}}$ and 0.001 $\frac{\mathrm{S}}{\mathrm{m}}$, and layer thicknesses of 20 m, 30 m and 10 m. The air layer has a thickness of 100 m and is assigned to a conductivity of 10^{-9} $\frac{\mathrm{S}}{\mathrm{m}}$. The $N_p = 753$ TX/RX positions are uniformly distributed at three profiles, parallel to the y-axis, that are centered at $x =$−200 m, 0 m and 200 m. The point altitude is allowed to vary between −54 m and −29 m and the point spacing in the y-direction is set to 4 m.

The principle functionality of the introduced forward operator was already demonstrated in a comparative study by Miensopust et al. (2014) and by Börner et al. (2012). In the following, the observed solutions at the TX/RX positions for the above described synthetic model are compared with reference solutions that are provided by the MarcoAir package, based on a

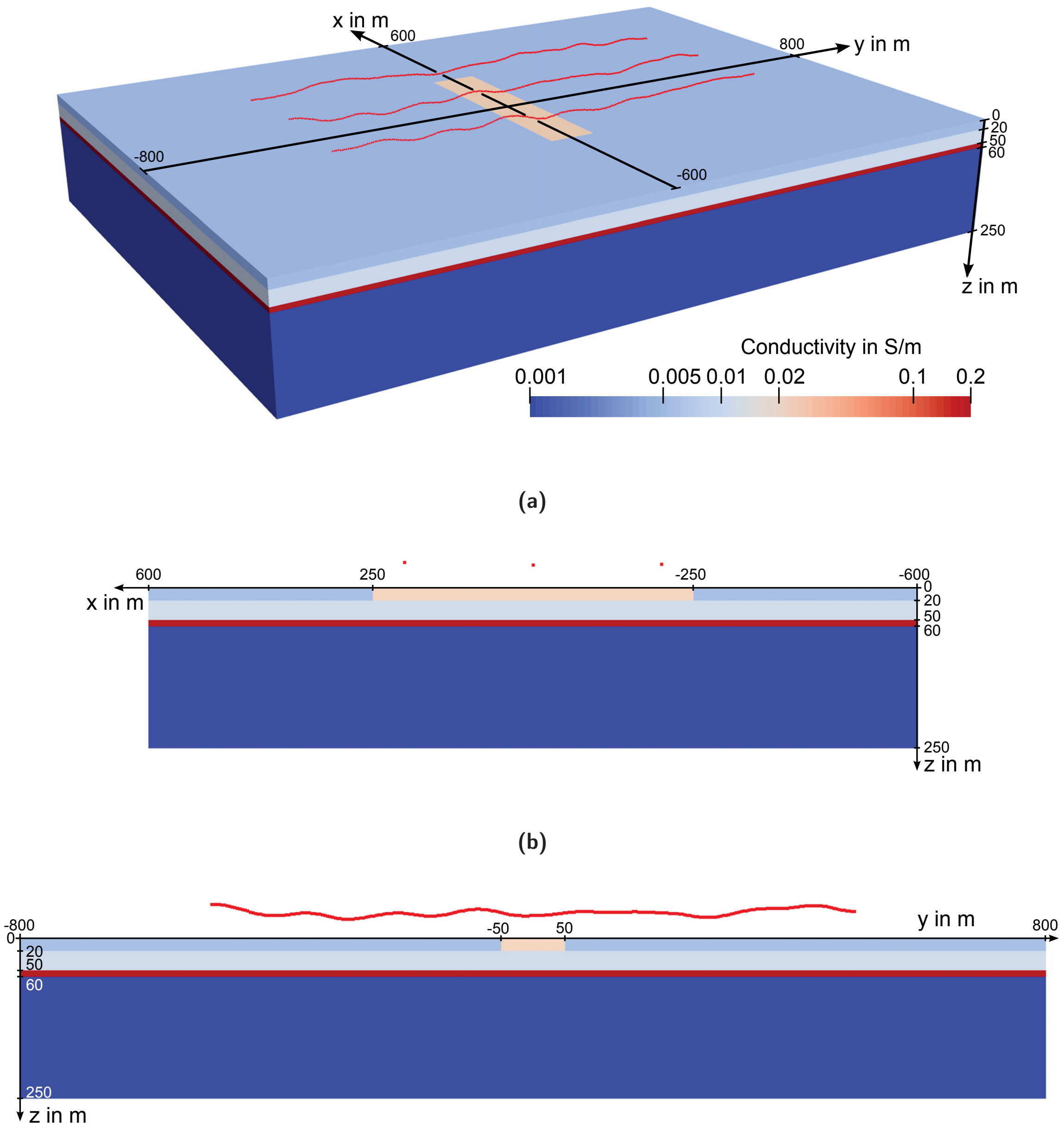

(a)

(b)

(c)

Figure 3.6: Synthetic model without the air layer a) full view, b) sketch of xz-plane at $y = 0$, c) sketch of yz-plane at $x = 0$. The red dots indicate the RX/TX positions, located on average at 40 m above the surface.

volume integral approach, and the LokiAir package, based on a finite elements discretization, both contained in the CSIRO/AMIRA's P223 suite (Raiche et al. 2007). The simulations were provided by Angelika Ullmann (Leibniz Institute for Applied Geophysics).

An adaptive grid refinement, based on the constraint of the physical property $\nabla\cdot \boldsymbol{h} = 0$, is used to derive an adequately dense model grid which ensures accurate forward solutions (Börner et al. 2012). It starts at a default grid, only containing the spatial information of the model domain, the layer boundaries, the block extent, and an additional node in the z-direction which is aligned with the mean profile height. The adaptive refinement approach exploits the evaluation of the volume weighted divergence of the secondary magnetic field (cf. (3.29) and (3.34))

$$\boldsymbol{c}_r(\omega_f) = \boldsymbol{V}\boldsymbol{d}^{\boldsymbol{h}}_{\text{sec},r}(\omega_f) := -\frac{1}{\mathrm{i}\omega\mu_0}\boldsymbol{V}\boldsymbol{D}\boldsymbol{C}^e\boldsymbol{u}_{\text{sec},r}(\omega_f) \overset{!}{=} \boldsymbol{0}_S, \tag{3.70}$$

for $r = 1, \dots, N_p$, which yields the *cumulative divergence*

$$\boldsymbol{c}_{\text{tot}}(\omega_f) := \sum_{r=1}^{N_p} |\boldsymbol{c}_r(\omega_f)| \quad \in \mathbb{R}^S, \tag{3.71}$$

that is used to act as an a-posteriori error indicator. As the solution of the forward problem is calculated in terms of the secondary field approach, only the discrete secondary magnetic fields have to be concerned. To consider the inhomogeneity of the grid spacings, each element of $\boldsymbol{d}^{\boldsymbol{h}}_{\text{sec}}$ is scaled with the respective cell volume, by the multiplication with the diagonal matrix of cell volumes $\boldsymbol{V} \in \mathbb{R}^{S\times S}$ (see appendix A.5). Thus, additional weight is put on those parts of $\boldsymbol{d}^{\boldsymbol{h}}_{\text{sec}}$ that are related to large cells, as they are expected to most likely deviate from the exact solution. In each refinement step, the evaluation is based on an individual frequency ω_f, for $f = 1, \dots, N_f$. Typically, the whole refinement iteration starts with a low frequency and is referred to the high frequencies in the subsequent progress where the number of refinement steps can be chosen arbitrarily. To avoid a refinement of the entire grid which quickly leads to a non-manageable large number of DOF, a uniform refinement, i. e. a subdivision of a single cell into 8 even cells, is only applied to a subset of the cells whose solutions exceed a threshold value

$$\boldsymbol{c}_{\text{tresh}} = (1 - t_{\text{frac}}) \max(\boldsymbol{c}_{\text{tot}}). \tag{3.72}$$

The fraction of respective cells $0 < t_{\text{frac}} \leq 100\%$ that are included in the refinement process can likewise be chosen arbitrarily.

Figure 3.8 and fig. 3.7 show the initial grid (top) and the grid after 6 refinement steps (bottom) for two different sections of the synthetic model. For the refinement iteration a setup of $\boldsymbol{t}_{\text{frac}} = [1, 0.5, 0.4, 0.3, 0.2, 0.2]$ with respect to $\boldsymbol{\omega} = [\omega_1, \omega_1, \omega_2, \omega_3, \omega_4, \omega_5, \omega_5]$ is chosen. The subscripts refer to the 5 frequencies 387 Hz, 1820 Hz, 8225 Hz, 41 550 Hz and 133 200 Hz. Starting with a default grid of 63 cells, the refinement leads to a final grid that comprises 130 200 cells with a total of 373 793 associated DOF. The black lines indicate the cell boundaries and the blue boxes symbolize the outline of the embedded block.

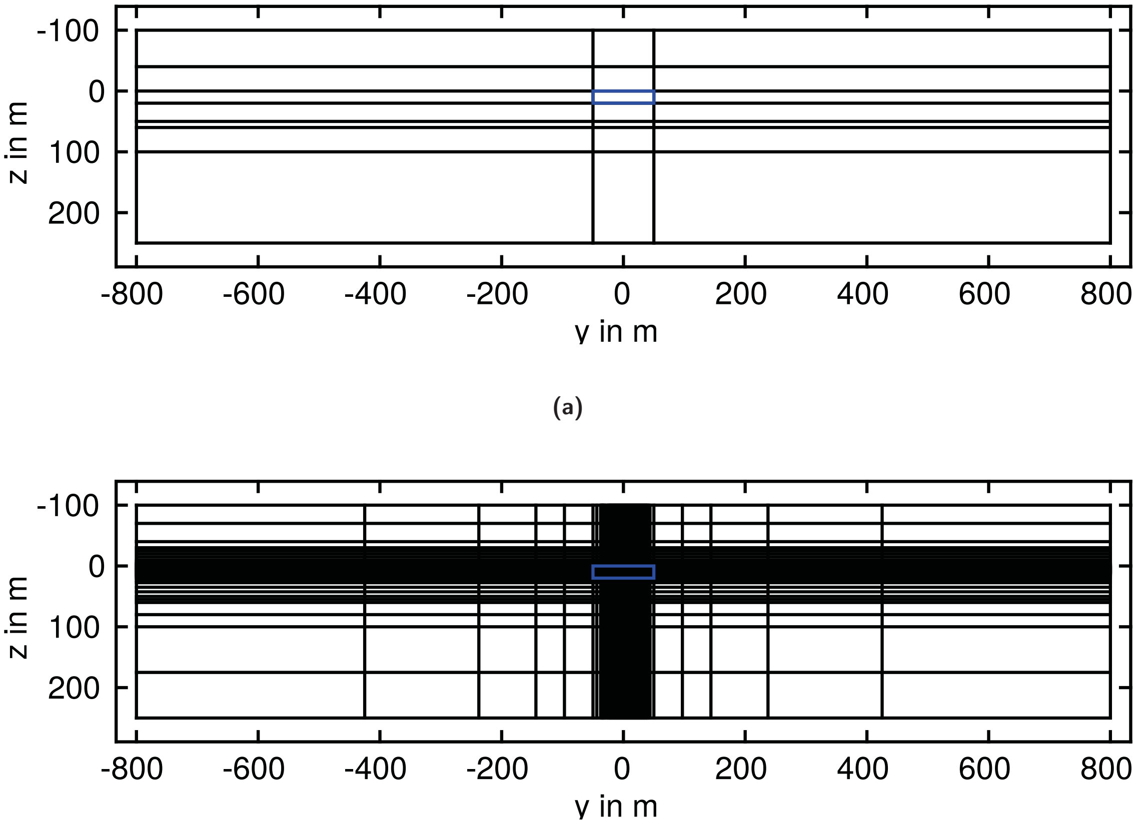

(a)

(b)

Figure 3.7: Vertical section of the tensor-product grid at 0 (a) and 6 (b) adaptive grid refinement steps.

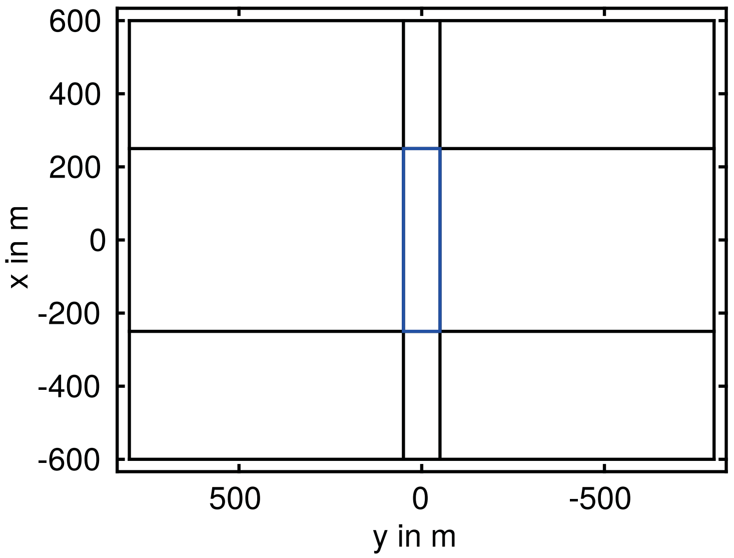

(a)

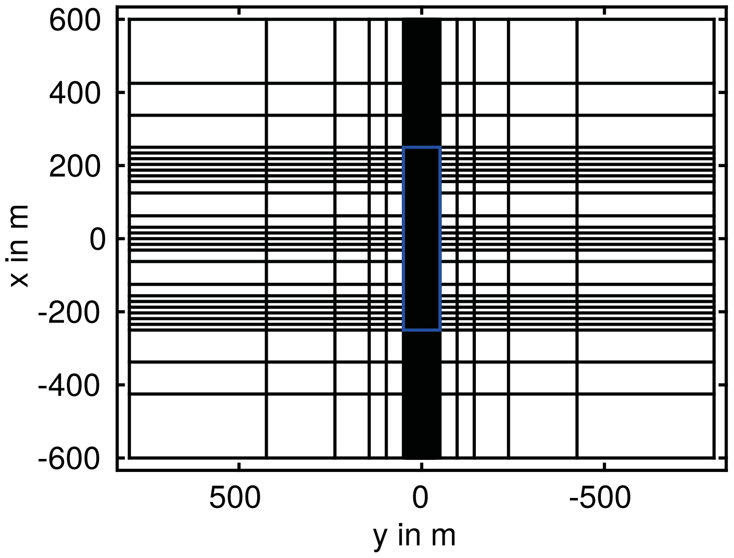

(b)

Figure 3.8: Horizontal section of the tensor-product grid at 0 (a) and 6 (b) adaptive grid refinement steps.

As the secondary field is considered to noticeably differ from zero only at the block vicinity, the observed grid refinement seems reasonable. The trace of the profile lines are visible due to the nearby high magnitude of the EM fields which likewise cause high contributions to the cumulative divergence. Since the refinement leads to grid spacings of below 1 m, the corresponding grid edges could not be resolved as individual lines in the bottom part of the figures.

The vertical component of the total magnetic field, i. e. the vector of synthetic data $\boldsymbol{d}$, derived from the forward solution $\boldsymbol{u}$ that is calculated at the final grid, is compared to the solutions which are obtained by the MarcoAir and the LokiAir packages. Therefore, the relative permittivity is set to zero for the entire model domain, including the embedded block. The resulting relative errors at the three profiles with respect to the solution of the presented forward algorithm are shown in figs. 3.9 to 3.11. The yellow vertical dashed lines indicate the horizontal boundaries of the embedded block and the black horizontal dashed lines narrow the $\pm 3\,\%$ error boundary. An overall good agreement with both reference solutions at all frequencies and in the area of 250 m around the embedded block can be obtained. The corresponding relative errors are basically below $3\,\%$. Conspicuous errors near the ends of the profiles with respect to the black curve, can be assigned to discretization errors at the model boundaries for LokiAir package. Since the influence of the secondary field, and hence the numerical solution, already vanishes in a distance of about 300 m from the profile center (see fig. 3.12), these errors can be neglected. Beside that, the figures indicate that the boundary assumptions (cf. section 3.2) for the expected anomalies, being located only at the model interior, can be considered as valid.

Setting the relative permittivity consistently to one, the major differences may be expected at the highest frequencies. In the following, only the central profile is considered. Figure 3.13 illustrates the relative error for the solution $\boldsymbol{d}(\boldsymbol{\epsilon}_r = 0)$ with respect to $\boldsymbol{d}(\boldsymbol{\epsilon}_r = 1)$. Both magnetic fields are obtained by the forward algorithm, presented in the thesis. Deviations of the quasi-static approximation from the full Helmholtz equation particularly appear in the real part of the solution for $f = 133\,200\,\mathrm{Hz}$. Furthermore, the small absolute error between $\boldsymbol{d}_{\mathrm{sec}}(\boldsymbol{\epsilon}_r = 0)$ and $\boldsymbol{d}_{\mathrm{sec}}(\boldsymbol{\epsilon}_r = 1)$ as shown in fig. 3.14, suggests that the changes in the total field solution can be exclusively assigned to the analytic primary fields which obviates the need for a comparison to other numerical solutions.

All calculations are carried out on 8 cores of an AMD Opteron$^{\mathrm{TM}}$processor 6136, running at 2.4 GHz with 256 GB of RAM. While the calculation of the analytic primary field $\boldsymbol{u}_{\mathrm{pri}}$ requires a total of 26 min, the secondary field $\boldsymbol{u}_{\mathrm{sec}}$ is evaluated in 15 min with the previously provided factorization of the system matrix $\boldsymbol{A}$ (13 min). The peak memory usage amounts 77.5 GB which accumulates at the N_p parallel triangular solves.

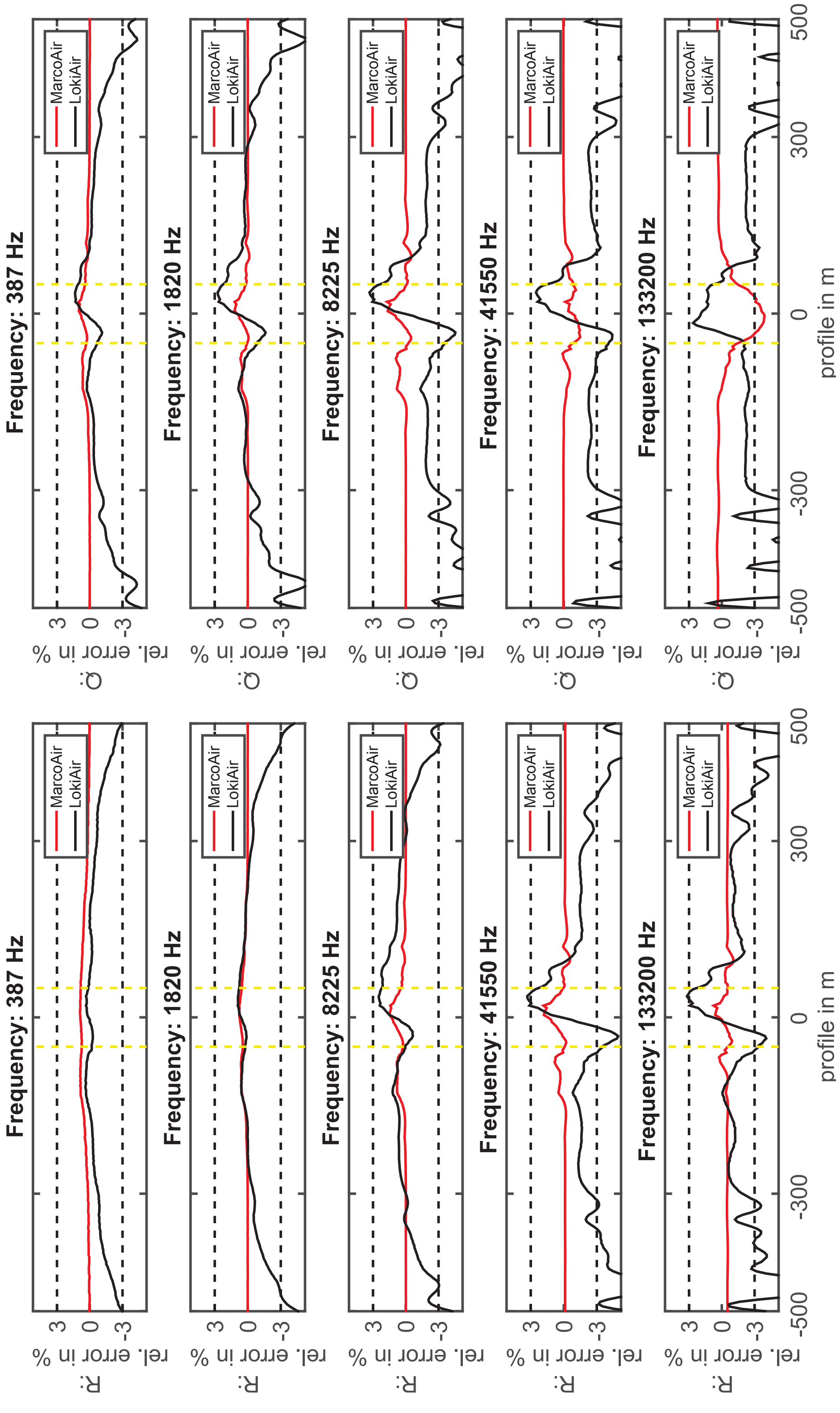

Figure 3.9: Relative errors of the real (left-hand side) and imaginary (right-hand side) parts of the data vectors along a profile in y-direction at $x = -200\,\mathrm{m}$.

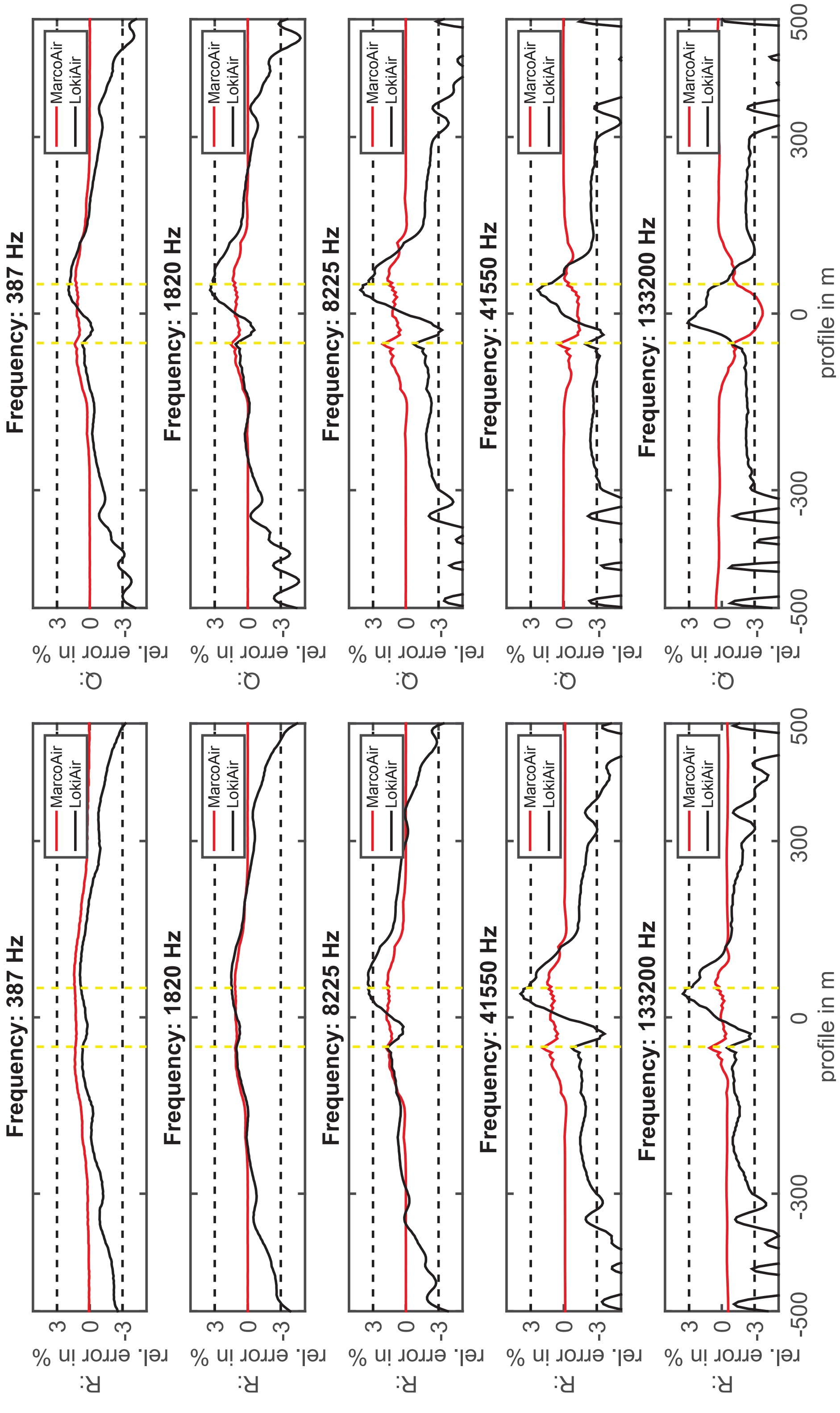

Figure 3.10: Relative errors of the real (left-hand side) and imaginary (right-hand side) parts of the data vectors along a profile in y-direction at $x = 0\,\mathrm{m}$.

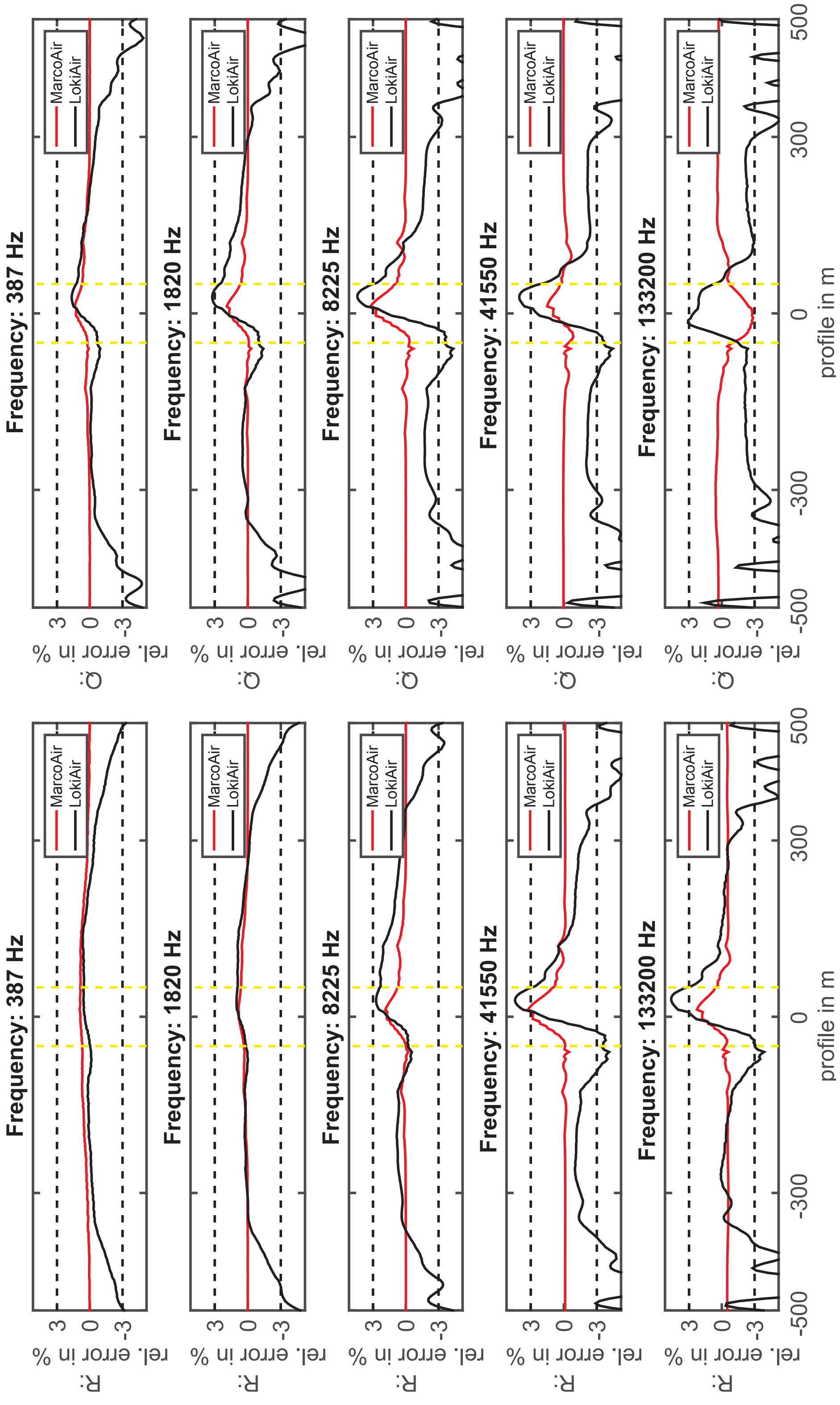

Figure 3.11: Relative errors of the real (left-hand side) and imaginary (right-hand side) parts of the data vectors along a profile in y-direction at $x = 200\,\mathrm{m}$.

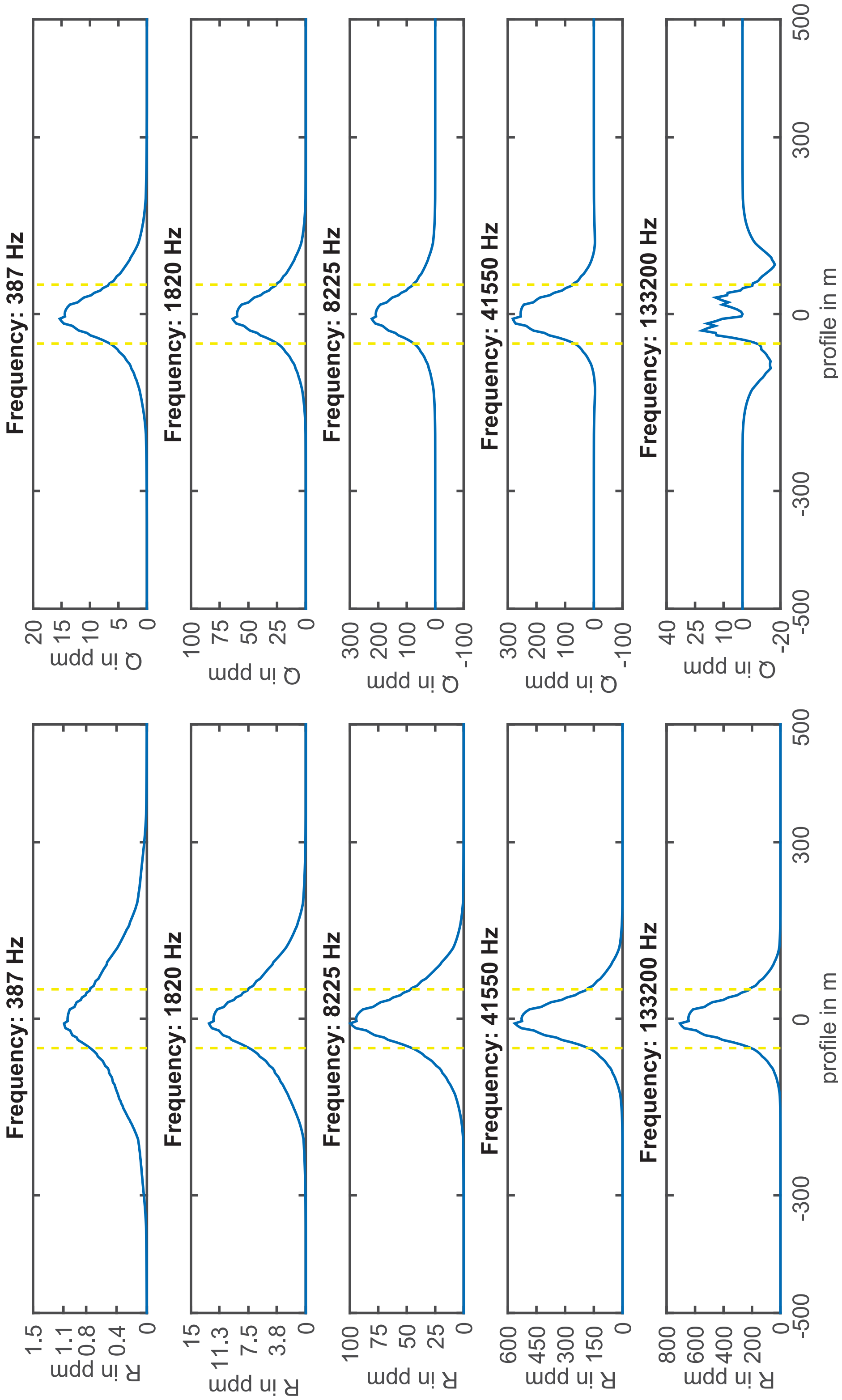

Figure 3.12: Real (left-hand side) and imaginary (right-hand side) parts of $\boldsymbol{d}_{\text{sec}}$ at the central profile ($x = 0\,\text{m}$).

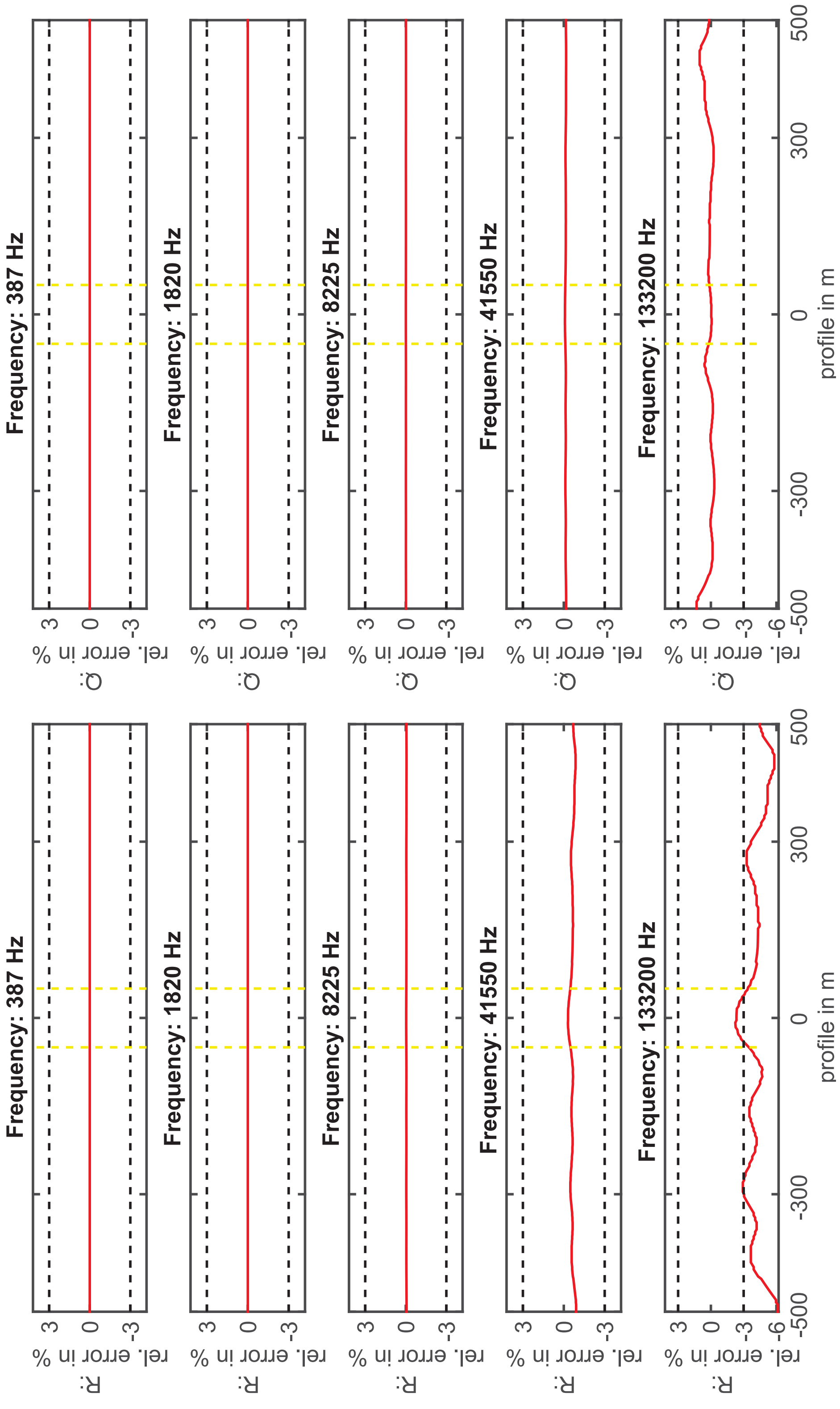

Figure 3.13: Relative error of the real (left-hand side) and imaginary (right-hand side) parts of $\boldsymbol{d}(\boldsymbol{\epsilon}_r = 0)$ with respect to $\boldsymbol{d}(\boldsymbol{\epsilon}_r = 1)$ along the central profile ($x = 0\,\mathrm{m}$).

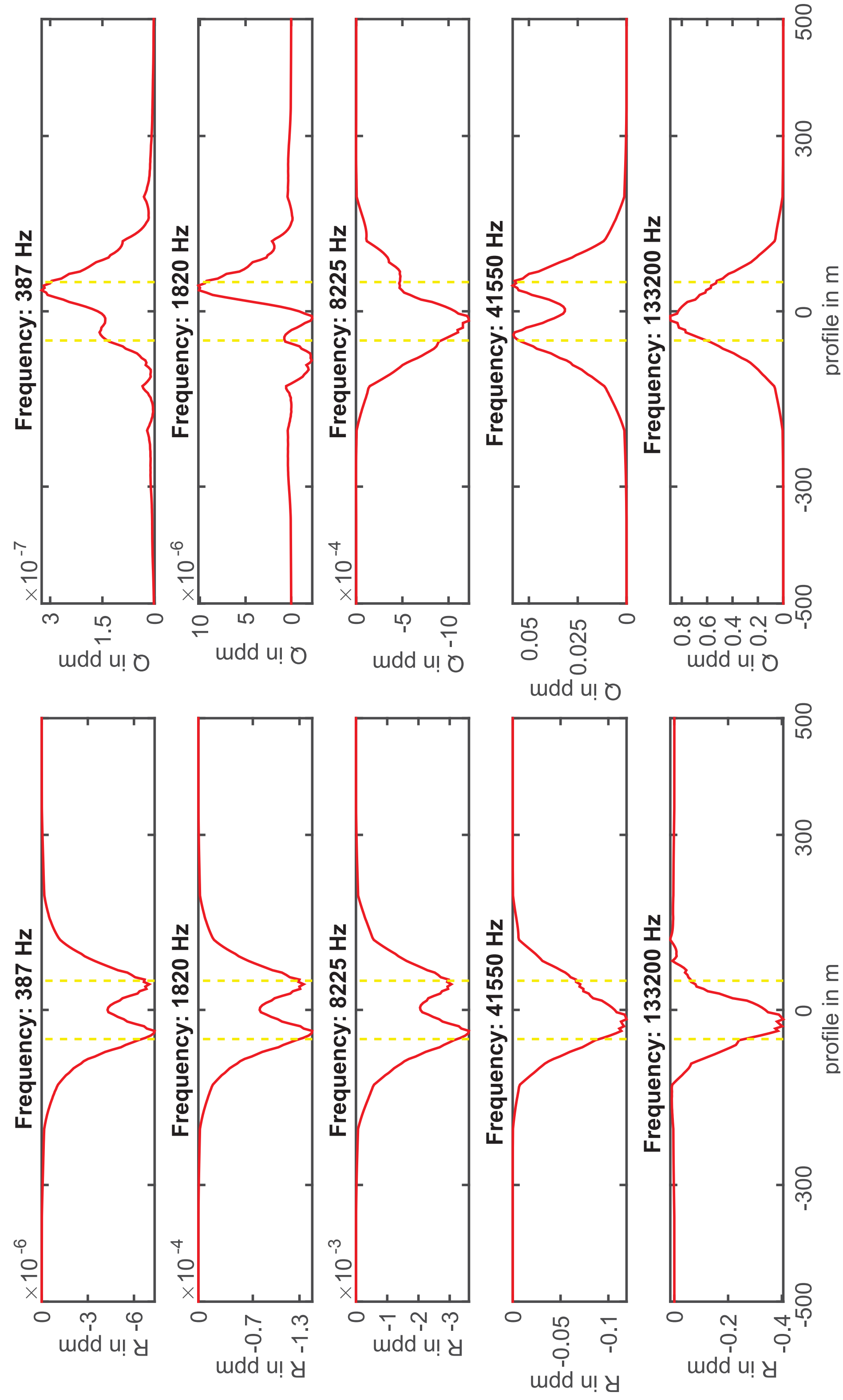

Figure 3.14: Absolute error of the real (left-hand side) and imaginary (right-hand side) parts of $\boldsymbol{d}_{\text{sec}}(\boldsymbol{\epsilon}_r = 0)$ with respect to $\boldsymbol{d}_{\text{sec}}(\boldsymbol{\epsilon}_r = 1)$ along the central profile ($x = 0\,\text{m}$).

4 Inverse problem

Notation

$(\cdot)_{\text{act}}$		$(\cdot)$, restricted to the active region
α	$\in \mathbb{R}_+$	step length
λ	$\in \mathbb{R}_+$	regularization parameter
Φ	$\in \mathbb{R}_+$	objective function
$\Phi_{\boldsymbol{d}}$	$\in \mathbb{R}_+$	data misfit norm
$\Phi_{\boldsymbol{m}}$	$\in \mathbb{R}_+$	model misfit norm
$\boldsymbol{d}(\boldsymbol{m})$	$\in \mathbb{C}^N$	synthetic data
$\boldsymbol{d}^{\text{obs}}$	$\in \mathbb{C}^N$	observed data
$\Delta\boldsymbol{d}$	$\in \mathbb{C}^N$	data residual
$\boldsymbol{j}_{\text{cum}}$	$\in \mathbb{C}^S$	cumulative sensitivity
$\boldsymbol{m}$	$\in \mathbb{R}$	parameter model
$\boldsymbol{m}_0$	$\in \mathbb{R}$	starting model
$\boldsymbol{m}_{\text{ref}}$	$\in \mathbb{R}$	reference model
$\Delta\boldsymbol{m}$	$\in \mathbb{R}$	model update
$\boldsymbol{J}$	$\in \mathbb{C}^{N\times M}$	sensitivity matrix (Jacobian matrix)
$\boldsymbol{L}$	$\in \mathbb{C}^{K\times M}$	shorthand form of $\partial_{\boldsymbol{m}}\boldsymbol{A}(\boldsymbol{m}) \times_2 \boldsymbol{u}$
$\boldsymbol{P}$	$\in \mathbb{C}^{S\times M}$	projection operator
$\boldsymbol{Q}$	$\in \mathbb{R}^{N\times K}$	measurement operator (interpolation operator)
$\boldsymbol{Q}_A$	$\in \mathbb{R}^{N\times K}$	explicit representation of $\boldsymbol{A}^{-1}\boldsymbol{Q}^\top$
$\boldsymbol{W}_d$	$\in \mathbb{R}^{N\times N}$	data weighting matrix
$\boldsymbol{W}_m$	$\in \mathbb{R}^{W\times M}$	model weighting matrix

4.1 Governing equations

Based on the capability of providing a synthetic data set $\boldsymbol{d} \in \mathbb{C}^N$, with $N = N_f N_p$, for arbitrary conductivity distributions $\boldsymbol{\sigma} \in \mathbb{R}^S$, the subsequent sections of the thesis provide the main building blocks for the 3-D HEM inversion routine. In the following, the aim is to determine a parameter or conductivity model from a set of measured or observed data $\boldsymbol{d}^{\text{obs}} \in \mathbb{C}^N$. Henceforth, the conductivity model is identified with the transformation

$$\boldsymbol{m}(\boldsymbol{\sigma}) := [\log(\sigma_i)]_{1\leq i\leq S} \quad \in \mathbb{R}^S, \tag{4.1}$$

which ensures the *model parameters* $\boldsymbol{m}$ to attain only physically reasonable values

$$\boldsymbol{\sigma}(\boldsymbol{m}) := [\mathrm{e}^{m_i}]_{1\leq i\leq S} \quad \in \mathbb{R}^S_+. \tag{4.2}$$

As there is an infinite number of possible models that equivalently explain a data set $\boldsymbol{d}^{\text{obs}}$, the inversion approach can only be realized in form of a numerical optimization or parameter identification strategy. This task is carried out by the well-known least-squares approach (Sen and Stoffa 1995; Nocedal and Wright 2006) which seeks to minimize the difference between the observed data $\boldsymbol{d}^{\text{obs}}$ and the synthetic data $\boldsymbol{d}(\boldsymbol{m})$, i. e.

$$\Phi_d(\boldsymbol{m}) = \frac{1}{2} \left\| \boldsymbol{W}_d \left[\boldsymbol{d}^{\text{obs}} - \boldsymbol{d}(\boldsymbol{m}) \right] \right\|_2^2 \to \min_{\boldsymbol{m}} \; s.\,t.\, \boldsymbol{m} \in \mathbb{R}^S. \tag{4.3}$$

The variable $\Phi_d(\boldsymbol{m}) \in \mathbb{R}_+$ denotes the *data misfit norm* or data norm that should be minimized and therein $\Delta\boldsymbol{d}(\boldsymbol{m}) = \boldsymbol{d}^{\text{obs}} - \boldsymbol{d}(\boldsymbol{m})$ is typically referred as *data residual.* For a scaling factor $0 < \eta(\omega) \leq 1$, which allows a controlled frequency-dependent damping, the *data weighting* matrix

$$\boldsymbol{W}_d := \left[\frac{\delta_{ij}}{\eta(\omega) \left| d_j^{\text{obs}} \right|} \right]_{1 \leq i,j \leq N} \in \mathbb{R}^{N \times N}, \tag{4.4}$$

with the Kronecker delta

$$\delta_{ij} = \begin{cases} 1 & \text{if } i = j \\ 0 & \text{if } i \neq j \end{cases}, \tag{4.5}$$

often also given in form of a data covariance matrix (Newman and Hoversten 2000; Farquharson and Oldenburg 2004), ensures a normalization of the frequency-related amplitude variation in the data (Pidlisecky et al. 2007). The amplitudes of the HEM data between the lowest ($f = 387\,\text{Hz}$) and highest frequency ($f = 133\,200\,\text{Hz}$) vary from two to three orders of magnitude which should be avoided if the inversion approach is based on the L^2-norm (4.3). Otherwise, these variations lead to an undesired weighting which suppresses the influence of the data from low frequencies. Incorporating the additional frequency-dependent damping via $\eta(\omega)$ might be useful if data from certain frequencies is assumed to be biased with high errors from a priori information. Hence, all data with respect to that frequency is scaled with the same factor.

In case of available a priori information about the model parameter distribution or to generally ensure the solvability of the typically ill-posed minimization problem, the least-squares approach can be extended with a Tikhonov type (Tikhonov and Arsenin 1977) regularization term

$$\Phi_m(\boldsymbol{m}) = \frac{1}{2} \left\| \boldsymbol{W}_m \left[\boldsymbol{m} - \boldsymbol{m}_{\text{ref}} \right] \right\|_2^2, \tag{4.6}$$

composing the *model roughness norm* $\Phi_m(\boldsymbol{m}) \in \mathbb{R}_+$. Therein, the *model weighting* matrix $\boldsymbol{W}_m \in \mathbb{R}^{W \times S}$ with $W \in \mathbb{N}$ is used to apply a variety of regularization schemes (cf. section 4.5.2) on the model parameter vector $\boldsymbol{m}$ or the difference between $\boldsymbol{m}$ and a given reference model $\boldsymbol{m}_{\text{ref}}$, e. g. the known 1-D background model. Common regularization schemes may be a Marquardt-Levenberg approach ($\boldsymbol{W}_m := \boldsymbol{I}$), gradient or second order derivative operators (*smoothness constraints*) (Nocedal and Wright 2006; Zhdanov 2009), or even a combination thereof. In general, $\Phi_m(\boldsymbol{m})$ represents the deviation from those constraints. The complete least-squares minimization problem for the resulting *objective function* $\Phi(\boldsymbol{m}) \in \mathbb{R}_+$ is given by

$$\Phi(\boldsymbol{m}) = \frac{1}{2} \left\| \boldsymbol{W}_d \left[\boldsymbol{d}^{\text{obs}} - \boldsymbol{d}(\boldsymbol{m}) \right] \right\|_2^2 + \frac{\lambda}{2} \left\| \boldsymbol{W}_m \left[\boldsymbol{m} - \boldsymbol{m}_{\text{ref}} \right] \right\|_2^2 \to \min_{\boldsymbol{m}}, \tag{4.7}$$

subject to

$$\boldsymbol{A}(\boldsymbol{m}) \boldsymbol{U}_{\text{sec}} = \boldsymbol{B}_{\text{sec}} \quad \text{on } \Omega \subset \mathbb{R}^3, \tag{4.8}$$

for all N_f frequencies and

$$\boldsymbol{m} \in \mathbb{R}^S. \tag{4.9}$$

The trade-off between both norms within $\Phi(\boldsymbol{m})$ is controlled by the scalar $\lambda \in \mathbb{R}_+$, the *regularization parameter*.

Since the vector of synthetic data $\boldsymbol{d}$ is assigned to the nonlinear forward problem, the solution of the inverse problem (4.7) to (4.9) is obtained by exploiting the well-known Gauss-Newton approach (Mackie and Madden 1993; Avdeev 2005, e. g.). This reliable method provides a good trade-off between robustness and convergence speed and is widely used in different variants, even in recent works (Siripunvaraporn et al. 2005; Martin 2009; Grayver and Bürg 2014). Beside that, a variety of methods, e. g. the Newton (Newman and Hoversten 2000; Nocedal and Wright 2006), the Quasi-Newton (Haber 2005; Avdeev and Avdeeva 2006), or the all-at-once (Haber and Uri M. Ascher 2000) approach, as well as the nonlinear conjugate gradient scheme (Rodi and Mackie 2001; Commer and Newman 2008) are commonly used to solve the nonlinear least-squares problem but are not considered in this thesis. Applying the Gauss-Newton method, an approximation of $\boldsymbol{d}(\boldsymbol{m})$ is derived from a linearization at an initial guess $\boldsymbol{m}_0$,

$$\boldsymbol{d}(\boldsymbol{m}) \approx \boldsymbol{d}(\boldsymbol{m}_0) + \boldsymbol{J}(\boldsymbol{m}_0)\Delta\boldsymbol{m}, \tag{4.10}$$

with the decoupled *model update*

$$\Delta\boldsymbol{m} = \boldsymbol{m} - \boldsymbol{m}_0, \tag{4.11}$$

and the Jacobian or *sensitivity* matrix

$$\boldsymbol{J}(\boldsymbol{m}) := \frac{\partial \boldsymbol{d}(\boldsymbol{m})}{\partial \boldsymbol{m}} \quad \in \mathbb{C}^{N \times S}, \tag{4.12}$$

denoting the partial derivatives of the data vector with respect to the model parameter $\boldsymbol{m}$. A detailed derivation of this matrix is explained in section 4.3. The linearization approach allows to reformulate (4.7) in terms of a single-norm expression

$$\Phi(\boldsymbol{m}) = \frac{1}{2} \left\| \begin{bmatrix} \boldsymbol{W}_d \Delta\boldsymbol{d} \\ \sqrt{\lambda}\boldsymbol{W}_m(\boldsymbol{m}_0 - \boldsymbol{m}_{\text{ref}}) \end{bmatrix} - \begin{bmatrix} \boldsymbol{W}_d \boldsymbol{J}(\boldsymbol{m}_0) \\ -\sqrt{\lambda}\boldsymbol{W}_m \end{bmatrix} \Delta\boldsymbol{m} \right\|_2^2 \to \min_{\boldsymbol{m}}, \tag{4.13}$$

with the initial data residual

$$\Delta\boldsymbol{d} = \boldsymbol{d}^{\text{obs}} - \boldsymbol{d}(\boldsymbol{m}_0), \tag{4.14}$$

which has to be solved iteratively for a series of model updates $\boldsymbol{m}_k = \boldsymbol{m}_{k-1} + \Delta\boldsymbol{m}_k$, for $k \in \mathbb{N}$.

Solving the least-squares problem with LSQR

Each model update $\Delta\boldsymbol{m}_k$ for a single Gauss-Newton step, or a step of the *outer iteration*, of the least-squares minimization problem (4.13) can be calculated iteratively, exploiting the LSQR algorithm (Paige and Saunders 1982). This type of a Krylov-subspace method can be considered mathematically equivalent method to the well-known CG algorithm but is supposed to be more capable of dealing with the problem-inherent ill-conditioning. Hence, each outer iteration is accompanied by an *inner iteration*, i. e. a complete LSQR iteration, which solves

$$\Phi(\boldsymbol{m}) = \frac{1}{2} \left\| \Delta\hat{\boldsymbol{d}} - \hat{\boldsymbol{J}} \Delta \boldsymbol{m} \right\|_2^2 \to \min_{\boldsymbol{m}} s.\,t.\, \boldsymbol{m} \in \mathbb{R}^S, \tag{4.15}$$

for a model update $\Delta\boldsymbol{m}$. In this context, complex arithmetic, i. e. the calculation of complex model updates, can be avoided by turning to a mathematically equivalent formulation (see appendix B.2). Therein, the complex-valued expressions in (4.13) are split up in a separate real and imaginary part which are concatenated afterward. With

$$\hat{\boldsymbol{J}} := \begin{bmatrix} \Re \begin{bmatrix} \boldsymbol{W}_d \boldsymbol{J}(\boldsymbol{m}_0) \\ -\sqrt{\lambda} \boldsymbol{W}_m \end{bmatrix} \\ \Im \begin{bmatrix} \boldsymbol{W}_d \boldsymbol{J}(\boldsymbol{m}_0) \\ -\sqrt{\lambda} \boldsymbol{W}_m \end{bmatrix} \end{bmatrix} \in \mathbb{R}^{2N \times S} \quad \text{and} \quad \Delta\hat{\boldsymbol{d}} := \begin{bmatrix} \Re \begin{bmatrix} \boldsymbol{W}_d \Delta \boldsymbol{d} \\ \sqrt{\lambda} \boldsymbol{W}_m (\boldsymbol{m}_0 - \boldsymbol{m}_{\text{ref}}) \end{bmatrix} \\ \Im \begin{bmatrix} \boldsymbol{W}_d \Delta \boldsymbol{d} \\ \sqrt{\lambda} \boldsymbol{W}_m (\boldsymbol{m}_0 - \boldsymbol{m}_{\text{ref}}) \end{bmatrix} \end{bmatrix} \in \mathbb{R}^{2N}, \tag{4.16}$$

the least-squares problem (4.15) is given as an equivalent formulation but completely real-valued and of double length.

Similar to the CG Method, the LSQR algorithm utilizes the Jacobian matrix $\boldsymbol{J}$ only as part of multiplications $\boldsymbol{u} = \boldsymbol{J}\boldsymbol{x}$ and $\boldsymbol{v} = \boldsymbol{J}^{\mathsf{H}}\boldsymbol{y}$ with the vectors $\boldsymbol{x} \in \mathbb{R}^S$ and $\boldsymbol{y} \in \mathbb{C}^N$. The evaluation of those products, that occur as independent part of multiplications with the entire matrix $\hat{\boldsymbol{J}}$, can be expressed in consistence to the formulation (4.15) to (4.16) but without the necessity to explicitly split up the Jacobian matrix. This can be obtained by transforming the result of the product $\boldsymbol{u} = \boldsymbol{J}\boldsymbol{x}$ into

$$\hat{\boldsymbol{u}} = \begin{bmatrix} \Re(\boldsymbol{u}) \\ \Im(\boldsymbol{u}) \end{bmatrix} \quad \in \mathbb{R}^{2N}, \tag{4.17}$$

and expressing $\boldsymbol{v} = \boldsymbol{J}^{\mathsf{H}}\boldsymbol{y}$ with $\boldsymbol{y}$ as

$$\boldsymbol{v} = \Re\left(\boldsymbol{J}^{\mathsf{H}}\boldsymbol{y}\right) = \begin{bmatrix} \Re(\boldsymbol{J}) \\ \Im(\boldsymbol{J}) \end{bmatrix}^{\top} \begin{bmatrix} \Re(\boldsymbol{y}) \\ \Im(\boldsymbol{y}) \end{bmatrix}, \tag{4.18}$$

without the additional rearrangement of the Jacobian matrix $\boldsymbol{J}$. The consistency of the above described procedure is shown in appendix B.3.

4.2 Normal equations

In order to solve linear least-squares problems, a common approach is to refer to the equivalent system of *normal equations*. By forming the gradient of the objective function with respect to the model parameter vector $\nabla_{\boldsymbol{m}}\Phi(\boldsymbol{m})$ and set it to zero, i. e. applying the necessary condition for getting a local extremum, the normal equations for (4.13) are given by

$$\Re\left(\begin{bmatrix} \boldsymbol{W}_d \boldsymbol{J}(\boldsymbol{m}_0) \\ -\sqrt{\lambda} \boldsymbol{W}_m \end{bmatrix}^{\mathsf{H}} \begin{bmatrix} \boldsymbol{W}_d \boldsymbol{J}(\boldsymbol{m}_0) \\ -\sqrt{\lambda} \boldsymbol{W}_m \end{bmatrix} \right) \Delta \boldsymbol{m} = \Re\left(\begin{bmatrix} \boldsymbol{W}_d \boldsymbol{J}(\boldsymbol{m}_0) \\ -\sqrt{\lambda} \boldsymbol{W}_m \end{bmatrix}^{\mathsf{H}} \begin{bmatrix} \boldsymbol{W}_d \Delta \boldsymbol{d} \\ \sqrt{\lambda} \boldsymbol{W}_m (\boldsymbol{m}_0 - \boldsymbol{m}_{\text{ref}}) \end{bmatrix} \right), \tag{4.19}$$

a real-valued linear system of equations (see (B.13)) which likewise can be solved iteratively for a series of model updates $\Delta\boldsymbol{m}_k$.

Solving the normal equations with CG

Typically, the symmetric and positive semi-definite system (4.19) is solved with an inner iteration of the (preconditioned) CG method (Hestenes and Stiefel 1952), as it is unsuitable to decompose the dense and relatively large system matrix with the help of direct solvers (Newman and Hoversten 2000). As indicated in section 4.1, the multiplication with $\boldsymbol{J}$ or $\boldsymbol{J}^{\mathsf{H}}$ are an integral part of every Krylov-subspace method. Moreover, applying the CG method on the normal equations only requires either products of the entire system matrix with a real-valued vector $\boldsymbol{x}$

$$\hat{\boldsymbol{A}}\boldsymbol{x} = \Re\left(\begin{bmatrix}\boldsymbol{W}_d\boldsymbol{J}(\boldsymbol{m}_0)\\ -\sqrt{\lambda}\boldsymbol{W}_m\end{bmatrix}^{\mathsf{H}}\begin{bmatrix}\boldsymbol{W}_d\boldsymbol{J}(\boldsymbol{m}_0)\\ -\sqrt{\lambda}\boldsymbol{W}_m\end{bmatrix}\right)\boldsymbol{x}, \tag{4.20}$$

or a single evaluation of the RHS

$$\hat{\boldsymbol{b}} = \Re\left(\begin{bmatrix}\boldsymbol{W}_d\boldsymbol{J}(\boldsymbol{m}_0)\\ -\sqrt{\lambda}\boldsymbol{W}_m\end{bmatrix}^{\mathsf{H}}\begin{bmatrix}\boldsymbol{W}_d\Delta\boldsymbol{d}\\ \sqrt{\lambda}\boldsymbol{W}_m(\boldsymbol{m}_0-\boldsymbol{m}_{\mathrm{ref}})\end{bmatrix}\right), \tag{4.21}$$

i. e. no subdivision of an intermediate result (cf. (4.17)) is required. Hence, the results of the multiplications $\boldsymbol{u} = \boldsymbol{J}\boldsymbol{x} \in \mathbb{C}^N$ can be used unchanged and only the real parts of the products $\boldsymbol{v} = \Re\left(\boldsymbol{J}^{\mathsf{H}}\boldsymbol{y}\right) \in \mathbb{R}^S$ finally need to be stored. To avoid the formation of the complex conjugate of $\boldsymbol{J}$, it holds for products with arbitrary vectors $\boldsymbol{y} \in \mathbb{C}^N$ that

$$\Re\left(\boldsymbol{J}^{\mathsf{H}}\boldsymbol{y}\right) = \Re\left(\overline{\boldsymbol{J}}^{\top}\boldsymbol{y}\right) = \Re\left(\overline{\left[\boldsymbol{J}^{\top}\overline{\boldsymbol{y}}\right]}\right), \tag{4.22}$$

where building the conjugate of the last expression can be neglected, since only the real part has to be considered. Furthermore, for (4.18) and also (4.22) even forming $\boldsymbol{J}^{\top}$ can be circumvented by simply exploiting

$$\boldsymbol{J}^{\top}\overline{\boldsymbol{y}} = \left[\overline{\boldsymbol{y}}^{\top}\boldsymbol{J}\right]^{\top}, \tag{4.23}$$

such that only an unmodified explicit expression for $\boldsymbol{J}$ is required to evaluate all occurring products.

4.3 Calculation of the Jacobian matrix $\boldsymbol{J}$

Keystone of the Gauss-Newton inversion algorithm is the effective evaluation of the Jacobian matrix $\boldsymbol{J}$. Employing the *sensitivity equation* approach of (Rodi 1976; McGillivray and Oldenburg 1990; Spitzer 1998) the Jacobian matrix (4.12) can directly be obtained from the discretization (3.13) to (3.16) by a series of forward solves, exploiting the decomposition of the system matrix $\boldsymbol{A}$ (cf. section 3.3). Although the numerical forward problem is formulated in terms of the secondary field (section 3.2), in practice a normalized total field that is reduced by the free-space source field is measured (section 3.6). Therefore, the inverse problem has to be expressed in terms of the total field $\boldsymbol{u}$. Considering a single frequency and TX position, the derivative of the total field with respect to the model parameters $\boldsymbol{m}$ is given by

$$\frac{\partial\boldsymbol{u}}{\partial\boldsymbol{m}} = \frac{\partial\left(\boldsymbol{A}^{-1}(\boldsymbol{m})\boldsymbol{b}\right)}{\partial\boldsymbol{m}}, \tag{4.24}$$

with

$$\begin{aligned} \boldsymbol{m} &= \boldsymbol{m}_{\text{pri}} + \boldsymbol{m}_{\text{sec}}, \\ \boldsymbol{u} &= \boldsymbol{u}_{\text{pri}}(\boldsymbol{m}_{\text{pri}}) + \boldsymbol{u}_{\text{sec}}(\boldsymbol{m} - \boldsymbol{m}_{\text{pri}}). \end{aligned} \tag{4.25}$$

In case of the HEM problem (also for most of the controlled source electromagnetics), the source is located in a medium where changes in the associated parameters are not expected during the inversion process. Hence, the primary parameter distribution $\boldsymbol{m}_{\text{pri}}$ is considered to be fixed during the whole inversion iteration, such that updates to the model parameters are solely associated with changes in the secondary parameter distribution. Accordingly

$$\frac{\partial \boldsymbol{u}}{\partial \boldsymbol{m}} = \frac{\partial \boldsymbol{u}_{\text{pri}}}{\partial \boldsymbol{m}} + \frac{\partial \boldsymbol{u}_{\text{sec}}}{\partial \boldsymbol{m}}, \tag{4.26}$$

where

$$\frac{\partial \boldsymbol{u}_{\text{pri}}}{\partial \boldsymbol{m}} = \boldsymbol{0}_S. \tag{4.27}$$

If in contrast, the source is located in an area where parameters are allowed to vary (cf. direct current methods), updates in the model parameters $\boldsymbol{m}$ have to be allocated also to the primary parameter distribution, in order to ensure the cancellation of the RHS in the vicinity of the source.

Based on the secondary field problem (3.16)

$$\begin{aligned} \boldsymbol{A}(\boldsymbol{m})\boldsymbol{u}_{\text{sec}} &= \left[\boldsymbol{A}(\boldsymbol{m}_{\text{pri}}) - \boldsymbol{A}(\boldsymbol{m})\right] \boldsymbol{u}_{\text{pri}} = \boldsymbol{b}_{\text{sec}}, \\ \boldsymbol{A}(\boldsymbol{m}_{\text{pri}})\boldsymbol{u}_{\text{pri}} &= \boldsymbol{b}, \end{aligned} \tag{4.28}$$

the derivatives with respect to the model parameter $\boldsymbol{m}$ are given by

$$\frac{\partial \boldsymbol{A}(\boldsymbol{m})}{\partial \boldsymbol{m}} \times_2 \boldsymbol{u}_{\text{sec}} + \boldsymbol{A}(\boldsymbol{m}) \frac{\partial \boldsymbol{u}_{\text{sec}}}{\partial \boldsymbol{m}} = \overbrace{+\frac{\partial \boldsymbol{A}(\boldsymbol{m}_{\text{pri}})}{\partial \boldsymbol{m}} \times_2 \boldsymbol{u}_{\text{pri}} + \boldsymbol{A}(\boldsymbol{m}_{\text{pri}}) \frac{\partial \boldsymbol{u}_{\text{pri}}}{\partial \boldsymbol{m}}}^{\frac{\partial \boldsymbol{b}}{\partial \boldsymbol{m}} = 0} \tag{4.29}$$

$$- \frac{\partial \boldsymbol{A}(\boldsymbol{m})}{\partial \boldsymbol{m}} \times_2 \boldsymbol{u}_{\text{pri}} - \boldsymbol{A}(\boldsymbol{m}) \frac{\partial \boldsymbol{u}_{\text{pri}}}{\partial \boldsymbol{m}}. \tag{4.30}$$

Two different types of the sensitivity equation can be observed from that, depending on whether the inversion approach is based on the total field (4.24), i. e.

$$\frac{\partial \boldsymbol{u}}{\partial \boldsymbol{m}} = \frac{\partial \boldsymbol{u}_{\text{pri}}}{\partial \boldsymbol{m}} + \frac{\partial \boldsymbol{u}_{\text{sec}}}{\partial \boldsymbol{m}} = -\boldsymbol{A}(\boldsymbol{m})^{-1} \frac{\partial \boldsymbol{A}(\boldsymbol{m})}{\partial \boldsymbol{m}} \times_2 \boldsymbol{u}, \tag{4.31}$$

or the secondary field (considered for the sake of completeness)

$$\frac{\partial \boldsymbol{u}_{\text{sec}}}{\partial \boldsymbol{m}} = -\boldsymbol{A}(\boldsymbol{m})^{-1} \frac{\partial \boldsymbol{A}(\boldsymbol{m})}{\partial \boldsymbol{m}} \times_2 \boldsymbol{u} - \frac{\partial \boldsymbol{u}_{\text{pri}}}{\partial \boldsymbol{m}}, \tag{4.32}$$

respectively. Concerning a variable $\boldsymbol{m}_{\text{pri}}$, inaccuracies may occur if the derivatives of the primary field cannot be obtained by an analytical expression. Thus, a discretization of the primary forward problem is required and with that, the solution of an additional sensitivity equation

$$\frac{\partial \boldsymbol{u}_{\text{pri}}}{\partial \boldsymbol{m}} = -\boldsymbol{A}(\boldsymbol{m}_{\text{pri}})^{-1} \frac{\partial \boldsymbol{A}(\boldsymbol{m}_{\text{pri}})}{\partial \boldsymbol{m}} \times_2 \boldsymbol{u}_{\text{pri}}. \tag{4.33}$$

The numerical calculated and the analytic primary fields can differ a lot from one another. With respect to (4.27), however, both variants, (4.31) and (4.32), are identical.

$\boldsymbol{J}$ in terms of the tensor and Hadamard product notation

To obtain the complete sensitivity matrix $\boldsymbol{J}$ (4.12) which is associated with the transformation of the solution vector, also the measurement operator $\boldsymbol{Q}$ (3.66) has to be incorporated. Since the frequencies can be treated independently, at first, $\boldsymbol{J}$ with respect to the N_p TX/RX positions is considered in terms of the Hadamard product notation (cf. section 3.6)

$$\boldsymbol{J}(\boldsymbol{m}) = \frac{\partial \boldsymbol{d}}{\partial \boldsymbol{m}} = \left(\boldsymbol{Q}^\top \circ \frac{\partial \boldsymbol{U}}{\partial \boldsymbol{m}}\right) \times_1 \mathbf{1}_K \quad \in \mathbb{C}^{N_p \times S}. \tag{4.34}$$

The measurement operator matrix can be extracted from the derivative as it is independent of $\boldsymbol{m}$. In terms of the tensor-based notation (cf. section 3.5), the matrix $\boldsymbol{J}$ can be composed of

$$\boldsymbol{J}(\boldsymbol{m}) := \left[\boldsymbol{j}_p(\boldsymbol{m})\right]_{1\leq p\leq S} = -\left[\boldsymbol{Q}^\top \circ \left(\boldsymbol{A}(\boldsymbol{m})^{-1}\boldsymbol{L}_p(\boldsymbol{m})\right)\right]_{1\leq p\leq S} \times_1 \mathbf{1}_K, \tag{4.35}$$

with

$$\widetilde{\boldsymbol{L}}(\boldsymbol{m}) := \frac{\partial \boldsymbol{A}(\boldsymbol{m})}{\partial \boldsymbol{m}} \times_2 \boldsymbol{U} = \mathrm{i}\omega\mu_0 \frac{\partial \boldsymbol{M}(\boldsymbol{m})}{\partial \boldsymbol{m}} \times_2 \boldsymbol{U} \quad \in \mathbb{C}^{K\times N_p \times S}. \tag{4.36}$$

In (4.35), the Hadamard product is applied on each slice $\boldsymbol{A}^{-1}\boldsymbol{L}_p$, providing a single column $\boldsymbol{j}_p \in \mathbb{C}^{N_p}$ of the Jacobian matrix $\boldsymbol{J}$.

At last, the complete sensitivity matrix, incorporating all N_f blocks with respect to the sequentially evaluated frequencies, is assembled by the concatenation

$$\boldsymbol{J} = \begin{bmatrix} \boldsymbol{J}^1 \\ \vdots \\ \boldsymbol{J}_1^{N_f} \end{bmatrix} \quad \in \mathbb{C}^{N\times S}. \tag{4.37}$$

As logarithmized conductivities are considered as model parameters (4.1), the derivative of the mass matrix part $\boldsymbol{M}$ w. r. t. the model parameter $\boldsymbol{m}$ is given by

$$\frac{\partial \boldsymbol{M}(\boldsymbol{\sigma}(\boldsymbol{m}))}{\partial \boldsymbol{m}} = \widetilde{\boldsymbol{T}} \times_3 \operatorname{diag}\left(\mathrm{e}^{\boldsymbol{m}}\right) \quad \in \mathbb{R}^{K\times K\times S}, \tag{4.38}$$

where the derivatives

$$\frac{\partial \boldsymbol{\sigma}(\boldsymbol{m})}{\partial \boldsymbol{m}} = \frac{\partial \mathrm{e}^{\boldsymbol{m}}}{\partial \boldsymbol{m}} = \operatorname{diag}\left(\mathrm{e}^{\boldsymbol{m}}\right) \quad \in \mathbb{R}^{S\times S}, \tag{4.39}$$

are incorporated. The exponential function is applied component-wise on the elements of $\boldsymbol{m}$. Although $\partial_{\boldsymbol{m}}\boldsymbol{M}$ is of the same sparsity pattern like $\widetilde{\boldsymbol{T}}$, it still depends on the model parameter $\boldsymbol{m}$.

Exploiting the permutability of the order of the occurring tensor products (see (3.47) to (3.49)),

$$\frac{\partial \boldsymbol{M}}{\partial \boldsymbol{m}} \times_2 \boldsymbol{u} = \left[\widetilde{\boldsymbol{T}} \times_3 \operatorname{diag}\left(\mathrm{e}^{\boldsymbol{m}}\right)\right] \times_2 \boldsymbol{u}, \tag{4.40}$$

can also be realized by

$$\frac{\partial \boldsymbol{M}}{\partial \boldsymbol{m}} \times_2 \boldsymbol{u} = \left[\widetilde{\boldsymbol{T}} \times_2 \boldsymbol{u}\right] \operatorname{diag}\left(\mathrm{e}^{\boldsymbol{m}}\right), \tag{4.41}$$

which is expected to be more effective, since only a single product with $\widetilde{\boldsymbol{T}}$ is required.

4.4 Explicit calculation of $\boldsymbol{J}$

As mentioned in section 3.6, the HEM problem is characterized in such a way that only one complex data value is obtained for a single transmitter position and frequency. Therefore, the computational costs for evaluating one datum always comprises the solution of a forward problem for one unique RHS vector $\boldsymbol{b}_{\text{sec}}$. This special property inevitably leads to the fact that calculating the Jacobian matrix explicitly requires the same computational effort as it would be required to implicitly calculate its action on a vector, because this operation also depends on the number of RHS vectors (Mackie and Madden 1993), i. e. the size of the block RHS $\boldsymbol{B}_{\text{sec}}$. Solving the minimization problem by using Krylov-subspace methods, the solution of even two products, $\boldsymbol{J}\boldsymbol{x}$ and $\boldsymbol{J}^{\mathsf{H}}\boldsymbol{y}$, is required such that the computational cost in this case is twice the effort of the explicit assembly of the Jacobian. On top of that, the implicit evaluation has to be carried out for each inner iteration step, while the explicit Jacobian matrix can be reused for all inner loop iterations. Hence, the explicit calculation of the Jacobian matrix is a crucial and advantageous approach for HEM data inversion. In contrast, typical ground-based controlled source electromagnetic problems are characterized by a large number of sampled data that is associated with only a few sources. In this situation, the implicit computation via the action of the Jacobian matrix on a vector, i. e. linear system solves related to a small number of columns that e. g. arise from $\widetilde{\boldsymbol{L}} \times_3 \boldsymbol{x}$ in case of $\boldsymbol{J}\boldsymbol{x}$, is less expensive than the explicit calculation of $\boldsymbol{J}$, even for a large number of inner iterations. The following part of this paragraph gives additional insight to the above mentioned issue.

Considering the vectorized problem notation (3.60) to (3.65), the complete Sensitivity matrix is given by

$$\boldsymbol{J} = -\boldsymbol{Q}\boldsymbol{A}^{-1}\frac{\partial \boldsymbol{A}}{\partial \boldsymbol{m}} \times_2 \boldsymbol{u} = -\boldsymbol{Q}\boldsymbol{A}^{-1}\boldsymbol{L} \quad \in \mathbb{C}^{N\times S}, \tag{4.42}$$

based on the derivation (4.31).

The costs of the explicit calculation of the Jacobian matrix by solving forward problems with $\boldsymbol{A}^{-1}$ is initially limited by the number of model parameters M that corresponds to the number of column vectors in $\boldsymbol{L}$, acting as separate RHS vectors. At this point, it is irrelevant how many data points N are concerned. However, in most of the geophysical applications, even for HEM surveys, the assumption $N < M$ is valid. To lower the computational costs it is reasonable to exploit the very sparse structure of the measurement operator $\boldsymbol{Q}$ and the symmetry property of $\boldsymbol{A}$.

A first approach exploits the fact that usually only C columns of $\boldsymbol{Q}$ contain non-zero elements, with $C \ll NK$. The idea is to identify those non-zero columns of

$$\boldsymbol{Q} \in \mathbb{C}^{N\times NK} \Rightarrow \boldsymbol{Q}_r \in \mathbb{C}^{N\times C}, \tag{4.43}$$

and the associated few rows of

$$\boldsymbol{R} := \boldsymbol{A}^{-1} \in \mathbb{C}^{NK\times NK} \Rightarrow \boldsymbol{R}_r \in \mathbb{C}^{C\times NK}, \tag{4.44}$$

and therefore explicitly build the reduced matrix $\boldsymbol{R}_r$. To get this matrix representation, it is necessary to solve C forward problems with the corresponding unit RHS vectors $\mathbf{e}_c^{NK}$, such that

$$\boldsymbol{R}_r := \left[\boldsymbol{A}^{-1}\mathbf{e}_c^{NK}\right]^{\top}_{1\le c\le C}. \tag{4.45}$$

Thereby, the desired rows of $\boldsymbol{R}_r$ are obtained, since the symmetry of $\boldsymbol{A}$ also leads to $\boldsymbol{A}^{-1} = \boldsymbol{A}^{-\top}$. Hence, it is possible to provide the sensitivity matrix $\boldsymbol{J}$, only by carrying out a matrix-matrix multiplication with $\boldsymbol{L}$

$$\boldsymbol{J}(\boldsymbol{m}) = -\boldsymbol{Q}_r \boldsymbol{R}_r(\boldsymbol{m})\boldsymbol{L}, \tag{4.46}$$

where

$$\boldsymbol{Q}_r \boldsymbol{R}_r \overset{!}{=} \boldsymbol{Q}\boldsymbol{A}^{-1} \quad \in \mathbb{C}^{N \times NK}. \tag{4.47}$$

In a second approach, the symmetry of $\boldsymbol{A}$ can likewise be used to solve N forward problems associated with the N rows of $\boldsymbol{Q}$ or the N columns of $\boldsymbol{Q}^\top$ (Zhang et al. 1995), giving an explicit representation

$$\boldsymbol{Q}_A := \boldsymbol{A}^{-1}\boldsymbol{Q}^\top. \tag{4.48}$$

This is particularly useful when $\boldsymbol{Q}$ has more non-zero columns than rows, i. e., $C > N$. Subsequently, the Jacobian matrix can be composed by (4.46), since $\boldsymbol{Q}_A^\top = \boldsymbol{Q}\boldsymbol{A}^{-1}$. In certain cases, e. g., if many RX positions are related to a single grid cell, the first variant should be preferred.

Moving on to the Hadamard product notation, the explicit Jacobian matrix for a single frequency can be obtained in a straight-forward fashion. For the entirety of RHS, $\boldsymbol{J}$ is given by a column-wise assembling

$$\left[\boldsymbol{j}_p(\boldsymbol{m})\right]_{1 \le p \le S} = -\left[\boldsymbol{Q}^\top \circ \left(\boldsymbol{A}(\boldsymbol{m})^{-1}\boldsymbol{L}_p(\boldsymbol{m})\right)_{1 \le p \le S}\right] \times_1 \mathbf{1}_K \quad \in \mathbb{C}^{N_p \times S}. \tag{4.49}$$

Considering just a single RHS,

$$\left[j_{i,p}(\boldsymbol{m})\right]_{1 \le p \le S} = -\left[\boldsymbol{q}^i \circ \left(\boldsymbol{A}(\boldsymbol{m})^{-1}\boldsymbol{l}_{p,i}(\boldsymbol{m})\right)\right]_{1 \le p \le S} \times_1 \mathbf{1}_K \quad \in \mathbb{C}^{1 \times S}, \tag{4.50}$$

only the i-th row of $\boldsymbol{J}$ is obtained which can also be described in common notation by

$$= -\left[\boldsymbol{q}^{i\top}\left(\boldsymbol{A}(\boldsymbol{m})^{-1}\boldsymbol{l}_{p,i}(\boldsymbol{m})\right)\right]_{1 \le p \le S} \times_1 1. \tag{4.51}$$

Exploiting the symmetry property

$$= -\left[\left(\boldsymbol{A}(\boldsymbol{m})^{-1}\boldsymbol{q}^i\right)^\top \boldsymbol{l}_{i,p}(\boldsymbol{m})\right]_{1 \le p \le S} \times_1 1, \tag{4.52}$$

$$= -\left[\left(\boldsymbol{A}(\boldsymbol{m})^{-1}\boldsymbol{q}^i\right) \circ \boldsymbol{l}_{i,p}(\boldsymbol{m})\right]_{1 \le p \le S} \times_1 \mathbf{1}_K, \tag{4.53}$$

and, again, incorporating multiple RHS

$$\left[\boldsymbol{j}_p(\boldsymbol{m})\right]_{1 \le p \le S} = -\left[\left(\boldsymbol{A}(\boldsymbol{m})^{-1}\boldsymbol{Q}^\top\right) \circ \boldsymbol{L}_p(\boldsymbol{m})\right]_{1 \le p \le S} \times_1 \mathbf{1}_K, \tag{4.54}$$

$$= -\left[\boldsymbol{Q}_A \circ \boldsymbol{L}_p(\boldsymbol{m})\right]_{1 \le p \le S} \times_1 \mathbf{1}_K, \tag{4.55}$$

an equivalent formulation to (4.46), based on the explicit representation $\boldsymbol{Q}_A$, can be obtained.

For each frequency $f = 1, \dots, N_f$, a unique $\boldsymbol{Q}_A^f$ that is related to a decomposition of the system matrix $\boldsymbol{A}^f$, and a unique tensor $\widetilde{\boldsymbol{L}}^f$, depending on the factor $\mathrm{i}\,\omega_f \mu$ (4.36), has to be evaluated such that the complete Jacobian matrix can be concatenated by (4.37).

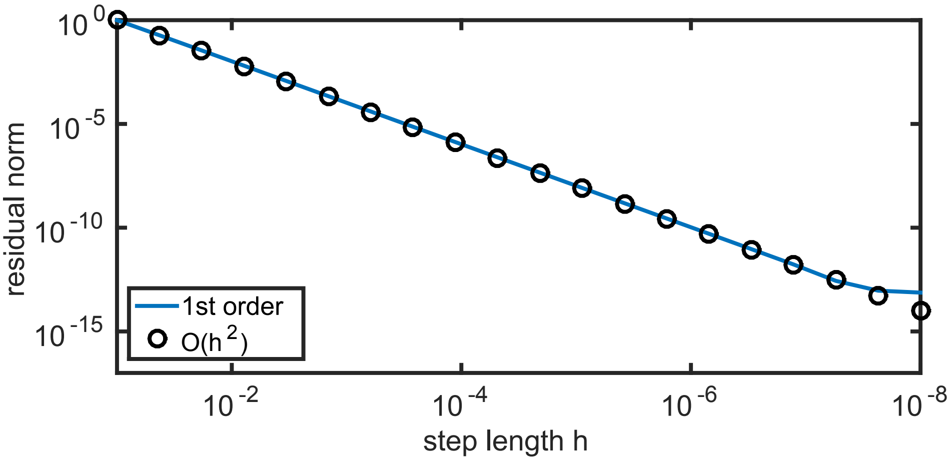

Figure 4.1: Convergence behavior of the Taylor series remainder for the linearization of the data vector $\boldsymbol{d}(\boldsymbol{m})$.

4.4.1 Validation of $\boldsymbol{J}$

In order to validate the calculated derivatives, a convenient approach is to check the convergence rate of the Taylor series remainder which is expected to show a $\mathcal{O}(h^2)$ behavior if a linearization is considered Haber (2014). Hence, the Jacobian matrix can be tested with regard to an incomplete Taylor series expansion of the data vector $\boldsymbol{d}(\boldsymbol{m})$, stopped at the first order, i. e.

$$\psi = \|\boldsymbol{d}(\boldsymbol{m}) - \boldsymbol{d}(\boldsymbol{m}_0) - h\boldsymbol{J}(\boldsymbol{m}_0)\Delta\boldsymbol{m}\|_2 \sim \mathcal{O}(h^2), \tag{4.56}$$

for an arbitrary starting model $\boldsymbol{m}_0$ and model update $\Delta\boldsymbol{m}$

$$\boldsymbol{m} = \boldsymbol{m}_0 + h\Delta\boldsymbol{m}, \tag{4.57}$$

and a step length

$$h \in \mathbb{R}_+ \to 0. \tag{4.58}$$

The asymptotic behavior, quantified in terms of the Euclidean norm, reduces to $\mathcal{O}(h)$ if $\boldsymbol{J}(\boldsymbol{m}) \neq \partial_{\boldsymbol{m}}\boldsymbol{d}(\boldsymbol{m})$. Figure 4.1 shows the residual norm ψ with respect to the step length $h \in \left[10^{-1}, 10^{-8}\right]$ which is logarithmically distributed. The residual is normalized to $\psi(h = 10^{-1})$ such that it can be matched with the $\mathcal{O}(h^2)$ asymptotic. As the residual fits the expected behavior, the derivatives, which are calculated independent from the grid and hence from discretization errors, can be considered as valid. Deviations between both curves at $h = 10^{-7}$ evoke from reaching the machine precision and can be neglected.

4.4.2 Performance study

To show the advantage of the explicit calculation of $\boldsymbol{J}$, fig. 4.2 illustrates the runtime (for a single frequency) required for the calculation of the product $\boldsymbol{J}^{\mathsf{H}}\boldsymbol{J}\boldsymbol{x}$ which is required within the inner iterations of each Gauss-Newton step (cf. section 4.1). The first variant (blue curve) only employs the decomposition of the system matrix $\boldsymbol{A}$ which requires two Gauss elimination steps for each of the N_p forward problems per frequency, e. g.

$$\begin{aligned} \boldsymbol{J}\boldsymbol{x} &= -\left[\boldsymbol{Q}^{\top} \circ \left(\boldsymbol{A}(\boldsymbol{m})^{-1}\boldsymbol{L}_p(\boldsymbol{m})\right)\right]_{1\le p\le S} \times_1 \boldsymbol{1}_K \times_3 \boldsymbol{x}, & (4.59)\\ &= -\left(\boldsymbol{1}_K \cdot \left[\boldsymbol{Q}^{\top} \circ \left(\boldsymbol{A}(\boldsymbol{m})^{-1}\hat{\boldsymbol{L}}(\boldsymbol{x})\right)\right]\right)^{\top}, & (4.60)\end{aligned}$$

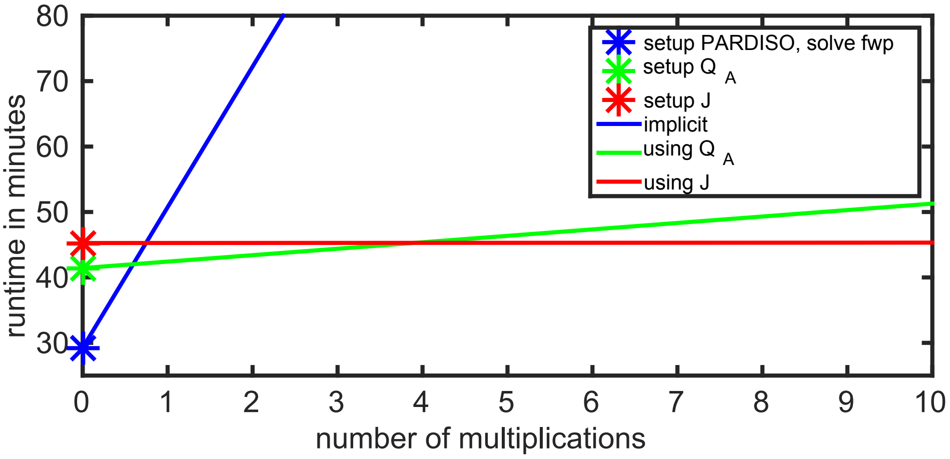

Figure 4.2: Timing study of calculating $\boldsymbol{J}^{\mathsf{H}}\boldsymbol{J}$ with different approaches. The blue, green, and red asterisk denote the setup time for the calculation of the decomposition of $\boldsymbol{A}$ and the solution $\boldsymbol{U}_{\text{sec}}$ via PARDISO, the calculation of the explicit representation of $\boldsymbol{Q}_A$, and the calculation of the explicit Jacobian matrix $\boldsymbol{J}$, respectively.

with

$$\hat{\boldsymbol{L}}(\boldsymbol{x}) = \sum_{p=1}^{S} \boldsymbol{L}_p(\boldsymbol{m}) x_p \quad \in \mathbb{C}^{K \times N_p}, \tag{4.61}$$

occurring in any multiplication with the Jacobian matrix. The green curve refers to an explicitly formed $\boldsymbol{Q}_A$ which does not require any further forward-backward substitutions but still needs the evaluation of multiple Hadamard products with arbitrary matrices $\hat{\boldsymbol{L}}$, i. e. for

$$\boldsymbol{J}\boldsymbol{x} = -\left(\boldsymbol{1}_K \cdot \left[\boldsymbol{Q}_A \circ \hat{\boldsymbol{L}}(\boldsymbol{x})\right]\right)^{\top}. \tag{4.62}$$

Finally, matrix-vector products with the explicit representation of $\boldsymbol{J}$ (red curve) are characterized by the highest set-up time but require almost no further computational effort, since only inexpensive matrix-vector multiplications have to be calculated. Considering this property, Krylov-subspace methods, applied to the inner iterations, can be used even without preconditioning strategies.

4.5 Regularization

Geophysical inverse problems, particularly the nonlinear EM inverse problems, are characterized by its conspicuous ambiguity and instability. In general difficult to manage, a regularization approach, however, offers the possibility to obtain physical reasonable solutions. It should be mentioned that each form of a regularized minimization thereby only constitutes a (stabilized) auxiliary problem which is unable to provide an ideal data fit (4.3). Down to the present day, there is no optimal global regularization strategy available but rather empirical determined and problem specific makeshifts.

To gain an acceptable convergence speed of the Gauss-Newton approach and therefore avoid creeping model updates (Newman and Hoversten 2000; Scales et al. 2001), a *global regularization* approach (Günther 2004) is used

$$\Phi_m(\boldsymbol{m}) = \frac{1}{2} \left\| \boldsymbol{W}_m \left[\boldsymbol{m} - \boldsymbol{m}_{\text{ref}}\right] \right\|_2^2. \tag{4.63}$$

Thereby, the model weighting matrix $\boldsymbol{W}_m$ is applied to the model parameter vector $\boldsymbol{m}$ although the solution of the Gauss-Newton iteration (4.13) is provided in form of a sequence of model updates $\Delta\boldsymbol{m}_k$. The additionally introduced reference model typically coincides with an a priori known background conductivity distribution and can be considered crucial for the restriction of the model parameter solution space. Thus, depending on the regularization parameter λ, the minimization algorithm is forced to remain in the vicinity of the reference model.

For $\boldsymbol{m}_{\text{ref}} = \boldsymbol{0}$ and $\boldsymbol{W}_m = \boldsymbol{I}$, the least squares solution of minimum norm can be obtained which coincides with the solution of the truncated singular value decomposition (Scales et al. 2001). Due to the choice of logarithmic model parameters some specific behaviors of the regularization need to be mentioned. As $\log(1) = 0$, the conductivity vector rather tends to $\boldsymbol{1}$ instead of $\boldsymbol{0}$ which is somehow contrary to the original intent of targeting preferably small conductivities with $\|\boldsymbol{m}\| \to \min$. If a regularization with respect to a reference model is used

$$\boldsymbol{m} - \boldsymbol{m}_{\text{ref}} = \log\left(\frac{\boldsymbol{\sigma}}{\boldsymbol{\sigma}_{\text{ref}}}\right), \tag{4.64}$$

the quotient of the involved conductivities is minimized, resulting in the same minimum norm constraint for both, the model parameters and conductivities.

4.5.1 Implicit regularization schemes

The finite-difference mesh, used for the numerical approximation of the forward problem, has to be designed such that field components can be evaluated without sacrificing too much accuracy. This can only be accomplished when spatial derivatives and averages of parameters are evaluated on extremely fine grids which is highlighted in fig. 3.8 and fig. 3.7. However, such a fine resolution of local inhomogeneities is not required when conductive structures have to be recovered from the data. In particular, the mesh spacings required to locally obtain a reasonable numerical forward solution may be in the order of centimeters, whereas the desired scale of conductive features for the inversion of those data is in the order of meters. Hence, the huge number of parameters to be recovered by solving the inverse problem may be under-determined in a local sense. The ill-posedness of the inverse problem can be reduced when certain parts of the forward or *computational grid* are combined to a coarser *parameter grid* which forms a nested subset of the fine grid. This strategy of reducing the number of model parameters provides an implicit regularization. The coarse parameter grid forms the point of departure for the computational grid, on which the discretization $\boldsymbol{\sigma} \in \mathbb{R}^S$ is defined. The latter is derived from the coarse grid by a nested grid refinement as described in section 3.7. For each refinement step a refinement number $r \in \mathbb{N}$ can be defined. The parameter and forward grid are related to r_{inv} and r_{fwd}, respectively. The associated parameter vector of the parameter grid is denoted by $\boldsymbol{\sigma}_{\text{inv}} \in \mathbb{R}^{S_{\text{inv}}}$ where $S_{\text{inv}} \leq S$. A typical grid hierarchy is shown in fig. 4.3 for the synthetic model, introduced in section 3.7. Uniform colors were assigned to regions of constant conductivity, i. e. the known background conductivity distribution $\boldsymbol{\sigma}_{\text{pri}}$. The trace of the fine forward grid, as indicated by the black lines on the right-hand side, results from a segmentation of the parameter cells (indicated as black lines on the left-hand side). Arbitrary intermediate stages of the grid hierarchy could be employed as parameter grids as long as $r_{\text{fwd}} \geq r_{\text{inv}}$.

Based on the cumulative sensitivities $\boldsymbol{j}_{\text{cum}}$, i. e. a superposition of the magnitudes of all individual footprints of the entire HEM survey, that are derived from $\boldsymbol{J}(\boldsymbol{\sigma}_{\text{pri}})$ with respect to

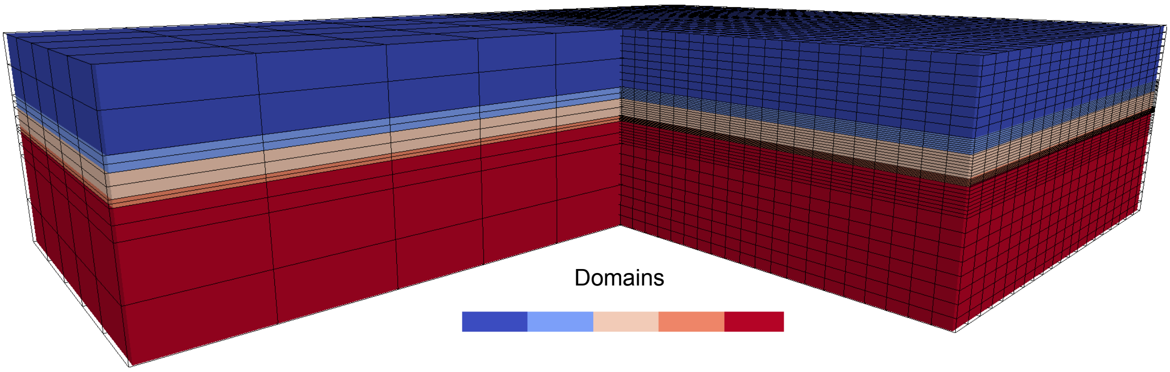

Figure 4.3: Parameter grid (rough black lines on left-hand side) and forward grid (fine black lines on right-hand side) defined on the regions of constant conductivity (areas of same color).

the a priori known background model on the computational grid:

$$\boldsymbol{j}_{\text{cum}} := \boldsymbol{V}^{-1} \sum_{i=1}^{N} \left[\left| \boldsymbol{j}_{i,j}(\boldsymbol{\sigma}_{\text{pri}}) \right| \right]^{\top}_{1 \le j \le S} \quad \in \mathbb{C}^{S}, \tag{4.65}$$

an *active* or inner region can be defined. This region is associated with the parametrization of the inverse problem, with $\boldsymbol{\sigma}_{\text{act}} \in \mathbb{R}^{M}$ and $M \le S_{\text{inv}} \le S$, on the level of the parameter grid. Only within this active region, changes in $\boldsymbol{m}_{\text{act}} = \log(\boldsymbol{\sigma}_{\text{act}})$ are explicitly allowed during the inversion iteration, whereas in the remaining parts of the model, the parameters keep the fixed value of the background model $\boldsymbol{\sigma}_{\text{pri}} \in \mathbb{R}^{S}$. As an example, fig. 4.4 shows the boundary of the active region derived from the magnitude of the cumulative sensitivity distribution over the known layered half-space model. The cumulative sensitivity represents the sum of all sensitivity footprints for the observation points that are marked by the white dots. Large values of the cumulative sensitivities, particularly related to areas near the surface and the embedded thin conductive layer, are indicated in red. The derivation of the extension of the active region from the cumulative sensitivity distribution can be chosen by hand (as done in fig. 4.4) or based on an arbitrary threshold for the elements of $\boldsymbol{j}_{\text{cum}}$. The most important benefit from defining such an inner region is the further reduction of the number of model parameters which diminishes the ill-conditioning of the inverse problem. Particularly, under-determined areas along the survey boundaries are excluded from the set of active cells. In addition, the approach is accompanied by a reduction of the computational costs of the minimization problem. Moreover, the violation of the forward problem boundary conditions (cf. section 3.2) is eliminated since deviations from the primary conductivity distribution are restricted to the model interior. It should be mentioned that incorporating a scaling by cell volumes in the calculation of the cumulative sensitivities (4.65) is crucial to obtain a “physical reasonable” image of the sensitivity distribution that is not depending on the underlying grid. The discrepancy is illustrated in fig. 4.5 where the cumulative sensitivity for the synthetic model problem is evaluated with respect to the frequency of $f = 1820\,\text{Hz}$. The elements of the Jacobian matrix naturally contain an integration over a respective cell volume such that the unscaled cumulative sensitivities (fig. 4.5b) always reflect the “mathematical reasonable”, i. e. grid-depending, image of the sensitivity distribution. In contrast to that, the physical reasonable sensitivity distribution, i. e. the superposition of nearly identically shaped sensitivity footprints (true for 1-D backgrounds) along the profile in y-direction, is expected to have its maximum being located at the profile center (fig. 4.5c).

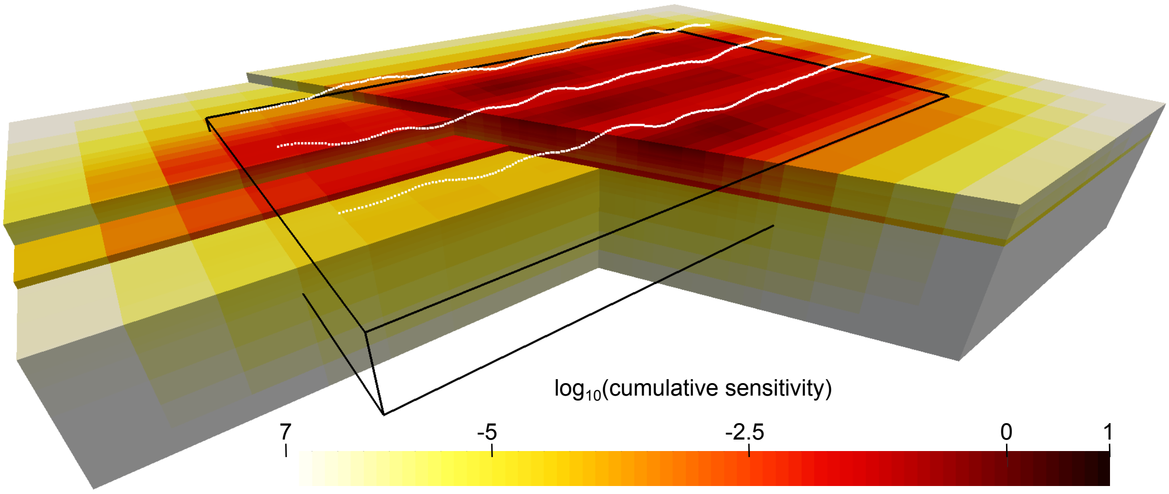

Figure 4.4: Cumulative sensitivity distribution for the stratified earth model. The black frame delineates the active region, in which model updates for the inverse problem are constructed. White dotted lines denote the survey's profile lines, where a single dot represents a TX/RX position.

To map the inversion results $\boldsymbol{\sigma}_{\text{act}} = \mathrm{e}^{\boldsymbol{m}_{\text{act}}} \in \mathbb{R}^M$, obtained in the active region and of the coarse parameter grid, to the complete and fine computational grid $\boldsymbol{\sigma} \in \mathbb{R}^S$, a *projection operator* $\boldsymbol{P} \in \mathbb{R}^{S\times M}$ is defined, which yields

$$\boldsymbol{\sigma} = (\boldsymbol{I} - \operatorname{diag}(\boldsymbol{P} \cdot \boldsymbol{1}_M))\, \boldsymbol{\sigma}_{\text{pri}} + \boldsymbol{P}\boldsymbol{\sigma}_{\text{act}}. \tag{4.66}$$

While the first term of (4.66) provides all non-active parts of the background conductivity $\boldsymbol{\sigma}_{\text{pri}}$, already defined on the forward grid, the second term projects $\boldsymbol{\sigma}_{\text{act}}$ from the parameter grid to the active parts of the forward grid. Hence, the summation of these complementary parts gives the (updated) total conductivity distribution $\boldsymbol{\sigma} \in \mathbb{R}^S$ on the forward grid. It holds that $\sigma_p = \sigma_{\text{pri},p}$ in all regions Ω_p which are not assigned to the active region.

Concerning the reduced model parameter vector related to the active region $\boldsymbol{m}_{\text{act}}$, the tensor-based representation of the mass matrix derivative (4.38) becomes

$$\frac{\partial \boldsymbol{M}}{\partial \boldsymbol{m}_{\text{act}}} = \widetilde{\boldsymbol{T}} \times_3 \left[\boldsymbol{P} \operatorname{diag}\left(\mathrm{e}^{\boldsymbol{m}_{\text{act}}}\right)\right] \quad \in \mathbb{R}^{K\times K\times M}, \tag{4.67}$$

with

$$\frac{\partial \boldsymbol{\sigma}(\boldsymbol{m})}{\partial \boldsymbol{m}_{\text{act}}} = \boldsymbol{P}\frac{\partial \boldsymbol{\sigma}_{\text{act}}(\boldsymbol{m})}{\partial \boldsymbol{m}_{\text{act}}} = \boldsymbol{P}\operatorname{diag}(\boldsymbol{\sigma}_{\text{act}}) \quad \in \mathbb{R}^{S\times M}. \tag{4.68}$$

For repeated multiplications with the tensor $\partial_{\boldsymbol{m}}\boldsymbol{M}$ (cf. section 4.4), e. g. if the Jacobian matrix is handled implicitly, it is advisable to store

$$\widetilde{\boldsymbol{T}}_{\boldsymbol{P}} := \widetilde{\boldsymbol{T}} \times_3 \boldsymbol{P} \quad \in \mathbb{R}^{K\times K\times M}, \tag{4.69}$$

as this tensor is independent of $\boldsymbol{m}$, and therefore needs to be computed only once. Hence,

$$\frac{\partial \boldsymbol{M}(\boldsymbol{m})}{\partial \boldsymbol{m}_{\text{act}}} \times_2 \boldsymbol{u} = \left[\widetilde{\boldsymbol{T}}_{\boldsymbol{P}} \times_2 \boldsymbol{u}\right] \operatorname{diag}(\boldsymbol{\sigma}_{\text{act}}) \quad \in \mathbb{R}^{K\times M}, \tag{4.70}$$

a matrix-matrix multiplication followed by a tensor-matrix and a tensor-vector product can be equivalently carried out by a single tensor-vector and a matrix-matrix product.

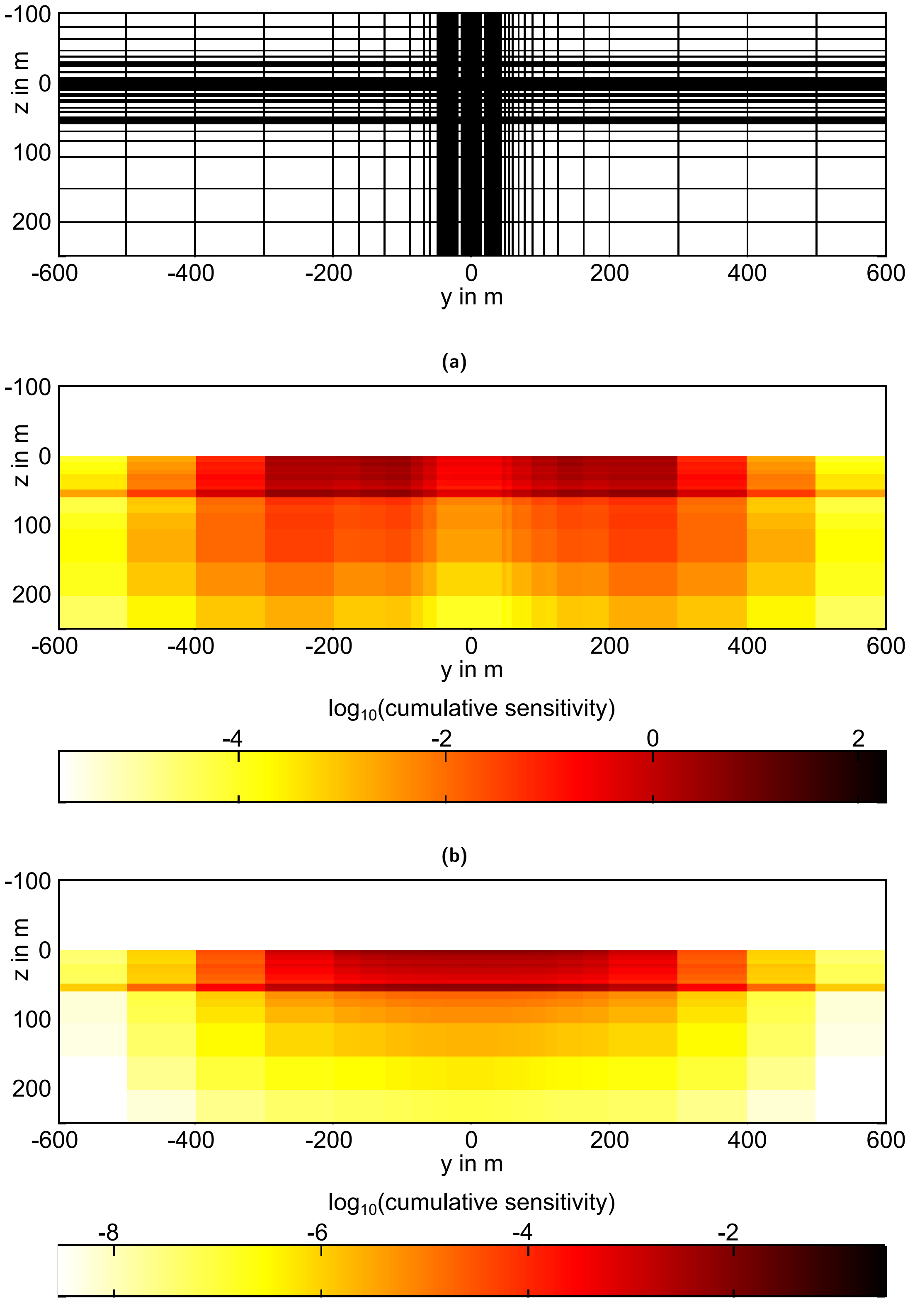

(a)

(b)

(c)

Figure 4.5: Sections of the cumulative sensitivity distribution ($f = 1820\,\mathrm{Hz}$) for the yz-plane at $x = 0\,\mathrm{m}$ with respect to the horizontal layered background model. While a) shows the inhomogeneously distributed edges of the grid on which the sensitivities are calculated, b) illustrates the unscaled cumulative sensitivities that are used within the inversion and c) represents the grid-independent, i. e. volume scaled, cumulative sensitivities.

4.5.2 Explicit regularization schemes

A variety of constraints on the model parameter vector can be incorporated by the model weighting matrix $\boldsymbol{W}_m$ (Vogel 2002; Nocedal and Wright 2006; Zhdanov 2009; Haber 2014). Since the presented inversion approach is build upon a forward operator, using a finite difference discretization based on a regular tensor-product grid (section 3.4), it is convenient to resort to the easily accessible first-order ($\boldsymbol{G}$) and second-order ($\boldsymbol{DG}$) spatial derivative operators. To directly apply $\boldsymbol{W}_m$ on the model parameter vector $\boldsymbol{m}_{\text{act}}$, these operators have to refer to the coarse parameter grid and can be adapted to the restriction of the active region by simply removing those rows or columns of the respective operator matrices which are associated with the non-active parameters. Hence,

$$\boldsymbol{G} \in \mathbb{R}^{K^h \times S_{\text{inv}}} \rightarrow \boldsymbol{G}_r \in \mathbb{R}^{K^h \times M}, \tag{4.71}$$

$$\boldsymbol{D} \in \mathbb{R}^{S_{\text{inv}} \times K^h} \rightarrow \boldsymbol{D}_r \in \mathbb{R}^{M \times K^h}, \tag{4.72}$$

the reduced gradient and divergence operators provide the first- and second-order derivatives for the active model parameter vector, preserving homogeneous boundary conditions at the interface of the active and non-active region. The model weighting matrix $\boldsymbol{W}_m$ finally arises from the concatenation

$$\boldsymbol{W}_m := \begin{bmatrix} w_0\boldsymbol{I} \\ w_1\boldsymbol{G}_r \\ w_2\boldsymbol{D}_r\boldsymbol{G}_r \end{bmatrix} \in \mathbb{R}^{W \times M}, \tag{4.73}$$

with

$$W = (M + K^h + M). \tag{4.74}$$

The arbitrary scalar weighting factors $w_0, w_1, w_2 \in \mathbb{R}_+$ allow to balance between a stabilized solution that approaches to the reference model $\boldsymbol{m}_{\text{ref}} \in \mathbb{R}^M$ by the part $w_0\boldsymbol{I} \in \mathbb{R}^{M \times M}$ or solutions that contain (smoothed) parameter jumps by the parts $w_1\boldsymbol{G}_r$ and $w_2\boldsymbol{D}_r\boldsymbol{G}_r$. Own numerical experiments on different synthetic models have shown that the influence of the three weighting operators on the resulting model decreases with an increase in the order of their derivative. Hence, a default balancing, using $w_0 \in \left[10^{-1}, 1\right]$, $w_1 \in \left[1, 10^1\right]$, and $w_2 \in \left[10^1, 10^2\right]$, is applied on the three components of $\boldsymbol{W}_m$.

Since HEM measurements are characterized by a very dense data distribution in the profile direction (separation often only a few meters) and comparatively large profile separations in the inter-profile direction (up to some hundreds of meters), a directional weighting is incorporated for the components of the first-order derivative operator

$$\boldsymbol{G}_r := \begin{bmatrix} g_x\boldsymbol{G}_{r,x} \\ g_y\boldsymbol{G}_{r,y} \\ g_z\boldsymbol{G}_{r,z} \end{bmatrix} \in \mathbb{R}^{K^h \times M}, \tag{4.75}$$

with the survey-depending arbitrary scalar weighting factors $g_x, g_y, g_z \in \mathbb{R}_+$. Hence, the strong anisotropy in the spatial data sampling can be counterbalanced in model parameter distribution $\boldsymbol{m}_{\text{act}}$ that is provided by the solution of the inverse problem. The influence of the directional weighting is illustrated in fig. 4.6. Two inversion results are shown which are associated to the same data set obtained for the synthetic test model. While in the upper part of the figure, the embedded block is resolved as three separated anomalous structures, strongly related to the location of the three profiles, in the lower part of the figure a coherent

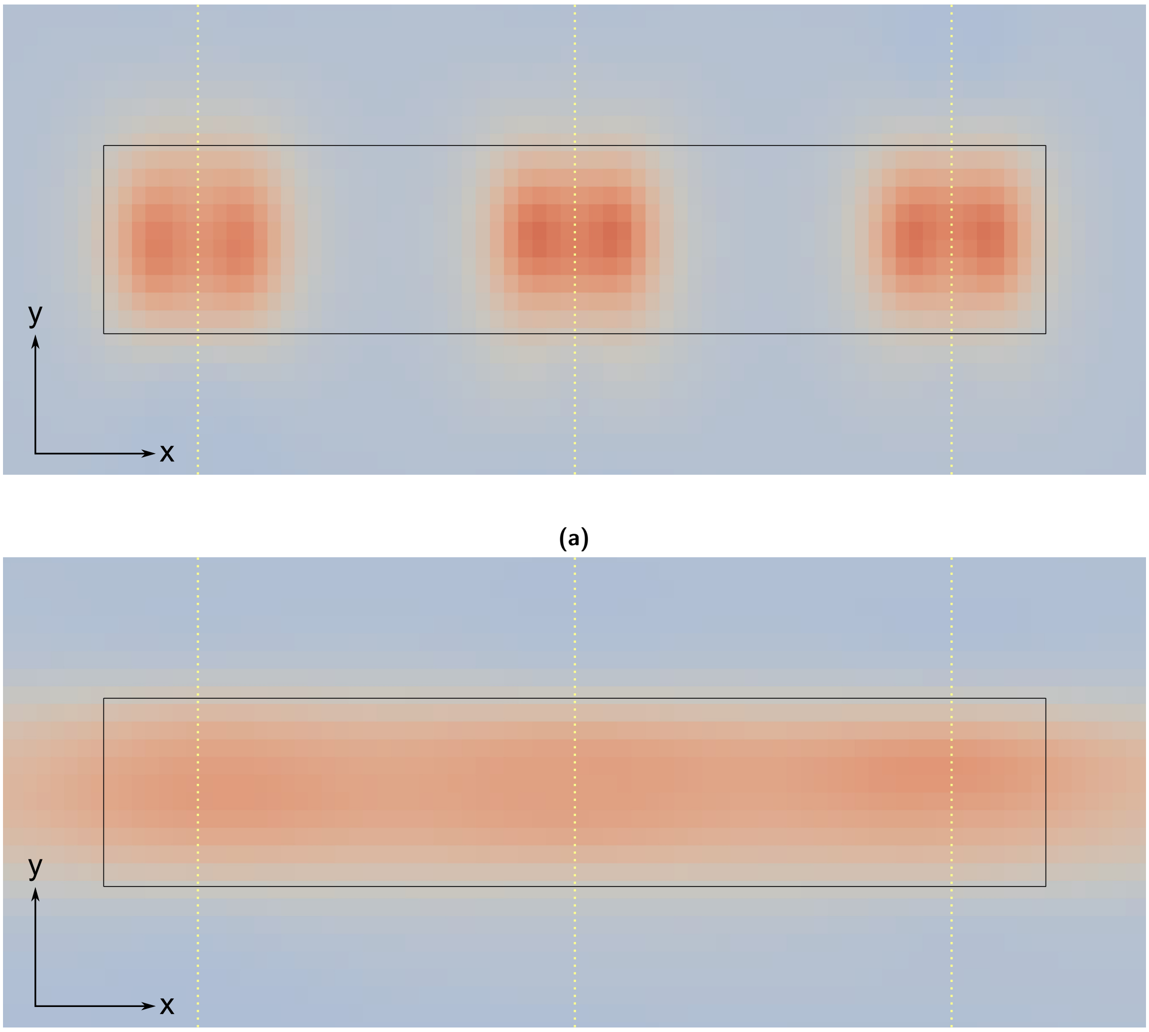

(a)

(b)

Figure 4.6: Section of an inverted conductivity distribution for the xy-plane at $z = 0\,\mathrm{m}$, obtained after 16 Gauss-Newton steps, a) no directional weighting b) directional weighting included. The black lines indicate the outline of the embedded block and the yellow dots mark the overlaying RX positions from the HEM survey.

conductive body is shown. For the latter, the ratio of the horizontal directional weighting factors ($g_x : g_y$) is chosen to be 35 : 1 whereat the ratio of the inter-profile to the in-line spacing was given by about 50 : 1. As it becomes visible at the left and right boundaries of the images, the spatial balancing of the data anisotropy on the one side provokes a minor overestimation of the block extend in the predominant direction on the other side. Furthermore, the effect of the derivative operators, i. e. particularly the action of $w_2 \boldsymbol{D}_r \boldsymbol{G}_{\boldsymbol{r}}$ on $\boldsymbol{m}_{\mathrm{act}}$, can be clearly recognized in fig. 4.6a. The trace of the strong conductive anomalies smooths out softly with increasing distance and proceeds smoothly to the background conductivity that is identified with the blue colored areas.

4.5.3 Regularization parameter λ

To ensure the convergence of the Gauss-Newton approach with respect to the solvability, the choice of an adapted regularization parameter λ is a crucial but likewise demanding task. A variety of approaches like the simply trial-and-error method, applied in Sasaki (2001), the L-curve criteria (Hansen and O'Leary 1993), general cross-validation (Golub et al. 1979), or approaches based on the discrepancy principle (Smith and Booker 1988, e. g.) have been proposed and are still the basis for ongoing studies and reviews (Haber and Oldenburg 2000; Farquharson and Oldenburg 2004; Bazán et al. 2012, e. g.). However, since most of these methods are either associated with linear inverse problems or they assume a priori knowledge, e. g. of the noise level, they furthermore require the solution of several additional forward problems within each outer iteration step, if λ is not kept on a fixed value. Particularly the latter constraint renders those approaches for the application to HEM inverse problems unsuitable.

In this thesis, a straight-forward approach is used which aims at minimal additional computational effort for the estimation of a rough initial regularization parameter λ_0. The main goal is to achieve a trade-off between the data misfit (Φ_d) and the model roughness (Φ_m) norm that is comparable to the L-curve criteria, i. e. to obtain smooth solutions which are related to the reference model $\boldsymbol{m}_{\mathrm{ref}}$ and still observe sufficiently small values for the objective function Φ. For $\Phi(\boldsymbol{m})_d \ll \lambda \Phi(\boldsymbol{m})_m$, even an increase in Φ may be observed, as the model parameters are rather forced to fit the regularization assumption, i. e. to assimilate the $\boldsymbol{m}_{\mathrm{ref}}$, than to minimize Φ_d. To obtain the initial estimate λ_0, a weighted ratio

$$\lambda_0 = \gamma \frac{\Phi_d(\boldsymbol{m}_{\mathrm{act},0})}{\Phi_m(\boldsymbol{m}_{\mathrm{act},0})}, \tag{4.76}$$

with respect to the starting model $\boldsymbol{m}_{\mathrm{act},0}$, is used. Own numerical experiments have revealed that, particularly in view of the explicit regularization set up shown in section 4.5.2, the choice of $\gamma \in \left[1, 10^2\right]$ always yields an appropriate guess. The evaluation of $\Phi_d(\boldsymbol{m}_{\mathrm{act},0})$ requires a factorization of $\boldsymbol{A}(\boldsymbol{m}_{\mathrm{act},0})$ which can be reused in the first Gauss-Newton iteration step. Hence, this approach manages without any additional computational effort.

Despite the estimation of λ_0, also the handling of the regularization parameter during the remaining outer iteration steps is a somehow unresolved problem. In dependence on Newman and Hoversten (2000), Lelièvre et al. (2012), and Yang et al. (2013), the regularization parameter λ is exponentially decreased by

$$\lambda_k = \lambda_0 \, \mathrm{e}^{-b(k-1)}, \tag{4.77}$$

within each of the $k = 1, \ldots, k_{\max}$ Gauss-Newton iteration steps, referred to as *cooling approach.* The arbitrary scalar $b \in (0, 1]$ is set to $b = 0.5$, by default.

4.6 Step length control

Calculating model updates for a linearized objective function Φ_{GN} (4.13) while originally aiming at minimizing the underlying nonlinear problem Φ (4.7), inevitably leads to certain discrepancies. At the worst, the model update obtained from a convergent inner iteration of the linearized problem may even result in an increase of the nonlinear objective function. This mostly results from model updates with too large magnitudes that can be observed predominantly at early Gauss-Newton iteration steps and which violates the linearization constraint (Nocedal and Wright 2006). To ensure the convergence of the Gauss-Newton method, an additional 1-D least-squares problem

$$\Phi(\alpha) = \frac{1}{2}\left\|\hat{\boldsymbol{d}}^{\mathrm{obs}} - \hat{\boldsymbol{d}}(\boldsymbol{m}(\boldsymbol{\alpha}))\right\|_2^2 \rightarrow \min_{\alpha}, \tag{4.78}$$

with

$$\boldsymbol{m}(\alpha) = \boldsymbol{m}_0 + \alpha\Delta\boldsymbol{m}, \tag{4.79}$$

and

$$\hat{\boldsymbol{d}}^{\mathrm{obs}} = \begin{bmatrix} \boldsymbol{W}_d\boldsymbol{d}^{\mathrm{obs}} \\ \sqrt{\lambda}\boldsymbol{W}_m\boldsymbol{m}_{\mathrm{ref}} \end{bmatrix}, \tag{4.80}$$

$$\hat{\boldsymbol{d}}(\boldsymbol{m}) = \begin{bmatrix} \boldsymbol{W}_d\boldsymbol{d}(\boldsymbol{m}) \\ \sqrt{\lambda}\boldsymbol{W}_m\boldsymbol{m} \end{bmatrix}, \tag{4.81}$$

has to be solved within each outer iteration, after a model update $\Delta\boldsymbol{m}$ is calculated. The solution of this problem yields an optimal step length α^* for the current model update towards the decent search direction of the respective Gauss-Newton step. For this purpose, an inexact *line search* strategy is considered which is based on a quadratic approximation to the nonlinear objective function

$$\Phi(\alpha) \approx \Phi_{\mathrm{quad}}(\alpha) = \mathrm{a}\alpha^2 + \mathrm{b}\alpha + \mathrm{c}, \tag{4.82}$$

where the unknown coefficients a, b, c are defined by the known function value $\Phi(\alpha = 0)$, the derivative $\partial_\alpha\Phi(\boldsymbol{m}(\alpha))$ at $\alpha = 0$, and an additionally evaluated objective function $\Phi(\alpha_0)$ at the default starting guess $\alpha_0 = 1$. Each evaluation of $\Phi(\alpha), \alpha \neq 0$, requires the additional solution of a forward problem with a modified system matrix $\boldsymbol{A}(\boldsymbol{m} + \alpha\Delta\boldsymbol{m})$. The minimum $\Phi_{\mathrm{quad}}(\alpha_0^*)$ (for all $\alpha \in \mathbb{R}_+$) of the approximating quadratic function is given by

$$\alpha_0^* = \frac{\Delta\boldsymbol{m}^\top\Re\left(\hat{\boldsymbol{J}}^{\mathsf{H}}\Delta\hat{\boldsymbol{d}}\right)}{2\left(\Phi(\alpha_0) - \alpha_0\Delta\boldsymbol{m}^\top\Re\left(\hat{\boldsymbol{J}}^{\mathsf{H}}\Delta\boldsymbol{m}\right) - \Phi(\alpha = 0)\right)} \cdot \frac{1}{\alpha_0^2} \tag{4.83}$$

with the residual

$$\Delta\hat{\boldsymbol{d}} = \hat{\boldsymbol{d}}^{\mathrm{obs}} - \hat{\boldsymbol{d}}(\boldsymbol{m}(\alpha)). \tag{4.84}$$

By analogy to (B.9), the directional derivative

$$\frac{\partial\Phi}{\partial\alpha} = -\Delta\boldsymbol{m}^\top\Re\left(\hat{\boldsymbol{J}}^{\mathsf{H}}\Delta\hat{\boldsymbol{d}}\right), \tag{4.85}$$

can be obtained by using the chain rule

$$\begin{aligned} \frac{\partial\Phi}{\partial\boldsymbol{m}}\frac{\partial\boldsymbol{m}}{\partial\alpha} &= (\nabla_{\boldsymbol{m}}\Phi)^\top\frac{\partial\boldsymbol{m}}{\partial\alpha} \\ &= \left(\frac{\partial\boldsymbol{m}}{\partial\alpha}\right)^\top\nabla_{\boldsymbol{m}}\Phi, \end{aligned} \tag{4.86}$$

and exploiting the commutativity of the inner product. Thereby, it holds that

$$\hat{\boldsymbol{J}} = \begin{bmatrix} \boldsymbol{W}_d \boldsymbol{J} \\ \sqrt{\lambda} \boldsymbol{W}_m \end{bmatrix}, \tag{4.87}$$

and

$$\frac{\partial \boldsymbol{m}(\alpha)}{\partial \alpha} = \Delta \boldsymbol{m}. \tag{4.88}$$

Only if the minimization already fails for α_0, e. g. when $\Phi(\alpha_0) > \Phi(\alpha = 0)$, the new guess is calculated, i. e. the minimum α_0^* of the quadratic approximation. Furthermore, using $\alpha_k = \alpha_{k-1}^*, k = 1, 2, \ldots, k_{\max}$ a line search iteration is established that is accordingly based on $\Phi_{\text{quad}}(\Phi(\alpha = 0), \partial_\alpha \Phi(\alpha = 0), \Phi(\alpha_k))$. Own numerical studies indicate that $\alpha_k \to 0$ even after very few steps. Therefore, with respect to the computational effort, the maximum number of line search steps is restricted to $k_{\max} = 3$. If $\alpha_0 = 1$ is already accepted, the line search algorithm causes nearly no further computational costs since the provided decomposition of $\boldsymbol{A}$ can be reused in the following Gauss-Newton step.

To ensure that the line search algorithm will converge towards a minimizer, a guess α_k has to fulfill the strong Wolfe conditions (Nocedal and Wright 2006) which consist of the *Armijo condition* and the *curvature condition*. The former reads

$$\Phi(\boldsymbol{m}_0 + \alpha_k \Delta \boldsymbol{m}) \leq \Phi(\boldsymbol{m}_0) + c_1 \alpha_k \Delta \boldsymbol{m}^\top \nabla_{\boldsymbol{m}} \Phi(\boldsymbol{m}_0) \quad \text{for} \quad c_1 \in (0, 1), \tag{4.89}$$

and ensures a decrease in the objective function that is smaller than the straight line defined by the RHS of (4.89). The parameter c_1, modifying the slope, is chosen to be quite small (e. g. following Nocedal and Wright (2006), $c_1 \approx 10^{-4}$). The *curvature condition*

$$\left| \Delta \boldsymbol{m}^\top \nabla_{\boldsymbol{m}} \Phi(\boldsymbol{m}_0 + \alpha_k \Delta \boldsymbol{m}) \right| \leq c_2 \left| \Delta \boldsymbol{m}^\top \nabla_{\boldsymbol{m}} \Phi(\boldsymbol{m}_0) \right| \quad \text{for} \quad c_2 \in (c_1, 1), \tag{4.90}$$

helps to avoid undersized step lengths by demanding a sufficiently smaller slope at the approximated minimizing function value $\Phi(\boldsymbol{m}_0 + \alpha_k \Delta \boldsymbol{m})$ compared to the origin at $\alpha = 0$. The gradient $\nabla_{\boldsymbol{m}} \Phi(\alpha = 0)$ is always supposed to be negative, since the solution to the (linearized) least-squares problem is expected to always yield a descent search direction, i. e. $\Delta \boldsymbol{m} : \Delta \boldsymbol{m}^\top \nabla_{\boldsymbol{m}} \Phi < 0$. Since the absolute value of both terms is considered in (4.90), also strong positive slopes are rejected. Typical values of c_2 are ≈ 0.9 (Nocedal and Wright 2006).

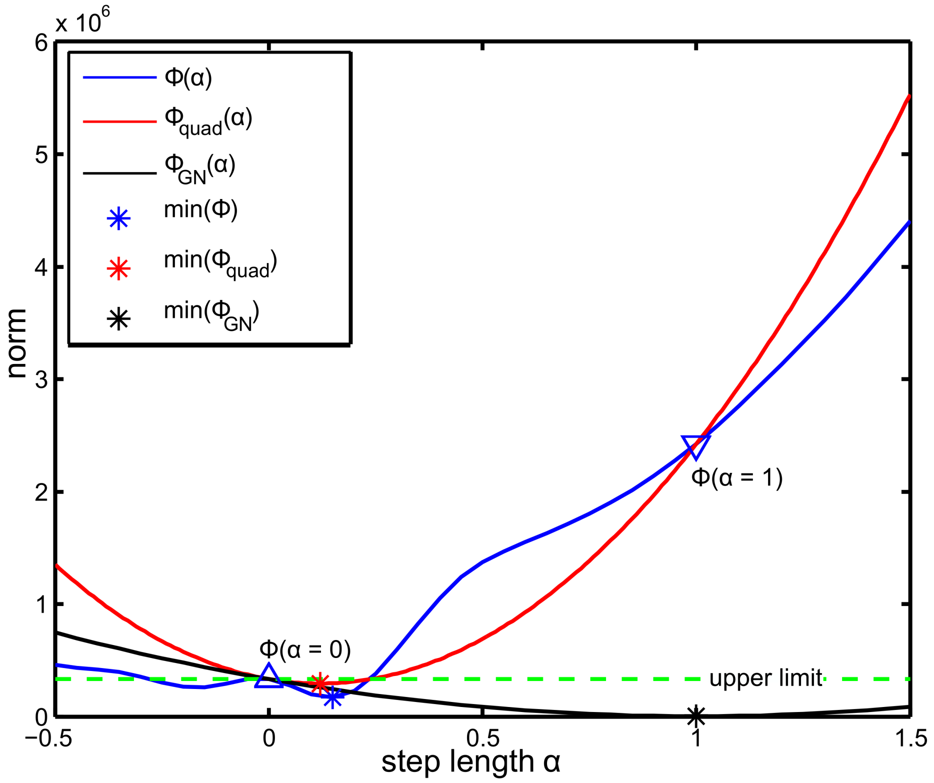

Figure 4.7: Comparison of the different definitions of the objective function for evaluations at $\alpha \in (-0.5, 1.5)$ and with a fixed model update vector $\Delta \boldsymbol{m}$.

As an example, fig. 4.7 shows the evaluated objective functions of the underlying nonlinear minimization problem Φ (blue curve), the linearized Gauss-Newton problem Φ_{GN} (black curve), and the quadratic approximation Φ_{quad} (red curve), generated from the known gradient and function value of Φ at $\alpha = 0$ (upward-pointing blue triangle) as well as the additionally evaluated function value $\Phi(\alpha = 1)$ (downward-pointing blue triangle). While the model update which results from the minimum of the linearized objective function (black asterisk) leads to a strong violation of the first Wolfe condition (green dotted line), the damped model update, derived from the minimum of the quadratic approximation (red asterisk), is sufficiently close to the true minimum of the nonlinear objective function (blue asterisk). Therefore it fulfills the Armijo condition (4.89).

5 Applications

5.1 Inversion of synthetic data

As a first inversion result, the presented inversion algorithm is applied to a synthetic data set which is obtained for the introduced test model (section 3.7). The active region of the parameter grid measures 700 m×900 m×100 m and is horizontally centered within the computational grid. The goal is to recover the conductivity distribution defined by $M = 119\,808$ parameter cells which are nested within a computational grid with $S = 172\,872$ cells. The discretized model leads to a number of DOF of $K = 492\,566$.

Because of inevitable discretization errors, a numerical approximation is expected to be incapable of reproducing the exact answer of a physical problem. Thus, also a numerical inversion algorithm, based on that discrete forward operator, is not able to provide the exact parameter distribution. To avoid the related *inverse crime* (Kaipio and Somersalo 2007), i. e. that the unique solution actually can be found from a synthetic data set, these data are generated with a different forward code, the MarcoAir package as contained in the P223Suite (Raiche et al. 2007). It provides the (synthetic) observed data $\boldsymbol{d}^{\mathrm{obs}}$ for the five frequencies, each with a fixed coil separation of 8 m. Additionally, Gaussian noise with a standard deviation of 2.5 % with respect to the undisturbed data is added.

A homogeneous starting model $\boldsymbol{m}_{\mathrm{act},0}(\boldsymbol{\sigma}_{\mathrm{pri}})$ is used that has been derived from the averaged background model of the layered half-space, for which the primary fields are calculated. Since the layered half-space already acts as the reference model, own numerical studies have shown that it is not advisable to additionally use it as the starting model. In this case, the regularization will only act as a weighting of the normal equations system matrix, that may lead to unwanted extreme model updates in the first Gauss-Newton iteration. Despite that, the evaluation of an initial regularization parameter (4.76) will inevitably fail, as the model roughness norm (4.6) is zero.

For the Tikhonov regularization set up, the combination of the identity matrix as well as first and second order spatial derivatives, applied to the model parameters, are incorporated. These are associated with the weighting factors $w_0 = 5 \times 10^{-1}$, $w_1 = 1$, and $w_2 = 10$. To counterbalance the spatial data anisotropy with the ratio 50 : 1 (inter-profile : in-line), a directional weighting with $g_x = 70$, $g_y = 2$, and $g_z = 4$ is used. The scaling factor for the evaluation of the initial regularization parameter λ_0 is set to $\gamma = 10$.

By applying the cooling approach to obtain a decrease of the regularization parameter with respect to the number of outer iterations, the ability of achieving a good data fitting is accompanied with a serious drawback: no estimate of the convergence properties can be stated out. In addition, the HEM method typically gives no prediction of a data uncertainty. Therefore, defining a global termination condition is a challenging task which is tackled with a straight-forward approach. It is based on the difference between two consecutive weighted

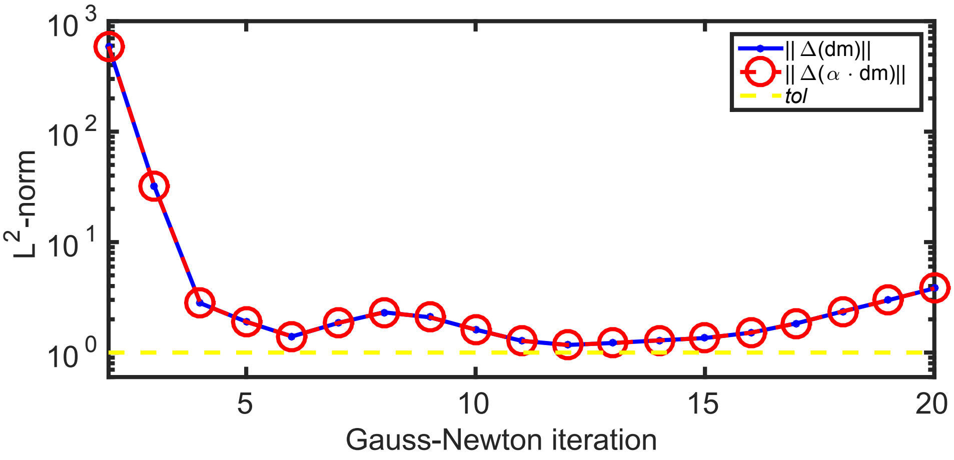

Figure 5.1: Difference between the previous and current model update, associated with the iteration number of the latter.

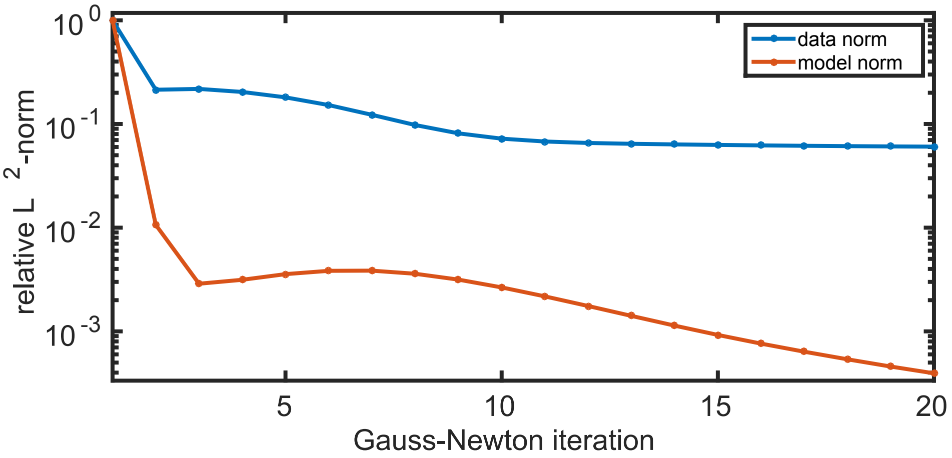

Figure 5.2: Convergence of the data misfit (blue curve) and the model roughness norm (green curve). Both norms are normalized to their initial value.

model updates

$$\chi_k = \|\alpha_k \boldsymbol{\Delta m}_k - \alpha_{k-1}\boldsymbol{\Delta m}_{k-1}\|\,, \tag{5.1}$$

which is expected to become small if the outer iteration is convergent. The idea is to subsequently terminate the Gauss-Newton iteration if these variations possess a minimum ($\chi \rightarrow \min_k$) or terminate it instantly if they drop below an arbitrary threshold ($\chi_k < tol$) which is set to $tol = 1$. The maximum number of allowed iterations is limited to 20. Figure 5.1 shows the differences between the consecutive model updates for the entire Gauss-Newton iteration. The outer iteration was not terminated until it reaches the allowed number of 20 iteration steps. The blue curve corresponds to the unweighted model update vectors and the red dashed curve illustrates the actual (weighted) model updates used for the outer iteration. If a step length of $\alpha = 1$ is accepted by the line search algorithm, both curves coincide as shown in the figure. For own inversion studies on different synthetic data sets, however, the termination approach was found to be not fully reliable. At first, in early iterations where a strong influence of the regularization due to the high regularization parameter is observed, χ often already shows a local minimum (cf. fig. 5.1). Furthermore, if *tol* is set quite low, the outer iteration terminates too late such that a strong heterogeneity in the obtained parameter model can be recognized. Therefore, it is still required to visually inspect the series of parameter models around the suggested final model and to manually terminate the outer iteration afterward. In the case of the presented synthetic model, the automatic termination at iteration 12 is accepted to give the “best” parameter model.

Figure 5.3 shows the final conductivity distribution, obtained from the inversion of the noisy synthetic data. The block within the top layer of the model is reconstructed satisfactorily with the expected minor overestimation of the spatial extent in the x-direction. The calculations are carried out on 8 of 32 cores of an Intel® Xeon® CPU E5-4620 processor running at 2.2 GHz with 512 GB of RAM. After 12 Gauss-Newton steps the relative data residual has reduced to 6.6×10^{-2} (fig. 5.2) giving an acceptable data fit that is exemplarily shown in fig. 5.4 and fig. 5.5 for the real and imaginary parts of the central profile. In fig. 5.4, the blue curves represent the observed data, while the red curves show the synthetic data, obtained for the response of the final parameter model. The relative error between the observed and synthetic data is illustrated in fig. 5.5. In general, the error is in the order of the synthetic noise level, roughly varying between ±3 %. The complete inversion run takes about 19 h (about 1.4 h per Gauss-Newton iteration) and requires a peak memory usage of 182 GB. The primary fields are evaluated in only 11.7 min.

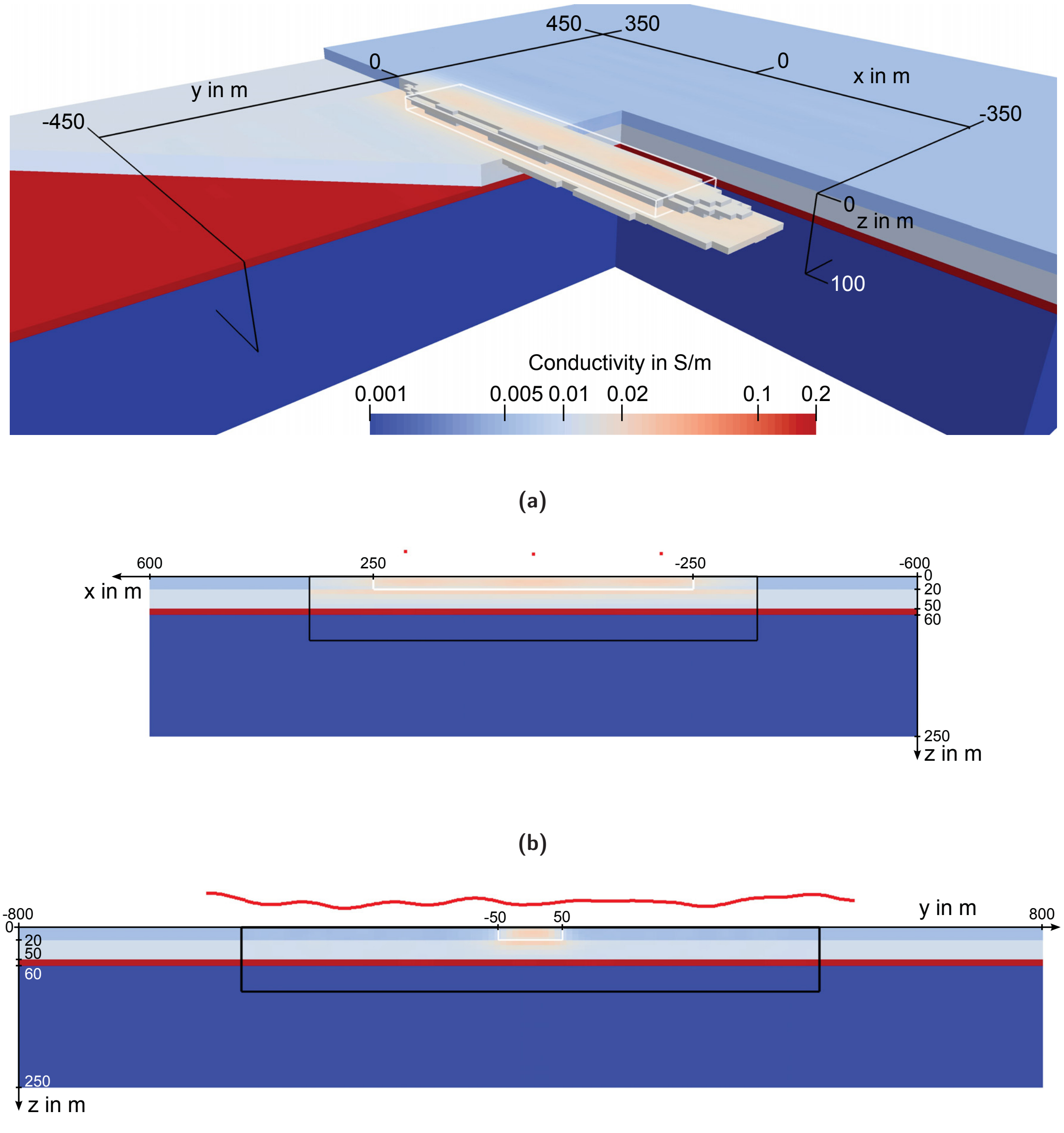

(a)

(b)

(c)

Figure 5.3: Conductivity distribution obtained after 12 Gauss-Newton steps. The black lines and the white boxes indicate the boundary of the inner area and the true boundaries of the embedded block, respectively. In a), the parameters associated with the resolved block, i. e. cells with a deviation from the true conductivity of 30 %, are highlighted against the background. b) shows a section of the inverted model at $y = 0$ (xz-plane). In c), a sketch of the yz-plane at $x = 0$ is presented. The red dots indicate the RX positions.

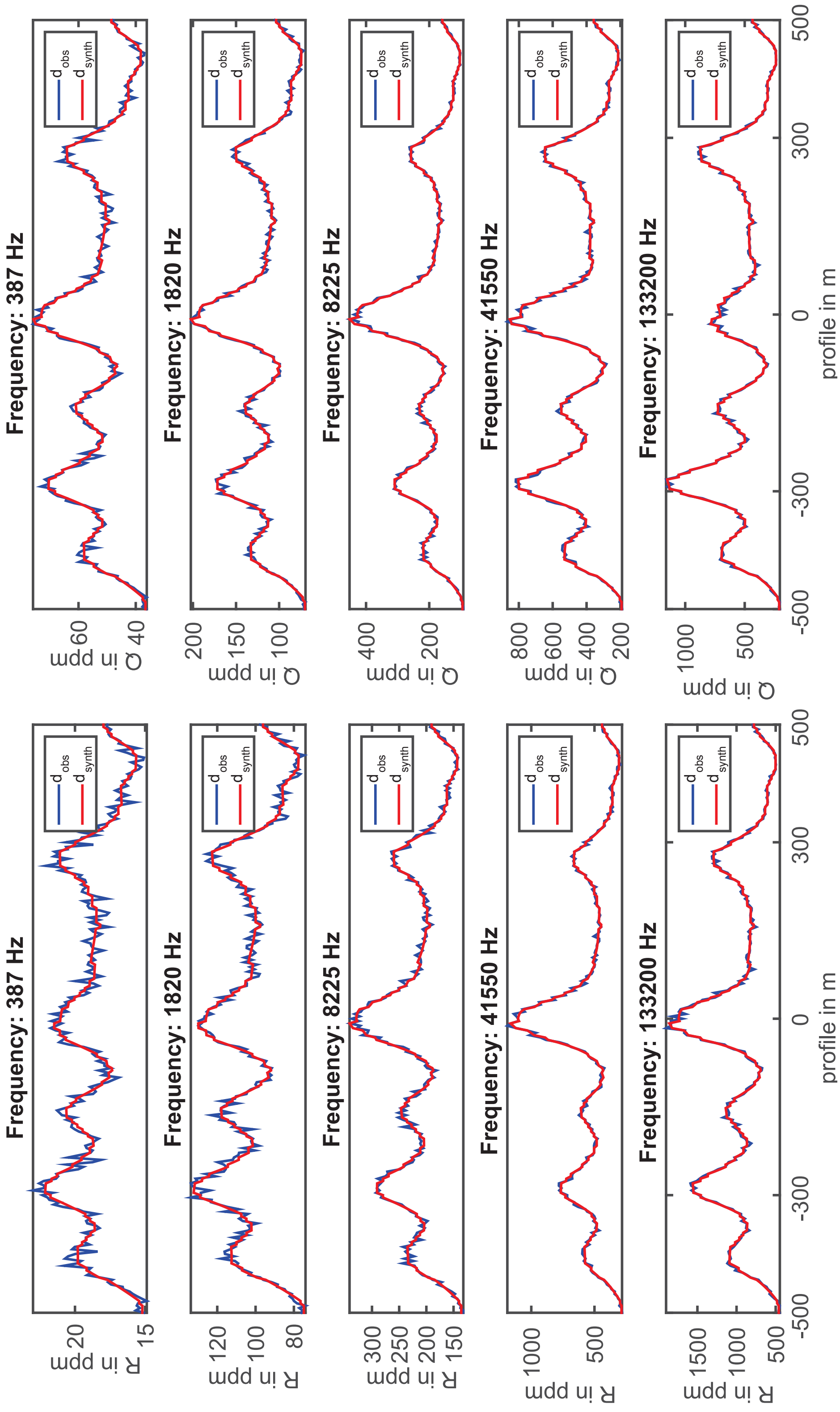

Figure 5.4: Real (left-hand side) and imaginary (right-hand side) parts of the observed field (blue curves) and the final model response (red curves), obtained from the 12th Gauss-Newton iteration, at the central profile for the 5 frequencies used.

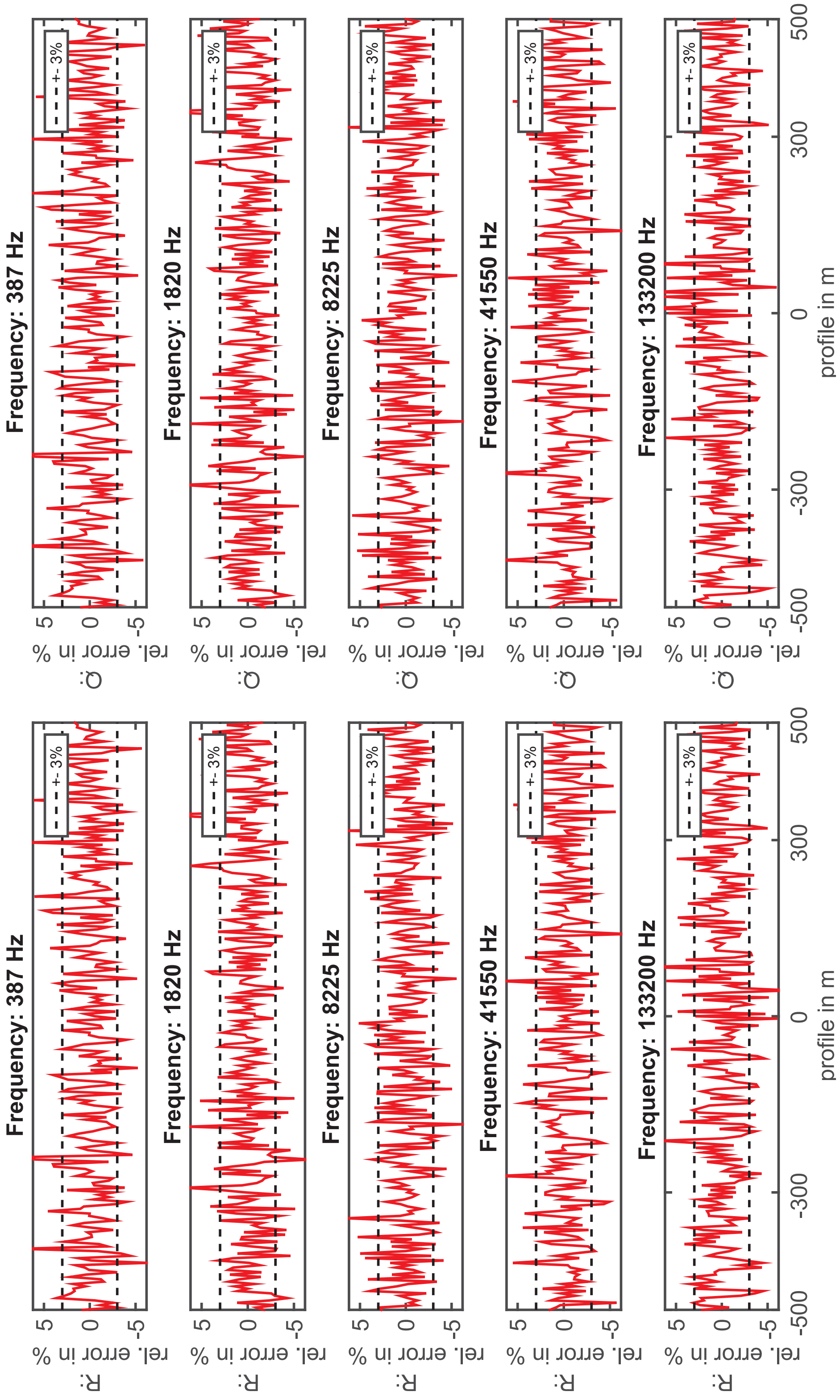

Figure 5.5: Real (left-hand side) and imaginary (right-hand side) parts of the relative error of the observed data with respect to the synthetic data, obtained from the 12th Gauss-Newton iteration, at the central profile for the 5 frequencies used.

5.2 Inversion of field data

The algorithm is finally applied to a field data set which has been collected by the BGR, the Leibniz Institute for Applied Geosciences, and the Geological Survey of Lower Saxony in May 2000 (Siemon, Eberle, et al. 2004). The survey is located in the north-west of Germany, near the city of Cuxhaven (fig. 5.6) and incorporates 15 flight profiles. The pathways of these profiles are illustrated in fig. 5.7. Here, a local coordinate system is used which is reduced by the coordinates of the survey midpoint and rotated such that the directions of the orthogonal profiles match the horizontal coordinate directions of the tensor-product grid, on which the underlying numerical problem is based on. The yellow lines indicate two power supply lines of the national grid which are intersected by the survey. Figure 5.8 shows a sketch of the survey and the corresponding topography. Due to the moderate variation in the elevation area as well as the spatial distance between the earth' surface and the HEM receiver, the influence of the topography on the observed data is considered to be negligible (Beard 2000).

The outermost boundary of fig. 5.7 and fig. 5.8 is associated with the size of the model domain, on which the forward problem is evaluated. The respective computational grid has a total extension of $5000\,\text{m}\times 5000\,\text{m}\times 500\,\text{m}$ and comprises $S = 253\,500$ cells which are associated with $K = 719\,175$ DOF. A homogeneous horizontal grid spacing leads to cell sizes of about $40\,\text{m}\times 40\,\text{m}$ in x- and y-direction. The grid node distance in z-direction increases from 7.5 m, near the surface, up to 30 m. On the area of about $8\,\text{km}^2$ a total of 10 126 TX/RX positions are distributed with an average in-line spacing of 4 m and an inter-profile spacing of about 1000 m on the three profiles that strike out in the x-direction, and an average inter-profile spacing of about 250 m on the remaining 12 profiles that are oriented in the y-direction. The observed data are obtained for four frequencies (384 Hz, 1830 Hz, 8610 Hz and 41 300 Hz) with corresponding coil separations of 6.87 m, 6.73 m, 6.59 m and 6.68 m. The active region of the parameter grid (the blue square denoting the horizontal boundaries) is chosen to measure $4000\,\text{m}\times 4000\,\text{m}\times 200\,\text{m}$ and is horizontally centered within the computational grid. In total, $M = 180\,224$ parameter cells have to be reconstructed. The calculations are carried out on 8 cores of an Intel® Xeon® CPU E5-4620 processor running at 2.2 GHz with 512 GB of RAM.

The Gauss-Newton iteration employs a homogeneous averaged background model as starting guess and includes a Tikhonov regularization with a combination of the identity matrix as well as first and second order spatial derivative operators. The associated weighting factors are $w_0 = 5 \times 10^{-4}$, $w_1 = 1$, and $w_2 = 10$. Now, the directional weighting is used to counterbalance the horizontal grid spacings with respect to the short node distances in the in z-direction by incorporating $g_x = 5$, $g_y = 5$, and $g_z = 7 \times 10^{-1}$. The scaling factor for the evaluation of the initial regularization parameter λ_0 is set to $\gamma = 10$. The reference model is given by a three layer model with conductivities of $1/160\,\frac{\text{S}}{\text{m}}$, $1/55\,\frac{\text{S}}{\text{m}}$ and $1/42\,\frac{\text{S}}{\text{m}}$ and layer thickness for the first two layers of 15 m and 45 m. A maximum number of 10 Gauss-Newton iteration steps is allowed. Although, a noticeable effect of displacement currents might occur only at the highest frequency (cf. section 3.7), a homogeneous relative permittivity of $\boldsymbol{\epsilon}_r = \mathbf{1}_S$ is assumed.

The very dense distribution of RX positions along the profiles hypothesizes a remarkable redundancy of information. In fact, inversions of different data subsets have shown that even a homogeneous reduction to 20 % of the data points leads to an identical parameter model compared to the model that is obtained for all 10 126 TX/RX positions. Hence, only $N = 2032$ observations are incorporated which tremendously reduces the required runtime and peak memory usage per outer iteration and therefore allows to rather increase the grid refinement.

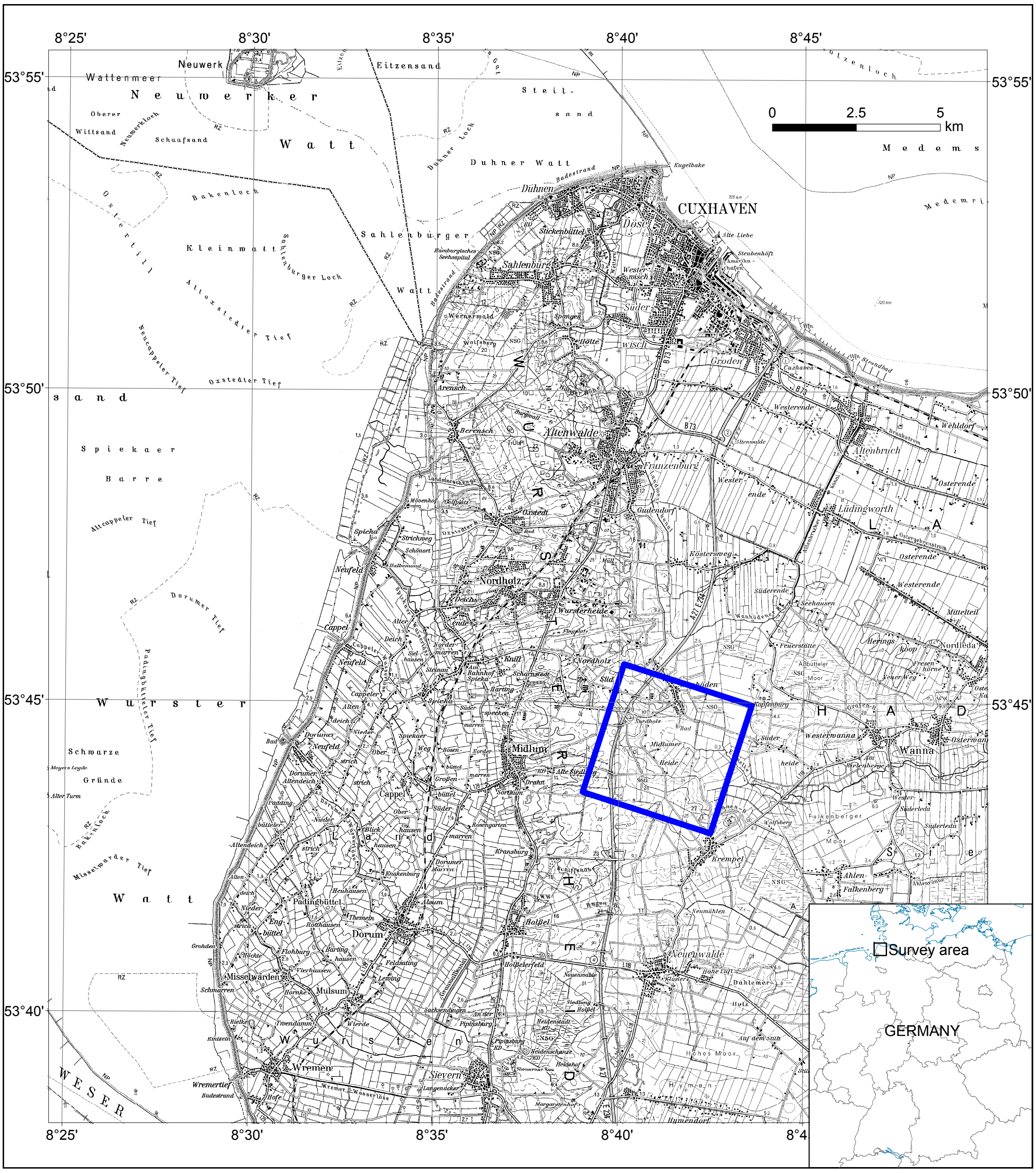

Figure 5.6: Location of the HEM survey, about 12 km south of the city of Cuxhaven. The blue square indicates the horizontal boundary of the active region of the inverse problem.
Source: Adapted from Angelika Ullmann, Leibniz Institute for Applied Geophysics (Ullmann, Scheunert, et al. 2015)

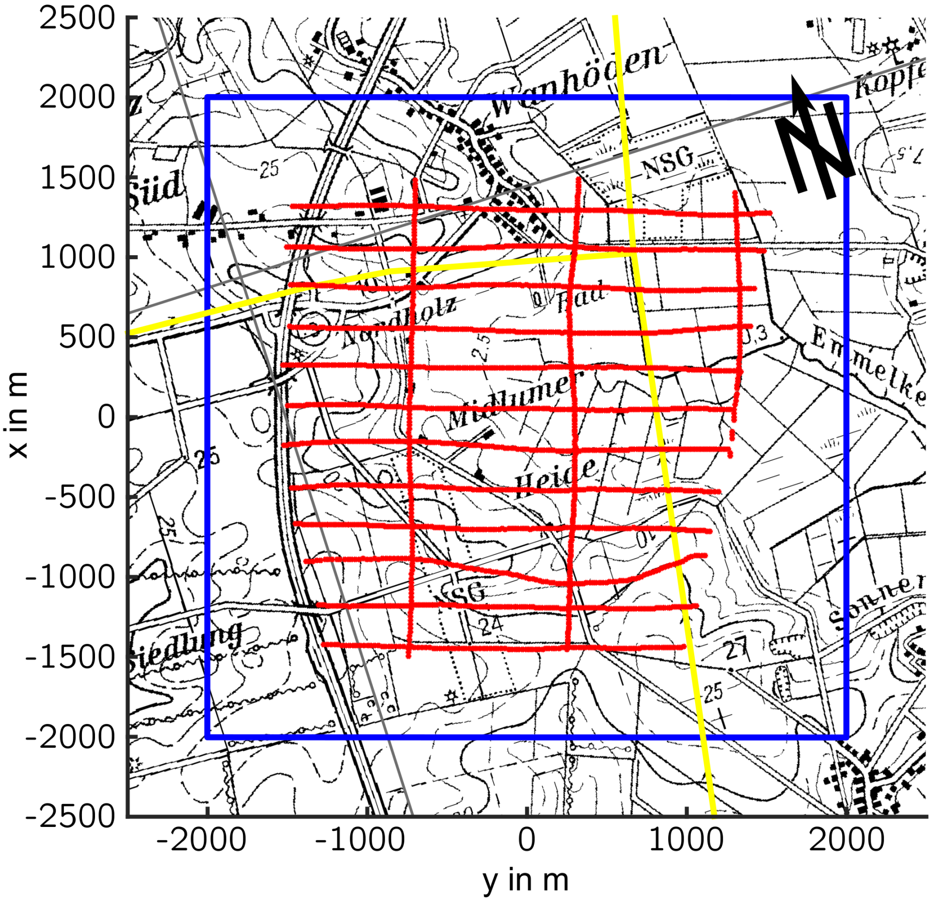

Figure 5.7: Location of the 15 survey profiles (red dots) within the active region (blue square). The yellow lines indicate the pathway of two power supply lines of the national grid.
Source: Adapted from Angelika Ullmann, Leibniz Institute for Applied Geophysics (Ullmann, Scheunert, et al. 2015)

Thus, potential discretization errors can be attenuated. The dependency of the computational effort on the number of TX/RX positions, as stated out in table 5.1, shows an approximately linear behavior. The respective calculations are carried out on the above described model domain and active region, but are based on a computational grid comprising only $S = 65\,340$ cells ($K = 183\,495$ DOF) and $M = 45\,056$ unknown model parameters.

The automatic termination approach suggests stopping at the seventh iteration (cf. fig. 5.9). For that a rather noisy parameter distribution for the topmost layers of the parameter grid is obtained. Hence, the final parameter model is chosen from the fifth Gauss-Newton iteration step by hand. It comprises the same distribution of conductive features but is more smooth due to the stronger influence of the regularization. For this early termination, a final relative data residual of 2×10^{-1} is achieved. Within further iteration steps a continuing decrease can be observed (cf. fig. 5.10) that results from the permanent attenuation of the regularization parameter.

For the entire Gauss-Newton iteration, a total runtime of 48.6 h and a peak memory usage of 279.8 GB is required. Thereby, the mean runtime for the solution of an entire forward problem (incorporating 4 frequencies and all 2032 RHS) amounts to about 7 h which represents 84 % of the single iteration runtime. In average, the LSQR method requires 208 inner steps where

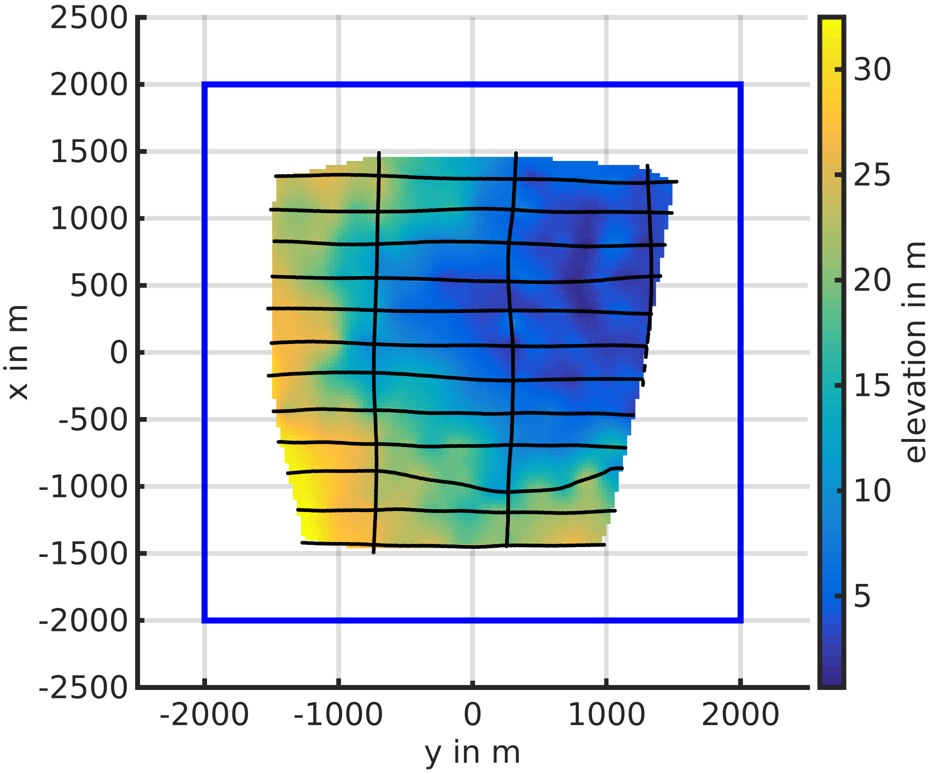

Figure 5.8: Survey profiles and the related earth surface elevation.

TX/RX positions	mean peak memory	mean iteration runtime
2032	59.7 GB	0.5 h
3380	90.6 GB	0.9 h
5067	148.5 GB	2.9 h
10126	277.2 GB	10 h

Table 5.1: Computational effort of a Gauss-Newton iteration evaluation with respect to the incorporated number of data points.

one step can be evaluated in only 12.1 s, exploiting the explicit Jacobian matrix. The primary field calculation takes 31.3 min.

The geological situation of the survey area is described in detail by Steinmetz et al. (2015). In general, a central tunnel valley structure with a high conductive sediment filling (particularly by clay in the uppermost parts) can be expected - a result of subglacial erosion processes. As it is not the aim of this study to elaborate on the geological plausibility of the inversion result, the validation of the obtained final parameter model is simply based on a comparative study. For that, results by Siemon, Eberle, et al. (2004), providing an apparent conductivity distribution with respect to a frequency-depending centroid depth, and Ullmann, Scheunert, et al. (2015), giving the five-layer solution of a 1-D laterally constrained inversion as introduced by Siemon, Auken, et al. (2009) are used. Since the 1-D results are obtained only at the TX/RX locations, they are horizontally interpolated on a grid with node spacings of 50 m in both directions. The solution of the 1-D inversion can be obtained in less than half an hour.

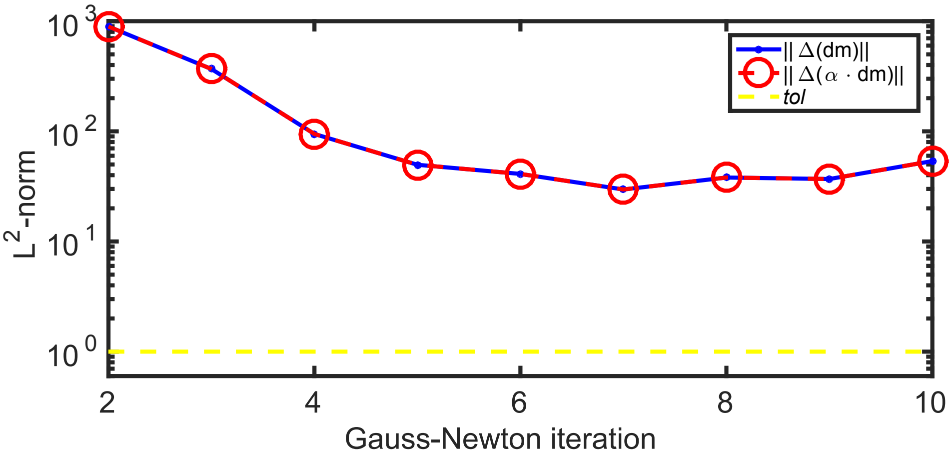

Figure 5.9: Difference between the previous and current model update, associated with the iteration number of the latter.

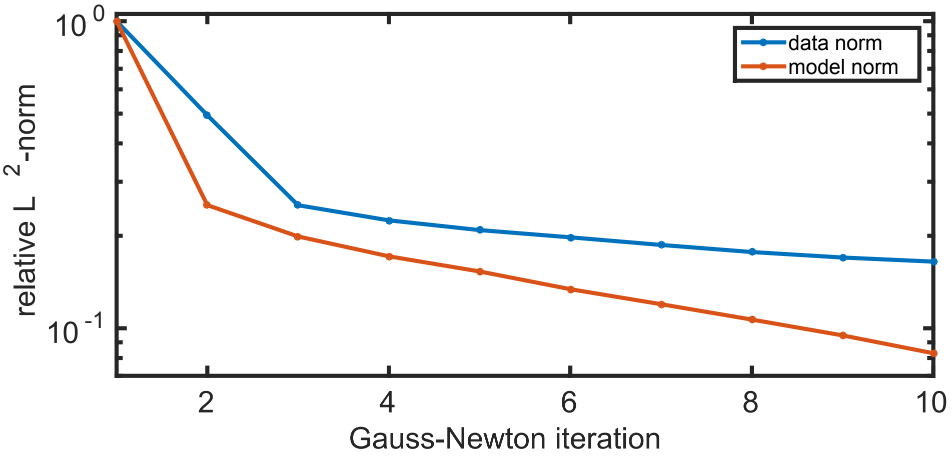

Figure 5.10: Convergence of the data misfit (blue curve) and the model roughness norm (green curve). Both norms are normalized to their initial value.

The horizontal parameter distributions near the earth' surface for the final 1-D and 3-D inversion results are illustrated fig. 5.11. The graphs are associated with the local coordinate system that is additionally restricted to the survey area extent. The solutions are marked by low conductivities, particularly in the areas of high elevation. This behavior disagrees with the assumption that in the inversion of HEM data, hills are typically related with positive anomalies (Jiracek 1990; Beard 2000). Therefore, those low conductive areas are considered not to result from topographic effects. A more likely explanation is a resistive coverage by sands and coarse-grained sediments (Siemon, Eberle, et al. 2004; Steinmetz et al. 2015). Although the data is already corrected for surface effects by various preprocessing, both solutions contain areas of high conductivity in the vicinity of the power supply lines.

As a by-product of the low conductivity beneath the surface, the sensitivity footprint is localized to the proximity of the TX/RX positions. Hence, the 3-D inversion result bares characteristic traces along the profile lines and areas in between which mainly rest on the reference model. This effect diminishes with the higher conductivity at increasing depth (cf. figs. 5.12 to 5.15) and therefore motivates to incorporate a model parameter depending weighting factor that varies according to the depth z of the cell midpoints.

Figures 5.12 to 5.15 show the 1-D and 3-D inversion results as well as the apparent conductivity[1] distribution for the four measured frequencies[2]. All three solutions are associated with a respective mean *centroid depth* (Sengpiel 1988; Siemon 2001) at which the apparent conductivities are related to. Minor artifacts at the survey margins can be ascribed to interpolation errors. A good overall agreement of the apparent conductivity distribution with the 3-D inversion result can be obtained for all four depths. Particularly, the conductive valley structure that rejuvenates with increasing depth is reconstructed in all three solutions. Following Steinmetz et al. (2015), a lower conductivity within the valley structure compared to the surrounding area (at a depth of $z = 90\,\mathrm{m}$), as predicted by the 1-D inversion, cannot be expected. Here, a more reasonable image is given by the solution of the 3-D inversion.

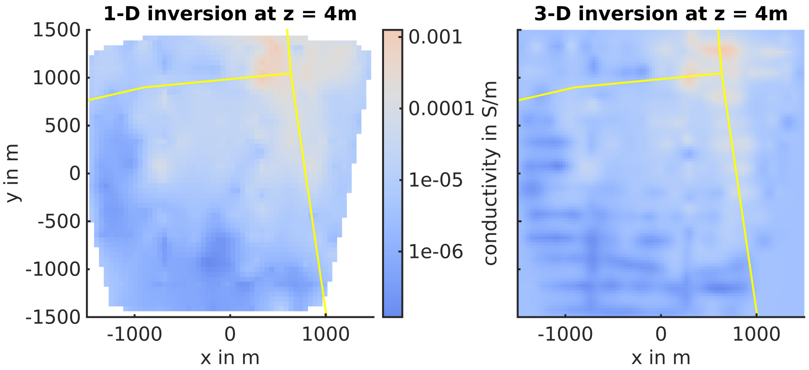

Figure 5.11: 1-D and 3-D inversion results for a horizontal slice, tight beneath the earth surface. The yellow lines indicate the pathways of two power supply lines.

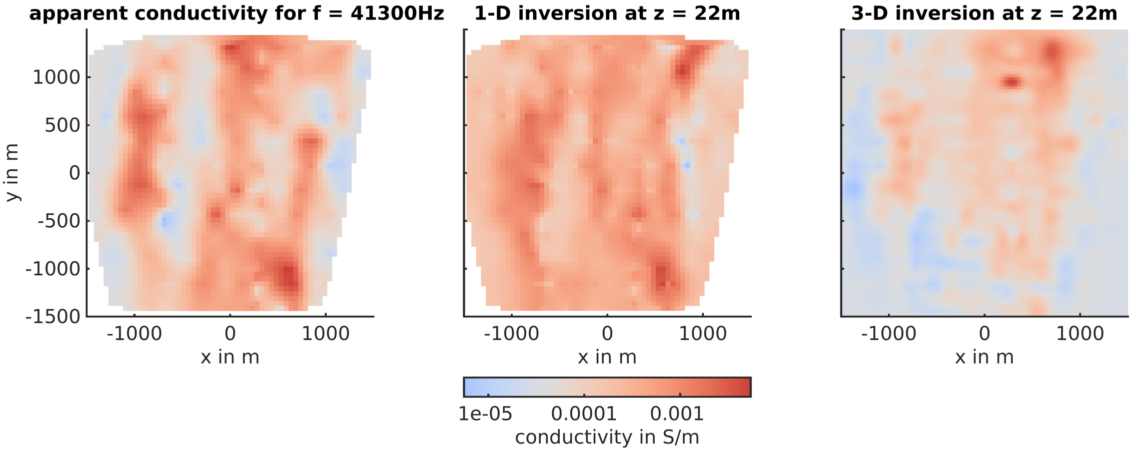

Figure 5.12: Apparent conductivity distribution and the 1-D and 3-D inversion results at a depth of $z = 22\,\mathrm{m}$.

---

[1] The conductivity of an equivalent half-space which leads to the same (frequency-depending) data at the observation point (Spies and Frischknecht 1991).

[2] The apparent conductivity is horizontally interpolated on the grid that is used for the results of the 1-D inversion.

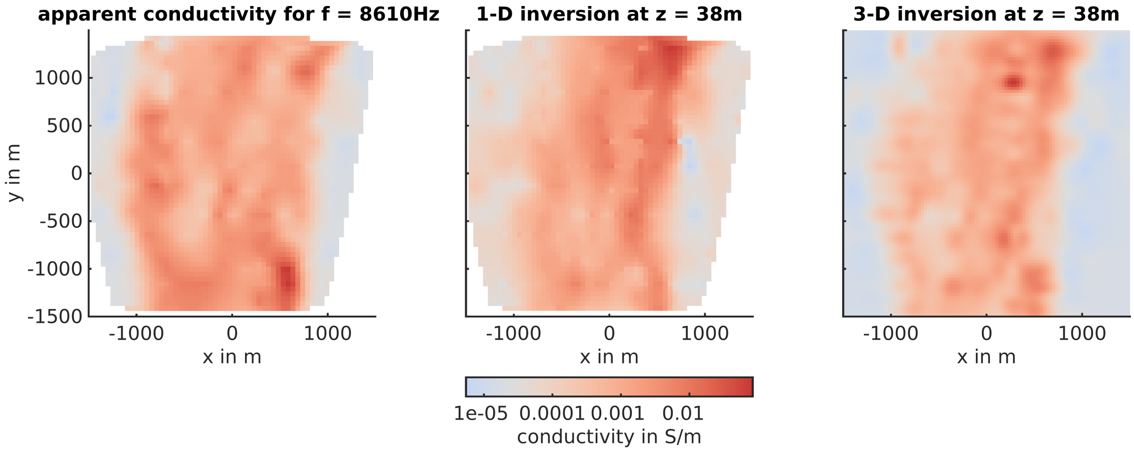

Figure 5.13: Apparent conductivity distribution and the 1-D and 3-D inversion results at a depth of $z = 38\,\mathrm{m}$.

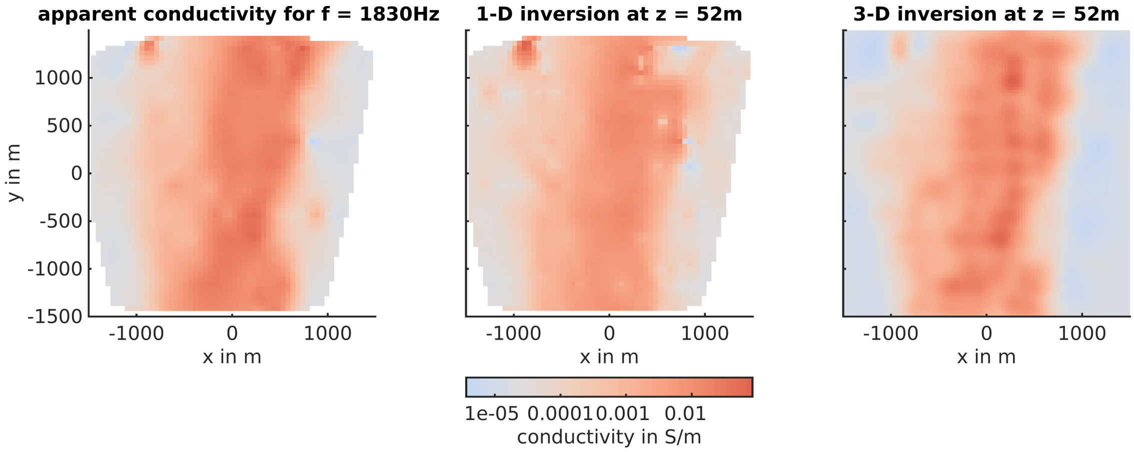

Figure 5.14: Apparent conductivity distribution and the 1-D and 3-D inversion results at a depth of $z = 52\,\mathrm{m}$.

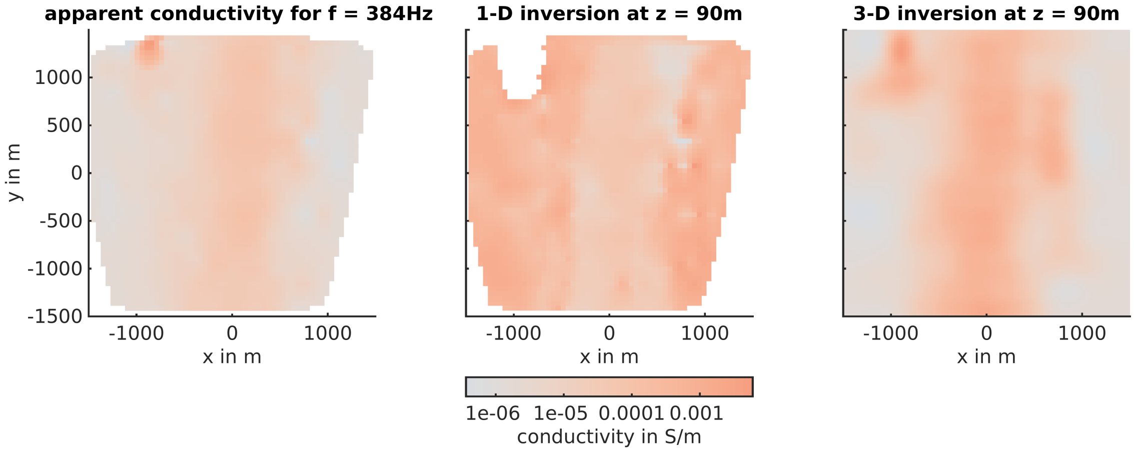

Figure 5.15: Apparent conductivity distribution and the 1-D and 3-D inversion results at a depth of $z = 90\,\mathrm{m}$.

In the following, the 3-D solution is compared to the 1-D results for a convincing subset of the survey profiles as shown in figs. 5.16 to 5.22, to visualize vertical cross sections of the parameter models. The series of vertical slices in the figures' part a) show the conductivity distributions beneath their respective TX/RX positions (black lines). These cross sections are projected onto the mean value of the coordinate, perpendicular to the profiles' directions. The 1-D and 3-D solutions are shifted in z-direction at each observation point according to the measured altitude. Additionally, the respective relative error between the observed data and the response of the final parameter model is shown in part b) of the figures.

It is found that for the vertical conductivity distribution, a good compliance of the 1-D and 3-D inversion results can be obtained. The comparatively high conductivity in the deeper areas of the 3-D solution result from the early termination of the Gauss-Newton iteration. Due to the strong impact of the regularization term on the parameter model within the first iteration steps, the conductivity distribution in the areas of low sensitivity (typically at increasing depths) is mostly influenced by the high conductivities in the reference model.

Typical artifacts in the 1-D solutions that arise from high conductive surface anomalies are often characterized by symmetric "flags" in the deeper areas of the sections. Those can be observed in fig. 5.16a at $x = 1300\,\mathrm{m}$, in fig. 5.19a at $y = -1100\,\mathrm{m}$, $400\,\mathrm{m}$ and $800\,\mathrm{m}$, in fig. 5.21a at $y = 750\,\mathrm{m}$, and in fig. 5.22a at $y = -900\,\mathrm{m}$. Because of the whole survey information being included in the 3-D inversion simultaneously, the algorithm can be expected to act much more robust on those data contamination. The higher stability of the 3-D inversion can clearly be recognized in the respective figures since no flag-like artifacts can be observed. Typically, the relative error between observed and synthetic data becomes quite large at the respective receiver positions (cf. part b) of the figures). Disturbances due to the power supply lines are the reason for high errors occurring at the profiles, striking out in the y-direction between $y = 500\,\mathrm{m}$ to $1000\,\mathrm{m}$ and for the profiles, striking out in the x-direction between $x = 900\,\mathrm{m}$ to $1000\,\mathrm{m}$.

The origin of discretization errors in the numerical solution of the forward problem becomes visible in the relative error for the frequencies greater than $f = 1830\,\mathrm{Hz}$: noticeable oscillations with a short wave wavelength indicate that an additional grid refinement is required to handle the secondary sources, caused by the conductivity gradient that results from the deviation of the parameter model from the reference model, particularly in the uppermost layers of the active region.

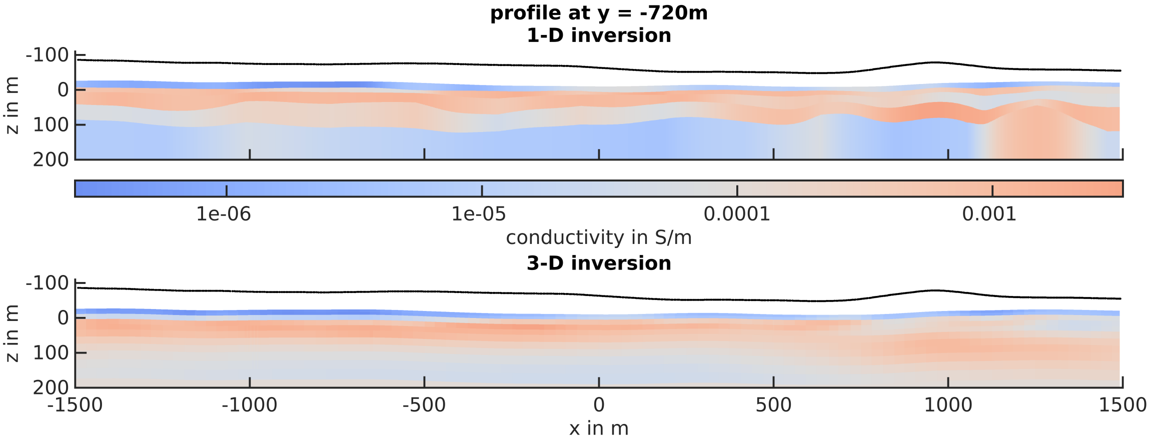

(a)

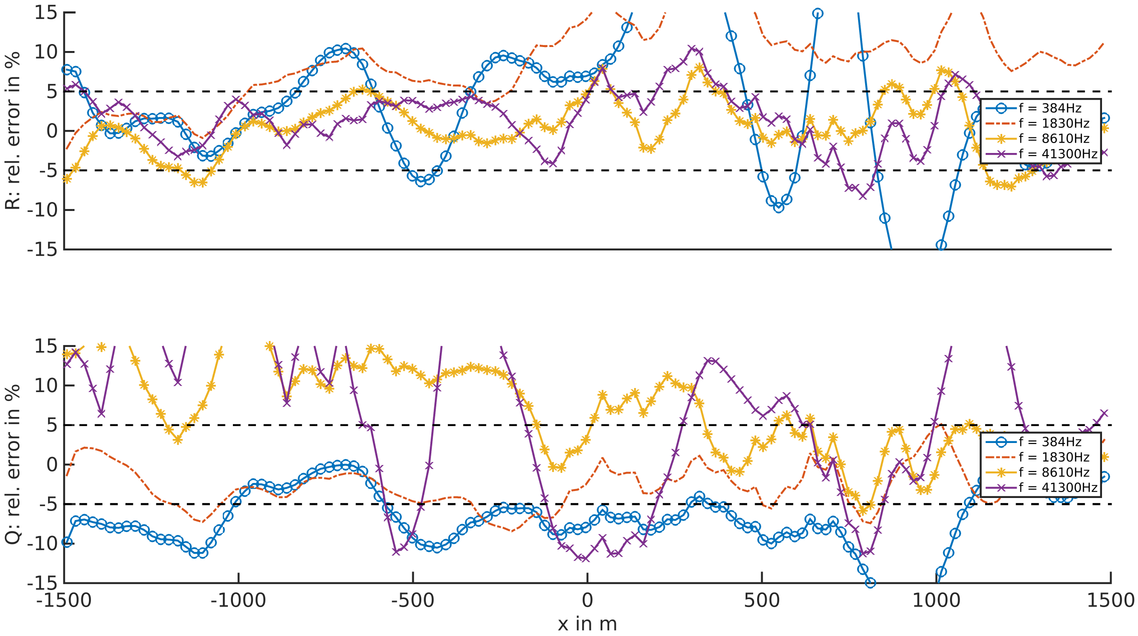

(b)

Figure 5.16: Inversion results for the profile in x-direction, approximately located at $y = -720\,\text{m}$.
a) Vertical section of the solution of the 1-D and 3-D inversion.
b) Relative error of the real (upper) and imaginary (lower) part between the observed data and the synthetic data, generated from the final 3-D inversion parameter model.

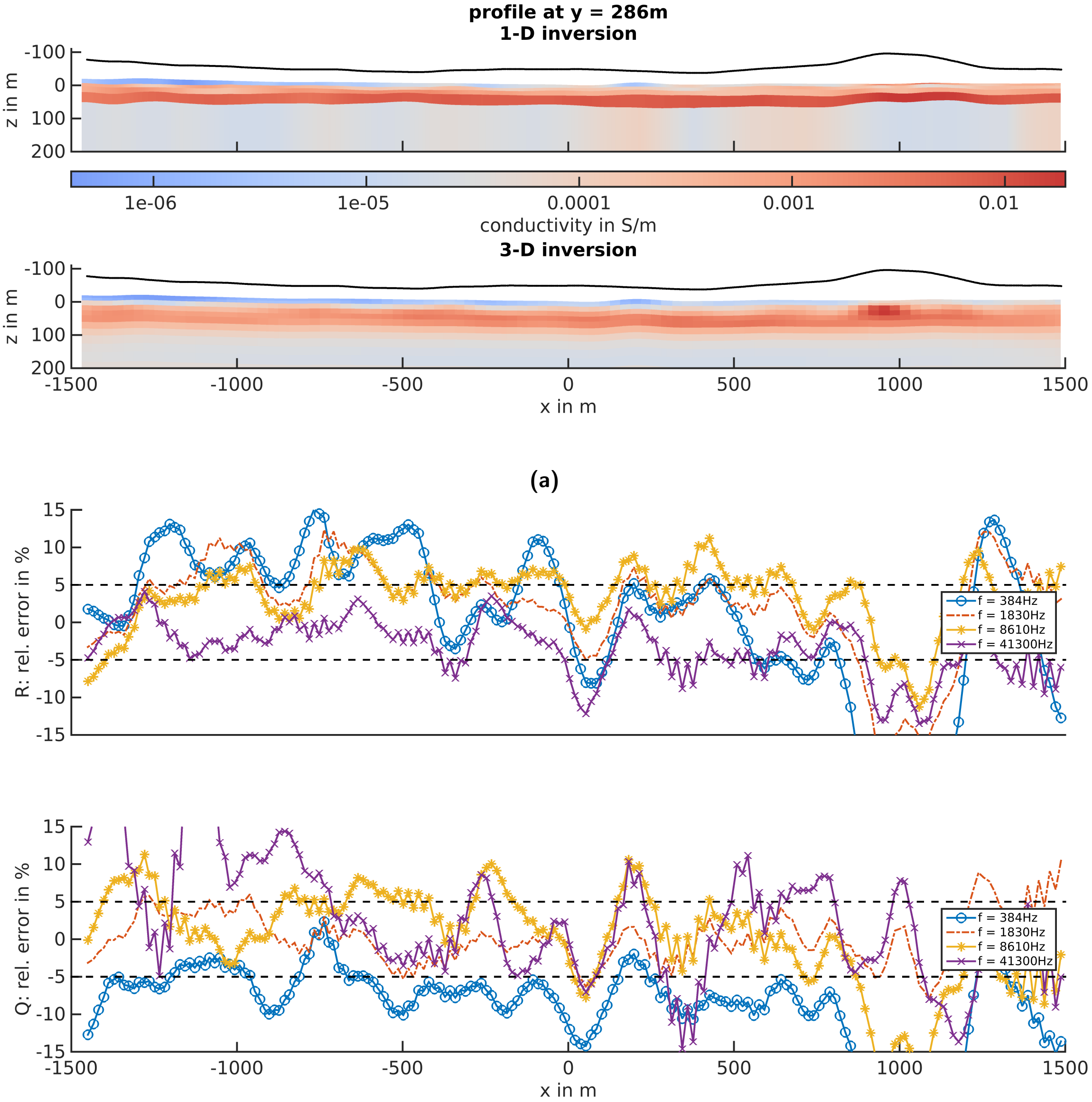

(a)

(b)

Figure 5.17: Inversion results for the profile in x-direction, approximately located at $y = 286\,\mathrm{m}$.
a) Vertical section of the solution of the 1-D and 3-D inversion.
b) Relative error of the real (upper) and imaginary (lower) part between the observed data and the synthetic data, generated from the final 3-D inversion parameter model.

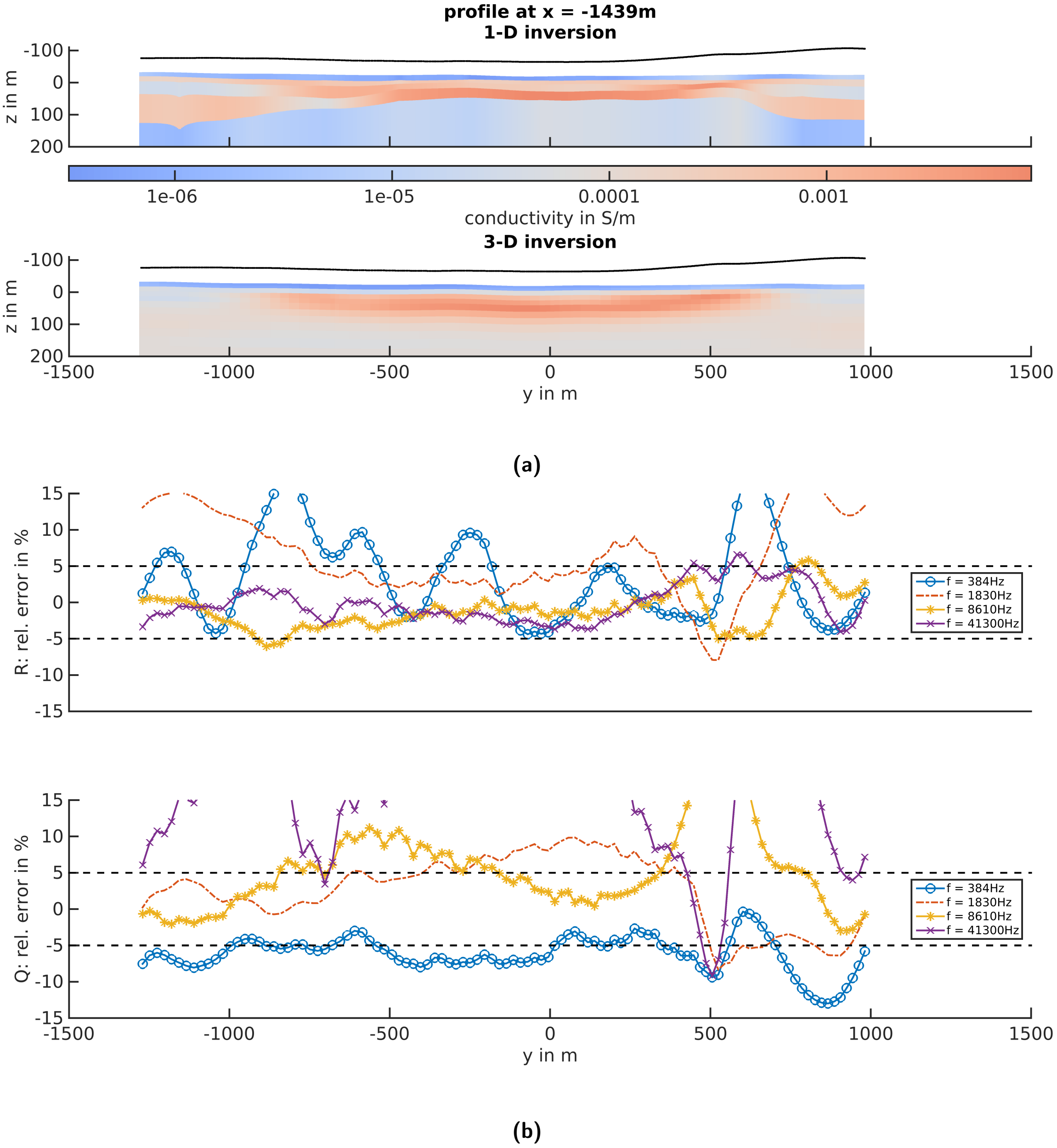

Figure 5.18: Inversion results for the profile in y-direction, approximately located at $x = -1439\,\mathrm{m}$.
a) Vertical section of the solution of the 1-D and 3-D inversion.
b) Relative error of the real (upper) and imaginary (lower) part between the observed data and the synthetic data, generated from the final 3-D inversion parameter model.

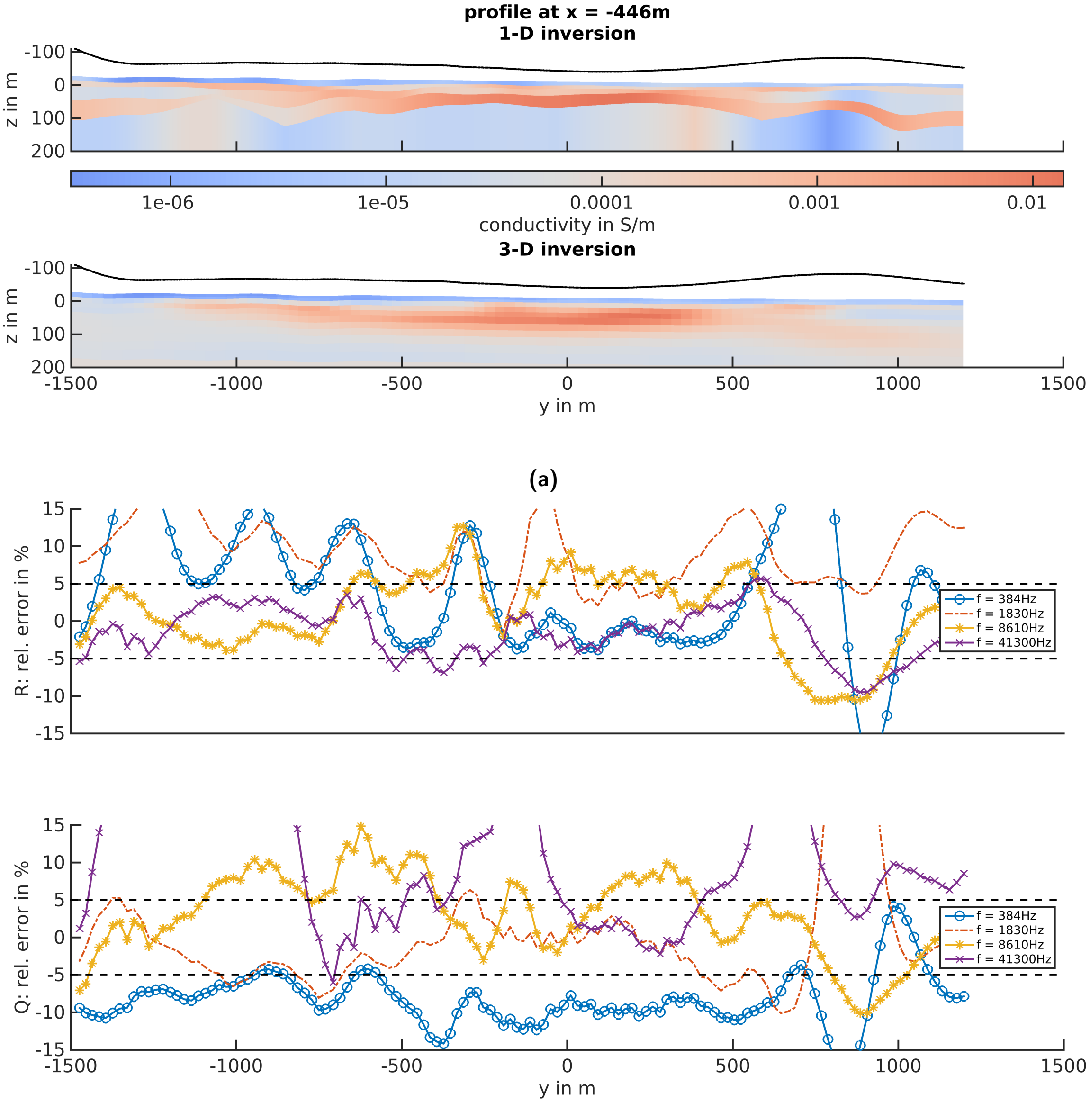

(a)

(b)

Figure 5.19: Inversion results for the profile in y-direction, approximately located at $x = -446\,\mathrm{m}$.
a) Vertical section of the solution of the 1-D and 3-D inversion.
b) Relative error of the real (upper) and imaginary (lower) part between the observed data and the synthetic data, generated from the final 3-D inversion parameter model.

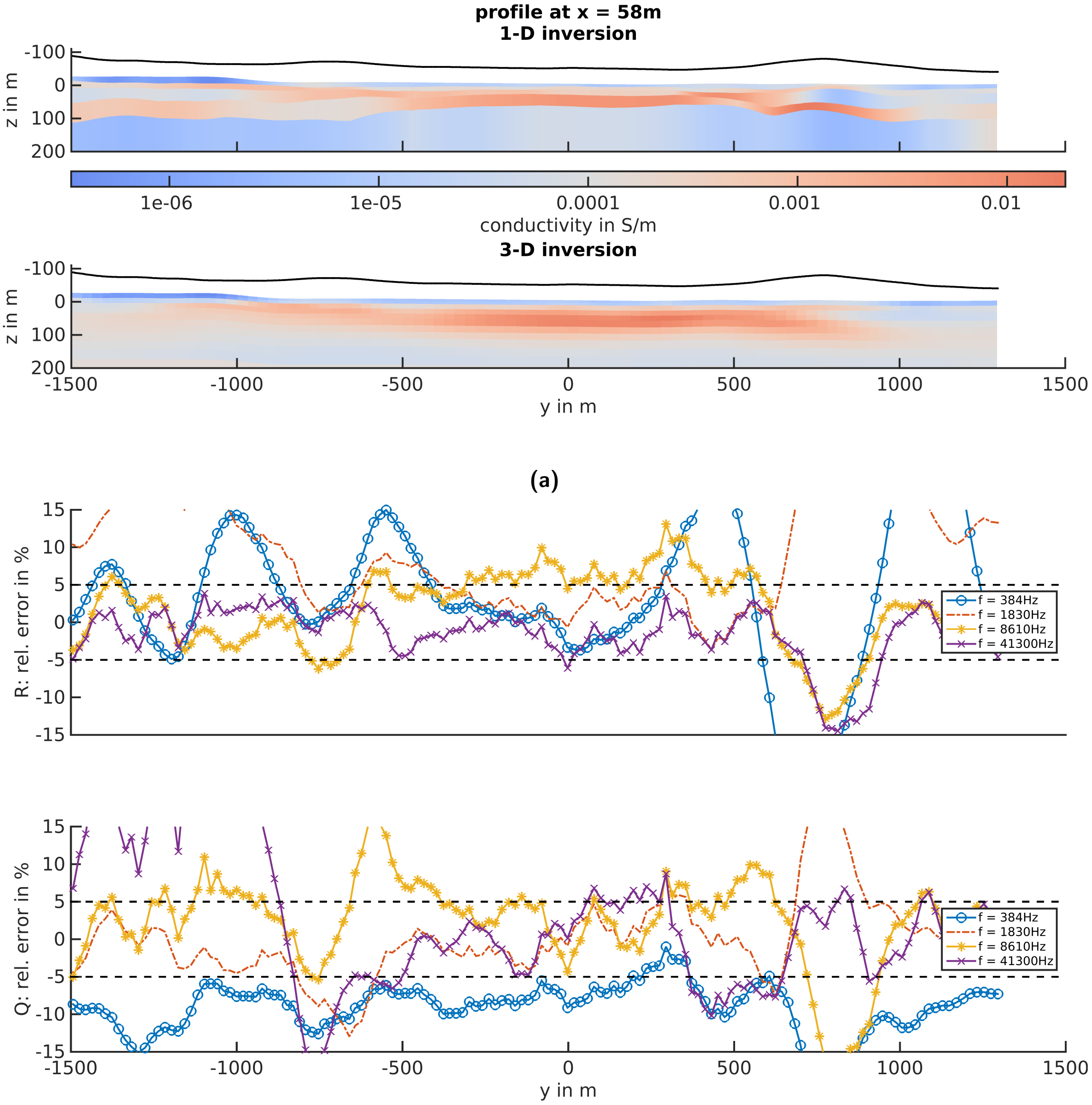

(a)

(b)

Figure 5.20: Inversion results for the profile in y-direction, approximately located at $x = 58\,\mathrm{m}$.
a) Vertical section of the solution of the 1-D and 3-D inversion.
b) Relative error of the real (upper) and imaginary (lower) part between the observed data and the synthetic data, generated from the final 3-D inversion parameter model.

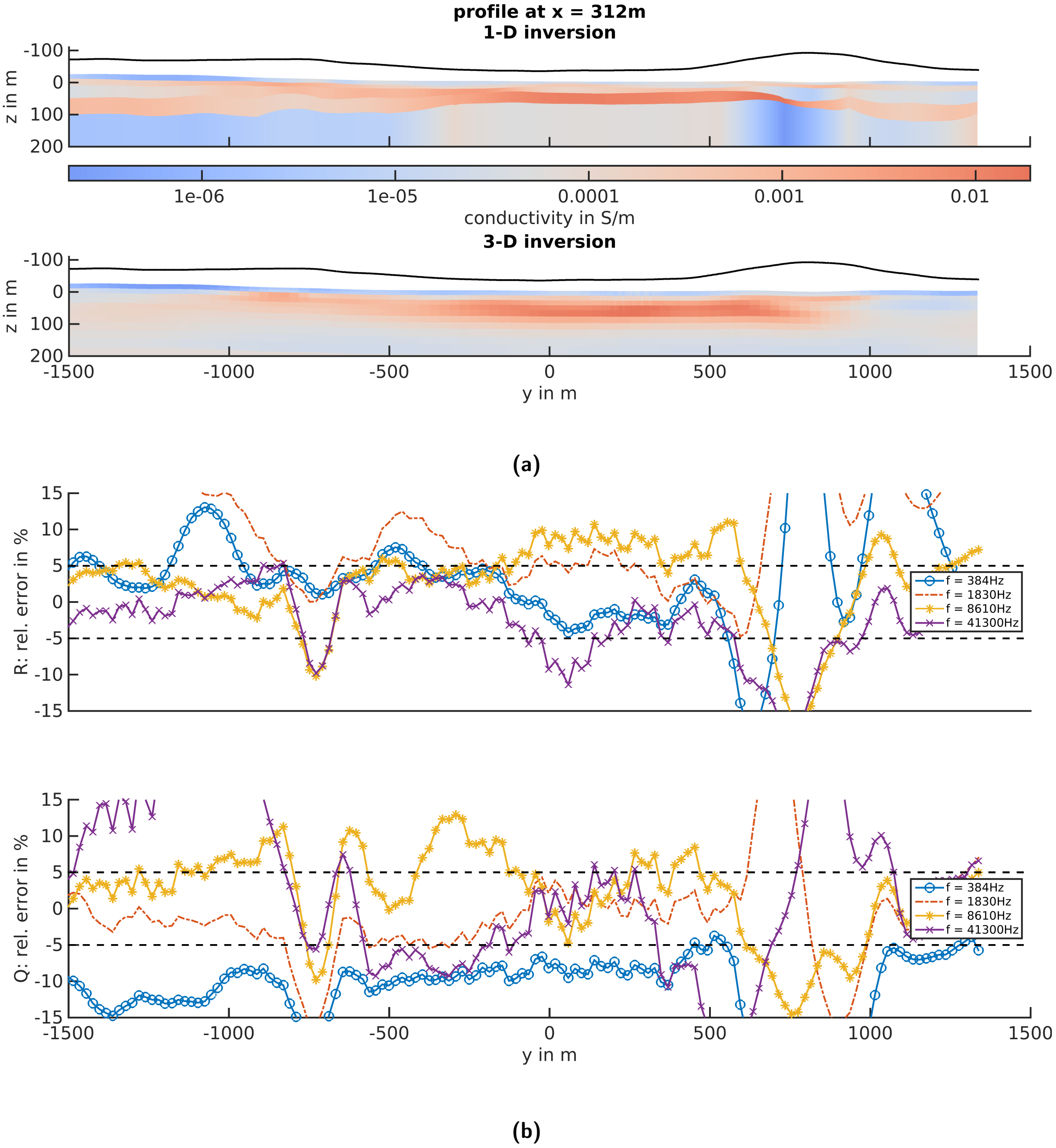

Figure 5.21: Inversion results for the profile in y-direction, approximately located at $x = 312\,\mathrm{m}$.
a) Vertical section of the solution of the 1-D and 3-D inversion.
b) Relative error of the real (upper) and imaginary (lower) part between the observed data and the synthetic data, generated from the final 3-D inversion parameter model.

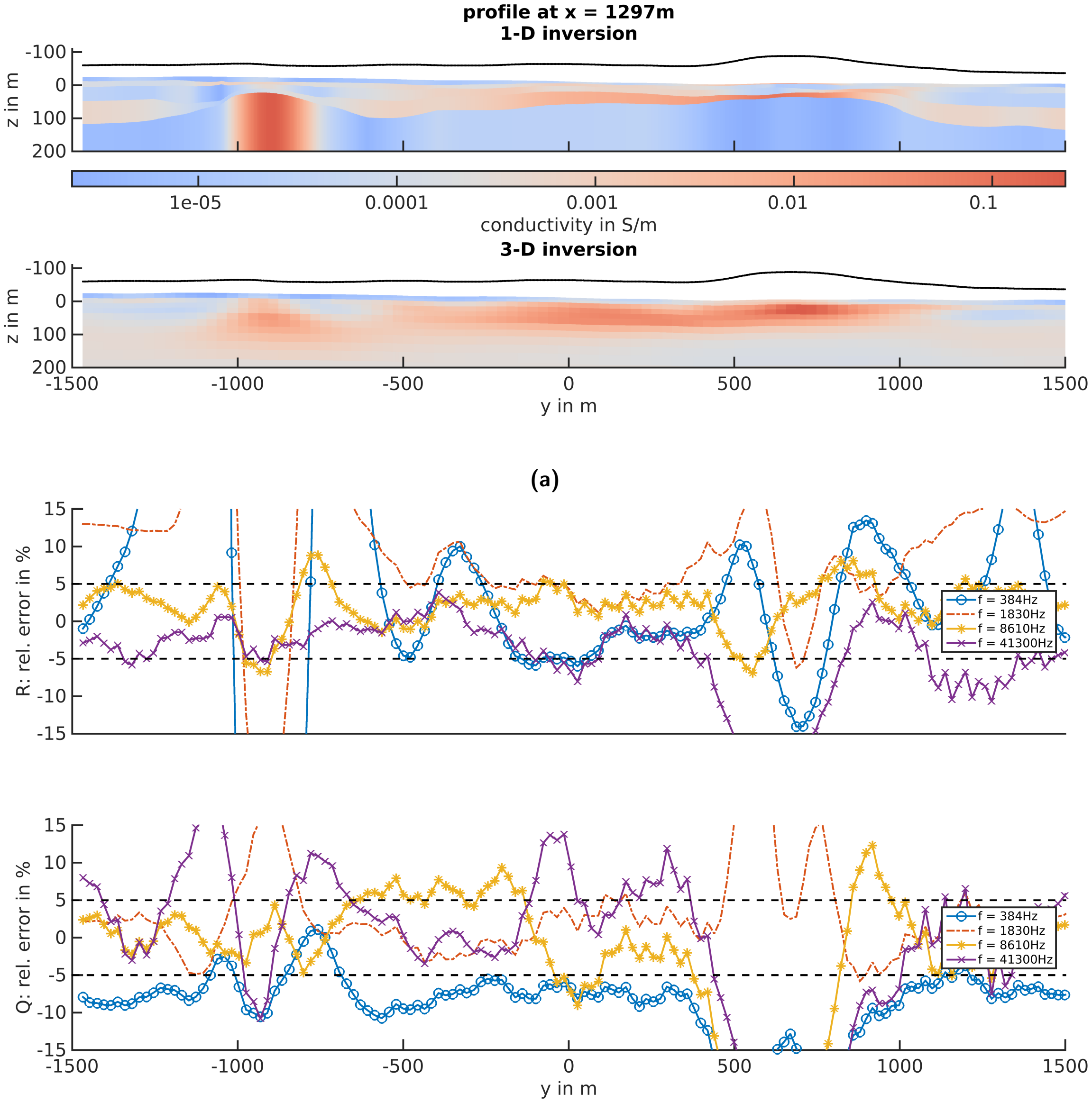

(a)

(b)

Figure 5.22: Inversion results for the profile in y-direction, approximately located at $x = 1297\,\mathrm{m}$.
a) Vertical section of the solution of the 1-D and 3-D inversion.
b) Relative error of the real (upper) and imaginary (lower) part between the observed data and the synthetic data, generated from the final 3-D inversion parameter model.

6 Summary

In this study, a full 3-D inversion algorithm is presented that is designed to be part of the cut-&-paste inversion concept. The primary motivation for the development of the introduced algorithm was the analysis of a number of HEM field surveys in the Northern German Lowlands, which were conducted to investigate the ground water distribution in the soil. Since this area exhibits only weak topography, a flat earth is assumed in the inversion concept. The 3-D cut-&-paste strategy presents a trade-off between accuracy and calculation speed: although slower than a purely 1-D treatment, a significant reduction in computing costs is achieved by omitting large areas in the 3-D numerical analysis and only focusing on the relevant area.

The thesis intends to highlight the theoretical background of the underlying finite difference forward operator as well as the constitutive inversion building blocks. The derivation of the analytic solution of the 1-D problem is given which is embedded in the numerical solution of the 3-D problem by exploiting the secondary field approach. Here, the analytical primary field calculation benefits from an interpolation approach which allows the effective handling of a huge number of sources without a significant loss of accuracy. A tensor-based problem formulation is introduced that is able to alleviate the description and implementation of the inversion problem and which allows an effective reassembling of the forward problem. Furthermore, an adapted description of the measurement operator, used to obtain arbitrary located synthetic data from the spatial fixed positions of the degrees of freedom, with respect to the block structure of the multiple sources is given.

The inverse problem is solved, exploiting the well-known Gauss-Newton approach and incorporating a Tikhonov-type regularization scheme. An explicit representation of the Jacobian matrix is illustrated which is regarded as crucial for the HEM data inversion and which benefits from the application of a direct solver strategy. Multiple multiplications with the explicit Jacobian matrix require nearly no additional computational effort and, thus, allow to omit the costly preconditioning for the Krylov-subspace methods that are used to solve the inherent least-squares problems. Beside implicit regularization approaches which aim at improving the inverse problem underdetermination by a reduction of the number of model parameters, a convenient explicit regularization set up for the practical inversion is presented. The latter exploits spatial derivative operators that are already provided by the discretization of the forward problem. Since the heterogeneity of the spatial data distribution may lead to artifacts within the inversion result, a counterbalancing is achieved by exploiting a directional weighting of the regularization operators. An initial regularization parameter is derived from the ratio of the data misfit and model roughness norm with a minimum of additional computational effort.

The fundamental functionality of the inversion concept is demonstrated, using a synthetic model and the above mentioned HEM field data. Thereby, the high redundancy within the field data enables to rigorously reduce the number of RHS without noticeably influencing the inversion result. The comparison of the field data inversion result with the solution of a common 1-D inversion approach shows an overall good agreement and hypothesizes the higher stability of the presented 3-D inversion algorithm.

For the future, the incorporation of a finite element forward operator which allows for topographical effects and, thus, facilitates the application of the 3-D inversion algorithm for arbitrary regions is envisioned. Since the neglect of the underground magnetic properties is a poor approximation for many measurement areas, such as for iron ore deposits, the variation of the magnetic permeability has to be included in future works of more general validity. Furthermore, the implementation of complex regularization strategies, such as the total variation approach, additional investigations concerning the choice of the regularization parameter, and the definition of a convenient terminating condition are under consideration.

7 Acknowledgements

Main parts of the research have been carried out in the AIDA and Multi-EM project funded by the German Ministry of Education and Research (BMBF) under the Geotechnologien Programm, grants 03G0735D and 037G0746B. Furthermore, the work has been funded by the Helmholtz Institute Freiberg for Resource Technology and the TU Bergakademie Freiberg.

Parts of the thesis are incorporated in the publication "‘Cut-&-Paste 3-D Inversion of Helicopter-borne Electromagnetic Data – I. 3-D Inversion Using the Explicit Jacobian and a Tensor-based Formulation"’ which was submitted to the Journal of Applied Geophysics in 2015 (currently in revised status).

Last but not least I would like to say “thank you” to all of the people that make the realization of this work possible. In the first place I want to express my deeply gratitude to Martin Afanasjew who was on hand with help and advice at any time during my PhD phase and who significantly advanced our projects with his programming skills. I am very thankful to Ralph-Uwe Börner, Mario Helm, Gunther Scheunert, and Saskia Stein for reading my drafts, pointing out mistakes, and helping me to overcome the pitfalls of the English language. Many thanks go to Bernhard Siemon and Angelika Ullmann for providing the 3-D modeling and 1-D inversion results I used for the comparisons. Many ideas were born and a lot of problems could be solved during the discussions with the members of our interdisciplinary working group, with the doctoral candidates of our institute and the project partners of AIDA and Multi-EM. Therefore, I am particularly grateful to Martin Afanasjew, Ralph-Uwe Börner, Felix Eckhofer, Michael Eiermann, Oliver Ernst, Antje Franke-Börner, Olaf Hellwig, Mario Helm, Maik Linke, Stephan Malecki, Marko Riedel, Bernhard Siemon, Klaus Spitzer, Saskia Stein, Angelika Ullmann, Feiyan Wang, Julia Weißflog, and Wenke Wilhelms. I would like to thank Klaus Spitzer for his supervising, as well as Esben Auken for his agreement to review my thesis. Since nothing would be possible without the sufficient amount of motivation, I highly appreciate every spoken word of encouragement and the patience of my wife Maria, the daily “Mensarunde”, and the “Tabakskollegium zu Stollberg”

A Finite difference scheme

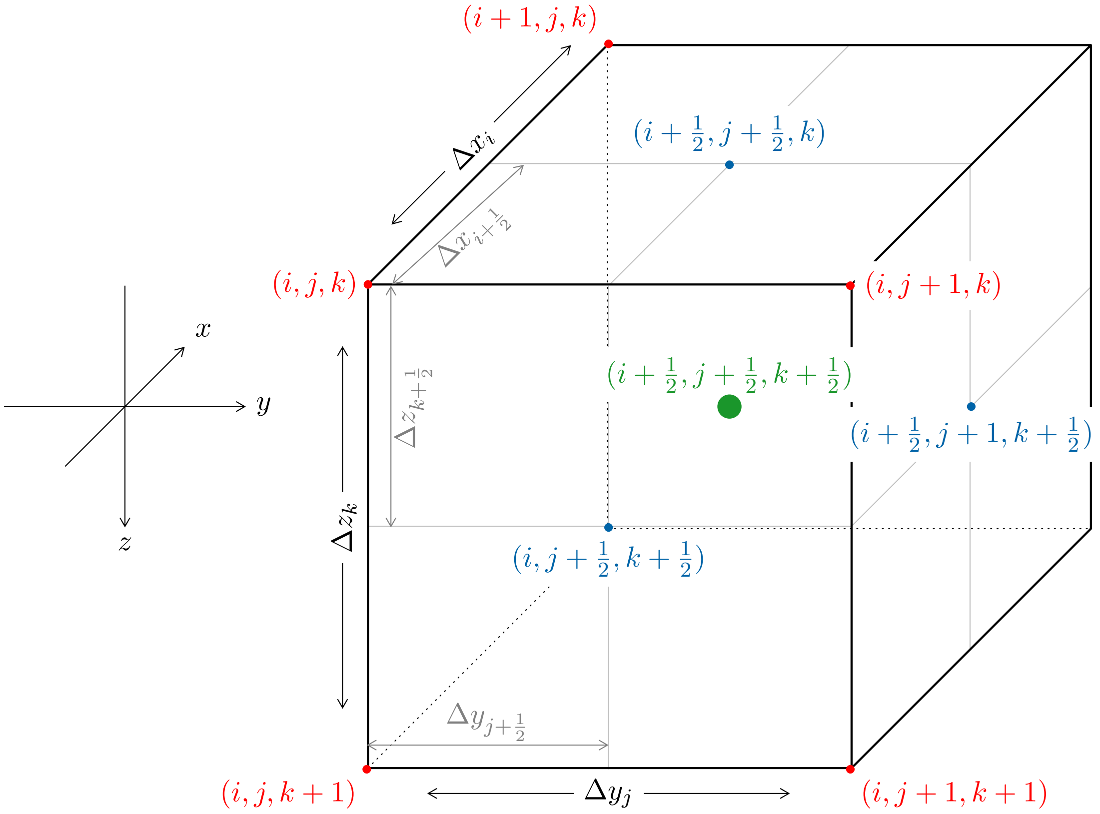

Figure A.1: Grid spacings defined on a tensor-product grid.

The grid spacings of to the underlying tensor-product grid, defined as shown in fig. A.1, are related to a right-handed Cartesian coordinate system with a downwards oriented z-axis. The indices

$$\begin{aligned} i &\rightarrow x_i, & i &= 1, \ldots, n_x + 1, \\ j &\rightarrow y_j, & j &= 1, \ldots, n_y + 1, \\ k &\rightarrow z_k, & k &= 1, \ldots, n_z + 1, \end{aligned} \tag{A.1}$$

describe the node positions with respect to the three coordinate directions. The cell midpoints are defined at $(i+\frac{1}{2}, j+\frac{1}{2}, k+\frac{1}{2})$. The variables

$$\begin{aligned} \Delta x_i &= x_{i+1} - x_i, & \Delta \boldsymbol{x} &= [\Delta x_i]_{1 \le i \le n_x}, \\ \Delta y_j &= y_{j+1} - y_j, & \Delta \boldsymbol{y} &= [\Delta y_j]_{1 \le j \le n_y}, \\ \Delta z_k &= z_{k+1} - z_k, & \Delta \boldsymbol{z} &= [\Delta z_k]_{1 \le k \le n_z}, \end{aligned} \tag{A.2}$$

denote the node distances in the x-, y-, and z-direction, respectively. Furthermore, the indices

$$\begin{aligned}
& & \Delta x_{i+\frac{1}{2}} &= \frac{x_{i+1}-x_i}{2}, & & \\
i+\tfrac{1}{2} &\quad\rightarrow & x_{i+\frac{1}{2}} &= x_i + \Delta x_{i+\frac{1}{2}}, & i &= 1,\dots,n_x, \\
& & \Delta y_{j+\frac{1}{2}} &= \frac{y_{j+1}-y_j}{2}, & & \\
j+\tfrac{1}{2} &\quad\rightarrow & y_{j+\frac{1}{2}} &= y_j + \Delta y_{j+\frac{1}{2}}, & j &= 1,\dots,n_y, \\
& & \Delta z_{k+\frac{1}{2}} &= \frac{z_{k+1}-z_k}{2}, & & \\
k+\tfrac{1}{2} &\quad\rightarrow & z_{k+\frac{1}{2}} &= z_k + \Delta z_{k+\frac{1}{2}}, & k &= 1,\dots,n_k,
\end{aligned} \tag{A.3}$$

are used to describe the spacings and positions of the half step sizes. Additionally,

$$\begin{aligned}
\Delta\hat{x}_i &= \Delta x_{i+\frac{1}{2}} + \Delta x_{i+\frac{3}{2}}, & \Delta\hat{\boldsymbol{x}} &= \left[\Delta\hat{x}_i\right]_{1\le i\le n_x-1}, \\
\Delta\hat{y}_j &= \Delta y_{j+\frac{1}{2}} + \Delta y_{j+\frac{3}{2}}, & \Delta\hat{\boldsymbol{y}} &= \left[\Delta\hat{y}_j\right]_{1\le j\le n_y-1}, \\
\Delta\hat{z}_k &= \Delta z_{k+\frac{1}{2}} + \Delta z_{k+\frac{3}{2}}, & \Delta\hat{\boldsymbol{z}} &= \left[\Delta\hat{z}_k\right]_{1\le k\le n_z-1},
\end{aligned} \tag{A.4}$$

denote the distances between the resulting inner nodes. For clarification, the relations of the spacings and nodes are shown in fig. A.2, exemplarily for the x-direction.

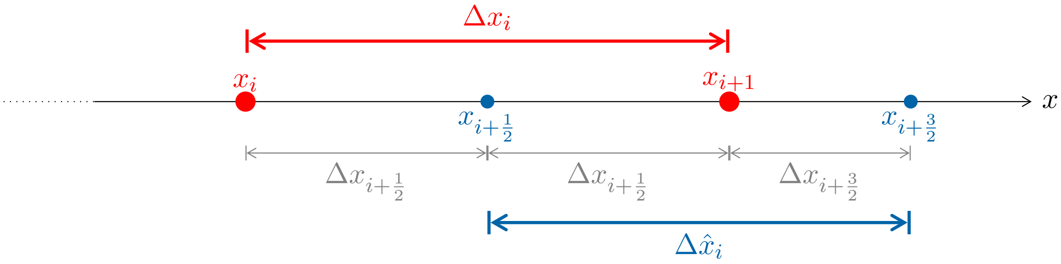

Figure A.2: Relation of grid spacings and node positions in the x-direction.

A.1 Ordering of the vector elements

For a lexicographic order, the solution vector $\boldsymbol{u} = \left[\boldsymbol{e}_x^\top, \boldsymbol{e}_y^\top, \boldsymbol{e}_z^\top\right]^\top \in \mathbb{C}^K$ with $\boldsymbol{e}_x \in \mathbb{C}^{K_x}$, $\boldsymbol{e}_y \in \mathbb{C}^{K_y}$, and $\boldsymbol{e}_z \in \mathbb{C}^{K_z}$, without elements on the boundary of the model domain, is composed of

$$\begin{aligned}
e_x(l_x) &= e_x(i+\tfrac{1}{2}, j+1, k+1), \\
&\quad i = 1,\dots,n_x;\ j = 1,\dots,n_y-1;\ k = 1,\dots,n_z-1, \\
&\quad l_x = i + (j-1)n_x + (k-1)n_x(n_y-1), \\
e_y(l_y) &= e_y(i+1, j+\tfrac{1}{2}, k+1), \\
&\quad i = 1,\dots,n_x-1;\ j = 1,\dots,n_y;\ k = 1,\dots,n_z-1, \\
&\quad l_y = i + (j-1)(n_x-1) + (k-1)(n_x-1)n_y, \\
e_z(l_z) &= e_z(i+1, j+1, k+\tfrac{1}{2}), \\
&\quad i = 1,\dots,n_x-1;\ j = 1,\dots,n_y-1;\ k = 1,\dots,n_z, \\
&\quad l_z = i + (j-1)(n_x-1) + (k-1)(n_x-1)(n_y-1),
\end{aligned} \tag{A.5}$$

where the l_x, l_y, l_z are *linear indices*, denoting the element numbers within $\boldsymbol{e}_x, \boldsymbol{e}_y, \boldsymbol{e}_z$ with respect to the appropriate variation of three coordinate indices i, j, k.

The components of the discrete magnetic field $\boldsymbol{h}^{\mathrm{d}} = \left[\boldsymbol{h}_x^\top, \boldsymbol{h}_y^\top, \boldsymbol{h}_z^\top\right]^\top \in \mathbb{C}^{K^h}$, with $\boldsymbol{h}_x \in \mathbb{C}^{K_x^h}$, $\boldsymbol{h}_y \in \mathbb{C}^{K_y^h}$, and $\boldsymbol{h}_z \in \mathbb{C}^{K_z^h}$, at the interior of the model domain are analogously given by

$$\begin{aligned}
h_x(l_x^h) &= h_x(i+1, j+\tfrac{1}{2}, k+\tfrac{1}{2}),\\
&\quad i = 1,\dots,n_x-1;\ j = 1,\dots,n_y;\ k = 1,\dots,n_z,\\
l_x^h &= i + (j-1)(n_x-1) + (k-1)(n_x-1)n_y,\\
h_y(l_y^h) &= h_y(i+\tfrac{1}{2}, j+1, k+\tfrac{1}{2}),\\
&\quad i = 1,\dots,n_x;\ j = 1,\dots,n_y-1;\ k = 1,\dots,n_z,\\
l_y^h &= i + (j-1)n_x + (k-1)n_x(n_y-1),\\
h_z(l_z^h) &= h_z(i+\tfrac{1}{2}, j+\tfrac{1}{2}, k+1),\\
&\quad i = 1,\dots,n_x;\ j = 1,\dots,n_y;\ k = 1,\dots,n_z-1,\\
l_z^h &= i + (j-1)n_x + (k-1)n_x n_y.
\end{aligned} \tag{A.6}$$

The parameter vector of the piecewise constant cell conductivities $\boldsymbol{\sigma} \in \mathbb{R}^S$ is formed of

$$\begin{aligned}
\sigma(l_\sigma) &= \sigma(i+\tfrac{1}{2}, j+\tfrac{1}{2}, k+\tfrac{1}{2}),\\
&\quad i = 1,\dots,n_x;\ j = 1,\dots,n_y;\ k = 1,\dots,n_z,\\
l_\sigma &= i + (j-1)n_x + (k-1)n_x n_y.
\end{aligned} \tag{A.7}$$

If a variation of the electric permittivity is allowed, the definitions of $\boldsymbol{\epsilon}$ and $\boldsymbol{\sigma}$ coincide with each other.

A.2 Discretization of the curl operators

To set up $\nabla\times\boldsymbol{h}$ with the help of difference quotients, a component-wise assembling of the appropriate discretization

$$\boldsymbol{C}^h = \begin{bmatrix} \boldsymbol{C}^h_{x,x} & \boldsymbol{C}^h_{x,y} & \boldsymbol{C}^h_{x,z} \\ \boldsymbol{C}^h_{y,x} & \boldsymbol{C}^h_{y,y} & \boldsymbol{C}^h_{y,z} \\ \boldsymbol{C}^h_{z,x} & \boldsymbol{C}^h_{z,y} & \boldsymbol{C}^h_{z,z} \end{bmatrix} \in \mathbb{R}^{K\times K^h}, \tag{A.8}$$

with

$$\begin{aligned}
&\boldsymbol{C}^h_{x,x} \in \mathbb{R}^{K_x\times K_x^h}, && \boldsymbol{C}^h_{x,y} \in \mathbb{R}^{K_x\times K_y^h}, && \boldsymbol{C}^h_{x,z} \in \mathbb{R}^{K_x\times K_z^h},\\
&\boldsymbol{C}^h_{y,x} \in \mathbb{R}^{K_y\times K_x^h}, && \boldsymbol{C}^h_{y,y} \in \mathbb{R}^{K_y\times K_y^h}, && \boldsymbol{C}^h_{y,z} \in \mathbb{R}^{K_y\times K_z^h},\\
&\boldsymbol{C}^h_{z,x} \in \mathbb{R}^{K_z\times K_x^h}, && \boldsymbol{C}^h_{z,y} \in \mathbb{R}^{K_z\times K_y^h}, && \boldsymbol{C}^h_{z,z} \in \mathbb{R}^{K_z\times K_z^h},
\end{aligned} \tag{A.9}$$

and

$$\boldsymbol{C}^h_{x,x} = \mathbf{0}_{K_x,K_x^h}, \quad \boldsymbol{C}^h_{y,y} = \mathbf{0}_{K_y,K_y^h}, \quad \boldsymbol{C}^h_{z,z} = \mathbf{0}_{K_z,K_z^h}, \tag{A.10}$$

is used. Here, the expression

$$\mathbf{0}_{M,N} := [0]_{1\le k\le M, 1\le l\le N} \in \mathbb{R}^{M\times N}, \tag{A.11}$$

denotes the zero matrix. The remaining non-zero submatrices are composed, exploiting central differences (four-point stencil) with

$$\begin{aligned}
\mathrm{i}\omega\epsilon\, e_x(i+\tfrac{1}{2},j+1,k+1) &\approx -\frac{h_y(i+\frac{1}{2},j+1,k+\frac{1}{2})-h_y(i+\frac{1}{2},j+1,k-\frac{1}{2})}{\Delta\hat{z}_k}\\
&\quad+\frac{h_z(i+\frac{1}{2},j+\frac{1}{2},k+1)-h_z(i+\frac{1}{2},j-\frac{1}{2},k+1)}{\Delta\hat{y}_j},\\
&\Downarrow\\
\mathrm{i}\omega\epsilon\, \boldsymbol{e}_x &= \boldsymbol{C}^h_{x,y}\boldsymbol{h}_y+\boldsymbol{C}^h_{x,z}\boldsymbol{h}_z,
\end{aligned}\tag{A.12}$$

$$\begin{aligned}
\mathrm{i}\omega\epsilon\, e_y(i+1,j+\tfrac{1}{2},k+1) &\approx \frac{h_x(i+1,j+\frac{1}{2},k+\frac{1}{2})-h_x(i+1,j+\frac{1}{2},k-\frac{1}{2})}{\Delta\hat{z}_k}\\
&\quad-\frac{h_z(i+\frac{1}{2},j+\frac{1}{2},k+1)-h_z(i-\frac{1}{2},j+\frac{1}{2},k+1)}{\Delta\hat{x}_i},\\
&\Downarrow\\
\mathrm{i}\omega\epsilon\, \boldsymbol{e}_y &= \boldsymbol{C}^h_{y,x}\boldsymbol{h}_x+\boldsymbol{C}^h_{y,z}\boldsymbol{h}_z,
\end{aligned}\tag{A.13}$$

$$\begin{aligned}
\mathrm{i}\omega\epsilon\, e_z(i+1,j+1,k+\tfrac{1}{2}) &\approx -\frac{h_x(i+1,j+\frac{1}{2},k+\frac{1}{2})-h_x(i+1,j-\frac{1}{2},k+\frac{1}{2})}{\Delta\hat{y}_j}\\
&\quad+\frac{h_y(i+\frac{1}{2},j+1,k+\frac{1}{2})-h_y(i-\frac{1}{2},j+1,k+\frac{1}{2})}{\Delta\hat{x}_i},\\
&\Downarrow\\
\mathrm{i}\omega\epsilon\, \boldsymbol{e}_z &= \boldsymbol{C}^h_{z,x}\boldsymbol{h}_x+\boldsymbol{C}^h_{z,y}\boldsymbol{h}_y,
\end{aligned}\tag{A.14}$$

where the denominator indices of the inner node spacings run according to the indices i, j, k of the electric field. The linear appropriate indices l_x, l_y, l_z, derived from the positions of e_x, e_y, e_z, refer to the row number and the linear indices l^h_x, l^h_y, l^h_z, derived from the positions of h_x, h_y, h_z, to the column number of the respective entries in the submatrices of $\boldsymbol{C}^h$. These comprise the sign and denominator, i. e. the geometric information, of the above mentioned expressions.

In the following, a detailed description of the matrices assembling shows the principle mechanism of how the discrete operators can be formulated, exploiting the properties of the underlying tensor-product grid. Defining a rectangular matrix $\boldsymbol{S}^{\boldsymbol{h}}_N$ with

$$\boldsymbol{S}^{\boldsymbol{h}}_N := \begin{bmatrix} -1 & 1 & & & \\ & -1 & 1 & & \\ & & \ddots & \ddots & \\ & & & -1 & 1 \end{bmatrix} \in \mathbb{N}^{N,N+1}, \tag{A.15}$$

individual 1-D finite differences can be derived for each of the occurring two-point stencils with respect to the three coordinate directions

$$\partial_x \to \boldsymbol{P}^{\boldsymbol{h}}_x \in \mathbb{R}^{(n_x-1)\times n_x} = [\mathrm{diag}\,(\Delta\hat{\boldsymbol{x}})]^{-1}\boldsymbol{S}^{\boldsymbol{h}}_{n_x-1}, \tag{A.16}$$

$$\partial_y \to \boldsymbol{P}^{\boldsymbol{h}}_y \in \mathbb{R}^{(n_y-1)\times n_y} = [\mathrm{diag}\,(\Delta\hat{\boldsymbol{y}})]^{-1}\boldsymbol{S}^{\boldsymbol{h}}_{n_y-1}, \tag{A.17}$$

$$\partial_z \to \boldsymbol{P}^{\boldsymbol{h}}_z \in \mathbb{R}^{(n_z-1)\times n_z} = [\mathrm{diag}\,(\Delta\hat{\boldsymbol{z}})]^{-1}\boldsymbol{S}^{\boldsymbol{h}}_{n_z-1}, \tag{A.18}$$

Here, $\operatorname{diag}(\boldsymbol{x})$ denotes a $L \times L$ diagonal matrix with the main diagonal elements formed by the vector $\boldsymbol{x}$ of length L. These 1-D expressions comprise the direction derivatives with respect to grid spacings $\Delta\hat{\boldsymbol{x}}$, $\Delta\hat{\boldsymbol{y}}$, and $\Delta\hat{\boldsymbol{z}}$. The stencils are complete, i. e. no boundary conditions have to be considered, as a single element of the solution vector $\boldsymbol{u}$, defined at the interior of the model domain, is always thoroughly surrounded by elements of the discrete magnetic field $\boldsymbol{h}^{\mathrm{d}}$. Finally, exploiting the *Kronecker product* which is defined for arbitrary matrices $\boldsymbol{A} \in \mathbb{R}^{N\times M}$ and $\boldsymbol{B} \in \mathbb{R}^{K\times L}$ by

$$\begin{aligned}\boldsymbol{C} &= \boldsymbol{A} \otimes \boldsymbol{B} \in \mathbb{R}^{NK\times ML} \\ &:= \begin{bmatrix} a_{1,1}\boldsymbol{B} & \cdots & a_{1,M}\boldsymbol{B} \\ \vdots & \ddots & \vdots \\ a_{N,1}\boldsymbol{B} & \cdots & a_{N,M}\boldsymbol{B} \end{bmatrix},\end{aligned} \tag{A.19}$$

the submatrices of $\boldsymbol{C}^h$ can be assembled by

$$\boldsymbol{C}^h_{x,y} = -\left[\boldsymbol{P}^{\boldsymbol{h}}_z \otimes \operatorname{diag}\left(\mathbf{1}_{n_y-1}\right) \otimes \operatorname{diag}\left(\mathbf{1}_{n_x}\right)\right], \tag{A.20}$$

$$\boldsymbol{C}^h_{x,z} = \left[\operatorname{diag}\left(\mathbf{1}_{n_z-1}\right) \otimes \boldsymbol{P}^{\boldsymbol{h}}_y \otimes \operatorname{diag}\left(\mathbf{1}_{n_x}\right)\right], \tag{A.21}$$

$$\boldsymbol{C}^h_{y,x} = \left[\boldsymbol{P}^{\boldsymbol{h}}_z \otimes \operatorname{diag}\left(\mathbf{1}_{n_y}\right) \otimes \operatorname{diag}\left(\mathbf{1}_{n_x-1}\right)\right], \tag{A.22}$$

$$\boldsymbol{C}^h_{y,z} = -\left[\operatorname{diag}\left(\mathbf{1}_{n_z-1}\right) \otimes \operatorname{diag}\left(\mathbf{1}_{n_y}\right) \otimes \boldsymbol{P}^{\boldsymbol{h}}_x\right], \tag{A.23}$$

$$\boldsymbol{C}^h_{z,x} = -\left[\operatorname{diag}\left(\mathbf{1}_{n_z}\right) \otimes \boldsymbol{P}^{\boldsymbol{h}}_y \otimes \operatorname{diag}\left(\mathbf{1}_{n_x-1}\right)\right], \tag{A.24}$$

$$\boldsymbol{C}^h_{z,y} = \left[\operatorname{diag}\left(\mathbf{1}_{n_z}\right) \otimes \operatorname{diag}\left(\mathbf{1}_{n_y-1}\right) \otimes \boldsymbol{P}^{\boldsymbol{h}}_x\right]. \tag{A.25}$$

In practice, the concatenation by means of Kronecker products relates the single elements of the 1-D expressions to the lexicographic order of the vector $\boldsymbol{h}^{\mathrm{d}}$ on the tensor-product grid.

Similarly, the assembling of

$$\boldsymbol{C}^e = \begin{bmatrix} \boldsymbol{C}^e_{x,x} & \boldsymbol{C}^e_{x,y} & \boldsymbol{C}^e_{x,z} \\ \boldsymbol{C}^e_{y,x} & \boldsymbol{C}^e_{y,y} & \boldsymbol{C}^e_{y,z} \\ \boldsymbol{C}^e_{z,x} & \boldsymbol{C}^e_{z,y} & \boldsymbol{C}^e_{z,z} \end{bmatrix} \in \mathbb{R}^{K^h\times K}, \tag{A.26}$$

composed of

$$\begin{aligned} &\boldsymbol{C}^e_{x,x} \in \mathbb{R}^{K^h_x\times K_x}, \quad \boldsymbol{C}^e_{x,y} \in \mathbb{R}^{K^h_x\times K_y}, \quad \boldsymbol{C}^e_{x,z} \in \mathbb{R}^{K^h_x\times K_z}, \\ &\boldsymbol{C}^e_{y,x} \in \mathbb{R}^{K^h_y\times K_x}, \quad \boldsymbol{C}^e_{y,y} \in \mathbb{R}^{K^h_y\times K_y}, \quad \boldsymbol{C}^e_{y,z} \in \mathbb{R}^{K^h_y\times K_z}, \\ &\boldsymbol{C}^e_{z,x} \in \mathbb{R}^{K^h_z\times K_x}, \quad \boldsymbol{C}^e_{z,y} \in \mathbb{R}^{K^h_z\times K_y}, \quad \boldsymbol{C}^e_{z,z} \in \mathbb{R}^{K^h_z\times K_z}, \end{aligned} \tag{A.27}$$

and

$$\boldsymbol{C}^e_{x,x} = \mathbf{0}_{K^h_x,K_x}, \quad \boldsymbol{C}^e_{y,y} = \mathbf{0}_{K^h_y,K_y}, \quad \boldsymbol{C}^e_{z,z} = \mathbf{0}_{K^h_z,K_z}, \tag{A.28}$$

is based on

$$
\begin{aligned}
-\mathrm{i}\omega\mu_0\, h_x(i+1, j+\tfrac{1}{2}, k+\tfrac{1}{2}) \approx &-\frac{e_y(i+1, j+\frac{1}{2}, k+2) - e_y(i+1, j+\frac{1}{2}, k+1)}{\Delta z_k} \\
&+\frac{e_z(i+1, j+2, k+\frac{1}{2}) - e_z(i+1, j+1, k+\frac{1}{2})}{\Delta y_j}, \\
&\Downarrow \\
-\mathrm{i}\omega\mu_0\, \boldsymbol{h}_x = &\, \boldsymbol{C}^e_{x,y}\boldsymbol{e}_y + \boldsymbol{C}^e_{x,z}\boldsymbol{e}_z,
\end{aligned}
\tag{A.29}
$$

$$
\begin{aligned}
-\mathrm{i}\omega\mu_0\, h_y(i+\tfrac{1}{2}, j+1, k+\tfrac{1}{2}) \approx &\ \frac{e_x(i+\frac{1}{2}, j+1, k+2) - e_x(i+\frac{1}{2}, j+1, k+1)}{\Delta z_k} \\
&-\frac{e_z(i+2, j+1, k+\frac{1}{2}) - e_z(i+1, j+1, k+\frac{1}{2})}{\Delta x_i}, \\
&\Downarrow \\
-\mathrm{i}\omega\mu_0\, \boldsymbol{h}_y = &\, \boldsymbol{C}^e_{y,x}\boldsymbol{e}_x + \boldsymbol{C}^e_{y,z}\boldsymbol{e}_z,
\end{aligned}
\tag{A.30}
$$

$$
\begin{aligned}
-\mathrm{i}\omega\mu_0\, h_z(i+\tfrac{1}{2}, j+\tfrac{1}{2}, k+1) \approx &-\frac{e_x(i+\frac{1}{2}, j+2, k+1) - e_x(i+\frac{1}{2}, j+1, k+1)}{\Delta y_j} \\
&+\frac{e_y(i+2, j+\frac{1}{2}, k+1) - e_y(i+1, j+\frac{1}{2}, k+1)}{\Delta x_i}, \\
&\Downarrow \\
-\mathrm{i}\omega\mu_0\, \boldsymbol{h}_z = &\, \boldsymbol{C}^e_{z,x}\boldsymbol{e}_x + \boldsymbol{C}^e_{z,y}\boldsymbol{e}_y,
\end{aligned}
\tag{A.31}
$$

where the row and column numbers for the entries in the submatrices of $\boldsymbol{C}^e$ are now given by the linear indices l^h_x, l^h_y, l^h_z, and l_x, l_y, l_z, respectively. The index of the denominators are associated with the discrete magnetic field indices. Considering the homogeneous boundary conditions (3.23), the matrix $\boldsymbol{S}^{\boldsymbol{e}}_N$, used to derive the 1-D FD operators for the electric field, is defined as

$$
\boldsymbol{S}^{\boldsymbol{e}}_N := \begin{bmatrix} 1 & & & \\ -1 & 1 & & \\ & \ddots & \ddots & \\ & & -1 & 1 \\ & & & -1 \end{bmatrix} = -\boldsymbol{S}^{\boldsymbol{h}\top}_N \in \mathbb{N}^{N+1,N}. \tag{A.32}
$$

The 1-D finite differences are assembled by

$$
\partial_x \rightarrow \boldsymbol{P}^{\boldsymbol{e}}_x \in \mathbb{R}^{n_x \times (n_x-1)} = [\mathrm{diag}\,(\Delta \boldsymbol{x})]^{-1} \boldsymbol{S}^{\boldsymbol{e}}_{n_x}, \tag{A.33}
$$

$$
\partial_y \rightarrow \boldsymbol{P}^{\boldsymbol{e}}_y \in \mathbb{R}^{n_y \times (n_y-1)} = [\mathrm{diag}\,(\Delta \boldsymbol{y})]^{-1} \boldsymbol{S}^{\boldsymbol{e}}_{n_y}, \tag{A.34}
$$

$$
\partial_z \rightarrow \boldsymbol{P}^{\boldsymbol{e}}_z \in \mathbb{R}^{n_z \times (n_z-1)} = [\mathrm{diag}\,(\Delta \boldsymbol{z})]^{-1} \boldsymbol{S}^{\boldsymbol{e}}_{n_z}. \tag{A.35}
$$

and the non-zero submatrices of $\boldsymbol{C}^e$ are assembled by

$$\begin{aligned}
\boldsymbol{C}^e_{x,y} &= -\left[\boldsymbol{P}^{\boldsymbol{e}}_z \otimes \operatorname{diag}\left(\mathbf{1}_{n_y}\right) \otimes \operatorname{diag}\left(\mathbf{1}_{n_x-1}\right)\right], && \text{(A.36)}\\
\boldsymbol{C}^e_{x,z} &= \quad\left[\operatorname{diag}\left(\mathbf{1}_{n_z}\right) \otimes \boldsymbol{P}^{\boldsymbol{e}}_y \otimes \operatorname{diag}\left(\mathbf{1}_{n_x-1}\right)\right], && \text{(A.37)}\\
\boldsymbol{C}^e_{y,x} &= \quad\left[\boldsymbol{P}^{\boldsymbol{e}}_z \otimes \operatorname{diag}\left(\mathbf{1}_{n_y-1}\right) \otimes \operatorname{diag}\left(\mathbf{1}_{n_x}\right)\right], && \text{(A.38)}\\
\boldsymbol{C}^e_{y,z} &= -\left[\operatorname{diag}\left(\mathbf{1}_{n_z}\right) \otimes \operatorname{diag}\left(\mathbf{1}_{n_y-1}\right) \otimes \boldsymbol{P}^{\boldsymbol{e}}_x\right], && \text{(A.39)}\\
\boldsymbol{C}^e_{z,x} &= -\left[\operatorname{diag}\left(\mathbf{1}_{n_z-1}\right) \otimes \boldsymbol{P}^{\boldsymbol{e}}_y \otimes \operatorname{diag}\left(\mathbf{1}_{n_x}\right)\right], && \text{(A.40)}\\
\boldsymbol{C}^e_{z,y} &= \quad\left[\operatorname{diag}\left(\mathbf{1}_{n_z-1}\right) \otimes \operatorname{diag}\left(\mathbf{1}_{n_y}\right) \otimes \boldsymbol{P}^{\boldsymbol{e}}_x\right]. && \text{(A.41)}
\end{aligned}$$

A.3 Discretization of the gradient and divergence operators

The gradient of the electric conductivity $\nabla\sigma = \left[\partial_x, \partial_y, \partial_z\right]^\top \sigma$ is represented by applying the matrix $\boldsymbol{G} = \left[\boldsymbol{G}_x^\top, \boldsymbol{G}_y^\top, \boldsymbol{G}_z^\top\right]^\top$, with $\boldsymbol{G}_x \in \mathbb{R}^{K_x^h \times S}$, $\boldsymbol{G}_y \in \mathbb{R}^{K_y^h \times S}$, and $\boldsymbol{G}_z \in \mathbb{R}^{K_z^h \times S}$, to the vector of piecewise constant cell conductivities $\boldsymbol{\sigma} \in \mathbb{R}^S$. Defining the directional derivatives to be located at the interfaces of adjacent cells, the spatial distribution of the solution $\boldsymbol{g}^{\boldsymbol{\sigma}} = \left[\boldsymbol{g}_x^{\boldsymbol{\sigma}\top}, \boldsymbol{g}_y^{\boldsymbol{\sigma}\top}, \boldsymbol{g}_z^{\boldsymbol{\sigma}\top}\right]^\top \in \mathbb{R}^{K^h}$, with $\boldsymbol{g}_x^{\boldsymbol{\sigma}} \in \mathbb{C}^{K_x^h}$, $\boldsymbol{g}_y^{\boldsymbol{\sigma}} \in \mathbb{C}^{K_y^h}$, and $\boldsymbol{g}_z^{\boldsymbol{\sigma}} \in \mathbb{C}^{K_z^h}$, coincides with the positions of the magnetic field components $\boldsymbol{h}^{\mathrm{d}}$. Using the central differences (two-point stencil), the assembling of $\boldsymbol{G}$ is component-wise based on

$$\begin{aligned}
g_x^{\boldsymbol{\sigma}}(i+1, j+\tfrac{1}{2}, k+\tfrac{1}{2}) &\approx \frac{\sigma(i+\frac{3}{2}, j+\frac{1}{2}, k+\frac{1}{2}) - \sigma(i+\frac{1}{2}, j+\frac{1}{2}, k+\frac{1}{2})}{\Delta\hat{x}_i},\\
&\Downarrow\\
\boldsymbol{g}_x^{\boldsymbol{\sigma}} &= \boldsymbol{G}_x\boldsymbol{\sigma}, && \text{(A.42)}
\end{aligned}$$

$$\begin{aligned}
g_y^{\boldsymbol{\sigma}}(i+\tfrac{1}{2}, j+1, k+\tfrac{1}{2}) &\approx \frac{\sigma(i+\frac{1}{2}, j+\frac{3}{2}, k+\frac{1}{2}) - \sigma(i+\frac{1}{2}, j+\frac{1}{2}, k+\frac{1}{2})}{\Delta\hat{y}_j},\\
&\Downarrow\\
\boldsymbol{g}_y^{\boldsymbol{\sigma}} &= \boldsymbol{G}_y\boldsymbol{\sigma}, && \text{(A.43)}
\end{aligned}$$

$$\begin{aligned}
g_z^{\boldsymbol{\sigma}}(i+\tfrac{1}{2}, j+\tfrac{1}{2}, k+1) &\approx \frac{\sigma(i+\frac{1}{2}, j+\frac{1}{2}, k+\frac{3}{2}) - \sigma(i+\frac{1}{2}, j+\frac{1}{2}, k+\frac{1}{2})}{\Delta\hat{z}_k},\\
&\Downarrow\\
\boldsymbol{g}_z^{\boldsymbol{\sigma}} &= \boldsymbol{G}_z\boldsymbol{\sigma}, && \text{(A.44)}
\end{aligned}$$

where the row and column numbers are given by the linear indices l_x^h, l_y^h, l_z^h, and l_σ, respectively. The submatrices are assembled by

$$\begin{aligned}
\boldsymbol{G}_x^{\boldsymbol{\sigma}} &= \left[\operatorname{diag}\left(\mathbf{1}_{n_z}\right) \otimes \operatorname{diag}\left(\mathbf{1}_{n_y}\right) \otimes \boldsymbol{P}_x^{\boldsymbol{h}}\right], && \text{(A.45)}\\
\boldsymbol{G}_y^{\boldsymbol{\sigma}} &= \left[\operatorname{diag}\left(\mathbf{1}_{n_z}\right) \otimes \boldsymbol{P}_y^{\boldsymbol{h}} \otimes \operatorname{diag}\left(\mathbf{1}_{n_x}\right)\right], && \text{(A.46)}\\
\boldsymbol{G}_z^{\boldsymbol{\sigma}} &= \left[\boldsymbol{P}_z^{\boldsymbol{h}} \otimes \operatorname{diag}\left(\mathbf{1}_{n_y}\right) \otimes \operatorname{diag}\left(\mathbf{1}_{n_x}\right)\right], && \text{(A.47)}
\end{aligned}$$

exploiting the appropriate 1-D operators (cf. (A.16) to (A.18)) that are defined at the inner node spacings.

To discretize $\nabla\cdot \boldsymbol{h} = [\partial_x, \partial_y, \partial_z]^\top \cdot \boldsymbol{h}$, represented by $\boldsymbol{d^h} = \boldsymbol{D}\boldsymbol{h}^{\mathrm{d}} \in \mathbb{C}^S$, the assembling of the matrix $\boldsymbol{D} = [\boldsymbol{D}_x, \boldsymbol{D}_y, \boldsymbol{D}_z] \in \mathbb{R}^{S\times K^h}$, with $\boldsymbol{D}_x \in \mathbb{R}^{S\times K^h_x}$, $\boldsymbol{D}_y \in \mathbb{R}^{S\times K^h_y}$, and $\boldsymbol{D}_z \in \mathbb{R}^{S\times K^h_z}$, is based on a six-point stencil

$$\begin{aligned}
d^{\boldsymbol{h}}(i+\tfrac{1}{2}, j+\tfrac{1}{2}, k+\tfrac{1}{2}) \approx{}& \frac{h_x(i+2, j+\frac{1}{2}, k+\frac{1}{2}) - h_x(i+1, j+\frac{1}{2}, k+\frac{1}{2})}{\Delta x_i} \\
&+ \frac{h_y(i+\frac{1}{2}, j+2, k+\frac{1}{2}) - h_y(i+\frac{1}{2}, j+1, k+\frac{1}{2})}{\Delta y_j} \\
&+ \frac{h_z(i+\frac{1}{2}, j+\frac{1}{2}, k+2) - h_z(i+\frac{1}{2}, j+\frac{1}{2}, k+1)}{\Delta z_k}, \\
&\Downarrow \\
\boldsymbol{d^h} ={}& \boldsymbol{D}_x\boldsymbol{h}_x + \boldsymbol{D}_y\boldsymbol{h}_y + \boldsymbol{D}_z\boldsymbol{h}_z. \qquad \text{(A.48)}
\end{aligned}$$

Here, the row numbers for entries in $\boldsymbol{D}_x$, $\boldsymbol{D}_y$, and $\boldsymbol{D}_z$ each are given by l_σ and the appropriate column numbers are given by l^h_x, l^h_y, l^h_z. Consistently, $\boldsymbol{d^h}$ is defined at the midpoints of the cells. The assembling of the submatrices with the help of the 1-D finite differences, associated with the cell spacings, can be realized by

$$\boldsymbol{D}_x = \left[\operatorname{diag}\left(\boldsymbol{1}_{n_z}\right) \otimes \operatorname{diag}\left(\boldsymbol{1}_{n_y}\right) \otimes \boldsymbol{P}^{\boldsymbol{e}}_x\right], \tag{A.49}$$

$$\boldsymbol{D}_y = \left[\operatorname{diag}\left(\boldsymbol{1}_{n_z}\right) \otimes \boldsymbol{P}^{\boldsymbol{e}}_y \otimes \operatorname{diag}\left(\boldsymbol{1}_{n_x}\right)\right], \tag{A.50}$$

$$\boldsymbol{D}_z = \left[\boldsymbol{P}^{\boldsymbol{e}}_z \otimes \operatorname{diag}\left(\boldsymbol{1}_{n_y}\right) \otimes \operatorname{diag}\left(\boldsymbol{1}_{n_x}\right)\right]. \tag{A.51}$$

Thus, homogeneous boundary conditions are applied to the derivatives at the boundary of the model domain.

A.4 Symmetrization of the system matrix

The symmetry of $\boldsymbol{K}$ and therefore of the system matrix $\boldsymbol{A}$ can be achieved by a left multiplication of the system (3.16) with the diagonal matrix $\boldsymbol{T}$, i. e. by a geometric weighting of each row of the matrices. For the component-wise definitions (A.8) and (A.26), it can be shown that

$$\boldsymbol{T} = \operatorname{diag}\left([\boldsymbol{t}_x, \boldsymbol{t}_y, \boldsymbol{t}_z]\right), \tag{A.52}$$

assembled by

$$\boldsymbol{t}_x \in \mathbb{R}^{1\times K_x} = [\Delta\hat{\boldsymbol{z}} \otimes \Delta\hat{\boldsymbol{y}} \otimes \Delta\boldsymbol{x}], \tag{A.53}$$

$$\boldsymbol{t}_y \in \mathbb{R}^{1\times K_y} = [\Delta\hat{\boldsymbol{z}} \otimes \Delta\boldsymbol{y} \otimes \Delta\hat{\boldsymbol{x}}], \tag{A.54}$$

$$\boldsymbol{t}_z \in \mathbb{R}^{1\times K_z} = [\Delta\boldsymbol{z} \otimes \Delta\hat{\boldsymbol{y}} \otimes \Delta\hat{\boldsymbol{x}}], \tag{A.55}$$

leads to the desired symmetric system of linear equations.

A.5 Assembling of the cell volume matrix $\boldsymbol{V}$

The cell volumes can be assembled by using the Kronecker product to concatenate the node distances Δx_i, Δy_j, and Δz_k with respect to the lexicographic order l_σ by

$$\boldsymbol{V} = \operatorname{diag}\left([\Delta\boldsymbol{z} \otimes \Delta\boldsymbol{y} \otimes \Delta\boldsymbol{x}]\right) \in \mathbb{R}^{S\times S}. \tag{A.56}$$

A.6 Assembling of the interpolation operator $\boldsymbol{i}$

As the data vector $\boldsymbol{d}$ comprises samples only of the vertical magnetic field, the interpolation operator $\boldsymbol{i} = \left[\boldsymbol{i}_x^\top, \boldsymbol{i}_y^\top, \boldsymbol{i}_z^\top\right]^\top \in \mathbb{R}^{K^h}$ has to act solely on the z-component $\boldsymbol{h}_z^{\mathrm{d}}$, i. e. on the transformed solution $\boldsymbol{h}^{\mathrm{d}} = \boldsymbol{C}^e \boldsymbol{u}_{\mathrm{sec}}$. Hence,

$$\begin{aligned} \boldsymbol{i}_x &= \boldsymbol{0}_{K_x^h}, \\ \boldsymbol{i}_y &= \boldsymbol{0}_{K_y^h}. \end{aligned} \tag{A.57}$$

Concerning an arbitrary point, located at $x_{i+\frac{1}{2}} \leq x \leq x_{i+\frac{3}{2}}$, $y_{j+\frac{1}{2}} \leq y \leq y_{j+\frac{3}{2}}$, $z_k \leq z \leq z_{k+1}$ within a rectangle (see fig. A.3), spanned by eight elements of $\boldsymbol{h}_z^{\mathrm{d}}$, the vertical magnetic field $h_z(x, y, z)$ at an arbitrary point within the rectangle is given by the trilinear interpolation

$$\begin{aligned} h_z(\boldsymbol{p}) = \Big[& h_z(i+\tfrac{1}{2}, j+\tfrac{1}{2}, k)\left(x_{i+\frac{3}{2}} - x\right)\left(y_{j+\frac{3}{2}} - y\right)\left(z_{k+1} - z\right) + \\ & h_z(i+\tfrac{3}{2}, j+\tfrac{1}{2}, k)\left(x - x_{i+\frac{1}{2}}\right)\left(y_{j+\frac{3}{2}} - y\right)\left(z_{k+1} - z\right) + \\ & h_z(i+\tfrac{1}{2}, j+\tfrac{3}{2}, k)\left(x_{i+\frac{3}{2}} - x\right)\left(y - y_{j+\frac{1}{2}}\right)\left(z_{k+1} - z\right) + \\ & h_z(i+\tfrac{3}{2}, j+\tfrac{3}{2}, k)\left(x - x_{i+\frac{1}{2}}\right)\left(y - y_{j+\frac{1}{2}}\right)\left(z_{k+1} - z\right) + \\ & h_z(i+\tfrac{1}{2}, j+\tfrac{1}{2}, k+1)\left(x_{i+\frac{3}{2}} - x\right)\left(y_{j+\frac{3}{2}} - y\right)\left(z - z_k\right) + \\ & h_z(i+\tfrac{3}{2}, j+\tfrac{1}{2}, k+1)\left(x - x_{i+\frac{1}{2}}\right)\left(y_{j+\frac{3}{2}} - y\right)\left(z - z_k\right) + \\ & h_z(i+\tfrac{1}{2}, j+\tfrac{3}{2}, k+1)\left(x_{i+\frac{3}{2}} - x\right)\left(y - y_{j+\frac{1}{2}}\right)\left(z - z_k\right) + \\ & h_z(i+\tfrac{3}{2}, j+\tfrac{3}{2}, k+1)\left(x - x_{i+\frac{1}{2}}\right)\left(y - y_{j+\frac{1}{2}}\right)\left(z - z_k\right)\Big] \frac{1}{\Delta\hat{x}_i \Delta\hat{y}_j \Delta z_k} \\ \Downarrow \\ h_z(x, y, z) = {} & \boldsymbol{i}_z \cdot \boldsymbol{h}_z^{\mathrm{d}}, \end{aligned} \tag{A.58}$$

where the geometric weights are associated with entries in the l_z^h-th position of $\boldsymbol{i}_z$, according to the involved element of $\boldsymbol{h}_z^{\mathrm{d}}$. The trilinear interpolation is derived from a composition of a set of linear interpolations. For the elements on a rectangle as shown in fig. A.3, this means to start with four linear interpolations e. g. on parallel edges in x-direction. Those solutions are interpolated in y-direction, and the resulting two solutions are finally interpolated in z-direction. Thereby, the order of the coordinate directions is irrelevant. A single 1-D interpolation, e. g. in x-direction at $x_{i+\frac{1}{2}} \leq x \leq x_{i+\frac{3}{2}}$, is given by

$$h_z(x) \approx h_z(x_{i+\frac{1}{2}}) + \frac{h_z(x_{i+\frac{3}{2}}) - h_z(x_{i+\frac{1}{2}})}{\left[x_{i+\frac{3}{2}} - x_{i+\frac{1}{2}}\right]} \left[x - x_{i+\frac{1}{2}}\right], \tag{A.59}$$

which equals a linearization at $h_z(x_{i+\frac{1}{2}})$. Additional auxiliary points, required to represent components near the model domains' boundary, are set to zero, according to the boundary condition (3.23) which might significantly reduce the interpolation accuracy at the boundaries vicinity.

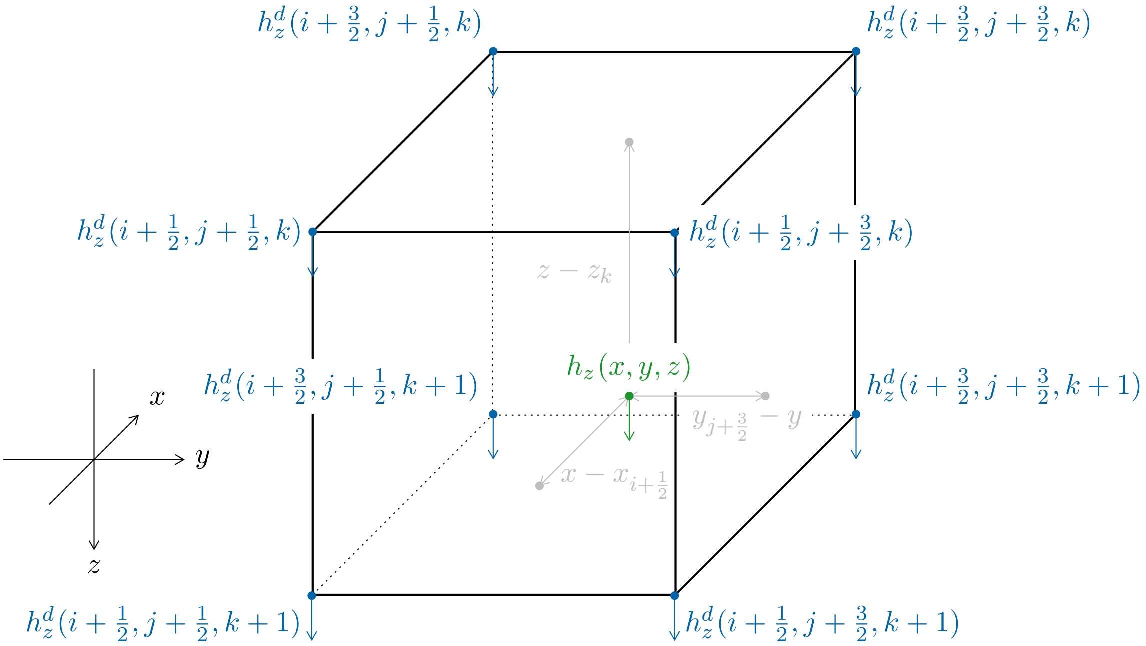

Figure A.3: Rectangular geometry that forms the basis of the trilinear interpolation of h_z.

A.7 Discretization of the mass matrix $\boldsymbol{M}$

Considering the finite difference discretization of (2.6), a simplification of the tensor handling can be achieved. Due to the diagonal structure of $\boldsymbol{M}$, it is possible to construct and store the tensor $\widetilde{\boldsymbol{T}}$ with the help of an auxiliary or *assembling* matrix $\boldsymbol{T}^{\mathrm{a}} \in \mathbb{R}^{K\times S}$, where

$$[t_{i,i,p}]_{1\le i\le K,1\le p\le S} = \left[t^{\mathrm{a}}_{i,p}\right]_{1\le i\le K,1\le p\le S}. \tag{A.60}$$

In principle, this implies to store the main diagonals of the tensor slices $\boldsymbol{T}_p$, $p = 1, \ldots, S$ as columns of $\boldsymbol{T}^{\mathrm{a}}$ which thereby contain the entire geometric information of the grid cells with respect to the FD discretization. A single cell is surrounded by a maximum of 12 DOF which determines the maximum number of non-zero entries in the respective column. Additionally, the DOF at the interior edges each are surrounded by four adjacent cells which gives the number of non-zero entries in the respective row. As a result of that approach, the mass matrix parts $\boldsymbol{M}$ and $\boldsymbol{S}$ can just be provided by

$$\boldsymbol{M} = \widetilde{\boldsymbol{T}} \times_3 \boldsymbol{\sigma} = \operatorname{diag}\left(\boldsymbol{T}^{\mathrm{a}}\boldsymbol{\sigma}\right), \tag{A.61}$$

and

$$\boldsymbol{S} = \widetilde{\boldsymbol{T}} \times_3 \boldsymbol{\epsilon} = \operatorname{diag}\left(\boldsymbol{T}^{\mathrm{a}}\boldsymbol{\epsilon}\right). \tag{A.62}$$

Furthermore, the $\times_3$ tensor-matrix product of $\widetilde{\boldsymbol{T}} \in \mathbb{R}^{K\times K\times S}$ and $\boldsymbol{X} \in \mathbb{R}^{S\times L}$ can be expressed by the right multiplication

$$[t_{i,i,p}x_{p,l}]_{1\le i\le K,1\le p\le S} = \left[t^{\mathrm{a}}_{i,p}x_{p,l}\right]_{1\le i\le K,1\le p\le S}. \tag{A.63}$$

The composition of the assembling matrix $\boldsymbol{T}^{\mathrm{a}} = \left[\boldsymbol{T}_x^{\mathrm{a}\top}, \boldsymbol{T}_y^{\mathrm{a}\top}, \boldsymbol{T}_z^{\mathrm{a}\top}\right]^\top \in \mathbb{R}^{K\times S}$, with $\boldsymbol{T}_x^{\mathrm{a}} \in \mathbb{R}^{K_x\times S}$, $\boldsymbol{T}_y^{\mathrm{a}} \in \mathbb{R}^{K_y\times S}$, and $\boldsymbol{T}_z^{\mathrm{a}} \in \mathbb{R}^{K_z\times S}$, can be attributed to a straightforward volume weighted average. The weighting factors are given by the ratio of a single cell volume to the total volume of the four adjacent cells which surrounds a DOF. Furthermore, as the DOF are related to solutions that are oriented in a certain coordinate direction, the weighting scheme is already given by face weighted averages that result from a composition of the weights in both orthogonal coordinate directions. This is because, the weighting factor for all involved cells in the direction parallel to the DOF is equal to 1, i. e. the cells spacings in that direction are identical. In fig. A.4, the weighting is exemplarily shown for $\sigma(e_z(i+1, j+1, k+\frac{1}{2}))$ that is related to a downwards oriented z-component of $\boldsymbol{u}$. The colored faces of the sub-rectangles are scaled by the size of the entire rectangle, acting as weight for the respective cell conductivities. A summation leads to the desired average conductivity at the blue circle, symbolizing the position of e_z.

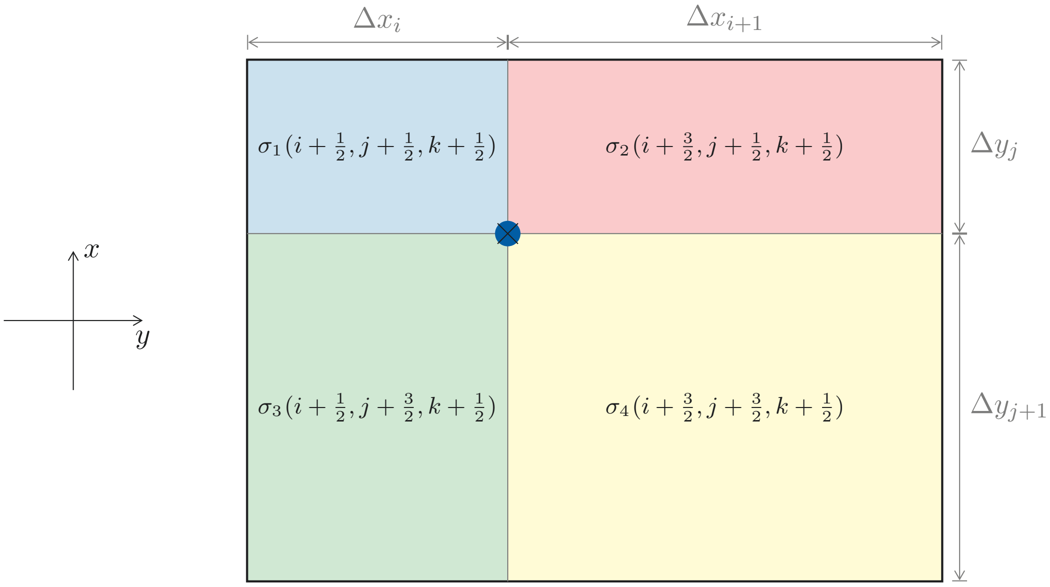

Figure A.4: Face weighted average for $\sigma(e_z(i+1, j+1, k+\frac{1}{2}))$, based on the sizes of cell faces and the total area $(\Delta x_i + \Delta x_{i+1})(\Delta y_i + \Delta y_{i+1})$.

Hence, the averaged conductivities that induce the diagonal entries of $\boldsymbol{M}$ are given by

$$\begin{aligned}\sigma(e_x(i+\tfrac{1}{2},j+1,k+1)) = {} & \frac{\Delta y_j}{\Delta y_j+\Delta y_{j+1}}\frac{\Delta z_k}{\Delta z_k+\Delta z_{k+1}}\sigma(i+\tfrac{1}{2},j+\tfrac{1}{2},k+\tfrac{1}{2}) \\ & + \frac{\Delta y_{j+1}}{\Delta y_j+\Delta y_{j+1}}\frac{\Delta z_k}{\Delta z_k+\Delta z_{k+1}}\sigma(i+\tfrac{1}{2},j+\tfrac{3}{2},k+\tfrac{1}{2}) \\ & + \frac{\Delta y_j}{\Delta y_j+\Delta y_{j+1}}\frac{\Delta z_{k+1}}{\Delta z_k+\Delta z_{k+1}}\sigma(i+\tfrac{1}{2},j+\tfrac{1}{2},k+\tfrac{3}{2}) \\ & + \frac{\Delta y_{j+1}}{\Delta y_j+\Delta y_{j+1}}\frac{\Delta z_{k+1}}{\Delta z_k+\Delta z_{k+1}}\sigma(i+\tfrac{1}{2},j+\tfrac{3}{2},k+\tfrac{3}{2}),\end{aligned} \tag{A.64}$$

$$\begin{aligned}\sigma(e_y(i+1,j+\tfrac{1}{2},k+1)) = {} & \frac{\Delta x_i}{\Delta x_i+\Delta x_{i+1}}\frac{\Delta z_k}{\Delta z_k+\Delta z_{k+1}}\sigma(i+\tfrac{1}{2},j+\tfrac{1}{2},k+\tfrac{1}{2}) \\ & + \frac{\Delta x_{i+1}}{\Delta x_i+\Delta x_{i+1}}\frac{\Delta z_k}{\Delta z_k+\Delta z_{k+1}}\sigma(i+\tfrac{3}{2},j+\tfrac{1}{2},k+\tfrac{1}{2}) \\ & + \frac{\Delta x_i}{\Delta x_i+\Delta x_{i+1}}\frac{\Delta z_{k+1}}{\Delta z_k+\Delta z_{k+1}}\sigma(i+\tfrac{1}{2},j+\tfrac{1}{2},k+\tfrac{3}{2}) \\ & + \frac{\Delta y_{j+1}}{\Delta y_j+\Delta y_{j+1}}\frac{\Delta z_{k+1}}{\Delta z_k+\Delta z_{k+1}}\sigma(i+\tfrac{3}{2},j+\tfrac{1}{2},k+\tfrac{3}{2}),\end{aligned} \tag{A.65}$$

$$\begin{aligned}\sigma(e_z(i+1,j+1,k+\tfrac{1}{2})) = {} & \frac{\Delta x_i}{\Delta x_i+\Delta x_{i+1}}\frac{\Delta y_j}{\Delta y_j+\Delta y_{j+1}}\sigma(i+\tfrac{1}{2},j+\tfrac{1}{2},k+\tfrac{1}{2}) \\ & + \frac{\Delta x_{i+1}}{\Delta x_i+\Delta x_{i+1}}\frac{\Delta y_j}{\Delta y_j+\Delta y_{j+1}}\sigma(i+\tfrac{3}{2},j+\tfrac{1}{2},k+\tfrac{1}{2}) \\ & + \frac{\Delta x_i}{\Delta x_i+\Delta x_{i+1}}\frac{\Delta y_{j+1}}{\Delta y_j+\Delta y_{j+1}}\sigma(i+\tfrac{1}{2},j+\tfrac{3}{2},k+\tfrac{1}{2}) \\ & + \frac{\Delta x_{i+1}}{\Delta x_i+\Delta x_{i+1}}\frac{\Delta y_{j+1}}{\Delta y_j+\Delta y_{j+1}}\sigma(i+\tfrac{3}{2},j+\tfrac{3}{2},k+\tfrac{1}{2}).\end{aligned} \tag{A.66}$$

The deduced submatrices of $\boldsymbol{T}^{\mathrm{a}}$ can, once again, be generated with the help of 1-D expressions that are concatenated with the help of the Kronecker product. At first, weight matrices $\boldsymbol{I}_x \in \mathbb{R}^{n_x-1\times n_x}$, $\boldsymbol{I}_y \in \mathbb{R}^{n_y-1\times n_y}$, and $\boldsymbol{I}_z \in \mathbb{R}^{n_z-1\times n_z}$, representing the ratios of two adjacent cells for all grid spacings with respect to a single coordinate direction, are defined by

$$\boldsymbol{I}_c := \begin{bmatrix} \frac{\Delta c_1}{\Delta c_1+\Delta c_2} & \frac{\Delta c_2}{\Delta c_1+\Delta c_2} & & \\ & \ddots & \ddots & \\ & & \frac{\Delta c_{n_c-1}}{\Delta c_{n_c-1}+\Delta c_{n_c}} & \frac{\Delta c_{n_c}}{\Delta c_{n_c-1}+\Delta c_{n_c}} \end{bmatrix}, \tag{A.67}$$

where the index c acts as place holder for x, y, or z. In a second step, these expressions are combined with the ratios in the respective second coordinate direction and are simultaneously expand to the whole tensor-product grid by

$$\boldsymbol{T}_x^{\mathrm{a}} = \left[\boldsymbol{I}_z \otimes \boldsymbol{I}_y \otimes \operatorname{diag}\left(\mathbf{1}_{n_x}\right)\right], \tag{A.68}$$

$$\boldsymbol{T}_y^{\mathrm{a}} = \left[\boldsymbol{I}_z \otimes \operatorname{diag}\left(\mathbf{1}_{n_y}\right) \otimes \boldsymbol{I}_x\right], \tag{A.69}$$

$$\boldsymbol{T}_z^{\mathrm{a}} = \left[\operatorname{diag}\left(\mathbf{1}_{n_z}\right) \otimes \boldsymbol{I}_y \otimes \boldsymbol{I}_x\right], \tag{A.70}$$

according to the lexicographic ordering of $\boldsymbol{u} = \left[\boldsymbol{e}_x^\top, \boldsymbol{e}_y^\top, \boldsymbol{e}_z^\top\right]^\top$ and $\boldsymbol{\sigma}$.

B Inverse problem

In the following, only the non-regularized least-squares problem $\Phi = \frac{1}{2}\|\boldsymbol{d}^{\mathrm{obs}} - \boldsymbol{d}(\boldsymbol{m})\|_2^2 \rightarrow \min_{\boldsymbol{m}}$ s. t. $\boldsymbol{m} \in \mathbb{R}^M$ for the complex vectors $\boldsymbol{d}^{\mathrm{obs}}, \boldsymbol{d}(\boldsymbol{m}) \in \mathbb{C}^N$ is considered. The subsequent derivations can be applied to the specific least-squares problem, introduced in chapter 4, w. l. o. g. Exploiting the properties of the L^2-norm, two mathematically equivalent formulations can be derived which exclusively provide real-valued model updates at the Gauss-Newton approach.

B.1 Formulation based on the Hermitian inner product

Concerning the Euclidean norm in case of a complex residual $\left\|\boldsymbol{d}^{\mathrm{obs}} - \boldsymbol{d}(\boldsymbol{m})\right\|_2^2$, the least-squares problem is induced by the Euclidean inner product of the complex vector space. For arbitrary vectors $\boldsymbol{u} = \boldsymbol{u}_r + i\boldsymbol{u}_i, \boldsymbol{v} = \boldsymbol{v}_r + i\boldsymbol{v}_i \in \mathbb{C}$ it holds that

$$\text{i)}\ \langle \boldsymbol{u}, \boldsymbol{v} \rangle = \boldsymbol{u}^{\mathsf{H}}\boldsymbol{v} = \overline{\boldsymbol{u}}^{\top}\boldsymbol{v} \tag{B.1}$$

$$\text{ii)}\ \|\boldsymbol{u}\|_2^2 := \langle \boldsymbol{u}, \boldsymbol{u} \rangle = \boldsymbol{u}^{\mathsf{H}}\boldsymbol{u} \in \mathbb{R} \tag{B.2}$$

$$\text{iii)}\ \boldsymbol{u} = \overline{\overline{\boldsymbol{u}}} \tag{B.3}$$

$$\text{iv)}\ \langle \boldsymbol{u}, \boldsymbol{v} \rangle = \overline{\langle \boldsymbol{v}, \boldsymbol{u} \rangle} \tag{B.4}$$

$$\text{v)}\ \boldsymbol{u} + \overline{\boldsymbol{u}} = 2\Re(\boldsymbol{u}), \tag{B.5}$$

where $\overline{\boldsymbol{u}}$ indicates the complex conjugate and $\boldsymbol{u}^{\mathsf{H}}$ means the conjugate transpose (Hermitian conjugate) of $\boldsymbol{u}$. By exploiting (B.2) and combining (B.4) and (B.5), the objective function is naturally assembled by solely real-valued blocks (Newman and Hoversten 2000, cf.)

$$\begin{aligned}\Phi &= \frac{1}{2}\left\|\boldsymbol{d}^{\mathrm{obs}} - \boldsymbol{d}(\boldsymbol{m})\right\|_2^2 = \frac{1}{2}\left[\boldsymbol{d}^{\mathrm{obs}} - \boldsymbol{d}\right]^{\mathsf{H}}\left[\boldsymbol{d}^{\mathrm{obs}} - \boldsymbol{d}\right] \\ &= \frac{1}{2}\left[\overbrace{\boldsymbol{d}^{\mathrm{obs}\,\mathsf{H}}\boldsymbol{d}^{\mathrm{obs}}}^{\in\mathbb{R}} \underbrace{-\boldsymbol{d}^{\mathrm{obs}\,\mathsf{H}}\boldsymbol{d} - \boldsymbol{d}^{\mathsf{H}}\boldsymbol{d}^{\mathrm{obs}}}_{-2\Re\left(\boldsymbol{d}^{\mathsf{H}}\boldsymbol{d}^{\mathrm{obs}}\right)} + \overbrace{\boldsymbol{d}^{\mathsf{H}}\boldsymbol{d}}^{\in\mathbb{R}}\right].\end{aligned} \tag{B.6}$$

For $\boldsymbol{d}^{\mathrm{obs}} = \boldsymbol{d}_r^{\mathrm{obs}} + i\boldsymbol{d}_i^{\mathrm{obs}}$ and $\boldsymbol{d} = \boldsymbol{d}_r + i\boldsymbol{d}_i$, (B.6) can be written component-wise by

$$\begin{aligned}\Phi = \frac{1}{2}\Bigg[&\boldsymbol{d}_r^{\mathrm{obs}\top}\boldsymbol{d}_r^{\mathrm{obs}} + \mathrm{i}\overbrace{\left(\boldsymbol{d}_r^{\mathrm{obs}\top}\boldsymbol{d}_i^{\mathrm{obs}} - \boldsymbol{d}_i^{\mathrm{obs}\top}\boldsymbol{d}_r^{\mathrm{obs}}\right)}^{=0} + \boldsymbol{d}_i^{\mathrm{obs}\top}\boldsymbol{d}_i^{\mathrm{obs}} \\ &- 2\Re\left(\boldsymbol{d}_r^{\top}\boldsymbol{d}_r^{\mathrm{obs}} + \mathrm{i}\boldsymbol{d}_r^{\top}\boldsymbol{d}_i^{\mathrm{obs}} - \mathrm{i}\boldsymbol{d}_i^{\top}\boldsymbol{d}_r^{\mathrm{obs}} + \boldsymbol{d}_i^{\top}\boldsymbol{d}_i^{\mathrm{obs}}\right) \\ &+ \boldsymbol{d}_r^{\top}\boldsymbol{d}_r + \mathrm{i}\underbrace{\left(\boldsymbol{d}_r^{\top}\boldsymbol{d}_i - \boldsymbol{d}_i^{\top}\boldsymbol{d}_r\right)}_{=0} + \boldsymbol{d}_i^{\top}\boldsymbol{d}_i\Bigg],\end{aligned} \tag{B.7}$$

where the symmetry property of the scalar product is used. The above expression can be vectorized to

$$\Phi = \frac{1}{2}\left\|\begin{bmatrix}\boldsymbol{d}_r^{\mathrm{obs}}\\ \boldsymbol{d}_i^{\mathrm{obs}}\end{bmatrix} - \begin{bmatrix}\boldsymbol{d}_r\\ \boldsymbol{d}_i\end{bmatrix}\right\|_2^2 = \frac{1}{2}\left\|\begin{bmatrix}\Re(\boldsymbol{d}^{\mathrm{obs}}-\boldsymbol{d})\\ \Im(\boldsymbol{d}^{\mathrm{obs}}-\boldsymbol{d})\end{bmatrix}\right\|_2^2 . \tag{B.8}$$

With $\boldsymbol{J} = \partial_{\boldsymbol{m}}\boldsymbol{d} \in \mathbb{C}^{N\times M}$, the gradient of the objective function (B.6) with respect to the model parameters, $\nabla_{\boldsymbol{m}}\Phi \in \mathbb{R}^M$, is given by

$$\begin{aligned}\nabla_{\boldsymbol{m}}\Phi &= \frac{1}{2}\left[0 - 2\Re\left(\boldsymbol{J}^{\mathsf{H}}\boldsymbol{d}^{\mathrm{obs}}\right) + 2\Re\left(\boldsymbol{J}^{\mathsf{H}}\boldsymbol{d}\right)\right]\\ &= -\Re\left(\boldsymbol{J}^{\mathsf{H}}\left[\boldsymbol{d}^{\mathrm{obs}} - \boldsymbol{d}\right]\right),\end{aligned} \tag{B.9}$$

which reads component-wise

$$\begin{aligned}\nabla_{\boldsymbol{m}}\Phi = \Re\Big(&\boldsymbol{J}_r^\top\boldsymbol{d}_r + \boldsymbol{J}_i^\top\boldsymbol{d}_i - \boldsymbol{J}_r^\top\boldsymbol{d}_r^{\mathrm{obs}} - \boldsymbol{J}_i^\top\boldsymbol{d}_i^{\mathrm{obs}}\\ &+ \boldsymbol{J}_r^\top i\boldsymbol{d}_i - \boldsymbol{J}_r^\top i\boldsymbol{d}_i^{\mathrm{obs}} - i\boldsymbol{J}_i^\top\boldsymbol{d}_r + i\boldsymbol{J}_i^\top\boldsymbol{d}_r^{\mathrm{obs}}\Big)\\ = -&\begin{bmatrix}\Re(\boldsymbol{J})\\ \Im(\boldsymbol{J})\end{bmatrix}^\top\left(\begin{bmatrix}\Re\left(\boldsymbol{d}^{\mathrm{obs}}-\boldsymbol{d}\right)\\ \Im\left(\boldsymbol{d}^{\mathrm{obs}}-\boldsymbol{d}\right)\end{bmatrix}\right).\end{aligned} \tag{B.10}$$

Considering the linearization

By referring to the Gauss-Newton approximation, the nonlinear forward operator $\boldsymbol{d}(\boldsymbol{m})$ is approximated by a linearization. Hence, already the object function Φ comprises a derivative of $\boldsymbol{d}$, i. e.

$$\boldsymbol{d}(\boldsymbol{m}) \approx \boldsymbol{d}(\boldsymbol{m}_0) + \boldsymbol{J}(\boldsymbol{m}_0)\Delta\boldsymbol{m},$$

where

$$\Delta\boldsymbol{m} = \boldsymbol{m} - \boldsymbol{m}_0. \tag{B.11}$$

With $\Delta\boldsymbol{d} = \boldsymbol{d}^{\mathrm{obs}} - \boldsymbol{d}(\boldsymbol{m}_0)$ it holds that

$$\begin{aligned}\Phi &= \frac{1}{2}\left\|\Delta\boldsymbol{d} - \boldsymbol{J}\Delta\boldsymbol{m}\right\|_2^2 = \frac{1}{2}[\Delta\boldsymbol{d} - \boldsymbol{J}\Delta\boldsymbol{m}]^{\mathsf{H}}[\Delta\boldsymbol{d} - \boldsymbol{J}\Delta\boldsymbol{m}]\\ &= \frac{1}{2}\left[\overbrace{\Delta\boldsymbol{d}^{\mathsf{H}}\Delta\boldsymbol{d}}^{\in\mathbb{R}}\underbrace{-\Delta\boldsymbol{d}^{\mathsf{H}}\boldsymbol{J}\Delta\boldsymbol{m} - \Delta\boldsymbol{m}^\top\boldsymbol{J}^{\mathsf{H}}\Delta\boldsymbol{d}}_{-2\Delta\boldsymbol{m}^\top\Re\left(\boldsymbol{J}^{\mathsf{H}}\Delta\boldsymbol{d}\right)} + \overbrace{\Delta\boldsymbol{m}^\top\underbrace{\boldsymbol{J}^{\mathsf{H}}\boldsymbol{J}}_{\in\mathbb{C}}\Delta\boldsymbol{m}}^{\in\mathbb{R}^{M\times M}}\right],\end{aligned} \tag{B.12}$$

and for the gradient that

$$\nabla_{\boldsymbol{m}}\Phi = \Re\left(\boldsymbol{J}^{\mathsf{H}}\boldsymbol{J}\right)\Delta\boldsymbol{m} - \Re\left(\boldsymbol{J}^{\mathsf{H}}\Delta\boldsymbol{d}\right). \tag{B.13}$$

Building $\Delta\boldsymbol{m}^\top$ instead of $\Delta\boldsymbol{m}^{\mathsf{H}}$ and excluding it from $\Re\left(\boldsymbol{J}^{\mathsf{H}}\boldsymbol{J}\Delta\boldsymbol{m}\right)$ is only validated by the general constraint that $\boldsymbol{m} \in \mathbb{R}$, set on the least-squares problem (cf. section 4.1).

B.2 Formulation based on the subdivision in real and imaginary parts

Considering the least-squares problem (B.6), it is possible to benefit from the properties of the Euclidean norm to develop completely real-valued expressions on a second way. Based on

$$\Phi = \frac{1}{2}\left\|\boldsymbol{d}^{\text{obs}} - \boldsymbol{d}(\boldsymbol{m})\right\|_2^2 = \frac{1}{2}\left\|(\boldsymbol{d}_r^{\text{obs}} + i\boldsymbol{d}_i^{\text{obs}}) - (\boldsymbol{d}_r + i\boldsymbol{d}_i)\right\|_2^2,$$

the square of the L^2-norm allows it to split the problem into

$$\begin{aligned}\Phi &= \frac{1}{2}\left\|(\boldsymbol{d}_r^{\text{obs}} - \boldsymbol{d}_r) + i(\boldsymbol{d}_i^{\text{obs}} - \boldsymbol{d}_i)\right\|_2^2,\\ &= \frac{1}{2}\left\|(\boldsymbol{d}_r^{\text{obs}} - \boldsymbol{d}_r)\right\|_2^2 + \frac{1}{2}\left\|i(\boldsymbol{d}_i^{\text{obs}} - \boldsymbol{d}_i)\right\|_2^2,\end{aligned}$$

and reformulate it as a real-valued problem of double length by making use of $\|ic\|_2^2 = \|c\|_2^2$, such that

$$\Phi = \frac{1}{2}\left\|\begin{bmatrix}\boldsymbol{d}_r^{\text{obs}}\\ \boldsymbol{d}_i^{\text{obs}}\end{bmatrix} - \begin{bmatrix}\boldsymbol{d}_r\\ \boldsymbol{d}_i\end{bmatrix}\right\|_2^2 = \frac{1}{2}\left\|\begin{bmatrix}\Re(\boldsymbol{d}^{\text{obs}} - \boldsymbol{d})\\ \Im(\boldsymbol{d}^{\text{obs}} - \boldsymbol{d})\end{bmatrix}\right\|_2^2. \tag{B.14}$$

The respective gradient is given by

$$\nabla_{\boldsymbol{m}}\Phi(\boldsymbol{m}) = -\begin{bmatrix}\Re(\boldsymbol{J})\\ \Im(\boldsymbol{J})\end{bmatrix}^{\top}\begin{bmatrix}\Re(\boldsymbol{d}^{\text{obs}} - \boldsymbol{d})\\ \Im(\boldsymbol{d}^{\text{obs}} - \boldsymbol{d})\end{bmatrix}, \tag{B.15}$$

which is equal to approach appendix B.1.

B.3 Consistency of operations

It holds for products of the Jacobian matrix $\boldsymbol{J} \in \mathbb{C}^{N\times M}$ with the vectors $\boldsymbol{x} \in \mathbb{R}^M$ that

$$\begin{bmatrix}\Re(\boldsymbol{J}(\boldsymbol{m})\boldsymbol{x})\\ \Im(\boldsymbol{J}(\boldsymbol{m})\boldsymbol{x})\end{bmatrix} = \begin{bmatrix}\Re(\boldsymbol{J}(\boldsymbol{m}))\\ \Im(\boldsymbol{J}(\boldsymbol{m}))\end{bmatrix}\boldsymbol{x}, \tag{B.16}$$

and with vectors $\boldsymbol{y} \in \mathbb{C}^N$ that

$$\begin{aligned}\Re\left(\boldsymbol{J}(\boldsymbol{m})^{\mathsf{H}}\boldsymbol{y}\right) &= \Re\left((\boldsymbol{J}_r + i\boldsymbol{J}_i)^{\mathsf{H}}(\boldsymbol{y}_r + i\boldsymbol{y}_i)\right),\\ &= \Re\left(\boldsymbol{J}_r^{\top}\boldsymbol{y}_r + i\boldsymbol{J}_r^{\top}\boldsymbol{y}_i - i\boldsymbol{J}_i^{\top}\boldsymbol{y}_r + \boldsymbol{J}_i^{\top}\boldsymbol{y}_i\right),\\ &= \boldsymbol{J}_r^{\top}\boldsymbol{y}_r + \boldsymbol{J}_i^{\top}\boldsymbol{y}_i,\\ &= \begin{bmatrix}\Re(\boldsymbol{J}(\boldsymbol{m}))\\ \Im(\boldsymbol{J}(\boldsymbol{m}))\end{bmatrix}^{\top}\begin{bmatrix}\Re(\boldsymbol{y})\\ \Im(\boldsymbol{y})\end{bmatrix}.\end{aligned} \tag{B.17}$$

Bibliography

Abramowitz, Milton and Irene A. Stegun (1972). *Handbook of Mathematical Functions with Formulas, Graphs, and Mathematical Tables.* 10th ed. Dover Publications.

Anderson, Walter L. (1975). *Improved Digital Filters for Evaluating Fourier and Hankel Transform Integrals.* Tech. rep. U.S. Geological Survey.

– (1982). "Fast Hankel Transforms Using Related and Lagged Convolutions". In: *ACM Transactions on Mathematical Software* 8.4, pp. 344–368.

Arab-Amiri, Ali Reza, Ali Moradzadeh, Nader Fathianpour, and Bernhard Siemon (2010). "Inverse Modeling of HEM Data Using a New Inversion Algorithm". In: *Journal of Mining & Environment* 1, pp. 9–20.

Aruliah, Dhavide A. and U. M. Ascher (2003). "Multigrid Preconditioning for Krylov Methods for Time-harmonic Maxwell's Equations in Three Dimensions". In: *SIAM Journal on Scientific Computing* 24, pp. 702–718.

Avdeev, Dimitry B. (2005). "Three-dimensional Electromagnetic Modelling and Inversion from Theory to Application". In: *Surveys in Geophysics* 26, pp. 767–799.

Avdeev, Dimitry B. and Anna D. Avdeeva (2006). "A Rigorous Three-dimensional Magnetotelluric Inversion". In: *Progress In Electromagnetics Research* 62, pp. 41–48.

Bazán, Fermín S. Viloche, Leonardo S. Borges, and Juliano B. Francisco (2012). "On a Generalization of Regińka's Parameter Choice Rule and its Numerical Realization in Large-scale Multi-parameter Tikhonov Regularization". In: *Applied Mathematics and Computation* 219, pp. 2100–2113.

Beard, Les P. (2000). "Comparison of Methods for Estimating Earth Resistivity from Airborne Electromagnetic Measurements". In: *Journal of Applied Geophysics* 45, pp. 239–259.

Becker, Alex, H. Frank Morrison, and K . Smits (1983). *Analysis of Airborne Electromagnetic Systems for Mapping Thickness of Sea Ice.* Tech. rep. Naval Ocean Research and Development Activity.

Börner, Ralph-Uwe (2010). "Numerical Modelling in Geo-Electromagnetics: Advances and Challenges". In: *Surveys in Geophysics* 31, pp. 225–245.

Börner, Ralph-Uwe, Oliver G. Ernst, and Klaus Spitzer (2012). "A 3-D Finite Difference Forward Modelling Framework for MT and CSEM Applications". In: *Protokoll über das 24. Schmucker-Weidelt-Kolloquium für Elektromagnetische Tiefenforschung, Neustadt an der Weinstraße, 19.-23. September , 2011.*

Christensen, Niels Bøie (1990). "Optimized Fast Hankel Transform Filters". In: *Geophysical Prospecting* 38, pp. 545–568.

Commer, Michael and Gregory A. Newman (2008). "New Advances in Three-dimensional Controlled-Source Electromagnetic Inversion". In: *Geophysical Journal International* 172, pp. 513–535.

Cox, Leif H., Glenn A. Wilson, and Michael S. Zhdanov (2010). “3D Inversion of Airborne Electromagnetic Data Using a Moving Footprint”. In: *Exploration Geophysics* 41, pp. 250–259.

– (2012). “3D Inversion of Airborne Electromagnetic Data”. In: *Geophysics* 77.4, WB59–WB69.

Cox, Leif H. and Michael S. Zhdanov (2007a). “Large Scale 3D Inversion of HEM Data Using a Moving Footprint”. In: *2007 SEG Annual Meeting, September 23 - 28, 2007, San Antonio, Texas.* Society of Exploration Geophysicists.

– (2007b). “Rapid and Rigorous 3D Inversion of Airborne Electromagnetic Data”. In: *SEG Technical Program Expanded Abstracts* 25, pp. 795–799.

Everett, Mark E. (2011). “Theoretical Developments in Electromagnetic Induction Geophysics with Selected Applications in the Near Surface”. In: *Surveys in Geophysics* 33, pp. 29–63.

Farquharson, Colin G. and Douglas W. Oldenburg (2004). “A Comparison of Automatic Techniques for Estimating the Regularization Parameter in Non-linear Inverse Problems”. In: *Geophysical Journal International* 156, pp. 411–425.

Fraser, Douglas C. (1972). “A new Multicoil Aerial Electromagnetic Prospecting System”. In: *Geophysics* 37, pp. 518–537.

– (1974). “Survey Experience with the Dighem AEM System”. In: *Canadian Institute of Mining, Metallurgy and Petroleum* April, pp. 97–103.

– (1978a). “Resistivity Mapping with an Airborne Multicoil Electromagnetic System”. In: *Geophysics* 43, pp. 144–172.

– (1978b). “Geophysics of the Montcalm Township Copper-Nickel Discovery”. In: *Canadian Institute of Mining, Metallurgy and Petroleum* January, pp. 99–104.

Ghosh, Deva P. (1971). “The Application of Linear Filter Theory to the Direct Interpretation of Geoelectrical Resistivity Sounding Measurements”. In: *Geophysical Prospecting* 19, pp. 192–217.

Golub, Gene H., Michael Heath, and Grace Wahba (1979). “Generalized Cross-validation as a Method for Choosing a Good Ridge Parameter”. In: *Technomatrics* 21, pp. 215–223.

Götze, Hans-Jürgen, Martin Afanasjew, Michael Alvers, Liliana Barrio-Alvers, Ralph-Uwe Börner, Christian Brandes, Rudolf Eröss, Peter Menzel, Uwe Meyer, Mathias Scheunert, Bernhard Siemon, Klaus Spitzer, Dominik Steinmetz, Johannes Stoll, Sudha, Bülent Tezkan, Angelika Ullmann, and Jutta Winsemann (2013). “Towards an Integrative Inversion and Interpretation of Airborne and Terrestrial Data”. Springer Publication.

Grayver, Alexander Vladimirovich (2013). “Three-dimensional Controlled-source Electromagnetic Inversion Using Modern Computational Concepts”. PhD thesis. Freie Universität Berlin.

Grayver, Alexander Vladimirovich and Markus Bürg (2014). “Robust and Scalable 3-d Geo-electromagnetic Modelling Approach Using the Finite Element Method”. In: *Geophysical Journal International* 198, pp. 110–125.

Günther, Thomas (2004). “Inversion Methods and Resolution Analysis for the 2D/3D Reconstruction of Resistivity Structures from DC Measurements”. PhD thesis. Technische Universität Bergakademie Freiberg.

Gutzmer, Jens and Andreas Klossek (2014). “Strategische Rohstoffe - Risikovorsorge”. In: ed. by Peter Kausch, Martin Bertau, Jens Gutzmer, and Jörg Matschullat. Springer Berlin

Heidelberg. Chap. Die Versorgung mit wirtschaftskritischen Rohstoffen – Eine Ursachensuche und -analyse, pp. 61–73.

Haas, Christian, Marcel Nicolaus, Sascha Willmes, Anthony Worby, and David Flinspach (2007). "Sea Ice and Snow Thickness and Physical Properties of an Ice Floe in the Western Weddell Sea and their Changes During Spring Warming". In: *Deep-Sea Research II* 55, pp. 963–974.

Haber, Eldad (2005). "Quasi-Newton Methods for Large-scale Electromagnetic Inverse Problems". In: *Inverse Problems* 21, pp. 305–323.

– (2014). *computational Methods in Geophysical Electromagnetics*. Ed. by Thomas A. Grandine. Society for Industrial and Applied Mathematics.

Haber, Eldad and Uri M. Ascher (2000). "On Optimization Techniques for Solving Nonlinear Inverse Problems". In: *Inverse Problems* 16, pp. 1263–1280.

Haber, Eldad and Stefan Heldmann (2007). "An Octree Multigrid Method for Quasi-static Maxwell's Equations with Highly Discontinuous Coefficients". In: *Journal of Computational Physics* 223, pp. 783–796.

Haber, Eldad and Douglas W. Oldenburg (2000). "A GCV Based Method for Nonlinear Ill-posed Problems". In: *Computational Geosciences* 4, pp. 41–63.

Hansen, Per Christian and Dianne Prost O'Leary (1993). "The Use of L-curve in the Regularization of Discrete Ill-posed Problems". In: *SIAM Journal on Scientific Computing* 14.6, pp. 1487–1503.

Hestenes, Magnus Rudolph and Eduard Stiefel (1952). "Methods of Conjugate Gradients for Solving Linear Systems". In: *Journal of Research of the National Bureau of Standards* 49.6, pp. 409–436.

Holladay, J. Scott and Bob Lo (1997). "Airborne Frequency-Domain EM - Review and Preview". In: *Proceedings of Exploration 97: Fourth Decennial International Conference on Mineral Exploration*. Ed. by G. Gubins A. 97, pp. 505–514.

Jiracek, George R. (1990). "Near-surface and Topographic Distortions in Electromagnetic Induction". In: *Surveys in Geophysics* 11, pp. 163–203.

Johansen, H. K. and K. Sørensen (1979). "Fast Hankel Transforms". In: *Geophysical Prospecting* 27, pp. 876–901.

Kaipio, Jari and Erkki Somersalo (2007). "Statistical Inverse Problems: Discretization, Model Reduction and Inverse Crimes". In: *Journal of Computational and Applied Mathematics* 198, pp. 493–504.

Karypis, George and Vipin Kumar (1998). "A Fast and High Quality Multilevel Scheme for Partitioning Irregular Graphs". In: *SIAM Journal on Scientific Computing* 20, pp. 359–392.

Knödel, Klaus, Heinrich Krummel, and Gerhard Lange (2005). *Handbuch zur Erkundung des Untergrundes von Deponien und Altlasten*. 2nd ed. Springer.

Lelièvre, Peter G., Colin G. Farquharson, and Charles A. Hurich (2012). "Joint Inversion of Seismic Traveltimes and Gravity Data on Unstructured Grids with Application to Mineral Exploration". In: *Geophysics* 77.1, K1–K15.

Liu, Guimin and Alex Becker (1990). "Two-dimensional Mapping of Sea-ice Keels with Airborne Electromagnetics". In: *Geophysics* 55, pp. 239–248.

Lowry, T., M. B. Allen, and P. N. Shive (1989). “Singularity Removal: A Refinement of Resistivity Modeling Techniques”. In: *Geophysics* 54, pp. 766–774.

Mackie, Randall L. and Theodore R. Madden (1993). “Three-dimensional Magnetotelluric Inversion Using Conjugate Gradients”. In: *Geophysical Journal International* 115, pp. 215–229.

Martin, Roland (2009). “Development and Application of 2D and 3D Transient Electromagnetic Inverse Solutions Based on Adjoint Green Functions: A Feasibility Study for the Spatial Reconstruction of Conductivity Distributions by Means of Sensitivities”. PhD thesis. Universität zu Köln.

McGillivray, Peter R. and Douglas W. Oldenburg (1990). “Methods for Calculating Fréchet Derivatives and Sensitivities for the Non-linear Inverse Problem: A Comparitive Study”. In: *Geophysical Prospecting* 38, pp. 499–524.

Miensopust, Marion P., Bernhard Siemon, Ralph-Uwe Börner, and Seyedmasoud Ansari (2014). “3-D Forward Modelling of Frequency-domain Helicopter-borne Electromagnetic Data: A Comparative Study”. In: *Protokoll über das 25. Schmucker-Weidelt-Kolloquium für Elektromagnetische Tiefenforschung, Kirchhundem-Rahrbach, 23.-27. September, 2013.*

Minsley, Burke J., Jared D. Abraham, Bruce D. Smith, James C. Cannia, Clifford I. Voss, M. Torre Jorgenson, Michelle A. Walvoord, Bruce K. Wylie, Lesleigh Anderson, Lyndsay B. Ball, Maryla Deszcz-Pan, Tristan P. Wellman, and Thomas A. Ager (2012). “Airborne Electromagnetic Imaging of Discontinuous Permafrost”. In: *Geophysical Research Letters* 39, pp. 1–8.

Newman, Gregory A. and David L. Alumbaugh (1995). “Frequency-domain Modelling of Airborne Electromagnetic Responses Using Staggered Finite Differences”. In: *Geophgsical Prospecting* 43, lO21–1O42.

– (2002). “Three-dimensional Induction Logging Problems, Part 2: A Finite-difference Solution”. In: *Surveys in Geophysics* 67.2, pp. 484–491.

Newman, Gregory A. and Gary Michael Hoversten (2000). “Solution Strategies for Two- and Three-dimensional Electromagnetic Inverse Problems”. In: *Inverse Problems* 16, pp. 1357–1375.

Nocedal, Jorge and Stephen J. Wright (2006). *Numerical Optimization.* 2nd ed. Springer.

Paige, Christopher C. and Michael A. Saunders (1982). “LSQR: An Algorithm for Sparse Linear Equations and Sparse Least Squares”. In: *ACM Transactions on Mathematical Software* 8.1, pp. 43–71.

Pidlisecky, Adam, Eldad Haber, and Rosemary Knight (2007). “RESINVM3D: A 3D Resistivity Inversion Package”. In: *Geophysics* 72, H1–H10.

Raiche, Art, Fred Sugeng, and Glenn Wilson (2007). “Practical 3D EM inversion - the P223F Software Suite”. In: *ASEG Extended Abstracts, 2007.*

Rodi, William L. (1976). “A Technique for Improving the Accuracy of Finite Element Solutions for Magnetotelluric Data”. In: *Geophysical Journal of the Royal Astronomical Society* 44, pp. 483–506.

Rodi, William L. and Randall L. Mackie (2001). “Nonlinear Conjugate Gradients Algorithm for 2-D Magnetotelluric Inversion”. In: *Geophysics* 66.1, pp. 174–187.

Saad, Yousef (2003). *Iterative Methods for Sparse Linear Systems.* 2nd ed. Society for Industrial and Applied Mathematics.

Sasaki, Yutaka (2001). "Full 3-D Inversion of Electromagnetic Data on PC". In: *Journal of Applied Geophysics* 46, pp. 45–54.

Sattel, Daniel (2005). "Inverting Airborne Electromagnetic (AEM) Data with Zohdy's Method". In: *Geophysics* 70, G77–G85.

Scales, John A., Martin L. Smith, and Sven Treitel (2001). *Introductory Geophysical Inverse Theory.* 1st ed. Samizdat Press.

Schenk, Olaf and Klaus Gärtner (2004). "Solving Unsymmetric Sparse Systems of Linear Equations with PARDISO". In: *Journal of Future Generation Computer Systems* 20, pp. 475–487.

– (2006). "On Fast Factorization Pivoting Methods for Symmetric Indefinite Systems". In: *Electronic Transactions on Numerical Analysis* 23, pp. 158–179.

Scheunert, Mathias, Ralph-Uwe Börner, and Bernhard Siemon (2013). "EM Fields of a VMD Calculated at Arbitrary Points within a Layered Half-space". In: *Protokoll über das 25. Schmucker-Weidelt-Kolloquium für Elektromagnetische Tiefenforschung.* Ed. by Ralph-Uwe Börner and Katrin Schwalenberg. Deutsche Geophysikalische Gesellschaft e. V.

Schwarzbach, Christoph (2009). "Stability of Finite Element Solutions to Maxwell's Equations in Frequency Domain". PhD thesis. Technische Universität Bergakademie Freiberg.

Schwarzbach, Christoph, Ralph-Uwe Börner, and Klaus Spitzer (2011). "Three-dimensional Adaptive Higher Order Finite Element Simulation for Geo-electromagnetics - a Marine CSEM Example". In: *Geophysical Journal International* 187, pp. 63–74.

Sen, Mrinal K. and Paul L. Stoffa (1995). *Global Optimization Methods in Geophysical Inversion.* 1st ed. Elsevier Science.

Sengpiel, K.-P. (1988). "Approximate Inversion of Airborne EM Data from a Multilayered Ground". In: *Geophysical Prospecting* 36, pp. 446–459.

Siemon, Bernhard (2001). "Improved and new Resistivity-depth Profiles for Helicopter Electromagnetic Data". In: *Journal of Applied Geophysics* 46, pp. 65–76.

– (2012). "Accurate 1D Forward and Inverse Modeling of High-frequency Helicopter-borne Electromagnetic Data". In: *Geophysics* 77, WB71–WB87.

Siemon, Bernhard, Esben Auken, and Anders Vest Christiansen (2009). "Laterally Constrained Inversion of Helicopter-borne Frequency-domain Electromagnetic Data". In: *Journal of Applied Geophysics* 67, pp. 259–268.

Siemon, Bernhard, Anders Vest Christiansen, and Esben Auken (2009). "A Review of Helicopter-borne Electromagnetic Methods for Groundwater Exploration". In: *Near Surface Geophysics* 7, pp. 629–646.

Siemon, Bernhard, Detlef G. Eberle, and Franz Binot (2004). "Helicopter-borne Electromagnetic Investigation of Coastal Aquifers in North-West Germany". In: *Zeitschrift für geologische Wissenschaften* 32, pp. 385–395.

Siripunvaraporn, Weerachai, Gary Egbert, Yongwimon Lenbury, and Makoto Uyeshima (2005). "Three-dimensional Magnetotelluric Inversion: Data-space Method". In: *Physics of the Earth and Planetary Interiors* 150, pp. 3–14.

Smith, J. Torquil and John R. Booker (1988). "Magnetotelluric Inversion for Minimum Structure". In: *Geophysics* 53.12, pp. 1565–1576.

Spies, B. R. and F. C. Frischknecht (1991). "Electromagnetic Sounding". In: *Electromagnetic Methods in Applied Geophysics*. Ed. by M. N. Nabighian. Vol. 2, Application, Parts A and B. Investigations in Geophysics 3. Society of Exploration Geophysicists. Chap. 6, pp. 285–426.

Spitzer, Klaus (1998). "The Three-dimensional DC Sensitivity for Surface and Subsurface Sources". In: *Geophysical Journal International* 134, pp. 736–746.

Steinmetz, Dominik, Jutta Winsemann, Christian Brandes, Bernhard Siemon, Angelika Ullmann, Helga Wiederhold, and Uwe Meyer (2015). "Towards an Improved Geological Interpretation of Airborne Electromagnetic Data: A Case Study from the Cuxhaven Tunnel Valley and its Neogene Host Sediments (Northwest Germany)". In: *Netherlands Journal of Geosciences*, pp. 1–27.

Telford, William Murray, Lloyd P. Geldart, and Robert Edward Sheriff (1990). *Applied Geophysics*. 2nd ed. Cambridge University Press.

Tikhonov, Andrey Nikolayevich and Vasiliy Y. Arsenin (1977). *Solutions of Ill-posed Problems*. Ed. by John B. Bell. Scripta Series in Mathematics. Winston.

Tølbøll, Rasmus Juhl and Niels Bøie Christensen (2006). "Robust 1D Inversion and Analysis of Helicopter Electromagnetic (HEM) Data". In: *Geophysics* 71, G53–G62.

Ullmann, Angelika, Mathias Scheunert, Martin Afanasjew, Ralph-Uwe Börner, Bernhard Siemon, and Klaus Spitzer (2015). "Cut-&-Paste 3-D Inversion of Helicopter-borne Electromagnetic Data – II. Combining 1-D and 3-D Inversion". In: *Journal of Applied Geophysics*. submitted.

Ullmann, Angelika, Bernhard Siemon, Mathias Scheunert, Martin Afanasjew, Ralph-Uwe Börner, Klaus Spitzer, and Marion Miensopust (2013). "Combined 1-D and 3-D Inversion of Helicopter-borne Electromagnetic Data". In: *Near Surface Geoscience 2013*.

Vogel, Curtis R. (2002). *Computational Methods for Inverse Problems*. Frontiers in Applied Mathematics.

Ward, Stanley H. and Gerald W. Hohmann (1988). "Electromagnetic Theory for Geophysical Applications". In: *Electromagnetic Methods in Applied Geophysics*. Ed. by M. N. Nabighian. Vol. 1, Theory. Investigations in Geophysics 3. Society of Exploration Geophysicists, pp. 130–311.

Wilson, Glenn A., Leif H. Cox, and Martin Cuma (2012). "Inverting Airborne Geophysical Data for Mega-cell and Giga-cell 3D Earth Models". In: *The Leading Edge* 31, pp. 316–321.

Xiong, Zonghou and Alan C. Tripp (1997). "3-D Electromagnetic Modeling for Near-surface Targets Using Integral Equations". In: *Geophysics* 62.4, pp. 1097–1106.

Yang, Dikun, Douglas W. Oldenburg, and Eldad Haber (2013). "3-D Inversion of Airborne Electromagnetic Data Parallelized and Accelerated by Local Mesh and Adaptive Soundings". In: *Geophysical Journal International* 196, pp. 1492–1507.

Yee, Kane S. (1966). "Numerical Solution of Initial Boundary Value Problems Involving Maxwell's Equations in Isotropic Media". In: *IEEE Transactions on Antennas and Propagation* 14, pp. 302–307.

Yin, Changchun and Greg Hodges (2005). "Influence of Displacement Currents on the Response of Helicopter Electromagnetic Systems". In: *Geophysics* 70.4, G95–G100.

– (2007). "Simulated Annealing for Airborne EM Inversion". In: *Geophysics* 72, F189–F195.

Zhang, Jie, Randall L. Mackie, and Theodore R. Madden (1995). "3-D Resistivity Forward Modeling and Inversion Using Conjugate Gradients". In: *Geophysics* 60, pp. 1313–1325.

Zhdanov, Michael S. (2009). *Geophysical Electromagnetic Theory and Methods.* 1st ed. Elsevier.

Zhdanov, Michael S. and Efthimios Tartaras (2002). “Three-dimensional Inversion of Multi-transmitter Electromagnetic Data Based on the Localized Quasi-linear Approximation”. In: *Geophysical Journal International* 148, pp. 506–519.

Zhengyong, Ren (2012). “New Developments in Numerical Modeling of Broadband Geo-electromagnetic Fields”. PhD thesis. ETH Zürich.

Versicherung

Hiermit versichere ich, dass ich die vorliegende Arbeit ohne unzulässige Hilfe Dritter und ohne Benutzung anderer als der angegebenen Hilfsmittel angefertigt habe; die aus fremden Quellen direkt oder indirekt übernommenen Gedanken sind als solche kenntlich gemacht.

Die Hilfe eines Promotionsberaters habe ich nicht in Anspruch genommen. Weitere Personen haben von mir keine geldwerten Leistungen für Arbeiten erhalten, die nicht als solche kenntlich gemacht worden sind.

Die Arbeit wurde bisher weder im Inland noch im Ausland in gleicher oder ähnlicher Form einer anderen Prüfungsbehörde vorgelegt.

27.11.2015 Mathias Scheunert